BEILSTEIN JOURNAL OF NANOTECHNOLOGY

Transport through molecular junctions

Edited by Jan M. van Ruitenbeek

Imprint

Beilstein Journal of Nanotechnology
www.bjnano.org
ISSN 2190-4286
Email: journals-support@beilstein-institut.de

The *Beilstein Journal of Nanotechnology* is published by the Beilstein-Institut zur Förderung der Chemischen Wissenschaften.

Beilstein-Institut zur Förderung der Chemischen Wissenschaften
Trakehner Straße 7–9
60487 Frankfurt am Main
Germany
www.beilstein-institut.de

Beilstein Journal of Nanotechnology

Transport through molecular junctions

Jan M. van Ruitenbeek

Editorial

Open Access

Address:
Kamerlingh Onnes Laboratory, Leiden Institute of Physics, Leiden University, Niels Bohrweg 2, 2333 CA Leiden, The Netherlands

Email:
Jan M. van Ruitenbeek - Ruitenbeek@physics.leidenuniv.nl

Beilstein J. Nanotechnol. **2011,** *2,* 691–692.
doi:10.3762/bjnano.2.74

Received: 04 October 2011
Accepted: 07 October 2011
Published: 18 October 2011

This article is part of the Thematic Series "Transport through molecular junctions".

Editor-in-Chief: T. Schimmel

Exploiting the rich design space of organic molecules for applications in future electronic devices is one of the main challenges in nanotechnology. Several groups have recently demonstrated, for a limited set of molecules, clear single-molecule characteristics and fair agreement with computations. Now that attaching leads to individual molecules has been demonstrated we naturally enter into the next exciting phase of the research, where molecule-specific properties can be engineered and studied.

The most prominent property that distinguishes organic molecules from inorganic quantum dots and nanowires is that they are floppy nano-objects with a strong coupling between charge transport and vibrational degrees of freedom (vibrons). This coupling is predicted to influence transport in dramatic ways as it may destroy the coherence of charge carriers on the molecules and can lead to strong nonequilibrium effects. Many exciting predictions have been discussed in the recent literature showing unique features of single-molecule junctions. These properties can be designed and controlled by chemists.

Studying them experimentally requires creating an interface between the molecules and at least two metallic leads. Standard nanofabrication techniques fall short by more than an order of magnitude in the distance and precision required for addressing molecules, which typically have a length of the order of one nanometre. Several methods have now been established that can meet the requirements, of which three are particularly prominent: The electrode separation can be mechanically adjusted at will, through piezoelectric actuators, in a setup based on a scanning tunnelling microscope. Alternatively, this can be achieved by mechanically controllable break junctions. A third, widely used method employs breaking of a thin wire by electromigration. Many methods have been explored for introducing the molecules into the junction, but in all cases there is an element of chance, and variations in the attachment of the molecule in the nanogap between the electrodes are common. It is now widely recognized that the variability in bonding, which is most clearly observed through the variability in conductance, is part of the physics of the problem and inherent to (single) molecular junctions. The study of such junctions requires the gathering of statistics covering many configurations.

The field of study of electron transport through molecular junctions requires input from many subdisciplines and this interdisciplinary character leads to many new initiatives and research

consortia. Theoretical research is strongly represented, and is leading the experiments. This illustrates the fact that many aspects are still unexplored, but also that experiments are difficult. The past has seen some premature claims and overly enthusiastic presentations of results that have later been proven hard to reproduce. Molecules are simply very small objects, and while we are capable of visualizing molecules by various techniques, such approaches are still incompatible with molecules being directly coupled to metallic leads. Consequently, the measured results are often interpreted based upon reasonable assumptions regarding the geometry of the molecular bonding. Our imagination has often been shown to be too limited to capture all aspects of the actual molecular device. More recently, new techniques have been developed that shed further light onto the problem and help build confidence in our interpretations. Apart from direct conductance measurements, one now measures properties such as thermopower, shot noise, Raman scattering, photo-induced switching, and gate-induced level shifts, all at the single-molecule level. Moreover, by systematic variation of the chemical structure of the molecule, it is possible to map out the dominant current-carrying pathways in the molecule and to systematically explore the effects of bond angles and side groups.

Our field of study also poses new challenges to theory and computational methods. Density functional theory is well established and the limits of its validity are well known when applied to bulk metallic systems, as well as to organic molecules in isolation. However, these two quite separate application areas need to be married together, and there is the additional problem of the nonequilibrium electron distribution resulting from the applied bias. The new challenges that this brings have attracted the attention of many of the best groups in world and important progress has been made in the theoretical and computational methods.

More recently, a new element has been added to the discussion. The electron flow is known to exert a force on the ions, which is responsible for the phenomenon of electromigration mentioned above. However, the microscopic theory for the effect is poorly understood. It has recently been shown, through seminal work by Todorov and his group, that the electron force is nonconservative. This implies that the current is capable of doing work and that it should be possible to devise molecular motors that are directly driven by an electron current.

I am pleased to see that we have succeeded in bringing together, in this Thematic Series, contributions of experimental and theoretical research in physics and chemistry from some of the most prominent groups in this field. The works published in this thematic series of the Beilstein Journal of Nanotechnology illustrate the vitality of the research and the many lines along which the research is developing. Together, the papers give a snapshot of where the field stands at this moment.

Jan M. van Ruitenbeek

Leiden, October 2011

Beilstein Journal of Nanotechnology

Interaction of spin and vibrations in transport through single-molecule magnets

Falk May[1,2], Maarten R. Wegewijs[*3,4] and Walter Hofstetter[1]

Full Research Paper

Open Access

Address:
[1]Institut für Theoretische Physik, Johann Wolfgang Goethe-Universität, 60438 Frankfurt/Main, Germany, [2]Max Planck Institute for Polymer Research, 55128 Mainz, Germany, [3]Institut für Theorie der Statistischen Physik, RWTH Aachen, 52056 Aachen, Germany and [4]Peter Grünberg Institut and JARA - Fundamentals of Information Technology, Forschungszentrum Jülich, 52425 Jülich, Germany

Email:
Maarten R. Wegewijs[*] - m.r.wegewijs@fz-juelich.de

* Corresponding author

Keywords:
molecular electronic devices; molecular magnets; nanoelectronic devices; quantum dots

Beilstein J. Nanotechnol. **2011,** *2,* 693–698.
doi:10.3762/bjnano.2.75

Received: 02 July 2011
Accepted: 03 September 2011
Published: 18 October 2011

This article is part of the Thematic Series "Transport through molecular junctions".

Guest Editor: J. M. van Ruitenbeek

Abstract

We study electron transport through a single-molecule magnet (SMM) and the interplay of its anisotropic spin with quantized vibrational distortions of the molecule. Based on numerical renormalization group calculations we show that, despite the longitudinal anisotropy barrier and small transverse anisotropy, vibrational fluctuations can induce quantum spin-tunneling (QST) and a QST-Kondo effect. The interplay of spin scattering, QST and molecular vibrations can strongly enhance the Kondo effect and induce an anomalous magnetic field dependence of vibrational Kondo side-bands.

Introduction

Transport measurements on nanometer-sized magnetic systems address the fundamental problem of how a few magnetic atoms in an anisotropic environment respond to an electron current [1]. Such an environment is provided, for instance, by ligand groups holding such atoms together in a single magnetic molecule contacted in a break junction [2,3]. A very similar situation arises for transport through magnetic atoms embedded in a molecular network on an insulating surface in an STM setup [4,5]. Such systems, which for simplicity we shall refer to as single-molecule magnets (SMM), constitute a single, large spin-moment with spin-anisotropy. The interplay with quantum transport provides new possibilities to study and control their molecular magnetism. For instance, tunneling allows access to several charge states of the SMM, which can exhibit enhanced magnetic properties [2]. When such charge states are only virtually accessible, effective spin–spin exchange interaction arises [4,5] and inelastic excitation of the spin moment is possible [2], allowing for time-dependent control [6]. A key result is that in

either regime the transport depends sensitively on the magnetic anisotropy of the SMM, which is characterized by spin-quadrupole terms in the Hamiltonian. A further new aspect is the recently demonstrated mechanical tuning of these anisotropy terms in a transport setup [3]. Although the effect of such molecular distortions on magnetization measurements of SMM crystal samples has been addressed [7-9], so far their dynamic effect on transport through an SMM have not been studied. One candidate that may enable the sensitive probing of such a coupling of the SMM *spin* to vibrations is a specific type of Kondo effect induced by quantum spin-tunneling (QST). This QST, through the energy barrier arising from a dominant uniaxial magnetic anisotropy term, relies on the presence of weak transverse anisotropy. Combined with the exchange tunneling to attached electrodes, a QST-Kondo resonance specific to SMMs can arise [10]. One might expect such QST-assisted Kondo transport to be simply suppressed by coupling of the spin to molecular vibrations, as this tends to increase the anisotropy barrier [9]. However, the dynamic effect of vibrational fluctuations and the possible competition between longitudinal and transverse spin–vibration coupling have not been studied so far, even though coupling to vibrations in the Kondo regime has been considered for spin-isotropic molecules [11-14].

In this paper we consider the modulation of the magnetic anisotropy of an SMM by a quantized vibrational mode distorting an SMM with half-integer spin. Strikingly, even *without* static transverse anisotropy, a QST-induced Kondo peak can arise in the differential conductance. This Kondo effect is dynamically generated by vibrational fluctuations which distort the SMM, and thereby allow the spin to fluctuate. More generally, a higher QST-Kondo temperature may result from spin-vibration coupling, which is relevant for experimental investigation of low temperature transport through SMMs. This enhancement of the interplay of Kondo spin scattering and QST by discrete vibrations indicates a possible avenue along which transport and quantum magnetism may be combined with nanomechanical effects.

Model and method

We consider an SMM strongly coupled to electronic leads at low temperature in the Coulomb blockade regime, where the charge on the SMM only changes virtually. We assume that the spin couples to a local vibrational mode with frequency Ω. The total Hamiltonian reads $H = H_{\rm SMM} + H_{\rm K}$ with

$$H_{\rm SMM} = -DS_z^2 + \frac{1}{2}E\left(S_+^2 + S_-^2\right) + \Omega b^\dagger b + \left[-D'S_z^2 + \frac{1}{2}E'\left(S_+^2 + S_-^2\right)\right]\left(b^\dagger + b\right) \quad (1)$$

$$H_{\rm K} = \sum_{k\sigma}\varepsilon_{k\sigma}a_{k\sigma}^\dagger a_{k\sigma} + J\mathbf{S}\cdot\mathbf{s} \quad (2)$$

Here S_z is the projection of the molecule's spin along its easy axis, which we choose to be the z-axis and $S_\pm = S_x \pm iS_y$. We consider here only half-integer values of the spin magnitude S, for which there is a Kondo effect at zero magnetic field [10], and later comment on the integer-spin case. Starting from an isolated molecule, the longitudinal anisotropy D splits the eigenstates of S_z into the inverted parabolic magnetic spectrum that is sketched in Figure 1 for the representative case of $S = 3/2$ used throughout this work. The zero-field splitting (ZFS) corresponds to the energy difference between the ground-state and the first magnetic excitation, and equals $\delta = (2S-1)D$ for $E = 0$ (and $E' = D' = 0$). The transverse anisotropy E breaks the continuous rotational symmetry about the easy-axis of the SMM, thereby causing spin-tunneling through the barrier. As shown in [9], vibrational modes modulate the magnetic anisotropy and can significantly contribute to the observed magnetic splittings. Here we additionally consider the dynamic effects of such coupling by allowing the dominant anisotropy parameters to depend linearly on the vibrational mode coordinate $Q = (b + b^\dagger)/\sqrt{2}$, through the coupling coefficients D' and E'. Here the operator b ($b^\dagger$) relaxes (excites) the vibration by one quantum. Thus, when the SMM vibrates, it lowers its symmetry and QST is enhanced. Importantly, this also holds for virtual quantum vibrations. We note that recently such a linear dependence of the D parameter on the pitch angle coordinate [15] in the tetra-iron(III) "propeller"-SMM used in [2] was measured. The conduction electron states, represented by the

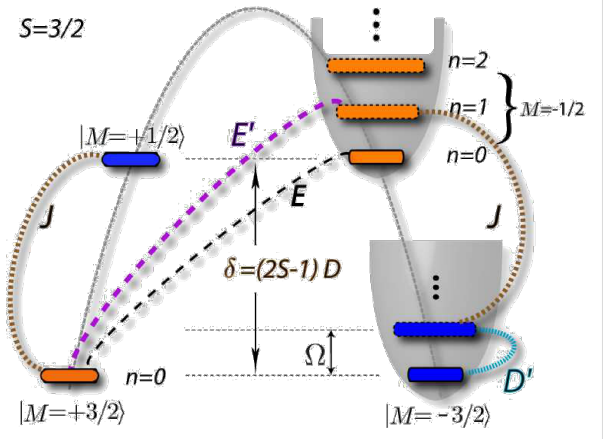

Figure 1: Magneto-mechanical excitation spectrum of the SMM with $S = 3/2$. Magnetic states, lying on an inverted parabola due to the static longitudinal anisotropy (D), each have vibrational excitations (n) on the upright parabolas. Magnetic transitions induced by Kondo spin-scattering (J), static anisotropy (E) and longitudinal (D') and transverse (E') spin-vibration coupling are indicated. Magnetic states in the two different Kramers' subspaces are marked blue and orange.

operators $a_{k\sigma}, a_{k\sigma}^{\dagger}$ in Equation 2, correspond to even combinations of left and right physical electronic states, and their bandwidth is given by $2W$. Finally, deep in the Coulomb blockade regime, the interaction of the SMM with the electrodes is given by an isotropic Heisenberg spin-exchange with the conduction band electron spin $\mathbf{s} = \frac{1}{2}\sum_{kk'}\sum_{\sigma\sigma'} a_{k\sigma}^{\dagger}\boldsymbol{\tau}_{\sigma\sigma'}a_{k'\sigma'}$ where $\boldsymbol{\tau}$ is the vector of Pauli matrices. The coupling J is assumed to be antiferromagnetic, which, as pointed out in [16], depends on the spins of the virtual charge states of the SMM [17,18]. One might expect that coupling to a molecular vibration suppresses the interaction of the SMM with the electrodes due to Franck–Condon overlap, effectively reducing J. However, for an isotropic spin of 1/2 it was shown that the effective spin-exchange amplitudes for processes that do not change the vibrational quantum number are hardly modified (in fact they may even be enhanced) and that the amplitude for processes that do change it are suppressed deep in the Coulomb blockade regime [11]. Therefore, we assume J to be independent of the vibrational coordinate in Equation 2.

The numerical results presented below for the zero-temperature differential conductance [19],

$$G(V) = \frac{e^2}{\hbar}\frac{\Gamma_L\Gamma_R}{\Gamma_L+\Gamma_R}\left(A(eV/2)+A(-eV/2)\right)$$

as a function of the bias voltage V, were obtained from the SMM spectral function $A(\omega)$. Here $\Gamma_{L,R}$ is the tunnel coupling of the SMM to the left and right electrode. We calculated $A(\omega) = \sum_{\sigma} A_{\sigma}(\omega)$ using the numerical renormalization group (NRG) from the equilibrium spectral function within the T-matrix approach [20]. In linear response to V, $A(0)$ provides a numerically exact result for the linear conductance through $G(0)$. Moreover, for strong asymmetric coupling of the SMM to the electrodes, the nonequilibrium corrections to the spectral function $A(\omega)$ are suppressed. In this case, the molecule will predominantly equilibrate with one electrode. Thus, the tunneling results only in a coupling of the spin to the combination of electrode operators that is symmetric with respect to the left/right electrode (our operators $a_{k\sigma}$ in Equation 2). Due to the finite bias there is an additional coupling of the even to the odd combination, which is proportional to the voltage V and the tunneling amplitude asymmetry. For sufficiently large asymmetry this coupling can be neglected and the function $G(V)$ provides a good first approximation to the nonlinear conductance as well for the low-lying excitations. From hereon we assume such a large asymmetry in our calculations, which results furthermore in an overall suppression of the conductance without altering the signatures of interest. Therefore the numerical results are normalized to the maximal achievable conductance. For all NRG calculations we used the NRG discretization parameter $\Lambda = 2$, kept in total $N_s = 4000$ states [21] and included 11 vibrational states on the SMM, which was sufficient to obtain results independent of the vibration number cutoff.

Static anisotropy

Even without the vibration ($E' = D' = 0$) or transport ($J = 0$) the SMM eigenstates are not spin eigenstates when $E \neq 0$. However, for the typical case of moderate transverse anisotropy, $E < D$, it still is convenient to label these mixed states by the dominant spin-eigenstate (M) in the superposition. Due to the two-fold spin-rotational symmetry of Equation 1 the mixing caused by E is only possible within the two subspaces spanned by $|\pm 1/2\rangle, |\mp 3/2\rangle$ (marked blue and orange in Figure 1). It was shown [10] that upon including exchange spin scattering with conduction band electrons (J) the interplay with the QST (generated by E) gives rise to a Kondo peak in the differential conductance. Due to the presence of the electrodes, spin fluctuations thus become significant at low temperature despite the presence of the anisotropy barrier of size DS^2 opposing SMM spin reversal. A hallmark of this QST-Kondo effect is that it is suppressed with decreasing ratio of E/D or increasing S (because the barrier grows). This QST-Kondo effect is clearly distinct from the under-screened high-spin Kondo effect [22], which arises for $S \geq 1$ in the limit without magnetic anisotropy and vibrations ($D = E = D' = E' = \Omega = 0$). Starting from this limit, introduction of the anisotropy barrier, $D > 0$, splits as well as suppresses the high-spin Kondo peak. The remnants of the high-spin Kondo peak are located at finite bias close to the ZFS scale $\delta = (2S - 1)D$, with possible renormalization to smaller values for large exchange interaction J [2].

These ZFS high-spin Kondo side-peaks have recently been studied in detail in several experiments [2-5]. The QST-Kondo peak, on the other hand, is located at zero bias in the absence of magnetic field. It has, to our knowledge, not been observed experimentally so far. One possible reason for this is that in SMMs typically $E/D < 1$ and the QST-Kondo temperature T_K is suppressed too much, reducing both the height and width of the peak (*without* splitting it).

Dynamic anisotropy

The anisotropic couplings of the large spin to the vibrational mode D' and E' are, however, also of importance [9], especially if the vibrational mode frequency energy Ω is low. The simplest effect of the longitudinal vibrational coupling D' is a polaronic shift that is different for each magnetic level. For $E = E' = 0$ one can shift the vibrational coordinate Q (or the operator b) in H_{SMM} by an S_z^2-dependent amount, resulting in an effective Hamiltonian with eigenvalues $E_{M,n} = -DM^2 - (D'^2/\Omega)M^4 + \Omega n$, where $M = -S,..,S$ and $n = 0,1,..$ are the quantum numbers of the

spin and the polaron, respectively. Each SMM eigenstate is thus dressed by vibrational excitations, as sketched in Figure 1. The effective static energy barrier opposing spin inversion is changed in shape and increased in height. This always results in an effectively *enhanced* ZFS $\delta \rightarrow \Delta$,

$$\Delta = \delta + \left(4S\left(S^2 - \frac{3}{2}S + 1\right) - 1\right)\frac{D'^2}{\Omega} \ . \qquad (3)$$

Based on this simple picture one may expect that the QST-Kondo effect is suppressed by coupling to vibrations. For fixed $E' = 0$ this is indeed the case, as can be seen in Figure 2. All reported numerical calculations were performed for parameters whose orders of magnitude relative to the typical bandwidth of several eV were chosen in agreement with known molecular parameters [15] and transport parameters [2]. The only exception to this is for the vibrational parameters E', D' and Ω, for which we performed a systematic study. We focus on low frequency modes on the scale of the anisotropy parameters, taking $\Omega = 0.5D$, for which the dynamic effects are most pronounced. We note that in STM setups [4-6] the anisotropy can be on the meV scale. For the spin value we take the next-to-lowest half-integer value $S = 3/2$, representative of the essential physics. Due to the moderate but nonvanishing static $E = 0.1D$, a zero-bias QST-Kondo peak (red) occurs, which is increasingly suppressed with the coupling D' due to an increased barrier. In addition two side-peaks are found at the effective ZFS $\omega \approx \pm\Delta$ given by Equation 3, as indicated by the dashed lines (and renormalized to a slightly smaller value due to the strong J). These peaks are the remnants of the $S = 3/2$ high-spin Kondo effect.

In Figure 3 we now focus on the dynamic effect of the spin–vibration coupling by first considering zero transverse anisotropy ($E = 0$). Without coupling to the vibrations there is no QST-Kondo peak. Switching on spin–vibration coupling of only one type, either $D' \neq 0$ and $E' = 0$ (black), or, $E' \neq 0$ and $D' = 0$ (blue), does not change this result. Only in the latter case, vibrational side-peaks appear in the spectrum at $\omega = \pm\Omega$ (renormalized to smaller value due to strong J). Strikingly, when both types of couplings are nonzero, a pronounced QST-Kondo peak appears, even though there is no transverse magnetic anisotropy $E = 0$ (red). This *vibration-induced* QST-Kondo effect is the central result of this work. We now first explain why it requires the presence of both longitudinal and transverse couplings, referring to the processes sketched in Figure 1. The Kondo effect is related to fluctuations between degenerate states of the SMM that are in opposite Kramers' subspaces [10]. Since $E = 0$, to reach states on the other side of the anisotropy barrier, a vibration-induced spin-tunneling of type E' is required, which

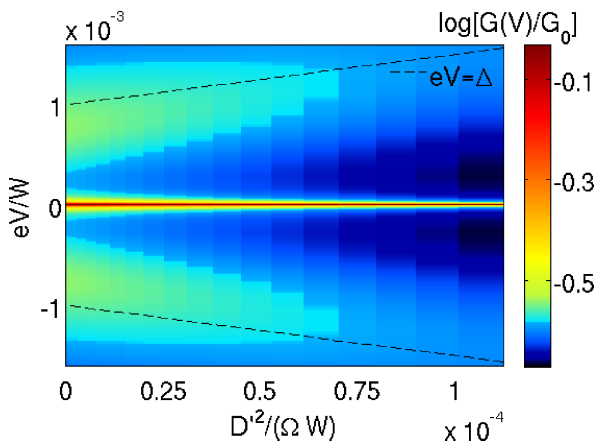

Figure 2: Logarithmic color plot of the SMM differential conductance $G(V)$ normalized to the value $G_0 = \left(e^2/h\right)\left(4\Gamma_L\Gamma_R/\left(\Gamma_L+\Gamma_R\right)^2\right)$ and for $T = 0$. Parameters are $S = 3/2$, $D = 5 \cdot 10^{-4}W$, $E = 0.1D$, $E' = 0$, $\Omega = 0.5D$, $J = 0.2W$ and D' is varied. The dashed line represents the renormalized ZFS from Equation 3.

however, involves a virtual vibrational excitation. An exchange scattering process (J), which changes the Kramers' subspace, cannot change the vibrational number at low energy [11]. This is why the two processes E' and J result only in a QST-Kondo side-peak in Figure 3, which is split at Ω and suppressed due to the inability to reach the vibrational ground-state. Only when a longitudinal spin-coupling D' is present as well, can the virtual vibrational excitation *coherently* reach the ground state and a full *zero-bias* QST-Kondo anomaly can develop, as the red curve in Figure 3 shows. One may say that due to the quantum fluctuations of the vibrational mode of the SMM, the magnetic symmetry is broken in virtual intermediate states, allowing for Kondo exchange scattering [12]. Therefore even for SMMs that have vanishing static E due to symmetry, spin-fluctuations may

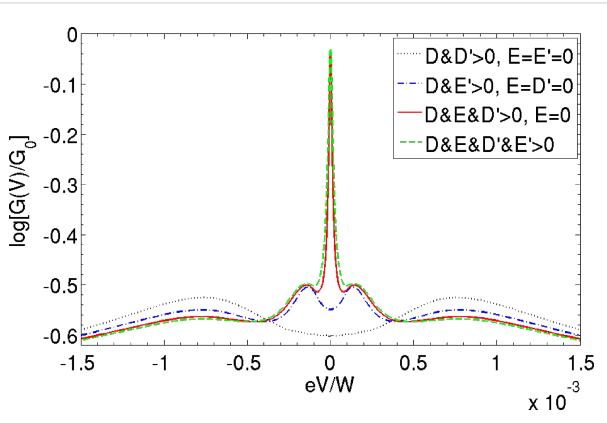

Figure 3: Effect of the spin–vibration coupling on the QST-Kondo peak: SMM differential conductance shown for various combinations of zero and nonzero values of the parameters. Nonzero values used: $D' = 0.04D$, $E' = 0.16D$ and $E = 0.02D$. Remaining parameters as in Figure 2.

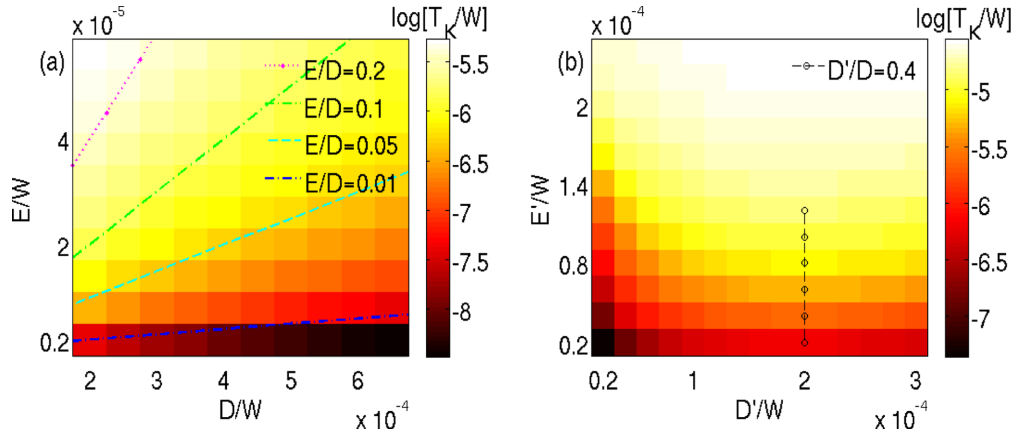

Figure 4: QST-Kondo temperature T_K in units of bandwidth $2W$ (log color scale) determined from the NRG level flow for $S = 3/2$ and $J = 0.2W$. (a) Static QST-Kondo effect: T_K as a function of the static anisotropy parameters D, E without spin-vibration coupling. Dashed contour lines indicate that T_K increases with the ratio E/D [10]. (b) Vibration-induced QST-Kondo effect: T_K as function of spin–vibration couplings D' and E' with $\Omega = 0.5D$ for static anisotropy, $D = 5 \cdot 10^{-4}W$ and $E = 0$. The dashed line marks the regime $D' > 0.4D$ where D' starts to suppress T_K, note the constant D here and also the offset: $T_K = 0$ for either $E' = 0$ or $D' = 0$. Results for small finite E are similar.

result in pronounced transport features due to the interplay of exchange scattering and intramolecular spin–vibration coupling. Clearly, the vibrational fluctuations can further assist the QST-Kondo effect when it is already present due to static E; this results in a higher Kondo temperature as shown in the green curve of Figure 3.

In Figure 4 we show the dependence of the QST-Kondo temperature T_K on the longitudinal and transverse static anisotropies and their respective vibration couplings D' and E'. T_K grows as both the transverse anisotropies are increased, since they both enhance QST. Whereas D always suppresses the QST-Kondo effect (Figure 4a) its fluctuations first enhance T_K by allowing QST between the Kramers degenerate ground-states. Eventually they will suppress T_K if the vibrational contribution to the anisotropy barrier $S^4D'^2/\Omega$, protecting the SMM against these processes, increases too much.

Finally, we show in Figure 5 how the experimentally accessible evolution of the conductance with a magnetic field reveals the different origin of the various peaks. For simplicity, we consider the field to be along the easy axis, as in some experiments [2,3], and we add the Zeeman term $-S_zH_z$ to H_{SMM} in Equation 1, absorbing the g-factor into the magnetic field. As the magnetic field is increased, the QST-Kondo peak is weakened and splits with the anomalous g-factor, $|\omega_{Kondo}| = 2SH_z$ [23]. This clearly indicates the origin of the QST-Kondo effect, since the ground-state Kramers' doublet $M = \pm S$ is split by $\Delta M = \pm 2S$. Strikingly, the vibrational side-peaks have the same strong field dependence, as they correspond to a similar transition offset in energy by Ω, that is, $|\omega_{vib}| = \Omega + 2SH_z$. In contrast to this, the high-spin Kondo peak (ZFS) evolves much slower in the magnetic field, independent of the spin magnitude S, thus $|\omega_{ZFS}| = \Delta + H_z$, signaling that it corresponds only to a transition with $\Delta M = \pm 1$. Comparing the above formulas for the peak evolution, indicated by dashed lines in Figure 5, we conclude that the QST-Kondo and high-spin Kondo effects are distinguishable, especially for SMM with large spin.

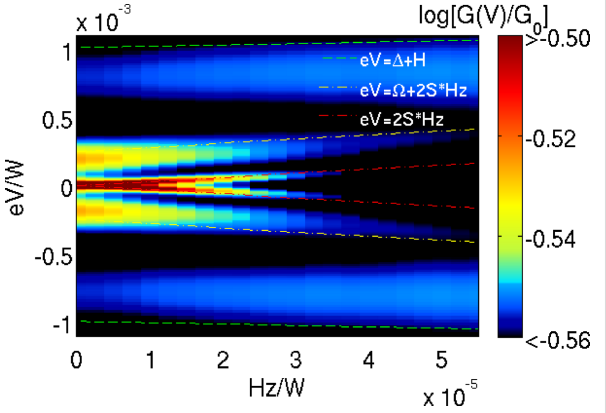

Figure 5: Magnetic field evolution of the differential conductance normalized to G_0 (log color scale) for the parameters of the red curve of Figure 3: $S = 3/2$, $E = 0.02D$, $D' = 0.04D$ and $E' = 0.16D$. Dashed lines mark the QST-Kondo (red) and vibrational side-peak (yellow) both evolving with an anomalous g-factor and zero-field, split, high-spin Kondo peak (blue).

Finally, we remark that for an SMM with integer spin S, there is no QST-Kondo effect at zero field, but instead a zero-bias conductance dip (for $0 < E < D$). As pointed out in [24] a transverse magnetic field results in a QST-Kondo effect, where similar spin-vibration effects as studied here could occur.

Conclusion

We have studied the interplay of spin and vibration on the conductance through a single-molecule magnet. Whereas longitudinal coupling to the vibration increases the zero-field splitting and suppresses the quantum spin-tunneling Kondo peak, a vibrationally induced quantum spin-tunneling Kondo effect can occur at zero bias if transverse coupling is present as well. The transition to virtual vibrational excited states and the transverse spin-mixing in these virtual states results in a Kondo effect, even in the absence of static transverse anisotropy. The interplay with vibrations can thus increase the quantum spin-tunneling Kondo temperature for a given static anisotropy, which may motivate further experimental investigation of low temperature transport though single-molecule magnets. The measurable magnetic field evolution of the conductance reveals that vibrational side-bands acquire an anomalous *g*-factor.

Acknowledgements

We acknowledge A. Cornia, J. Kortus, J. Paaske and T. Costi for stimulating discussions and support from NanoSci-ERA.

References

1. Bogani, L.; Wernsdorfer, W. *Nat. Mater.* **2008,** *7,* 179. doi:10.1038/nmat2133
2. Zyazin, A. S.; van den Berg, J. W.; Osorio, E. A.; van der Zant, H. S.; Konstantinidis, N. P.; May, F.; Leijnse, M.; Hofstetter, W.; Wegewijs, M. R.; Danieli, C.; Cornia, A. *Nano Lett.* **2010,** *10,* 3307. doi:10.1021/nl1009603
3. Parks, J. J.; Champagne, A. R.; Costi, T. A.; Shum, W. W.; Pasupathy, A. N.; Neuscamman, E.; Flores-Torres, S.; Cornaglia, P. S.; Aligia, A. A.; Balseiro, C. A.; Chan, G. K.-L.; Abruña, H. D.; Ralph, D. C. *Science* **2010,** *328,* 1370. doi:10.1126/science.1186874
4. Otte, A.; Ternes, M.; von Bergmann, K.; Loth, S.; Brune, H.; Lutz, C.; Hirjibehedin, C.; Heinrich, A. *Nat. Phys.* **2008,** *4,* 847. doi:10.1038/nphys1072
5. Otte, A.; Ternes, M.; Loth, S.; Lutz, C.; Hirjibehedin, C.; Heinrich, A. *Phys. Rev. Lett.* **2009,** *103,* 107203. doi:10.1103/PhysRevLett.103.107203
6. Loth, S.; von Bergmann, K.; Ternes, M.; Otte, A. F.; Lutz, C.; Heinrich, A. *Nat. Phys.* **2010,** *6,* 340. doi:10.1038/nphys1616
7. Leuenberger, M. N.; Loss, D. *Phys. Rev. B* **2000,** *61,* 1286. doi:10.1103/PhysRevB.61.1286
8. Pohjola, T.; Schoeller, H. *Phys. Rev. B* **2000,** *62,* 15026. doi:10.1103/PhysRevB.62.15026
9. Kortus, J.; Baruah, T.; Bernstein, N.; Pederson, M. R. *Phys. Rev. B* **2002,** *66,* 092403. doi:10.1103/PhysRevB.66.092403
10. Romeike, C.; Wegewijs, M. R.; Hofstetter, W.; Schoeller, H. *Phys. Rev. Lett.* **2006,** *96,* 196601. doi:10.1103/PhysRevLett.96.196601
11. Paaske, J.; Flensberg, K. *Phys. Rev. Lett.* **2005,** *94,* 176801. doi:10.1103/PhysRevLett.94.176801
12. Kikoin, K.; Kiselev, M. N.; Wegewijs, M. R. *Phys. Rev. Lett.* **2006,** *96,* 176801. doi:10.1103/PhysRevLett.96.176801
13. Balseiro, C. A.; Cornaglia, P. S.; Grempel, D. R. *Phys. Rev. B* **2006,** *74,* 235409. doi:10.1103/PhysRevB.74.235409
14. Cornaglia, P. S.; Usaj, G.; Balseiro, C. A. *Phys. Rev. B* **2007,** *76,* 241403. doi:10.1103/PhysRevB.76.241403
15. Gregoli, L.; Danieli, C.; Barra, A.-L.; Neugebauer, P.; Pellegrino, G.; Poneti, G.; Sessoli, R.; Cornia, A. *Chem.–Eur. J.* **2009,** *15,* 6456. doi:10.1002/chem.200900483
16. González, G.; Leuenberger, M. N.; Mucciolo, E. R. *Phys. Rev. B* **2008,** *78,* 054445. doi:10.1103/PhysRevB.78.054445
17. Aligia, A. A.; Balseiro, C. A.; Proetto, C. R. *Phys. Rev. B* **1986,** *33,* 6476. doi:10.1103/PhysRevB.33.6476
18. Lustfeld, H. *Physica B+C* **1980,** *100,* 191. doi:10.1016/0378-4363(80)90005-4
19. Meir, Y.; Wingreen, N. S. *Phys. Rev. Lett.* **1992,** *68,* 2512. doi:10.1103/PhysRevLett.68.2512
20. Costi, T. A. *Phys. Rev. Lett.* **2000,** *85,* 1504. doi:10.1103/PhysRevLett.85.1504
21. Bulla, R.; Costi, T. A.; Pruschke, T. *Rev. Mod. Phys.* **2008,** *80,* 395. doi:10.1103/RevModPhys.80.395
22. Koller, W.; Hewson, A. C.; Meyer, D. *Phys. Rev. B* **2005,** *72,* 045117. doi:10.1103/PhysRevB.72.045117
23. Romeike, C.; Wegewijs, M. R.; Hofstetter, W.; Schoeller, H. *Phys. Rev. Lett.* **2011,** *106,* 019902(E). doi:10.1103/PhysRevLett.106.019902
24. Leuenberger, M. N.; Mucciolo, E. R. *Phys. Rev. Lett.* **2006,** *97,* 126601. doi:10.1103/PhysRevLett.97.126601

License and Terms

Beilstein Journal of Nanotechnology

An MCBJ case study: The influence of π-conjugation on the single-molecule conductance at a solid/liquid interface

Wenjing Hong[1], Hennie Valkenier[2], Gábor Mészáros[1,3], David Zsolt Manrique[4], Artem Mishchenko[1], Alexander Putz[5], Pavel Moreno García[1], Colin J. Lambert[4], Jan C. Hummelen[2] and Thomas Wandlowski[*1]

Full Research Paper

Open Access

Address:
[1]Department of Chemistry and Biochemistry, University of Bern, Freiesstrasse 3, CH-3012, Bern, Switzerland, [2]Stratingh Institute for Chemistry and Zernike Institute for Advanced Materials, University of Groningen, Nijenborgh 4, 9747 AG Groningen, The Netherlands, [3]Institute of Materials and Environmental Chemistry, Chemical Research Centre, Hungarian Academy of Sciences, Pusztaszeriút 59-67, H-1025 Budapest, Hungary, [4]Lancaster University, Department of Physics, Lancaster LA1 4YB, England and [5]Institute of Bio- and Nanosystems IBN 3 and Center of Nanoelectronic Systems for Informational Technology, Research Center Juelich, D-52425 Juelich, Germany

Email:
Thomas Wandlowski* - thomas.wandlowski@dcb.unibe.ch

* Corresponding author

Keywords:
anthraquinone; π-conjugation; mechanically controlled break junction; single-molecule conductance

Beilstein J. Nanotechnol. **2011,** *2,* 699–713.
doi:10.3762/bjnano.2.76

Received: 08 July 2011
Accepted: 28 September 2011
Published: 18 October 2011

This article is part of the Thematic Series "Transport through molecular junctions".

Guest Editor: J. M. van Ruitenbeek

Abstract

π-Conjugation plays an important role in charge transport through single molecular junctions. We describe in this paper the construction of a mechanically controlled break-junction setup (MCBJ) equipped with a highly sensitive log *I*–*V* converter in order to measure ultralow conductances of molecular rods trapped between two gold leads. The current resolution of the setup reaches down to 10 fA. We report single-molecule conductance measurements of an anthracene-based linearly conjugated molecule (**AC**), of an anthraquinone-based cross-conjugated molecule (**AQ**), and of a dihydroanthracene-based molecule (**AH**) with a broken conjugation. The quantitative analysis of complementary current–distance and current–voltage measurements revealed details of the influence of π-conjugation on the single-molecule conductance.

Introduction

Molecular electronics has expanded tremendously during the past ten years [1-13]. A comprehensive understanding of charge transport through single molecules and tailored nanojunctions is a fundamental requirement for further electronic-circuit and device design. For instance, the role of length [14,15] and molecular conformation [13,16] and as well as of the anchoring group and of the contacting leads [17,18] was studied to develop correlations between charge-transport characteristics and molecular structure. Furthermore, π-conjugation plays an essential role in charge transport through single molecular junctions, and has attracted great interest in organic synthesis [19,20], conductance measurements [1,3,8-10,16,21-23] as well as in theoretical calculations [1,24,25]. In particular, single-molecule conductance measurements provide direct access to unravel the influence of π-conjugation on the molecular (-junction) conductance. However, due to the relative low conductance of broken-conjugated and cross-conjugated rigid rodlike molecules [26], reliable transport measurements through these types of molecular junctions are still a challenging topic.

Charge-transport characteristics of single molecules or of a few molecules trapped between two leads were studied in various experimental platforms. These include scanning tunneling microscopy (STM) [27-29], current probe atomic force microscopy (CP-AFM) [30-32], scanning tunneling spectroscopy (STS) or STM-break junction (STM-BJ) [13,15,16,33-36], crossed-wire geometry [37], nanoparticle junctions [38,39], mechanically controlled break junctions (MCBJ) [40-45], electromigration setups [46,47], nanopores [48], and liquid metal junctions employing mercury [49,50] or eutectic alloys of gallium and indium (EGaIn) [51].

STM-BJ and MCBJ are the two most popular and reliable approaches for single-molecule conductance measurements. Reed et al. [40], Kergueris et al. [41], Reichert et al. [42] and Smit et al. [43] pioneered the MCBJ technique to measure charge transport through single molecules. Xu et al. developed an STM-BJ technique based on the formation and breaking of thousands of individual molecular junctions by repeatedly approaching and withdrawing a STM tip towards and away from a substrate in the presence of sample molecules [34]. The MCBJ technique, as compared with the STM-BJ approach, allows control of the separation between two electrodes with extremely high stability and precision [52], which attracted great interest with respect to its application in molecular charge-transport studies [40-45].

In the present paper we explore the influence of π-conjugation on the conductance of single-molecule junctions of oligo-phenylene ethynylene (OPE)-type molecules contacted to gold leads. We have chosen three rigid dithiolated molecular wires with different conjugation patterns: An anthracene-based linearly conjugated wire (**AC**), an anthraquinone-based cross-conjugated wire (**AQ**), and a dihydroanthracene-based wire with a broken π-conjugation (**AH**) (Figure 1).

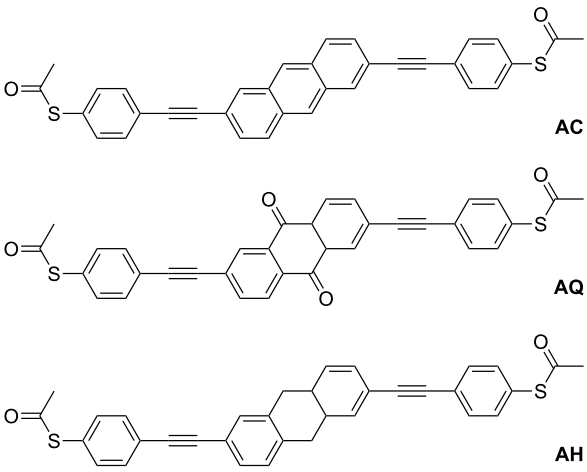

Figure 1: Molecular structures of **AC**, **AQ**, and **AH**.

The transport characteristics in single molecular junctions were investigated by conductance–distance as well as continuous current–voltage measurements in complementary MCBJ and STM-BJ experiments. In particular, a custom-designed MCBJ setup was equipped with a high-sensitivity logarithmic *I–V* converter [53] , which enabled current measurements down to 10 fA with a high dynamic range.

The paper is organized as follows: We will first introduce our novel instrumental and methodological developments, and we shall subsequently focus on one case study. We present quantitative MCBJ experiments of a family of custom-designed OPE-type rigid molecular rods at a solid/liquid interface. In particular, we will address the influence of π-conjugation on the single-junction conductance.

Experimental

System configuration

The MCBJ technique provides a high mechanical stability [52] due to the short distance between the two free-standing electrode-tip ends and the support. In consequence, molecular junction stretching and formation processes can be controlled with high precision and stability on the time scale of seconds, even at room temperature and in solution. The construction of an "ideal" platform for charge-transport measurements of single molecular junctions at solid/liquid interfaces requires the

consideration of the following key factors: The variation of the conductance in different types of single-molecule systems, as well as the tunneling decay in the subnanometer scale demands precise current measurements in a high dynamic range, from microamperes (μA) down to a few femtoamperes (fA). Moreover, the current changes over five to eight orders of magnitude in a few milliseconds, which requires a fast response in the current measurements.

The second requirement relates to the motion control of the pushing rod. The pushing rod bends the sample substrate, thus enabling the adjustment of the distance between the two gold electrodes (attenuation ratio ~0.01). The pushing distance reaches several hundreds of micrometers, while the resolution is controlled at the subnanometer level. Experiments with notched-wire samples show a characteristic displacement ratio between the vertical (pushing rod) and the horizontal (nanoscale gap between the leads) movement of about 0.01. Lithographically prepared samples were reported with displacement ratios ranging between 10^{-4} to 10^{-6} [54]. On the other hand, notched gold-wire samples with a typical displacement ratio of 0.01 are rather sensitive to mechanical vibrations, which could interfere with the exact horizontal adjustment of the distance between the two electrodes. As a consequence, mechanical vibration due to the movement of the pushing rod should be minimized as much as possible.

Thirdly, single-molecule measurements are often rather sensitive to the ambient environment, in particular to oxygen and to light. As a consequence, a closed liquid cell with inert gas protection and a continuous liquid flow is also needed. To match these three requirements, we constructed a MCBJ setup with a logarithmic *I*–*V* converter and implemented the *z*-movement of the pushing rod by combining a piezo stack and a stepper motor. Both design principles ensured a highly dynamic and precise current measurement, a long-distance *z*-movement, and subnanometer resolution. The implemented liquid cell has a filling volume of 150 μL. A tubing system for inert solution exchange and gas purging is also attached (Figure 2).

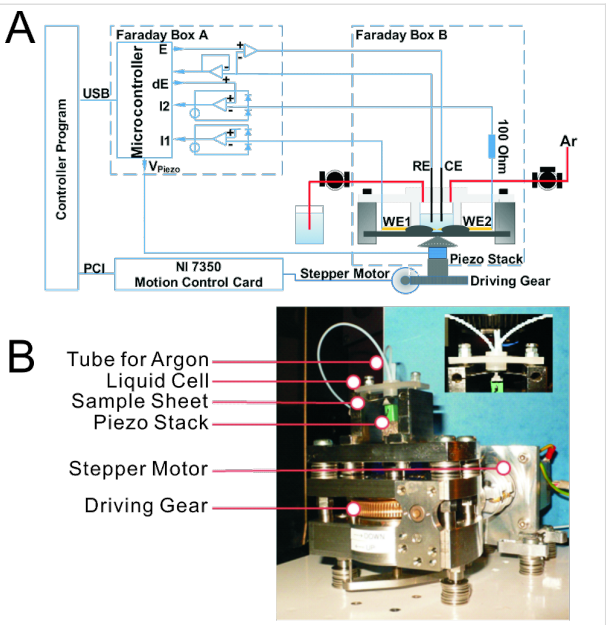

Figure 2: (A) Schematics of the system configuration and (B) pictures of the mechanical part in the MCBJ setup. The inset shows a detailed view of the liquid cell including the sample holder. For clarity, the Faraday shielding boxes were removed.

Electronics design

Controller and current-measurement units

The MCBJ controller is based on a laboratory-built bipotentiostat. Two custom-designed bipolar and tunable logarithmic *I*–*V* converters [53] were implemented for measuring the current of the two gold leads labeled as working electrodes WE1 and WE2. The reference electrode RE and the counter electrode CE serve to control the potential. The driving signal of the piezo stack is supplied by an additional A/D-converter output of the controlling unit. The setup also permits the implementation of advanced functions during measurements with various trigger options, such as multistep, stop-and-hold movements or more complex modulations of the vertical *z*-displacement.

Buffered data acquisition and all timing-sensitive functions are performed directly by the onboard trigger operations of the microcontroller. The PC attached serves only as the user interface. The communication through an opto-isolated USB interface proceeds with a sampling rate of up to 12.5 kHz for the simultaneous recording of three data channels.

The controller unit provides three analog control signals. The first one controls the potential of WE1, which is particularly important for advanced electrochemical experiments with the MCBJ setup. The second one controls the voltage difference between the two working electrodes WE1 and WE2 (bias voltage), which drives the current through the two gold electrodes for the conductance measurements. The third channel controls the voltage output for the piezo stack in the range of 0 to 50 V allowing the displacement of the piezo stack down to 10 μm.

The stable and precise operation of the logarithmic *I*–*V* converter over a wide dynamic current range requires strict temperature control. In order to avoid any interference with the temperature-control unit we applied an analog PID controller with diodes as heating elements, which kept the temperature of the current-sensing diodes of the logarithmic *I*–*V* converter within ±0.05 K.

Noise control and electronics shielding

Two metallic Faraday boxes are used, one for the mechanical unit and the other for the controller unit (c.f. Figure 2) in order to avoid electronic cross talk between the different functional parts of the setup. The two electrodes of the MCBJ setup are connected to the controller through special low-noise coaxial cables. Operation of the stepper motor introduces considerable noise. As a consequence and to avoid this kind of interference, the stepper motor is placed outside the Faraday box. Furthermore, the stepper motor is used only for the coarse approach, and then switched off during the actual measurements, leaving only the piezo actuator in operation. The rotating coarse motion is transferred through a drive bearing through the hole in the shielding box to the pushing rod. This leads to an assembly of the mechanical unit with the piezo stack being the only electronic component inside the shielding box of the mechanical unit. In order to reduce possible electrical interference, the piezo stack is shielded with an additional compartment constructed from metalized-plastic fabrics. All shielding parts are connected to ground.

Motion control

The motion control of the MCBJ set up is based on the combination of a stepper motor (Accu-coder 95511 from Encoder Production) with a piezo stack on top. The moving distance is 17 μm for a voltage range of 110 V. Typically we applied a voltage between 0 and 50 V. The mechanical part of the MCBJ is positioned on a vibration-isolation breadboard (Newport RG Breadboard), which is mounted on a passive granite table to further decrease the interference from ambient mechanical vibrations and shock waves.

The tunneling current between the two working electrodes WE1 and WE2 at a given bias voltage, the latter typically ranging from 0.020 V to 0.200 V, is chosen as the feedback signal. The pushing process starts with the stepper motor. Once a current decrease is detected, which represents the breaking of the gold–gold contact, the stepper motor is paused, and the *z*-motion control is switched to the piezo stack. The pushing rod is subsequently only driven by the application of a voltage to the piezo stack, which is ramped at a preset rate (between 0.01 $V \cdot s^{-1}$ and 25 $V \cdot s^{-1}$).

The voltage output for the piezo stack communicates with an onboard trigger. The trigger senses the tunneling current, which is converted to the respective conductance. If the conductance reaches the noise threshold ($G < 10^{-8}\ G_0$; dashed line I in Figure 3), the voltage ramp for the piezo stack stops and after a preset waiting time (typically 0.5 s; dashed line II in Figure 3) the piezo voltage decreases at an adjustable rate. In other words, the pushing rod withdraws, and the gold–gold contact is formed again. Once the detected current reaches a preset "high limit" (typically 10 G_0; dashed line III in Figure 3), the voltage ramp for the piezo stack is paused for up to 0.5 s, and a new cycle starts following an identical protocol. The entire traces, as acquired during the opening and closing process, were recorded for further data analysis.

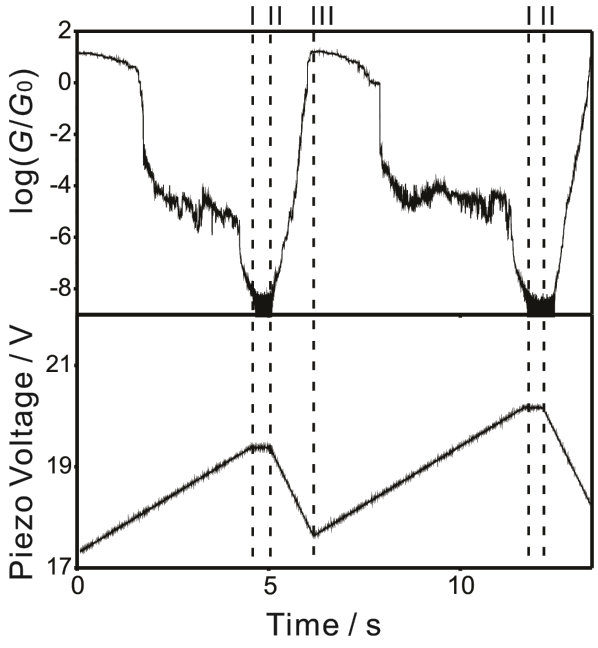

Figure 3: Conductance and voltage output for the piezo stack versus time for 0.1 mM **AC** in THF/decane (v:v = 1:4) under an Ar atmosphere at 0.10 V bias voltage.

The initial position for every opening/closing cycle may change due to changes in the gold–gold contact geometry, especially in the beginning of the experiments. However, as soon the voltage for the piezo stack output approachs one of the limits (lower limit: 0 V; higher limit: 50 V), the piezo stack is reset to a neutral position and the stepper motor is reactivated to form or to break gold–gold contacts. After such a "pre-conditioning period", which typically lasts up to 30 min for a newly started experiment, no further resetting is needed.

The distance between the two gold electrodes in the MCBJ setup is calibrated with the assumption that the tunneling decay is identical to that in a STM-BJ setup under the same experimental conditions. Conductance–distance traces representing a well-defined tunneling response, e.g., without molecular plateaus, were recorded in a STM-BJ and in a MCBJ configuration. Subsequently the decay constant ($\log[\Delta G/G_0]/\Delta z = 5.5\ nm^{-1}$) of the STM-BJ experiments was chosen to scale the traces acquired in the MCBJ setup.

Sample preparation

For MCBJ experiments, the following sample preparation protocol was applied: The sample templates were spring steel sheets (30 mm × 10 mm with 0.2 mm thickness), which were cleaned in boiling 25% nitric acid and Milli-Q water, and dried in a stream of argon. A gold wire of 100 µm in diameter was subsequently fixed on these sheets with two drops of preheated epoxy (40 °C, mixture of 100 STYCAST 2850 FT epoxy resin with catalyst 9; LakeShore, Westerville, OH). The distance between the two drops of epoxy glue was adjusted to be less than 500 µm. Next, the sample was conditioned overnight at 60 °C for epoxy polymerization. The freely suspended part of the wire was notched with a scalpel blade under an optical microscope to fabricate a constriction point. The as-prepared sample sheets were cleaned in boiling Milli-Q water for 15 min, rinsed with isopropanol and dried with argon before each experiment.

The Kel-F liquid cell including its cover, Kalrez O-ring and Teflon tubes for argon purging and solution exchange were cleaned in three alternating boiling cycles in 25% nitric acid and Milli-Q water to remove absorbed contaminants.

The sample sheet was first mounted on the sample holder of the MCBJ setup. Subsequently, the liquid cell was installed on top of the sample with a Kalrez O-ring attached to prevent leakage of the solution. The closed liquid cell was flushed with argon through an inert-gas cycling system to remove oxygen, and then the solution containing the test molecule was pumped into the liquid cell through a triple valve. The last step was repeated three times to reduce contaminations. Subsequently, the input and output valves for solution exchange and gas purging were closed, and the experiment started.

STM-BJ experiment

Basic principles of the STM-BJ experiment, data analysis and sample preparation were described previously [16,33].

Organic synthesis

The synthesis of the antraquinone-based cross-conjugated wire **AQ** followed a method reported previously [55]. Details on the synthesis of the anthracene-based linearly conjugated wire **AC** and of the molecular wire with broken symmetry **AH** will be communicated elsewhere [14,56]. The three dithiol-terminated molecular wires were synthesized with acetyl-protecting groups. Careful MCBJ and STM-BJ screening experiments with **AC** indicated that a high yield of single-molecule junctions is obtained in the absence as well as in the presence of in situ deprotecting agents, such as tetrabutyl ammonium hydroxide or triethylamine. As a consequence, and to keep the number of different species in the sample solution to a minimum [57], we performed the subsequent experiments with the acetyl-protected derivatives in the sample solution without implementing an additional deprotection step.

Results and Discussion

Conductance–distance measurements

Stretching traces

The measurements of conductance–distance traces in the MCBJ set up were carried out with 50 nm·s^{-1} as the typical rate for the movement of the pushing rod in the breaking process. This value translates into an approximate lateral movement between the two gold leads of about 1 nm. All data shown in the following sections and used for the analysis represent opening traces, which were recorded after breaking a gold–gold contact. Figure 4 shows six typical examples of individual traces in a log-conductance versus distance representation for the

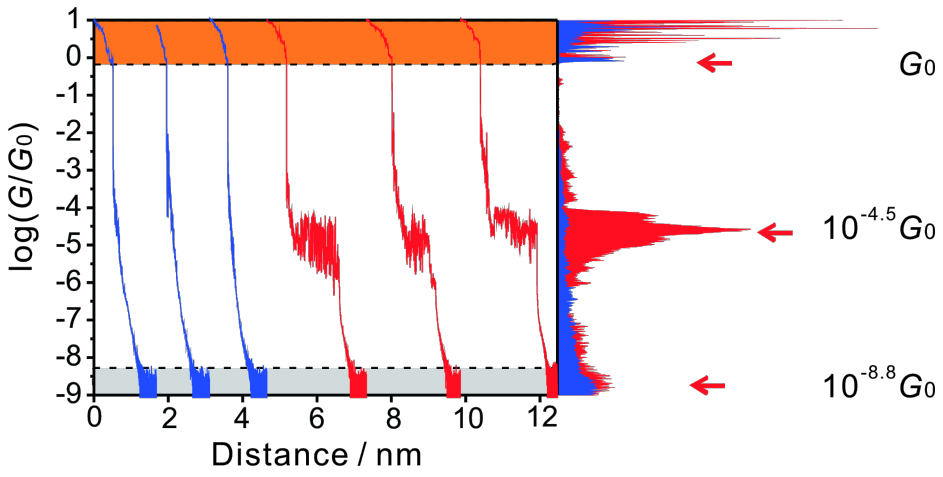

Figure 4: Individual conductance–distance traces and histogram constructed from these sets of three traces for **AC** at a bias voltage V_{bias} = 0.10 V in THF/decane (v:v = 1:4) under Ar atmosphere. The most probable conductance is indicated.

anthracene-based linear molecular wire **AC**. All curves start with characteristic steps and plateaus in the region between 10 and 1 G_o (orange part), representing the breaking of gold–gold atomic contacts. The last step is observed around 1 G_0. After the gold–gold monatomic contact is broken, the two "separated" gold electrodes snap back and a nanogap is created with typical conductances ranging between 10^{-2} G_0 and 10^{-4} G_0. The snap-back process is too fast to be recorded with better resolution. At lower conductances we observed two distinctly different types of traces, those without molecular plateaus (blue curves, around 67 % of all data recorded) and those with molecular plateaus (red curves, around 33 % of all data recorded) in the range of 10^{-4} to 10^{-5} G_0. The noise level is reached below $10^{-8.2}$ G_0, which provides a wide window of over eight orders of magnitude for the single-molecule conductance measurements.

The blue traces in Figure 4 represent a tunneling response between the two broken gold leads through the solution without the formation of a molecular junction. These data were chosen for distance calibration. The red curves in Figure 4 indicate the successful formation of gold|**AC**|gold molecular junctions with a characteristic plateau. The three representative individual traces reveal a single plateau conductance at around $10^{-4.5}$ G_0, which indicates the formation of a single-molecule junction between the two electrodes. The current noise is attributed to the thermal vibration of the molecular junction at room temperature. The conductance traces exhibit an abrupt decrease upon breaking of the molecular junction until the noise level is reached. The most probable conductance of the molecular junction was obtained by statistical analysis of the data. The resulting histogram, as constructed from the three red traces, is plotted in the right panel of Figure 4. The graph reveals a sharp and clear conductance peak at $10^{-4.5}$ G_0, which is equal to 2.5 nS, the most probable single-molecular junction conductance of **AC** from a limited data set of three individual traces. (Note that the complete, statistically significant analysis is reported below in the section "Comparative conductance measurements of AC with AQ and AH"). Applying the same analysis method to the blue traces did not lead to any clear feature between 10^{-1} G_0 and 10^{-8} G_0, which supports the assignment of the two types of traces.

Continuous current–voltage (*I–V*) measurement

I–V curves in the stretching process

The high mechanical stability of the MCBJ setup provides a unique platform to create stable gold|molecule|gold junctions with a lifetime of several seconds. For *I–V* measurements we controlled the opening and closing cycles by slowly moving the pushing rod at a rate of 0.5 nm·s^{-1} and we swept simultaneously the bias voltage V_{bias} from −0.4 V to +0.4 V at a rate of 25 V·s^{-1} at various positions. This approach resulted in a set of *I–V* curves spanning a range of conductance during a single opening and closing cycle, which correspond variously to the Au–Au contacts (Figure 5A), the formation of molecular junctions (Figure 5B), the tunneling through the solvent and, finally, the approach to the noise level (Figure 5C). *I–V* traces of the gold–gold contacts are linear, and represent ohmic characteristics, whereas *I–V* curves of the molecular junctions are nonlinear. They provide an important test platform to estimate the relative positions of molecular levels and the Fermi levels of the leads, based on a comparison with ab initio transport calculations and the corresponding transmission curves [58].

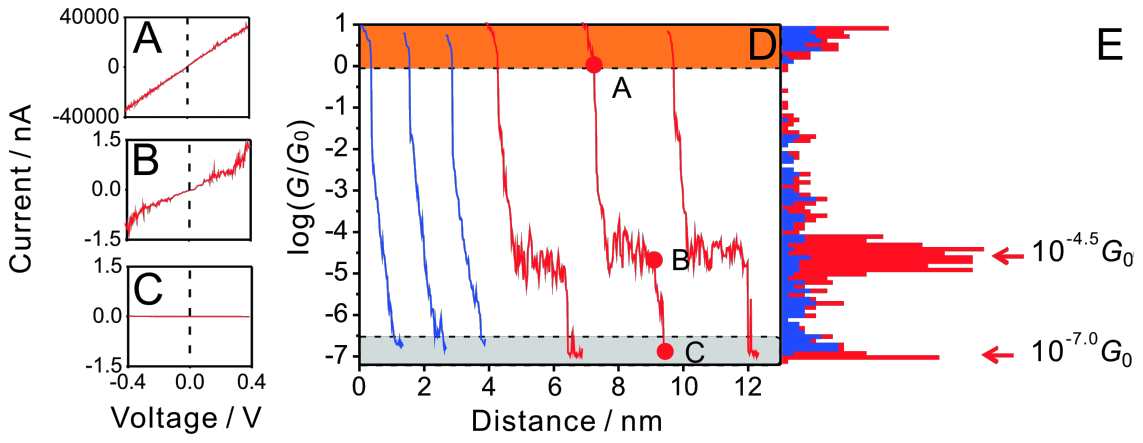

Figure 5: (A–C) Individual current–voltage curves of (A) a gold–gold contact, (B) a gold|**AC**|gold molecular junction, and (C) tunneling response through the solvent upon approaching the noise level. (D) Traces constructed from the slopes of individual *I–V* curves as recorded simultaneously during a slow stretching half cycle, with (red traces) and without (blue traces) the formation of a molecular junction. The red circles indicate the positions where the *I–V* curves shown in panels (A) to (C) were recorded. (E) Conductance histogram as constructed from the data points plotted in panel D. Other conditions: 0.1 mM in THF/decane (v:v = 1:4), Ar atmosphere.

For comparison with the conductance–distance measurements shown in Figure 4, we calculated the slopes of the linear parts (typically in the range between −0.30 to 0.30 V) of individual *I–V* curves at different stages of the stretching process. We emphasize that each data point represents the conductance extracted from one *I–V* curve in the zero-bias limit. Initially (orange area in Figure 5D), all *I–V* curves exhibit the conductance of gold–gold contacts. Once this contact is broken, either one of two families of curves is observed. The blue traces in Figure 5D represent tunneling through the solvent without the formation of a molecular junction. The dotted $\log(G/G_0)$ versus distance traces are linear until the noise level is reached. The second type of curves (red traces in Figure 5D) showed well-developed molecular plateaus. Employing 0.5 $nm \cdot s^{-1}$ as the pulling rate to separate the two gold electrodes enables the acquisition of 30 to 40 individual *I–V* curves in the conductance range of **AC** molecular junctions around $10^{-4.5}$ G_0 during a single stretching trace. Data points below 10^{-5} G_0 represent tunneling through the solvent and, finally, the approach to the noise level (grey region in Figure 5D). The statistical analysis, based on counting the number of data points per conductance interval in each individual trace, leads to the construction of the conductance histograms. The graph in Figure 5E shows a well-resolved maximum located at $10^{-4.5}$ G_0, despite the limited number of data points (ca. 200 from three traces). This value represents the most probable conductance of a gold|**AC**|gold single-molecule junction, and is in perfect agreement with the result of the continuous current–distance measurements (Figure 4). The coincidence demonstrates convincingly the reliability of both experimental approaches chosen.

Statistical analysis of *I–V* curves of molecular junctions

Thermal vibrations as well as switching events between different configurations and conductance states in a molecular junction require a careful statistical analysis of several thousands of individual traces to extract the "most probable" *I–V* characteristics of a certain molecule under a given set of experimental conditions. This approach is particularly important for single-molecule experiments at a solid/liquid interface at room temperature.

Figure 6A shows a 2-D histogram of 2500 *I–V* traces as recorded during individual stretching events in the region of molecular junction formation, i.e., from $10^{-4.3}$ to $10^{-4.7}$ G_0. The color code demonstrates clearly the existence of preferred conductance states. Next we determined for each bias voltage V_{bias} the most probable current value and its standard deviation from a Gaussian fit. The choice of a Gaussian fit is justified because the distribution of the measured current preferentially originates from thermal vibration and electronic noise, which are both completely random processes.

Figure 6B illustrates the most probable *I–V* master curve of **AC** attached to two gold leads as obtained from the statistical analysis of individual traces in $-0.40\ V < V_{Bias} < 0.40\ V$. The shape of the *I–V* trace provides additional information for exploring the nature of the transport process. In a first approximation, we considered a single-level model in the low-bias limit and with the molecules coupled equally to the leads. We thus evaluated the experimentally observed *I–V* characteristics based on the following expression ([1] page 366, and [18]):

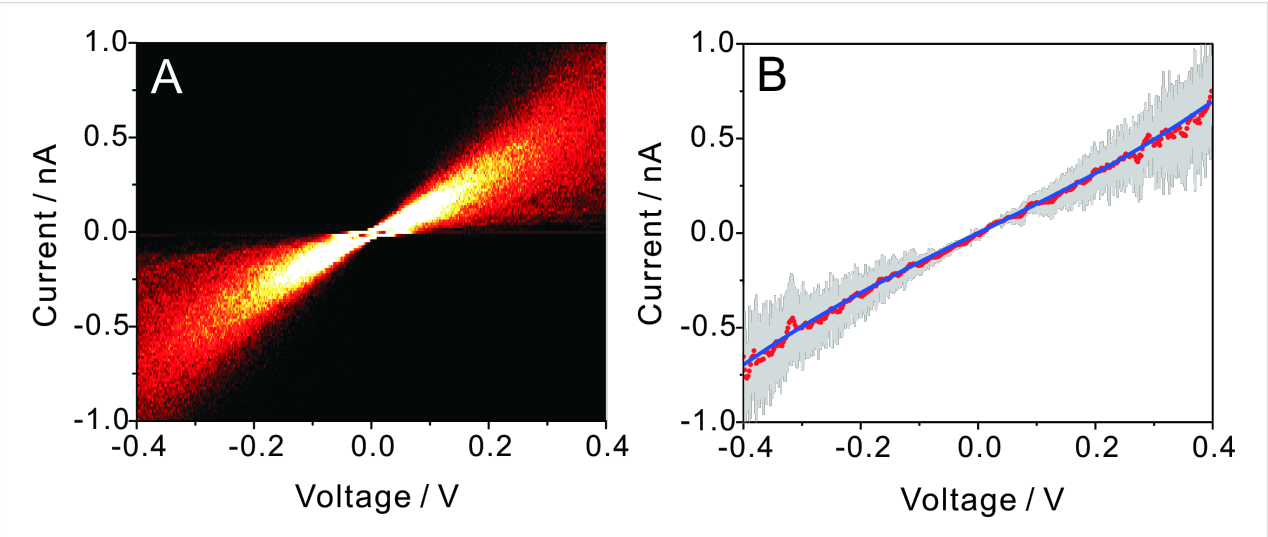

Figure 6: (A) 2-D *I–V* histogram constructed from 2500 individual traces recorded during a current–distance stretching experiment, stretching rate 0.5 $nm \cdot s^{-1}$, in the molecular junction region for 0.1 mM **AC** in THF/decane. (B) *I–V* "master curve" (red) and its standard deviation (error bar) obtained from Gaussian fits at constant bias voltages of the data plotted in panel A, and the corresponding model fitting (blue).

$$I(V)=\frac{2e}{h}2\Gamma\left(\arctan\frac{\frac{eV}{2}-\Delta\varepsilon_0}{2\Gamma}+\arctan\frac{\frac{eV}{2}+\Delta\varepsilon_0}{2\Gamma}\right) \quad (1)$$
$$\approx aG_0V+bG_0V^3$$

where $\Delta\varepsilon_0=\varepsilon_0-\mu$ is the energy of a molecular level ε_0 relative to the Fermi energy, and Γ is the resonance level width. The first expression is obtained by integrating a Lorentzian form for the transmission coefficient

$$T(E)=\frac{4\Gamma^2}{(E-\Delta\varepsilon_0)^2+4\Gamma^2}$$

over a bias window $\mu\mp(eV/2)$. The second expression, which is a cubic function with coefficients *a* and *b*, is expressed by Taylor expansion of the first, which yields

$$a=\frac{1}{\frac{\Delta\varepsilon_0^2}{4\Gamma^2}+1}$$

and

$$b=e^2\frac{1}{3\Gamma^2}\frac{3\frac{\Delta\varepsilon_0^2}{4\Gamma^2}-4}{\left(\frac{\Delta\varepsilon_0^2}{4\Gamma^2}+4\right)^3}.$$

In practice, *a* and *b* are obtained by fitting the cubic function to the experimentally measured *I*–*V* curve, and $\Delta\varepsilon_0$ and Γ are then obtained from the inverse relations:

$$(\Delta\varepsilon_0)^2=e^2\frac{a(1-a)(3-4a)}{12b} \quad (2)$$

and

$$4\Gamma^2=e^2\frac{a^2(3-4a)}{12b}. \quad (3)$$

Fitting the model, as represented by Equation 1 to Equation 3, to the experimental *I*–*V* master curve of **AC** in the range of −0.40 V to 0.40 V provides an estimate of the two parameters as $\Delta\varepsilon_0=-0.53$ eV (see text below) and $\Gamma=0.0012$ eV. The negative sign is concluded from the following: Considering the Fermi energy of gold as −5.0 eV, we estimated −5.53 eV as the position of the E_{HOMO} level. This result is in good agreement with AM1-RHF calculations, performed with Hyperchem Release 7.52, and the level alignment, based on UPS data, of a related **AQ**-type molecular wire, $E_{HOMO}(Hyperchem_{corr})=-5.74$ eV [14]. The HOMO–LUMO gap is estimated at 2.90 eV from the onset of UV–vis spectra in CH_2Cl_2 [14]. Based on these data we conclude that transport through **AQ**-type molecular junctions is HOMO-dominated.

The coupling parameter Γ appears to be rather small as compared to those for other dithiole-terminated molecular wires attached to gold leads [1,18]. These deviations might be related to the simplicity of the model chosen.

Comparison between *I*–*V* and conductance–distance measurements of AC by MCBJ and STM-BJ

Figure 7 compares the conductance histogram of **AC**, constructed from the above *I*–*V* data (c.f. Figure 5 but now based on the analysis of 60,000 individual traces, which contain thousands of *I*–*V* curves in the molecular junction region, blue diagram in Figure 7), with that obtained from the analysis of 500 current–distance traces of the MCBJ setup (black diagram, without any data selection, c.f. also Figure 4). We also added the histogram (red diagram) that was obtained from the statistical analysis of 2000 individual traces acquired with our STM-BJ setup [15,16,33]. Both the red and the black graphs display clear peaks at 1 G_0 and $10^{-4.4}$–$10^{-4.5}$ G_0, which are assigned to the breaking of a monatomic gold–gold contact and the single molecular junction conductance of **AC** trapped between two gold leads, respectively. The good agreement between the results of the three different experimental approaches indicates the reliability of the measurements as well as the independence of the single-molecule conductance values of the present system from the measurement techniques chosen.

Histograms based on the MCBJ and STM-BJ data are distinctly different with respect to the noise level. Due to different preamplifier designs and stabilization concepts, the noise level of the STM-BJ setup is reached at around $10^{-6.0}$ G_0 (red asterisk in Figure 7), whereas the noise level of the MCBJ stage is significantly lower and appears to interfere with the junction response only below $10^{-8.5}$ G_0 (black asterisk in Figure 7). In consequence, we were able to resolve an additional molecular junction-related feature around $10^{-7.2}$ G_0 in the MCBJ transport experiments of **AC**, which is equal to 4.9 pS. We note that the new feature could not be detected in the STM-BJ experiments due to the sensitivity limitations.

The conductance histogram based on the statistical analysis of *I*–*V* traces (blue diagram in Figure 7) was constructed from

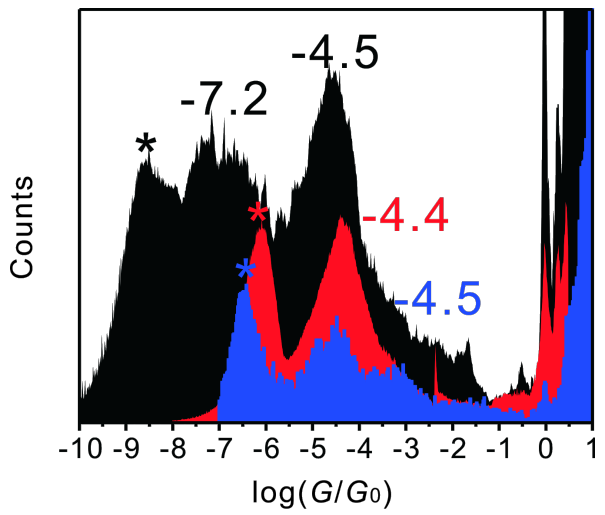

Figure 7: Conductance histograms of 0.1 mM **AC** in THF/decane (v:v = 1:4). Black: From 500 current–distance stretching curves in a MCBJ setup. Red: From 2000 current–distance stretching curves recorded in an STM-BJ experiment, with 0.10 V bias voltage. Blue: Based on 60,000 individual *I*–*V* traces measured simultaneously in the range of −0.40 to 0.40 V, in the molecular junction region of the above MCBJ experiment.

60,000 individual curves, which were recorded simultaneously with the 500 stretching traces. The analysis revealed a clear molecular junction conductance peak of $10^{-4.5}$ G_0, which is in good agreement with the most probable values as extracted from the MCBJ and STM-BJ conductance–distance measurements. However, the low conductance range (<$10^{-6.5}$ G_0) could not be monitored reliably due to the relatively slow response of the log *I*–*V* converter in the pA range. The *I*–*V* converter could not follow precisely enough the current change in the low-conductance range upon sweeping the bias voltage at a rate of 25 V·s^{-1}.

Comparative conductance measurements of AC with AQ and AH

Figure 8 shows 1-D conductance histograms and 2-D conductance–distance histograms of **AC**, **AQ**, **AH** and, for comparison, also the target-molecule-free THF/decane solution, as obtained in a series of MCBJ measurements. All experiments were carried out under identical conditions and analyzed with the strategies introduced above. We note that the histograms constructed for the blank control experiment (Figure 8D and Figure 8H) do not show any significant conductance peaks, except the one attributed to the breaking of the monatomic gold–gold contact around G_0 and the feature at $10^{-8.8}$ G_0. The latter represents the noise level. The slight increase of the baseline in the histograms results from contributions of the gap-modulated tunneling current, which originates from variations in the solvent conformation as well as from the "snap-back" distances of the gold–gold nanocontacts upon breaking the leads [59,60].

Figure 8B reveals a clear peak at $10^{-7.0}$ G_0 (7.8 pS) in the conductance histogram of the cross-conjugated anthraquinone wire **AQ**. This feature is well separated from the noise level, which is located at $10^{-8.8}$ G_0. The junction conductance of **AQ** is approximately 300 times lower than that of **AC**. This trend demonstrates that the cross-conjugated motif of **AQ** indeed gives rise to a lower conductance as compared to the linear-conjugated **AC**, which is in agreement with ab initio transport calculations predicting a destructive quantum interference present in **AQ**, but which is absent in **AC** molecular bridges [24]. From a technical point of view, the accessibility and reliability of the low conductance data for the **AQ** molecular junction also illustrates the high sensitivity of our new MCBJ setup.

Figure 8C shows the 1-D conductance histogram of the dihydroanthracene wire **AH** with a broken π-conjugation. The plot reveals one main feature at $10^{-6.3}$ G_0 (39 pS) and a faint second feature around $10^{-4.5}$ G_0 (2.5 nS), the latter being 5 times larger and close to the data reported for **AC**.

Complementary to the 1-D histograms we also constructed, based on the above individual conductance–distance traces, 2-D conductance–distance histograms [61]. In an attempt to define a common reference point for all of the conductance–distance, we selected the position where the current reaches 0.1 G_0 to define the relative zero of the distance scale [33]. The color code in Figures 8E to Figure 8H is chosen such that the red areas indicate a higher data density at the respective conductance–distance point. In agreement with the 1-D plot of **AC** in Figure 8A, Figure 8E shows a clear and dominant molecular plateau around $10^{-4.5}$ G_0 and a second, less dense patch of data points, around $10^{-7.2}$ G_0 indicating a low conductance feature. The 2-D histogram of **AQ** reveals only one clear molecular feature, which is found around $10^{-7.0}$ G_0 (Figure 8F). On the other hand, the 2-D histogram of **AH** (Figure 8G) mainly displays a molecular feature around $10^{-6.3}$ G_0 but also a weak intensity patch at $10^{-4.5}$ G_0, which coincide with the main peak and a weak secondary feature shown in the 1-D conductance histograms (Figure 8C). We comment that the overall evolution of the minority feature of **AH** is close to the main conductance peak of **AC**.

We further analyze the stretching distance from the breaking of gold–gold contacts until the noise level is reached (from 10^{-1} G/G_0 to 10^{-8} G/G_0). We extracted the most probable stretching distance of breaking for the high conductance plateau of **AC** in the range of 10^{-1} G/G_0 to 10^{-6} G/G_0 to explore further details of the low-conductance state. As illustrated in

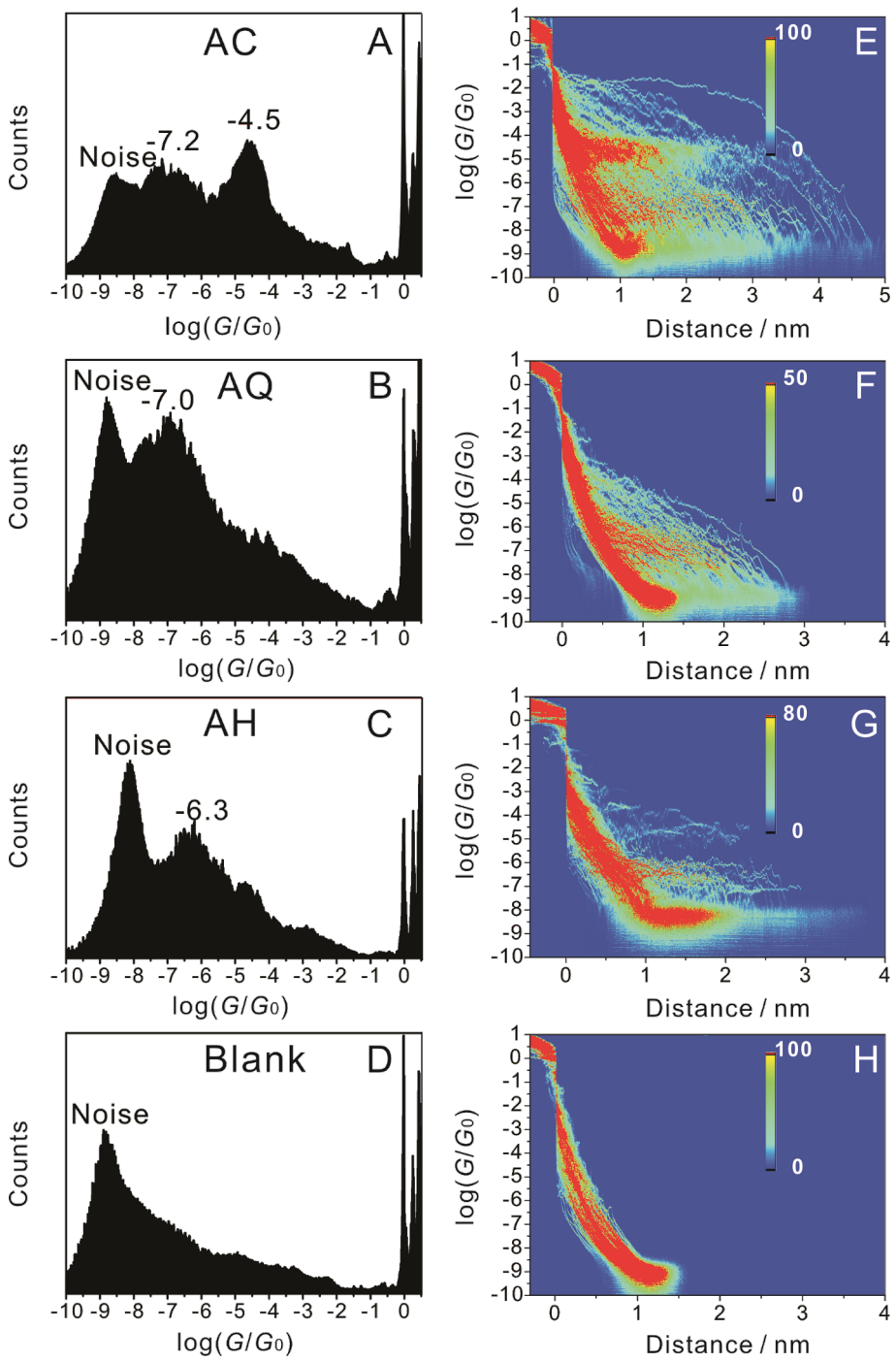

Figure 8: 1-D conductance histograms and conductance–distance 2-D histograms constructed from 500 individual traces of **AC** (panels A and E), **AQ** (panels B and F), **AH** (panels C and G) and for the blank control experiment (panels D and H) in THF/decane (v:v = 1:4) under Ar atmosphere at 0.10 V bias voltage in the MCBJ setup. The molecule concentration was 0.1 mM, and the stretching rate was around 1 nm·s^{-1}.

Figure 9A, we observed two, clearly separate peaks. The first peak, located around 1 nm, is assigned to a tunneling feature without the formation of a molecular junction (blue traces in Figure 4). The second peak, which evolves at longer stretching distances, results from the formation of a molecular junction and reflects properties of a true molecular plateau (red traces in Figure 4). The most probable "relative" stretching distance at which the **AC** molecular junction breaks is 2.5 nm, while the most probable stretching distance up to the end of the high-conductance molecular plateau is obtained as 2.3 nm (inset in

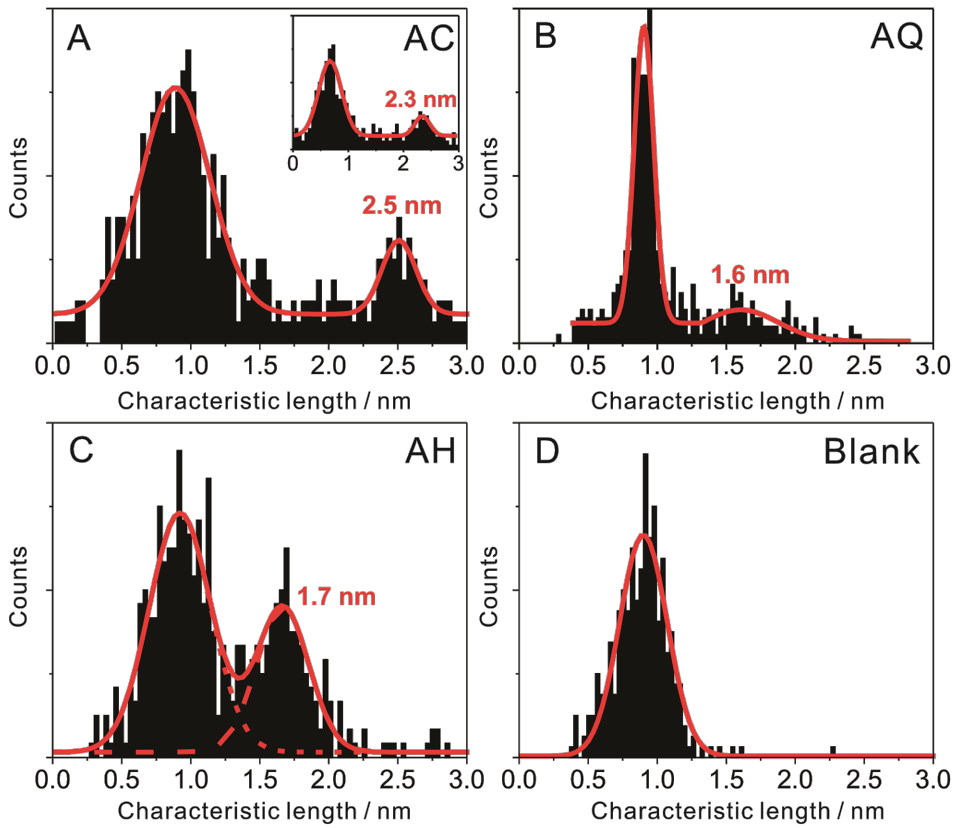

Figure 9: Plateau-length distributions (black) and Gaussian fits (red) of (A) **AC** (B) **AQ** (C) **AH** and (D) the blank control system, as constructed from the data shown in Figure 8. The conductance range selected for the plateau length analysis ranges between 0.1 G_0 and 10^{-8} G_0. The inset in panel (A) represents the plateau length analysis of **AC** in a limited conductance range from 0.1 G_0 to 10^{-6} G_0 in order to extract the length of the main conductance plateau.

Figure 9A). The difference of 0.2 nm is attributed to a low-conductance feature. The most probable "real" plateau length of the gold|**AC**|gold junctions is estimated at 3 nm by adding the "snap-back" distance of 0.65 nm [17,59,60] resulting from the breaking of the monatomic gold–gold contact. This value is slightly higher than the molecular length of **AC** (2.7 nm). We propose that the strong gold–thiole bond leads to the "pulling-out" of surface gold atoms just before the breaking of the molecular junction. The low-conductance feature is attributed to π-stacking interactions between two molecules attached only at one end of the leads [44,62]. For a more detailed and critical discussion of possible junction geometries and molecular mechanisms of junction breaking, we refer to our forthcoming papers [14,17].

Figure 9B and Figure 9C show that the "relative" plateau length of **AQ** amounts to 1.6 nm, while **AH** is estimated at 1.7 nm. After correction with the snap-back distance one obtains 2.25 nm and 2.35 nm. Both values are smaller than the molecular length, which indicates that most of the molecular junctions break before they are completely elongated, which is distinctly different behaviour compared to **AC**. We note that the maximum in the adsorbate-free control experiment at around 0.9 nm (Figure 9D) results from tunneling and noise contributions, and is not related to the formation of gold|molecule|gold junctions. Introducing a "relative" distance of 1.25 nm as a threshold for the identification of a molecular junction, we calculated the junction formation probability from the plateau-length analysis and obtained the following values: 33% out of all traces for **AC**, 32% for **AH** and 14% for **AQ**. Clearly, the molecular structure of each of the three OPE-type species influences the bonding of the molecule to the gold-electrodes as well as the formation probability of the junction.

Based on the analysis above, we suggest the following as the most probable scenario to explain the features of a stretching trace in the high conductance regime of **AC**: The gold leads retract ("snap-back") upon breaking of an atomic gold–gold contact (configurations 1 and 2 in Figure 10B). Subsequently, the **AC** molecule "slides" into the junction and connects finally to both gold electrodes. The conductance changes slightly upon further pulling [63] until the molecule is completely trapped

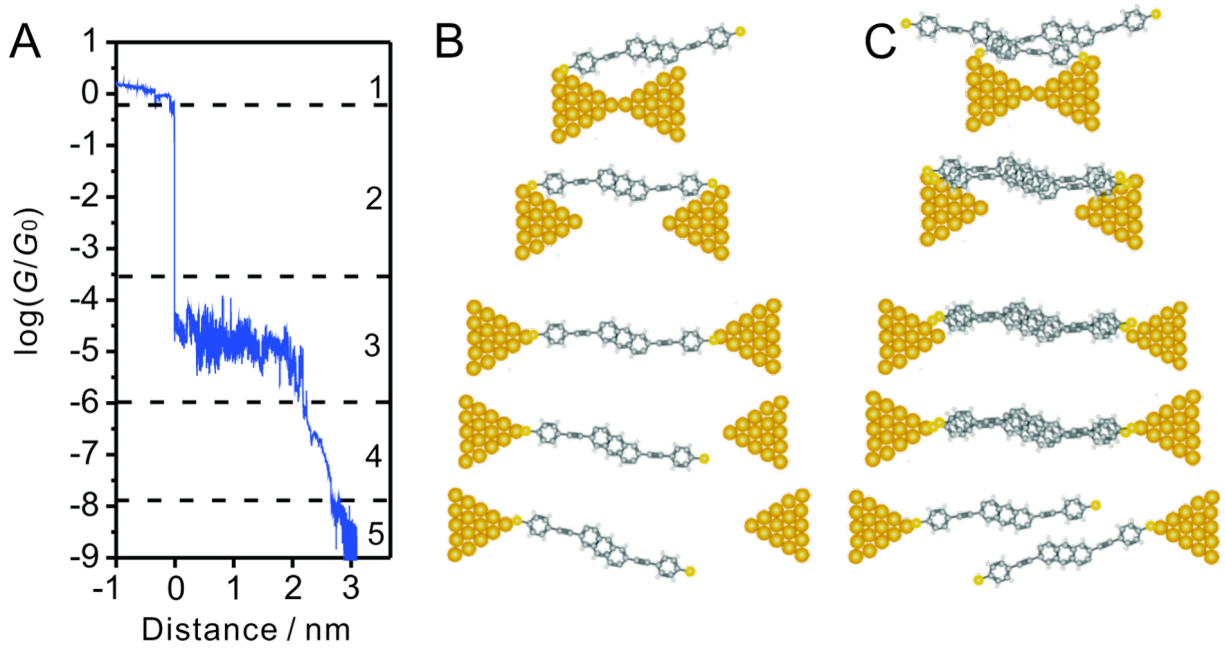

Figure 10: Model of the breaking process of the Au|**AC**|Au junction. (A) A typical trace with labels indicating various stages of the process. (B) Model of the formation and breaking of a single-molecule junction. (C) Model for a scenario involving the stacking of two molecules.

(configuration 3 in Figure 10), which leads to the most probable conductance value of $10^{-4.5}$ G_0 for a single gold|**AC**|gold junction. Further pulling causes an elongation of the Au–thiol bond until the junction breaks. The low-conductance feature is attributed to the formation of molecular stacks after breaking of the gold leads [44,62]. A tentative scenario is illustrated in Figure 10C. Both processes may occur sequentially if more than one molecule is trapped in the junction. This interpretation is based on experimentally observed "stacking" trends in single-molecule junctions formed by dithiolated or monothiolated OPE-type molecules attached to two adjacent gold leads [44,62].

We also note that the high conductance value of a gold|**AC**|gold junction follows the trend $\ln G = \ln A - \beta \cdot L$, with L as molecular length, A = 10,819.6 nS and β = 3.4 nm^{-1} as experimentally observed for the length dependence of a family of dithiol-terminated OPE-molecules [14]. β is the tunneling decay constant, which is approximately 2.5 times smaller than typical values for aliphatic molecular wires.

AQ and **AH** form only one type of molecular junction, which we attribute to the "high" conductance type. However, the two most probable values obtained do not follow the above trend for the conductance versus length dependence of unsubstituted dithiolated OPE molecules. Both values, $10^{-7.0}$ G_0 for the cross-conjugated anthraqinone **AQ** and $10^{-6.3}$ G_0 for the dihydroanthracene **AH** are significantly smaller than predicted from this correlation. The data of Figure 8 reveal the following trend in single-junction conductance: **AC** > **AH** > **AQ** for this series of molecules with identical lengths. This trend thus clearly shows the influence of the π-conjugation pattern on the single-molecule conductance. The even lower conductance of the cross-conjugated molecule **AQ** as compared to the dihydroanthracene **AH** wire is attributed to a destructive quantum interference in the **AQ**-type junction [24,56]. Complementary data from single-molecule I–V traces were only accessible for **AC** (section "Continuous current–voltage (I–V) measurement"), and not for **AQ** and **AH**. The rather low junction-conductance characteristics of these two molecules as recorded simultaneously during single stretching traces were too much distorted by the onset of instrumental noise.

Furthermore, the most probable molecular junction lengths of **AQ** and **AH** are smaller than the molecular length indicating that the junctions breaks more frequently before the molecule assumes an extended atop–atop configuration between the two ends of the gold leads. A peculiarity appears in the form of a weak conductance feature observed for **AH** around $10^{-4.5}$ G_0 (Figure 8C and Figure 8H). The similarity to the main conductance feature of **AC** (Figure 8A and Figure 8E) suggests that the second conductance peak of **AH** may come from the partial oxidation of **AH** to **AC**.

Finally, we notice that the same sequence of conductance values as found in the MCBJ-experiments (**AC** > **AQ** > **AH**) was also

observed in current-probe atomic force microscopy (CP–AFM) [64] and EGaIn studies [65] of these three molecules. However, the absolute conductance values were about two (CP–AFM) to five (EGaIn) orders of magnitude larger. This difference is attributed to the contact area in the CP–AFM and EGaln setups. The conductance data acquired in such configurations represent the integral sum over parallel molecular junctions in asymmetric contact geometries, which is distinctly different from the single-molecule data reported in this paper. Furthermore, the number of bridging molecules, which contribute to the measured charge-transfer characteristics in the large-area molecular junctions, is not directly accessible, thus preventing the downscaling to an "effective" single-molecule-junction response.

Conclusion

We described in this paper the construction of a mechanically controlled break-junction setup (MCBJ) equipped with a highly sensitive log *I–V* converter to measure ultralow conductances of molecular rods formed between two gold leads. In particular, we carried out quantitative single-molecule conductance experiments on linearly conjugated, cross-conjugated, and broken-conjugated examples of dithiolated molecules of the OPE family. The current sensitivity of the setup reaches down to 10 fA. Our experiments demonstrate that the conductance of the linearly conjugated molecule **AC** is several hundred times higher than that of the broken π-conjugated molecule **AH**, and the conductance of **AH** is about five times higher than that of the cross-conjugated molecule **AQ**. The latter result is attributed to destructive quantum interference present in the **AQ** molecular bridge [24]. All dithiolated molecules are of similar length (~2.6 nm), but only **AC** appears to be capable of forming a large number of fully extended gold|molecule|gold junctions. The other two molecules **AQ** and **AH** form junctions that break before reaching full extension.

These experimentally observed trends in the values of the single-molecule conductances as well as in the stability of the respective molecular junctions reveal the key role of π-conjugation in the charge transport through rigid-rod OPE-type single-molecule junctions. Moreover, the good agreement between the different measurement approaches employed in this paper (current–distance and current–voltage traces from MCBJ and STM-BJ) confirm the reliability of our measurements. The observation of similar trends in the main conductance values discovered in single-molecule (MCBJ, STM-BJ) and parallel-molecule junction experiments (CP–AFM, EGaln junctions) confirms the complementarity of the various experimental platforms, in both their similarities as well as their distinct differences.

Acknowledgements

The authors are grateful to the Swiss National Science Foundation (200021_124643; 200020_122069, Sinergia CRSII2_126969; NFP 62 406240_126 108) and the ITN FP7 Network FUNMOLS for financial support. T.W. also acknowledges valuable discussions with M. Calame, University of Basel, on technical details of the MCBJ setup. H.V. acknowledges NanoNed, funded by the Dutch Ministry of Economic Affairs, for financial support (project GMM.6973). G.M. was partially supported by the Hungarian Scientific Research Fund (OTKA K-67874) and by the Hungarian Science and Technology Foundation (CZ-3/2009).

References

1. Cuevas, J. C.; Scheer, E. In *Molecular Electronics: An Introduction to Theory and Experiment;* Reed, M., Ed.; World Scientific Series in Nanoscience and Nanotechnology, Vol. 1; World Scientific: Singapore, Hackensack, NJ, 2010.
2. Troisi, A.; Ratner, M. A. *Small* **2006,** *2,* 172–181. doi:10.1002/smll.200500201
3. Chen, F.; Hihath, J.; Huang, Z. F.; Li, X. L.; Tao, N. J. *Annu. Rev. Phys. Chem.* **2007,** *58,* 535–564. doi:10.1146/annurev.physchem.58.032806.104523
4. Weibel, N.; Grunder, S.; Mayor, M. *Org. Biomol. Chem.* **2007,** *5,* 2343–2353. doi:10.1039/b703287k
5. Galperin, M.; Ratner, M. A.; Nitzan, A.; Troisi, A. *Science* **2008,** *319,* 1056–1060. doi:10.1126/science.1146556
6. Akkerman, H. B.; de Boer, B. *J. Phys.: Condens. Matter* **2008,** *20,* 013001. doi:10.1088/0953-8984/20/01/013001
7. Heath, J. R. *Annu. Rev. Mater. Res.* **2009,** *39,* 1–23. doi:10.1146/annurev-matsci-082908-145401
8. McCreery, R. L.; Bergren, A. J. *Adv. Mater.* **2009,** *21,* 4303–4322. doi:10.1002/adma.200802850
9. Mayor, M. *Chimia* **2010,** *64,* 348–420. http://www.chimia.ch/x_data/heft_pdf/ACF5DFE.pdf
10. Malen, J. A.; Yee, S. K.; Majumdar, A.; Segalman, R. A. *Chem. Phys. Lett.* **2010,** *491,* 109–122. doi:10.1016/j.cplett.2010.03.028
11. Moth-Poulsen, K.; Bjornholm, T. *Nat. Nanotechnol.* **2009,** *4,* 551–556. doi:10.1038/nnano.2009.176
12. Nichols, R. J.; Haiss, W.; Higgins, S. J.; Leary, E.; Martin, S.; Bethell, D. *Phys. Chem. Chem. Phys.* **2010,** *12,* 2801–2815. doi:10.1039/b922000c
13. Venkataraman, L.; Klare, J. E.; Nuckolls, C.; Hybertsen, M. S.; Steigerwald, M. L. *Nature* **2006,** *442,* 904–907. doi:10.1038/nature05037
14. Kaliginedi, V.; Valkenier, H.; Moreno, P.; Hummelen, J. C.; Wandlowski, T. Unpublished results.
15. Li, C.; Pobelov, I.; Wandlowski, T.; Bagrets, A.; Arnold, A.; Evers, F. *J. Am. Chem. Soc.* **2008,** *130,* 318–326. doi:10.1021/ja0762386
16. Mishchenko, A.; Vonlanthen, D.; Meded, V.; Burkle, M.; Li, C.; Pobelov, I. V.; Bagrets, A.; Viljas, J. K.; Pauly, F.; Evers, F.; Mayor, M.; Wandlowski, T. *Nano Lett.* **2010,** *10,* 156–163. doi:10.1021/nl903084b
17. Hong, W.; Manrique, D. Z.; Moreno, P.; Kaliginedi, V.; Gulcur, M.; Lambert, C.; Wandlowski, T., Unpublished results.
18. Zotti, L. A.; Kirchner, T.; Cuevas, J. C.; Pauly, F.; Huhn, T.; Scheer, E.; Erbe, A. *Small* **2010,** *6,* 1529–1535. doi:10.1002/smll.200902227

19. Tour, J. M. *Acc. Chem. Res.* **2000,** *33,* 791–804. doi:10.1021/ar0000612
20. Toyota, S. *Chem. Rev.* **2010,** *110,* 5398–5424. doi:10.1021/cr1000628
21. Salomon, A.; Cahen, D.; Lindsay, S.; Tomfohr, J.; Engelkes, V. B.; Frisbie, C. D. *Adv. Mater.* **2003,** *15,* 1881–1890. doi:10.1002/adma.200306091
22. Huber, R.; Gonzalez, M. T.; Wu, S.; Langer, M.; Grunder, S.; Horhoiu, V.; Mayor, M.; Bryce, M. R.; Wang, C. S.; Jitchati, R.; Schönenberger, C.; Calame, M. *J. Am. Chem. Soc.* **2008,** *130,* 1080–1084. doi:10.1021/ja0767940
23. Diez-Perez, I.; Hihath, J.; Hines, T.; Wang, Z. S.; Zhou, G.; Müllen, K.; Tao, N. J. *Nat. Nanotechnol.* **2011,** *6,* 226–231. doi:10.1038/nnano.2011.20
24. Markussen, T.; Schiötz, J.; Thygesen, K. S. *J. Chem. Phys.* **2010,** *132,* 224104. doi:10.1063/1.3451265
25. Liu, H. M.; Wang, N.; Zhao, J. W.; Guo, Y.; Yin, X.; Boey, F. Y. C.; Zhang, H. *ChemPhysChem* **2008,** *9,* 1416–1424. doi:10.1002/cphc.200800032
26. Gholami, M.; Tykwinski, R. R. *Chem. Rev.* **2006,** *106,* 4997–5027. doi:10.1021/cr0505573
27. Donhauser, Z. J.; Mantooth, B. A.; Kelly, K. F.; Bumm, L. A.; Monnell, J. D.; Stapleton, J. J.; Price, D. W., Jr.; Rawlett, A. M.; Allara, D. L.; Tour, J. M.; Weiss, P. S. *Science* **2001,** *292,* 2303–2307. doi:10.1126/science.1060294
28. Andres, R. P.; Bein, T.; Dorogi, M.; Feng, S.; Henderson, J. I.; Kubiak, C. P.; Mahoney, W.; Osifchin, R. G.; Reifenberger, R. *Science* **1996,** *272,* 1323–1325. doi:10.1126/science.272.5266.1323
29. Repp, J.; Meyer, G.; Paavilainen, S.; Olsson, F. E.; Persson, M. *Science* **2006,** *312,* 1196–1199. doi:10.1126/science.1126073
30. Wold, D. J.; Haag, R.; Rampi, M. A.; Frisbie, C. D. *J. Phys. Chem. B* **2002,** *106,* 2813–2816. doi:10.1021/jp013476t
31. Cui, X. D.; Primak, A.; Zarate, X.; Tomfohr, J.; Sankey, O. F.; Moore, A. L.; Moore, T. A.; Gust, D.; Harris, G.; Lindsay, S. M. *Science* **2001,** *294,* 571–574. doi:10.1126/science.1064354
32. Fan, F. R. F.; Yang, J. P.; Cai, L. T.; Price, D. W., Jr.; Dirk, S. M.; Kosynkin, D. V.; Yao, Y. X.; Rawlett, A. M.; Tour, J. M.; Bard, A. J. *J. Am. Chem. Soc.* **2002,** *124,* 5550–5560. doi:10.1021/ja017706t
33. Mishchenko, A.; Zotti, L. A.; Vonlanthen, D.; Burkle, M.; Pauly, F.; Cuevas, J. C.; Mayor, M.; Wandlowski, T. *J. Am. Chem. Soc.* **2011,** *133,* 184–187. doi:10.1021/ja107340t
34. Xu, B. Q.; Tao, N. J. *Science* **2003,** *301,* 1221–1223. doi:10.1126/science.1087481
35. Tao, N. J. *Phys. Rev. Lett.* **1996,** *76,* 4066–4069. doi:10.1103/PhysRevLett.76.4066
36. Haiss, W.; van Zalinge, H.; Higgins, S. J.; Bethell, D.; Hobenreich, H.; Schiffrin, D. J.; Nichols, R. J. *J. Am. Chem. Soc.* **2003,** *125,* 15294–15295. doi:10.1021/ja038214e
37. Seferos, D. S.; Trammell, S. A.; Bazan, G. C.; Kushmerick, J. G. *Proc. Natl. Acad. Sci. U. S. A.* **2005,** *102,* 8821–8825. doi:10.1073/pnas.0500002102
38. Dadosh, T.; Gordin, Y.; Krahne, R.; Khivrich, I.; Mahalu, D.; Frydman, V.; Sperling, J.; Yacoby, A.; Bar-Joseph, I. *Nature* **2005,** *436,* 677–680. doi:10.1038/nature03898
39. Liao, J.; Bernard, L.; Langer, M.; Schönenberger, C.; Calame, M. *Adv. Mater.* **2006,** *18,* 2444–2447. doi:10.1002/adma.200601001
40. Reed, M. A.; Zhou, C.; Muller, C. J.; Burgin, T. P.; Tour, J. M. *Science* **1997,** *278,* 252–254. doi:10.1126/science.278.5336.252
41. Kergueris, C.; Bourgoin, J. P.; Palacin, S.; Esteve, D.; Urbina, C.; Magoga, M.; Joachim, C. *Phys. Rev. B* **1999,** *59,* 12505–12513. doi:10.1103/PhysRevB.59.12505
42. Reichert, J.; Ochs, R.; Beckmann, D.; Weber, H. B.; Mayor, M.; von Löhneysen, H. *Phys. Rev. Lett.* **2002,** *88,* 176804. doi:10.1103/PhysRevLett.88.176804
43. Smit, R. H. M.; Noat, Y.; Untiedt, C.; Lang, N. D.; van Hemert, M. C.; van Ruitenbeek, J. M. *Nature* **2002,** *419,* 906–909. doi:10.1038/nature01103
44. Wu, S. M.; Gonzalez, M. T.; Huber, R.; Grunder, S.; Mayor, M.; Schönenberger, C.; Calame, M. *Nat. Nanotechnol.* **2008,** *3,* 569–574. doi:10.1038/nnano.2008.237
45. Lörtscher, E.; Ciszek, J. W.; Tour, J.; Riel, H. *Small* **2006,** *2,* 973–977. doi:10.1002/smll.200600101
46. Park, J.; Pasupathy, A. N.; Goldsmith, J. I.; Chang, C.; Yaish, Y.; Petta, J. R.; Rinkoski, M.; Sethna, J. P.; Abruna, H. D.; McEuen, P. L.; Ralph, D. C. *Nature* **2002,** *417,* 722–725. doi:10.1038/nature00791
47. Osorio, E. A.; Bjornholm, T.; Lehn, J. M.; Ruben, M.; van der Zant, H. S. J. *J. Phys.: Condens. Matter* **2008,** *20,* 374121. doi:10.1088/0953-8984/20/37/374121
48. Chen, J.; Reed, M. A.; Rawlett, A. M.; Tour, J. M. *Science* **1999,** *286,* 1550–1552. doi:10.1126/science.286.5444.1550
49. Slowinski, K.; Fong, H. K. Y.; Majda, M. *J. Am. Chem. Soc.* **1999,** *121,* 7257–7261. doi:10.1021/ja991613i
50. Haag, R.; Rampi, M. A.; Holmlin, R. E.; Whitesides, G. M. *J. Am. Chem. Soc.* **1999,** *121,* 7895–7906. doi:10.1021/ja990230h
51. Chiechi, R. C.; Weiss, E. A.; Dickey, M. D.; Whitesides, G. M. *Angew. Chem., Int. Ed.* **2008,** *47,* 142–144. doi:10.1002/anie.200703642
52. Agrait, N.; Yeyati, A. L.; van Ruitenbeek, J. M. *Phys. Rep.* **2003,** *377,* 81–279. doi:10.1016/s0370-1573(02)00633-6
53. Meszaros, G.; Li, C.; Pobelov, I.; Wandlowski, T. *Nanotechnology* **2007,** *18,* 424004. doi:10.1088/0957-4484/18/42/424004
54. Grüter, L. Mechanical Controllable Break Junction in a Liquid Environment: A Tool to Measure Single Molecules. Ph.D. Thesis, University of Basel, Swizerland, 2005.
55. van Dijk, E. H.; Myles, D. J. T.; van der Veen, M. H.; Hummelen, J. C. *Org. Lett.* **2006,** *8,* 2333–2336. doi:10.1021/ol0606278
56. Valkenier, H.; Guédon, C. M.; Markussen, T.; Thygesen, K. S.; van der Molen, S. J.; Hummelen, J. C. Unpublished results.
57. Valkenier, H.; Huisman, E. H.; van Hal, P. A.; de Leeuw, D. M.; Chiechi, R. C.; Hummelen, J. C. *J. Am. Chem. Soc.* **2011,** *133,* 4930–4939. doi:10.1021/ja110358t
58. Lörtscher, E.; Weber, H. B.; Riel, H. *Phys. Rev. Lett.* **2007,** *98,* 176807. doi:10.1103/PhysRevLett.98.176807
59. Kamenetska, M.; Koentopp, M.; Whalley, A. C.; Park, Y. S.; Steigerwald, M. L.; Nuckolls, C.; Hybertsen, M. S.; Venkataraman, L. *Phys. Rev. Lett.* **2009,** *102,* 126803. doi:10.1103/PhysRevLett.102.126803
60. Quek, S. Y.; Kamenetska, M.; Steigerwald, M. L.; Choi, H. J.; Louie, S. G.; Hybertsen, M. S.; Neaton, J. B.; Venkataraman, L. *Nat. Nanotechnol.* **2009,** *4,* 230–234. doi:10.1038/nnano.2009.10
61. Martin, C. A.; Ding, D.; Sorensen, J. K.; Bjornholm, T.; van Ruitenbeek, J. M.; van der Zant, H. S. J. *J. Am. Chem. Soc.* **2008,** *130,* 13198–13199. doi:10.1021/ja804699a
62. Martin, S.; Grace, I.; Bryce, M. R.; Wang, C. S.; Jitchati, R.; Batsanov, A. S.; Higgins, S. J.; Lambert, C. J.; Nichols, R. J. *J. Am. Chem. Soc.* **2010,** *132,* 9157–9164. doi:10.1021/ja103327f
63. Haiss, W.; Wang, C. S.; Grace, I.; Batsanov, A. S.; Schiffrin, D. J.; Higgins, S. J.; Bryce, M. R.; Lambert, C. J.; Nichols, R. J. *Nat. Mater.* **2006,** *5,* 995–1002. doi:10.1038/nmat1781
64. Guédon, C. M.; Valkenier, H.; Markussen, T.; Thygesen, K. S.; Hummelen, J. C.; van der Molen, S. J. Unpublished results.

65. Fracasso, D.; Valkenier, H.; Hummelen, J. C.; Solomon, G. C.; Chiechi, R. C. *J. Am. Chem. Soc.* **2011,** *133,* 9556–9563. doi:10.1021/ja202471m

Beilstein Journal of Nanotechnology

Charge transport in a zinc–porphyrin single-molecule junction

Mickael L. Perrin*[1], Christian A. Martin[1], Ferry Prins[1], Ahson J. Shaikh[2], Rienk Eelkema[2], Jan H. van Esch[2], Jan M. van Ruitenbeek[3], Herre S. J. van der Zant[1] and Diana Dulić[1]

Letter

Open Access

Address:
[1]Kavli Institute of Nanoscience, Delft University of Technology, Lorentzweg 1, Delft, The Netherlands, [2]Department of Chemical Engineering, Delft University of Technology, Julianalaan 136, 2628 BL Delft, The Netherlands and [3]Kamerlingh Onnes Laboratory, Leiden University, Niels Bohrweg 2, 2333 CA Leiden, The Netherlands

Email:
Mickael L. Perrin* - m.l.perrin@tudelft.nl

* Corresponding author

Keywords:
mechanically controllable break junction; molecular conformation; molecular electronics; porphyrin; single-molecule transport

Beilstein J. Nanotechnol. **2011,** *2,* 714–719.
doi:10.3762/bjnano.2.77

Received: 27 July 2011
Accepted: 26 September 2011
Published: 18 October 2011

This article is part of the Thematic Series "Transport through molecular junctions".

Associate Editor: R. Naaman

Abstract

We have investigated charge transport in ZnTPPdT–Pyr (TPPdT: 5,15-di(*p*-thiolphenyl)-10,20-di(*p*-tolyl)porphyrin) molecular junctions using the lithographic mechanically controllable break-junction (MCBJ) technique at room temperature and cryogenic temperature (6 K). We combined low-bias statistical measurements with spectroscopy of the molecular levels in the form of $I(V)$ characteristics. This combination allows us to characterize the transport in a molecular junction in detail. This complex molecule can form different junction configurations, having an observable effect on the trace histograms and the current–voltage ($I(V)$) measurements. Both methods show that multiple, stable single-molecule junction configurations can be obtained by modulating the interelectrode distance. In addition we demonstrate that different ZnTPPdT–Pyr junction configurations can lead to completely different spectroscopic features with the same conductance values. We show that statistical low-bias conductance measurements should be interpreted with care, and that the combination with $I(V)$ spectroscopy represents an essential tool for a more detailed characterization of the charge transport in a single molecule.

Introduction

The break-junction method represents a popular choice to investigate the electronic transport through metal–molecule–metal junctions [1-6]. While repeatedly breaking and fusing two metallic electrodes, the low-bias conductance is monitored as a function of the electrode displacement. Such low-bias transport measurements have been

extensively used to study the dependence of the molecular conductance on the length [1,2], conformation [3,4] and anchoring groups [5,6] of rod-like molecules. However, as the bias range is very limited, the main contribution to the current is off-resonance transport. As such, spectroscopic information about molecular energy levels involved in the charge transport is lacking.

Here, we investigate charge transport through a zinc(II) porphyrin [zinc(II) 5,15-di(*p*-thiolphenyl)-10,20-di(*p*-tolyl)porphyrin] with an axial pyridine ligand in both the low-bias and the high-bias regime. Porphyrins are interesting for this purpose as they are complex, non-rodlike molecules, which can form different stable conformations [7,8], especially when functionalized with metal-bound axial pyridine ligands [9]. Using the mechanically controllable break-junction (MCBJ) technique, we study the low-bias conductance as a function of the electrode displacement. In addition, we perform current–voltage measurements at different electrode spacings in order to gain spectroscopic information in the high-bias regime.

The MCBJ technique is an elegant way to control the spacing between two metallic electrodes with subatomic ($<10^{-10}$ m) resolution [10-12]. This control is achieved by bending a substrate supporting a pair of partially suspended electrodes, in a three-point bending mechanism. Upon bending of the substrate, a nanosized gap is formed between the electrodes, which can be mechanically adjusted and which is impressively stable on the order of several hours, even at room temperature [13,14]. The layout of the technique is schematically presented in Figure 1b.

All experiments were performed in high vacuum ($<10^{-6}$ mbar). Prior to the experiments, a complex of zinc(II) 5,15-di(*p*-thiolphenyl)-10,20-di(*p*-tolyl)porphyrin and pyridine (ZnTPPdT–Pyr) (see Figure 1a for the structural formula) was dissolved in dichloromethane (DCM) and deposited on the unbroken electrodes by means of self-assembly from solution. Two thiol groups on opposite sides of the molecule are used as anchoring groups. After deposition, the junctions are broken in vacuum at room temperature. The aforementioned stability of the electrodes allows us to characterize charge transport through ZnTPPdT–Pyr by performing two types of experiments. First, we measure at room temperature the low-bias conductance of the molecule as a function of the electrode stretching. Second, we perform spectroscopy of the molecular energy levels by measuring current–voltage characteristics at fixed electrode spacings; this was done both at room temperature and cryogenic temperature (6 K).

Results

To obtain the conductance value of the most probable contact geometry we repeatedly broke and fused the electrodes [15-17] between conductances of $1\cdot10^{-5}$ G_0 and 10 G_0, while measuring the current at a fixed bias voltage (100 mV). Each breaking event produced a "breaking trace" of the conductance, which is plotted as $\log_{10}(G)$ versus the electrode displacement d. Sets of 500 consecutive breaking traces from individual junctions were then binned in time and in electrode displacement. As we are interested in the breaking dynamics of the junctions beyond the point of rupture of the last monatomic gold contact (defined as $d = 0$), only conductance values below one quantum unit $G_0 = 2e^2/h$ (the resistance of a single gold atom) are considered. The results are plotted as two-dimensional "trace histograms", in which areas of high counts represent the most typical breaking behavior of the molecular junction [18,19].

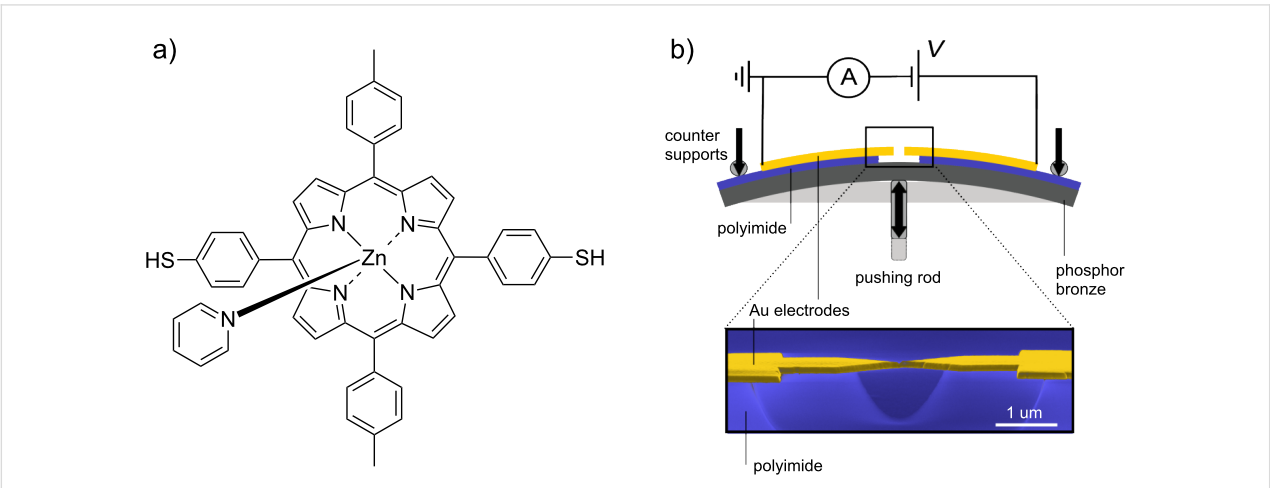

Figure 1: Structural formula of ZnTPPdT–Pyr (b) Top: Setup of the mechanically controllable break-junction (MCBJ). Bottom: Scanning electron micrograph of a MCBJ device (colorized for clarity). The scale bar shows that the suspended bridge is about 1 µm in length.

In Figure 2, we show trace histograms as well as examples of individual breaking traces for a junction exposed to (a) the solvent DCM and (b) ZnTPPdT–Pyr. All measured curves are included, i.e., no data selection was employed. We measured several samples with ZnTPPdT–Pyr molecules as well as DCM references. The features shown in Figure 2a and Figure 2b are representative of all these measurements. In the junction that was exposed to the pure solvent without porphyrin molecules (Figure 2a), the Au-bridge is stretched until a single-atom contact is formed, visible (only in the individual offset traces) as a plateau around the conductance quantum ($G \sim G_0$). Upon further stretching, the monatomic contact is broken and the conductance decreases sharply and abruptly to ~10^{-3} G_0 due to relaxation of the electrode tips. Beyond this point, electron tunneling between the electrodes leads to a fast conductance decay with stretching (visible as the orange tail), as expected for tunneling through a single barrier.

In contrast to this fast tunneling decay, introduction of the porphyrin molecules by self-assembly in the junction led to pronounced plateaus at different conductance values in the sub-G_0 regime. The observation of such plateaus in the breaking traces is commonly taken as a signature of the formation of a molecular junction [15-17]. Figure 2b shows that the plateaus can be horizontal or sloped. Some traces consist of a few plateaus at different conductance values. The representative breaking traces that are included in Figure 2b display a set of such plateaus. In strong contrast to measurements on rod-like molecules, averaging over 500 traces does not lead to a narrow region of high counts in the trace histograms. Instead, two distinct regions with high counts are visible; a high-conductance region around 10^{-1} G_0, and a sloped low-conductance region ranging from 10^{-3} G_0 to 10^{-5} G_0. Although clear plateaus are observed in the single breaking traces, averaging over hundreds of traces washes out the molecular signature. Hence, a complementary method is required to study charge transport in more detail.

We therefore measured current–voltage characteristics ($I(V)$s) at a fixed electrode spacing, in the 10^{-2}–10^{-5} G_0 conductance

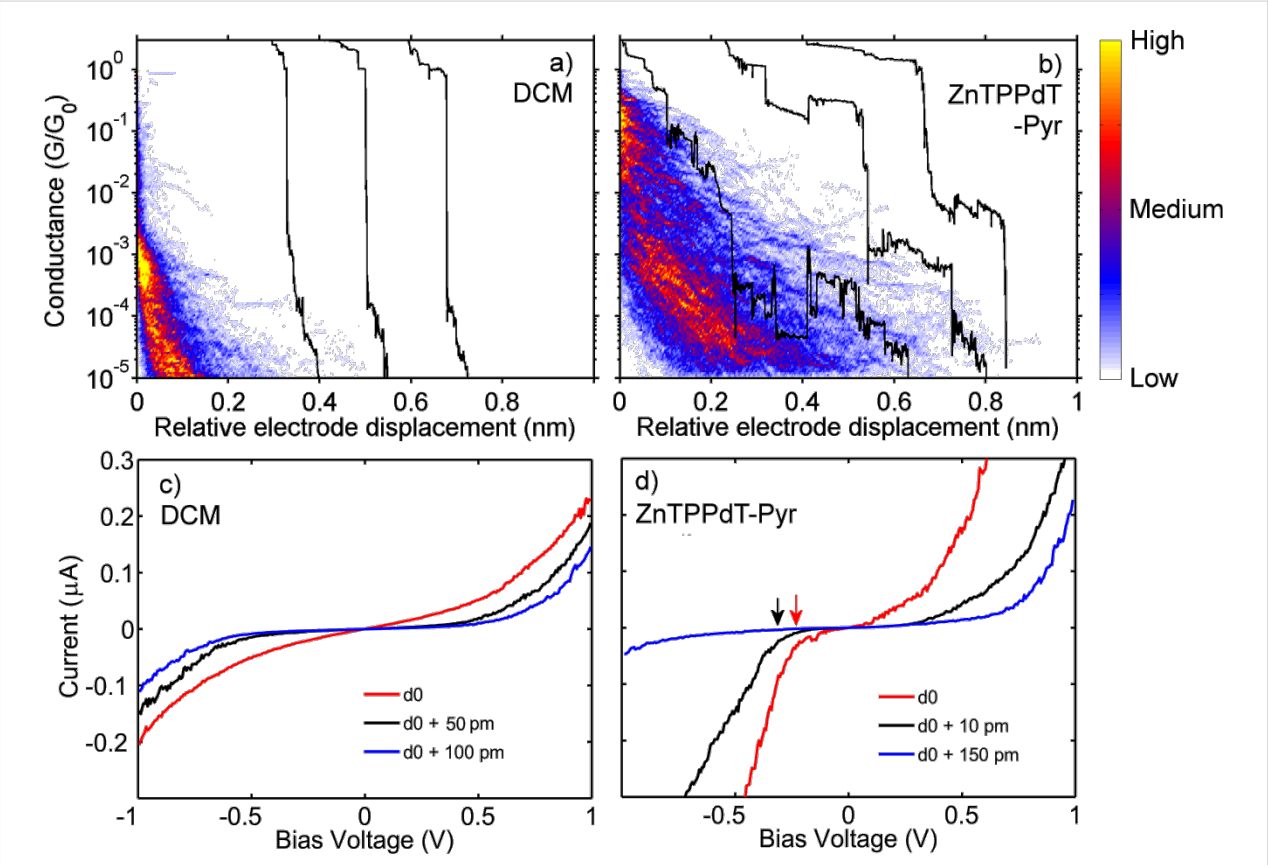

Figure 2: Trace histograms constructed from 500 consecutive breaking traces taken at room temperature and 100 mV bias for junctions exposed to (a) the solvent DCM only, and (b) to ZnTPPdT–Pyr. Regions of high counts represent the most probable breaking behavior of the contact. The black curves are examples of individual breaking traces (offset along the horizontal axis, d, for clarity). For the construction of the trace histograms, the zero of the relative electrode displacement for each curve was set to the point where the conductance drops sharply below 1 G_0. (c) Current–voltage characteristics taken at various electrode spacings starting from the initial value d_0 of junctions exposed to the solvent DCM, and (d) to ZnTPPdT–Pyr.

region. In between the $I(V)$ measurements, the interelectrode distance was gradually increased or decreased in steps of about 10 pm, without fusing the electrodes to form a metallic contact. In this way, changes in the configurations of the molecular junctions occurring as a function of electrode spacing can be accurately probed. $I(V)$s taken at room temperature for several electrode spacings of the junctions exposed to DCM and ZnTPPdT–Pyr are presented in Figure 2c and Figure 2d, respectively. For each series, all the presented $I(V)$s are taken from the same breaking sequence.

$I(V)$s of a junction exposed to DCM (Figure 2c) exhibit the characteristic single-barrier tunneling shape and show the expected current decrease upon increasing the electrode spacing. In contrast, $I(V)$ characteristics on the ZnTPPdT–Pyr junction show a sharper current onset, marked by arrows in Figure 2d. This observation may be viewed as a molecular fingerprint as the marked points correspond to the onset of resonant transport through an energy level of the molecule (either vibrational or electronic). Interestingly, the current onset strongly depends on the interelectrode distance. At d_0 it is located around −250 mV. After a step of about 10 pm in the electrode distance, the onset shifted to around −350 mV. Increasing the inter-electrode distance by an additional 140 pm, shifted the onset at negative bias to a location outside the bias window. Note furthermore the asymmetry in the curves in Figure 2d, which increases as the electrodes move further apart (i.e., the blue curve in Figure 2d). For the three $I(V)$s we also determined the conductance at the same bias voltage as used to construct the trace histograms, i.e., at 100 mV. For the red, black and blue $I(V)$ curve we obtain conductance values of $2.0{\cdot}10^{-3}$, $1.6{\cdot}10^{-4}$ and $1.6{\cdot}10^{-4}$ G_0 respectively. Interestingly, small changes in electrode distance (~10 pm) can induce significant changes in the shape of the $I(V)$ characteristics and the low-bias conductance (compare, e.g., the red and black curves). Opening the junction further (black and blue curves) results in no change of the conductance value at 100 mV, but in different $I(V)$ shapes.

Spectroscopic features become more pronounced at low temperature as the junction stability increases, and both the thermal noise and thermal broadening decrease. We therefore cooled down the junctions to cryogenic temperature (6 K) while keeping the zero-bias conductance at a fixed value (around $1{\cdot}10^{-4}$ G_0) with a feedback loop. In Figure 3a and Figure 3b, we present low-temperature $I(V)$s of junctions exposed to (a) DCM and (b) ZnTPPdT–Pyr solution, for different electrode spacings. $I(V)$s of the junction exposed to DCM show the characteristic tunneling shape, without any molecular signature, as was also found at room temperature. A notable difference, however, is the significant reduction of the noise.

The $I(V)$s of the junction containing ZnTPPdT–Pyr now show sharp step-like features, which are more pronounced than those in Figure 2d. We numerically determined the differential conductance (dI/dV) as displayed in Figure 3c. In the dI/dV curves, the steplike features are visible as resonance peaks, which are marked in the figure with arrows of the corresponding color. For clarity, the dI/dV curves are offset vertically, and the dI/dV-curve represented by the black curve is magnified 100 times. The origin of these resonances can be electronic or vibrational [20-22]. Independent of their origin, their pos-

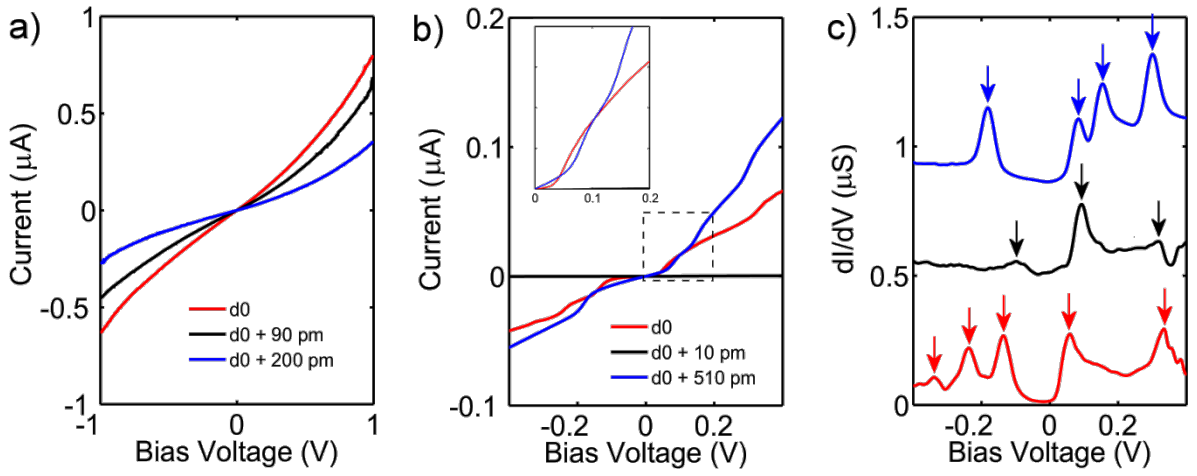

Figure 3: Low-temperature $I(V)$ characteristics of junctions exposed to (a) DCM and (b) ZnTPPdT–Pyr. The DCM sample clearly shows vacuum-tunneling behavior. The porphyrin sample exhibits Coulomb blockade and steps. (c) dI/dV of a junction exposed to a ZnTPPdT–Pyr solution; curves are offset vertically for clarity. Resonances correspond to electronic or vibrational energy levels of the molecular junction. Note, for the black line the dI/dV has been scaled by a factor of 100.

ition reveals the alignment of the corresponding energy level with respect to the Fermi energy of the electrodes [23]. For a distance of d_0 (red curve), five pronounced resonances are present, located at −339 mV, −283 mV, −153 mV, 58 mV and 334 mV. For the conductance at 100 mV we obtain a value of $2.1 \cdot 10^{-3}$ G_0. Increasing the distance by 10 pm (black curve) drastically changes the molecular energy spectrum, with one distinct resonance at 94 mV, and two fainter peaks around −99 mV and 319 mV. Here, the conductance at 100 mV is $1.2 \cdot 10^{-5}$ G_0. Increasing the distance by an additional 500 pm (blue curve) again leads to changes in the molecular energy spectrum; in this case four pronounced resonances are located at −238 mV, −136 mV, 58 mV and 334 mV. For the conductance we again obtain a value of $2.1 \cdot 10^{-3}$ G_0.

Discussion

Comparing first the red and black curve in Figure 3c, we see that within a change in the electrode displacement of 10 pm, the number of energy levels involved in the electronic transport as well as their exact energy drastically changed. A major jump of two orders of magnitude in the low-bias conductance was observed as well. This suggests an abrupt change in the molecule–electrode interaction, presumably caused by a change in molecular conformation. A similar change in molecular conformation was also observed in the room temperature $I(V)$s as demonstrated by the red and black curves in Figure 2; the onset for the current increase shifted by −100 mV and the conductance dropped by one order of magnitude within 10 pm. These observations support the conclusion drawn from the trace histogram measurements: The molecule can adopt different stable conformations, leading to plateaus at different conductance values in the breaking traces. Comparing the red and blue curves in Figure 3c, which were taken are at a separation of 510 pm, we see that their molecular energy spectra strongly differ, but that their low-bias conductance is similar (Figure 3b, inset). Similar behavior was also observed at room temperature (Figure 2d). This suggests that different stable junction configurations with very different spectroscopic signatures can exhibit the same low-bias conductance.

For most of the low-bias break-junction measurements on rod-like molecules it is assumed that repetitive fusing and breaking of the molecular junction provides the most probable conductance value [15-17]. Multiple conductance peaks are often attributed to the formation of multiple molecular bridges connected in parallel [15,24]. The strength of the molecule–metal chemical bond is considered to play a central role in determining the single-molecule conductance values. Our results on the Zn-porphyrin molecule with a pyridine axial group show that different conductance values can also result from the stretching or fusing of a molecular junction. As considerable changes in the conductance values and spectra already occur for a displacement as small as 10 pm, we conclude that neither the molecule–electrode chemical bond nor the electrode configuration itself can be held responsible. More likely, varying the electrode distance changes the molecular conformation, which in turn leads to abrupt changes in the molecule–electrode interaction. Our findings also show that $I(V)$ characteristics taken at different electrode spacings can exhibit distinct different spectroscopic features but a similar low-bias conductance. This indicates that different junction geometries can lead to similar conductance values in the trace histograms. Therefore, as changes in the configuration of the molecular junction are not always reflected in the low-bias trace histograms, supporting high-bias $I(V)$ characteristics are essential for the interpretation of such histograms.

Conclusion

In summary, we investigated charge transport in ZnTPPdT–Pyr molecular junctions using the lithographic MCBJ technique. We combined low-bias statistical measurements with spectroscopy measurements of the molecular levels in the form of $I(V)$ characteristics. This unique combination allows us to probe different junction configurations and monitor changes in the molecular-level alignment upon fusing or breaking of a molecular junction. Both methods show that multiple stable single-molecule junction configurations can be obtained by stretching or fusing the junction. In addition we demonstrate that different ZnTPPdT–Pyr junction configurations can lead to different spectroscopic features for similar low-bias conductance values. Thus, $I(V)$-spectroscopy measurements can provide additional information compared to statistical low-bias conductance histograms, enabling a more in-depth characterization of the charge transport through a single molecule.

Supporting Information

Supporting Information features detailed information on sample preparations and measurement procedures.

Supporting Information File 1

Experimental details.
[http://www.beilstein-journals.org/bjnano/content/supplementary/2190-4286-2-77-S1.pdf]

Acknowledgements

This research was carried out with financial support from the Dutch Foundation for Fundamental Research on Matter (FOM) and the VICI (680-47-305) grant from The Netherlands Organisation for Scientific Research (NWO).

References

1. Xiao, X.; Xu, B.; Tao, N. *J. Am. Chem. Soc.* **2004,** *126,* 5370–5371. doi:10.1021/ja049469a
2. Li, X.; He, J.; Hihath, J.; Xu, B.; Lindsay, S. M.; Tao, N. *J. Am. Chem. Soc.* **2006,** *128,* 2135–2141. doi:10.1021/ja057316x
3. Venkataraman, L.; Klare, J. E.; Nuckolls, C.; Hybertsen, M. S.; Steigerwald, M. L. *Nature* **2006,** *442,* 904–907. doi:10.1038/nature05037
4. Mishchenko, A.; Vonlanthen, D.; Meded, V.; Bürkle, M.; Li, C.; Pobelov, I. V.; Bagrets, A.; Viljas, J. K.; Pauly, F.; Evers, F.; Mayor, M.; Wandlowski, T. *Nano Lett.* **2010,** *10,* 156–163. doi:10.1021/nl903084b
5. Park, Y. S.; Whalley, A. C.; Kamenetska, M.; Steigerwald, M. L.; Hybertsen, M. S.; Nuckolls, C.; Venkataraman, L. *J. Am. Chem. Soc.* **2007,** *129,* 15768–15769. doi:10.1021/ja0773857
6. Chen, F.; Li, X.; Hihath, J.; Huang, Z.; Tao, N. *J. Am. Chem. Soc.* **2006,** *128,* 15874–15881. doi:10.1021/ja065864k
7. Qiu, X. H.; Nazin, G. V.; Ho, W. *Phys. Rev. Lett.* **2004,** *93,* 196806. doi:10.1103/PhysRevLett.93.196806
8. Brede, J.; Linares, M.; Kuck, S.; Schwöbel, J.; Scarfato, A.; Chang, S.-H.; Hoffmann, G.; Wiesendanger, R.; Lensen, R.; Kouwer, P. H. J.; Hoogboom, J.; Rowan, A. E.; Bröring, M.; Funk, M.; Stafström, S.; Zerbetto, F.; Lazzaroni, R. *Nanotechnology* **2009,** *20,* 275602. doi:10.1088/0957-4484/20/27/275602
9. Perrin, M. L.; Prins, F.; Martin, C. A.; Shaikh, A. J.; Eelkema, R.; van Esch, J. H.; Briza, T.; Kaplanek, R.; Kral, V.; van Ruitenbeek, J. M.; van der Zant, H. S. J.; Dulić, D. *Angew. Chem., Int. Ed.*, in press. doi:10.1002/anie.201104757
10. van Ruitenbeek, J. M.; Alvarez, A.; Piñeyro, I.; Grahmann, C.; Joyez, P.; Devoret, M. H.; Esteve, D.; Urbina, C. *Rev. Sci. Instrum.* **1996,** *67,* 108–111. doi:10.1063/1.1146558
11. Rubio, G.; Agraït, N.; Vieira, S. *Phys. Rev. Lett.* **1996,** *76,* 2302–2305. doi:10.1103/PhysRevLett.76.2302
12. Scheer, E.; Agraït, N.; Cuevas, J. C.; Yeyati, A. L.; Ludoph, B.; Martín-Rodero, A.; Bollinger, G. R.; van Ruitenbeek, J. M.; Urbina, C. *Nature* **1998,** *394,* 154–157. doi:10.1038/28112
13. Martin, C. A.; Ding, D.; van der Zant, H. S. J.; van Ruitenbeek, J. M. *New J. Phys.* **2008,** *10,* 065008. doi:10.1088/1367-2630/10/6/065008
14. Dulić, D.; Pump, F.; Campidelli, S.; Lavie, P.; Cuniberti, G.; Filoramo, A. *Angew. Chem., Int. Ed.* **2009,** *48,* 8273–8276. doi:10.1002/anie.200902168
15. Xu, B. Q.; Tao, N. J. *Science* **2003,** *301,* 1221–1223. doi:10.1126/science.1087481
16. Gonzalez, M. T.; Wu, S.; Huber, R.; van der Molen, S. J.; Schönenberger, C.; Calame, M. *Nano Lett.* **2006,** *6,* 2238–2242. doi:10.1021/nl061581e
17. Venkataraman, L.; Klare, J. E.; Tam, I. W.; Nuckolls, C.; Hybertsen, M. S.; Steigerwald, M. L. *Nano Lett.* **2006,** *6,* 458–462. doi:10.1021/nl052373+
18. Martin, C. A.; Ding, D.; Sørensen, J. K.; Bjørnholm, T.; van Ruitenbeek, J. M.; van der Zant, H. S. J. *J. Am. Chem. Soc.* **2008,** *130,* 13198–13199. doi:10.1021/ja804699a
19. Kamenetska, M.; Koentopp, M.; Whalley, A. C.; Park, Y. S.; Steigerwald, M. L.; Nuckolls, C.; Hybertsen, M. S.; Venkataraman, L. *Phys. Rev. Lett.* **2009,** *102,* 126803. doi:10.1103/PhysRevLett.102.126803
20. Osorio, E. A.; O'Neill, K.; Stuhr-Hansen, N.; Nielsen, O. F.; Bjørnholm, T.; van der Zant, H. S. J. *Adv. Mater.* **2007,** *19,* 281–285. doi:10.1002/adma.200601876
21. Reichert, J.; Ochs, R.; Beckmann, D.; Weber, H. B.; Mayor, M.; v. Löhneysen, H. *Phys. Rev. Lett.* **2002,** *88,* 176804. doi:10.1103/PhysRevLett.88.176804
22. Kubatkin, S.; Danilov, A.; Hjort, M.; Cornil, J.; Brédas, J.-L.; Stuhr-Hansen, N.; Hedegård, P.; Bjørnholm, T. *Nature* **2003,** *425,* 698–701. doi:10.1038/nature02010
23. Thijssen, J. M.; van der Zant, H. S. J. *Phys. Status Solidi B* **2008,** *245,* 1455–1470. doi:10.1002/pssb.200743470
24. Gonzalez, M. T.; Brunner, J.; Huber, R.; Wu, S.; Schönenberger, C.; Calame, M. *New J. Phys.* **2008,** *10,* 065018. doi:10.1088/1367-2630/10/6/065018

License and Terms

Beilstein Journal of Nanotechnology

Nonconservative current-induced forces: A physical interpretation

Tchavdar N. Todorov*[1], Daniel Dundas[1], Anthony T. Paxton[1] and Andrew P. Horsfield[2]

Full Research Paper

Open Access

Address:
[1]Atomistic Simulation Centre, School of Mathematics and Physics, Queen's University Belfast, Belfast BT7 1NN, UK and [2]Department of Materials, Imperial College, London SW7 2AZ, UK

Email:
Tchavdar N. Todorov* - t.todorov@qub.ac.uk; Daniel Dundas - d.dundas@qub.ac.uk

* Corresponding author

Keywords:
atomic-scale conductors; current-induced forces; failure mechanisms; nanomotors

Beilstein J. Nanotechnol. **2011,** *2,* 727–733.
doi:10.3762/bjnano.2.79

Received: 30 June 2011
Accepted: 20 September 2011
Published: 27 October 2011

This article is part of the Thematic Series "Transport through molecular junctions".

Guest Editor: J. M. van Ruitenbeek

Abstract

We give a physical interpretation of the recently demonstrated nonconservative nature of interatomic forces in current-carrying nanostructures. We start from the analytical expression for the curl of these forces, and evaluate it for a point defect in a current-carrying system. We obtain a general definition of the capacity of electrical current flow to exert a nonconservative force, and thus do net work around closed paths, by a formal noninvasive test procedure. Second, we show that the gain in atomic kinetic energy over time, generated by nonconservative current-induced forces, is equivalent to the uncompensated stimulated emission of directional phonons. This connection with electron–phonon interactions quantifies explicitly the intuitive notion that nonconservative forces work by angular momentum transfer.

Introduction

Electron–nuclear interactions lie at the heart of the transport properties of nanoscale conductors. Even in the limit of elastic (phonon-free) conduction, the nature and positions of nuclei in a nanojunction determine the external potential, experienced by current-carrying electrons, and, together with electron–electron interactions, determine the current–voltage spectrum of the system. Allowing nuclei to respond to current-induced forces introduces two additional elements: Current-driven displacements and Joule heating. Current-induced forces arise, fundamentally, through momentum transfer from the electron flow to nuclei, and are familiar from the field of electromigration [1]. An alternative, but fundamentally equivalent, way to think about them is as nonequilibrium corrections to interatomic bonding forces. In considering these forces, it is often conveni-

ent to adopt the Born–Oppenheimer approximation, adapted to the nonequilibrium conditions in a nanoconductor: We think of nuclei as heavy, slow classical particles, and imagine that, as nuclei move, electrons always remain in the steady state appropriate for the given set of instantaneous nuclear positions; we then calculate the force on a nucleus exerted by the mean electron density in the system (including appropriate Pulay corrections, if an incomplete electronic basis is used) [2-5]. Joule heating, on the other hand, is due to the finite mass of nuclei, and results from the recoil of nuclei in inelastic collisions with electrons [6-10]. The combined effect of the two is the driving force behind electromigration-type phenomena [2,6,7]: Current-induced forces modify atomic migration barriers; together with local heating, this results in thermally activated current-induced atomic rearrangements, or even failure.

Recently, a new and rather different aspect of current-induced forces has received attention: Their nonconservative character, and their resultant ability to do net work on individual atoms, or groups of atoms, around closed paths [1,11-14]. The practical consequences of this mechanism for sustained energy transfer from electrical current into atomic motion are only just starting to be explored. Two aspects of the effect that are of immediate interest are its capacity to drive an atomic-scale motor, and its possible potent role as a cause for dramatic mechanical failure [12-14]. Indeed, the notion that current can drive rotary motion, under appropriate conditions, is highly intuitive [15,16], and is increasingly being seen as a common, rather than rare, effect in nanoscale conductors [17]. The essential physics behind the nonconservative component of current-induced forces is that of a waterwheel driven by a flow [12]. For quantum-mechanical electron flow interacting with classical nuclei, the effect is quantified precisely by an analytical result for the curl of these forces [12,18]. Yet, there is a gap to be bridged between the formal result and the intuitive physics.

The aim of the present short paper is to bridge this gap, and extract explicitly the gas-flow picture of nonconservative current-induced forces. We then make a second connection, by showing that the work done by these forces around closed paths is equivalent to the uncompensated stimulated emission of directional phonons, characterised by the sign of their angular momentum. This second result will close the gap between the nonconservative effect and the more familiar fundamental physics of electron–phonon interactions.

Results and Discussion

The gas-flow picture

Under steady-state conditions, in the absence of phonons, the electronic properties of a nanoscale conductor are parametric functions of the classical nuclear positions. So too are the current-induced forces on the nuclei. The nonconservative component of these forces is characterised by the generalised curl expression [12,18]

$$\frac{\partial F_J(Q)}{\partial Q_I}-\frac{\partial F_I(Q)}{\partial Q_J}=4\pi\mathrm{Im}\mathrm{Tr}\{\hat{F}_I(Q)\hat{D}(\mu,Q)\hat{F}_J(Q)\Delta\hat{\rho}(Q)\}. \quad (1)$$

Here, and throughout the paper, we work in the small-bias limit. For our present purposes, we work with noninteracting electrons and zero magnetic fields.

In Equation 1, Q denotes a collection of generalised classical coordinates $\{Q_I\}$; $F_I(Q)$ is the current-induced force on coordinate Q_I; $\hat{D}(\mu,Q)=\delta[\mu-\hat{H}_e(Q)]$ is the operator for the electronic density of states, evaluated at the Fermi level μ; $\Delta\hat{\rho}(Q)$ is the nonequilibrium part of the one-electron density matrix (that is, the difference between the steady-state current-carrying density matrix and the equilibrium density matrix); finally, $\hat{F}_I(Q)$ is the force operator

$$\hat{F}_I(Q)=-\frac{\partial\hat{H}_e(Q)}{\partial Q_I}, \quad (2)$$

where $\hat{H}_e(Q)$ is the one-electron Hamiltonian, as a parametric function of the classical degrees of freedom Q.

Equation 1 is intriguing but lacks transparency. We now probe its physical content as follows. We immerse a point defect, with position vector $\mathbf{R}=(X,Y,Z)$ and a scattering potential $\hat{v}(\mathbf{R})=C\delta(\hat{\mathbf{r}}-\mathbf{R})$, in the electron flow. Here, $\mathbf{r}=(x,y,z)$ denotes the electron position. We shall use the defect to directly measure the ability of the flow to exert a nonconservative force.

We have

$$\hat{\mathbf{F}}(\mathbf{R})=-C\nabla_{\mathbf{R}}\delta(\hat{\mathbf{r}}-\mathbf{R})=C\nabla_{\mathbf{r}}\delta(\hat{\mathbf{r}}-\mathbf{R}). \quad (3)$$

Below, we deliberately treat C as small and work to the lowest nontrivial order in this parameter. Taking the trace in Equation 1 in the continuum $\mathbf{r}$-representation,

$$(\nabla_{\mathbf{R}}\times\mathbf{F}(\mathbf{R}))_Z=4\pi\mathrm{Im}\int \mathrm{d}\mathbf{r}\mathrm{d}\mathbf{r}'F_X(\mathbf{r},\mathbf{R})D(\mathbf{r},\mathbf{r}',\mathbf{R},\mu)\times F_Y(\mathbf{r}',\mathbf{R})\Delta\rho(\mathbf{r}',\mathbf{r},\mathbf{R}). \quad (4)$$

We also have

$$j_\nu(\mathbf{r},\mathbf{R})=\frac{\hbar}{m}\mathrm{Im}\left(\frac{\partial\Delta\rho(\mathbf{r},\mathbf{r}',\mathbf{R})}{\partial\nu}\right)_{\mathbf{r}=\mathbf{r}'} \quad (5)$$

$$(\nabla_{\mathbf{r}} \times \mathbf{j}(\mathbf{r},\mathbf{R}))_z = \frac{2\hbar}{m}\mathrm{Im}\left(\frac{\partial^2 \Delta\rho(\mathbf{r},\mathbf{r}',\mathbf{R})}{\partial y \partial x'}\right)_{\mathbf{r}=\mathbf{r}'}, \quad (6)$$

where ν = *x*,*y*,*z* and $\mathbf{j}(\mathbf{r},\mathbf{R})$ is the electron particle-current density.

Then, to lowest order in *C*, we obtain

$$\nabla_{\mathbf{R}} \times \mathbf{F}(\mathbf{R}) = \frac{2\pi m C^2}{\hbar}\left\{\nabla_{\mathbf{r}} \times [D(\mathbf{r},\mu)\mathbf{j}(\mathbf{r})]\right\}_{\mathbf{r}=\mathbf{R}}, \quad (7)$$

where $D(\mathbf{r},\mu) = D(\mathbf{r},\mathbf{r},\mu)$ and $\mathbf{j}(\mathbf{r})$ are the local density of states at the Fermi level and the particle-current density *in the absence of the point scatterer*. Therefore, Equation 7 defines an *intrinsic property* of the current flow: Its "curl-generating" capacity. The point defect above serves as a noninvasive test particle that probes this property. One can picture situations in which this intrinsic curl vanishes but yet there still is a nonzero curl to higher order in the coupling between the scatterer and the electrons. One example of this interesting possibility would be an atom weakly bonded to a structure, where the weak bonding enables current to flow through the atom in the first place.

Equation 7 is completely general and makes no assumptions about the nature and structure of the conductor. We will now simplify it further as follows. We assume that all electronic properties vary slowly in space, and we attribute a local Fermi momentum, $p(\mathbf{r})$, to the electrons. We now have a semiclassical gas flow in a, locally, jellium-like environment. Next, we observe that for jellium

$$\sigma = \frac{2\pi}{\hbar}C^2\left[\frac{D(\mathbf{r},\mu)}{p(\mathbf{r})/m}\right]_{\mathbf{r}=\mathbf{R}} = \sigma_{\mathrm{tr}} \quad (8)$$

is the scattering cross section of the defect. In the assumed, locally free-electron-like medium, in 3D, to lowest order in *C*, σ is a constant (since $D(\mathbf{r},\mu) \propto p(\mathbf{r})$), and is equal also to the transport cross section, σ_{tr}. Hence,

$$\nabla_{\mathbf{R}} \times \mathbf{F}(\mathbf{R}) = \sigma_{\mathrm{tr}}\left\{\nabla_{\mathbf{r}} \times [p(\mathbf{r})\mathbf{j}(\mathbf{r})]\right\}_{\mathbf{r}=\mathbf{R}}. \quad (9)$$

Thus, (the curl of) the force on the test particle is proportional to (the curl of) the local momentum flux of the flow, $[p(\mathbf{r})\mathbf{j}(\mathbf{r})]$, with a constant of proportionality σ_{tr}. At this stage, quantum mechanics has all but disappeared from the problem: We have a classical interaction between a, generally, spatially nonuniform steady gas flow and an elastic scatterer in its path.

Finally, recognising

$$\sigma_{\mathrm{tr}}\left[p(\mathbf{r})\mathbf{j}(\mathbf{r})\right]_{\mathbf{r}=\mathbf{R}} = \mathbf{F}_{\mathrm{wind}}(\mathbf{R}) \quad (10)$$

as the electron-wind force in electromigration, we have

$$\nabla_{\mathbf{R}} \times \mathbf{F}(\mathbf{R}) = \nabla_{\mathbf{R}} \times \mathbf{F}_{\mathrm{wind}}(\mathbf{R}). \quad (11)$$

Therefore, we have shown from first principles that the point of departure, Equation 1, is an algebraic statement of Sorbello's thought experiment [1] to prove that this force is, in general, a nonconservative force. We have shown, further, that the key quantity responsible for this property is the curl of the local electron momentum-current density.

Nonconservative work as directional phonon emission

We will now relate the nonconservative current-induced forces on atoms to the intuitive idea of the waterwheel. To this end, we will show that the work done by these forces around closed paths corresponds exactly to the stimulated generation of directional phonons, characterised by their angular momentum. Consider a flux of electrons travelling through an elastic medium. Intuitively, we expect the flux to preferentially emit phonons with momentum parallel to the electron flow. This becomes evident, when we consider the setup in Figure 1.

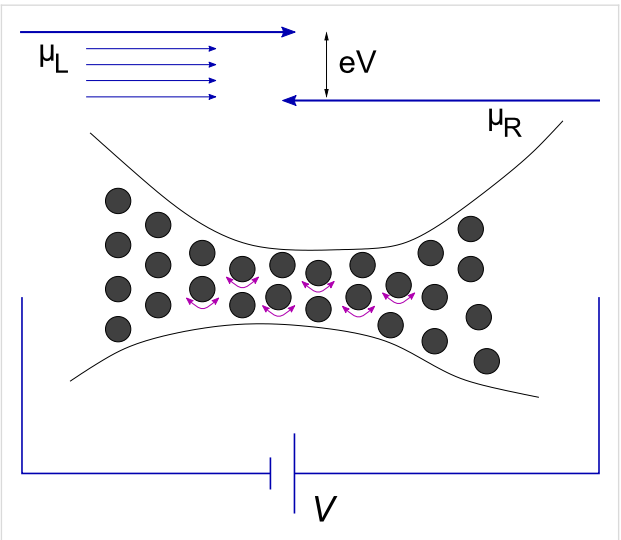

Figure 1: An electrode–junction–electrode system in the Landauer picture. The details are discussed in the text.

A nanostructure is connected to two electrodes, each in turn connected to its own battery terminal serving as a particle reservoir. The left reservoir injects right-travelling electrons with electrochemical potential

$$\mu_L = \mu + eV/2, \tag{12}$$

and the right reservoir injects left-travelling electrons with electrochemical potential

$$\mu_R = \mu - eV/2, \tag{13}$$

where V is the applied bias.

The current comes from the energy window between μ_R and μ_L, where there are partially-populated electron states. A right-travelling electron in this energy window can emit a right-travelling phonon, and scatter into a left-travelling state. But the reverse process is suppressed, due to the population imbalance between the two sets of electron states. Hence, we expect a directional preference of the emitted phonons. Since the rate of stimulated emission increases with growing phonon population, we might expect the process to have the ability to feed on itself. We will show below that this is the physical origin of the nonconservative current-induced forces.

Consider two independent generalised oscillator coordinates X and Y, with the same angular frequency, ω. Here, X and Y could be two individual atomic degrees of freedom (not necessarily of the same atom), or they could be collective normal modes. In all cases, we assume, as our starting point, that the modes X and Y describe *standing waves*. The Hamiltonian for the two oscillator degrees of freedom is

$$\hat{H}_{\rm osc} = \frac{1}{2M}\left(\hat{P}_X^2 + \hat{P}_Y^2\right) + \frac{1}{2}M\omega^2\left(\hat{X}^2 + \hat{Y}^2\right), \tag{14}$$

where P_X and P_Y are the corresponding canonical momenta, and M is a mass-like parameter.

We now form new modes, which we label by (+) and (−), with annihilation operators

$$\hat{A}_+ = \frac{1}{2}\sqrt{\frac{M\omega}{\hbar}}\left(\hat{X} - \mathrm{i}\hat{Y}\right) + \frac{\mathrm{i}}{2}\sqrt{\frac{1}{M\hbar\omega}}\left(\hat{P}_X - \mathrm{i}\hat{P}_Y\right) \tag{15}$$

$$\hat{A}_- = \frac{1}{2}\sqrt{\frac{M\omega}{\hbar}}\left(\hat{X} + \mathrm{i}\hat{Y}\right) + \frac{\mathrm{i}}{2}\sqrt{\frac{1}{M\hbar\omega}}\left(\hat{P}_X + \mathrm{i}\hat{P}_Y\right). \tag{16}$$

They obey

$$[\hat{A}_+, \hat{A}_+^\dagger] = 1 = [\hat{A}_-, \hat{A}_-^\dagger], \tag{17}$$

with all other commutators equal to zero. The inverse relations are

$$\hat{X} = \frac{1}{2}\sqrt{\frac{\hbar}{M\omega}}\left(\hat{A}_+ + \hat{A}_+^\dagger + \hat{A}_- + \hat{A}_-^\dagger\right) \tag{18}$$

$$\hat{Y} = \frac{1}{2\mathrm{i}}\sqrt{\frac{\hbar}{M\omega}}\left(\hat{A}_+^\dagger - \hat{A}_+ + \hat{A}_- - \hat{A}_-^\dagger\right) \tag{19}$$

$$\hat{P}_X = \frac{1}{2\mathrm{i}}\sqrt{M\hbar\omega}\left(\hat{A}_+ + \hat{A}_- - \hat{A}_+^\dagger - \hat{A}_-^\dagger\right) \tag{20}$$

$$\hat{P}_Y = \frac{1}{2}\sqrt{M\hbar\omega}\left(\hat{A}_+ + \hat{A}_+^\dagger - \hat{A}_- - \hat{A}_-^\dagger\right). \tag{21}$$

The new modes diagonalise the Hamiltonian as follows

$$\hat{H}_{\rm osc} = \hbar\omega\left(\hat{N}_+ + \frac{1}{2} + \hat{N}_- + \frac{1}{2}\right), \tag{22}$$

where

$$\hat{N}_+ = \hat{A}_+^\dagger\hat{A}_+ \,,\ \hat{N}_- = \hat{A}_-^\dagger\hat{A}_-. \tag{23}$$

The physical significance of the new modes can be seen by considering the angular momentum

$$\hat{L}_Z = \hat{X}\hat{P}_Y - \hat{Y}\hat{P}_X = \hbar\left(\hat{N}_+ - \hat{N}_-\right). \tag{24}$$

Thus, the "anticlockwise" mode (+) carries positive angular momentum (in the direction, perpendicular to the abstract X–Y plane) and the "clockwise" mode (−) carries negative angular momentum. By coupling these two directional phonon modes to electrons, we will see that the electron current pumps energy into one, while damping the other.

The coupling between electrons and phonons is described by scattering theory. The unperturbed, phonon-free state of the current-carrying electrons is that of the usual Landauer picture [5]. In this picture, electrons in the phonon-free steady state are described by two sets of stationary one-electron Lippmann–Schwinger scattering states. One set, $\{|\psi_l\rangle\}$ with energies $\{E_l\}$, originate from the left electrode, and are scattered elastically at the junction, with partial backscattering into the left electrode and partial transmission into the right electrode; the other set, $\{|\psi_r\rangle\}$ with energies $\{E_r\}$, originate

from the right electrode, with partial backscattering into the right electrode and partial transmission to the left. In the absence of bound states (which we assume here), the two form a complete orthonormal set. The left reservoir populates states l, in a grand-canonical ensemble with electrochemical potential μ_L (and a chosen electronic temperature); the right reservoir populates states r with electrochemical potential μ_R. It is convenient to define the density of states operators [5]

$$\begin{aligned}\hat{D}_L(E) &= \sum_l |\psi_l\rangle\delta(E-E_l)\langle\psi_l|,\\ \hat{D}_R(E) &= \sum_r |\psi_r\rangle\delta(E-E_r)\langle\psi_r|,\end{aligned} \tag{25}$$

with

$$\hat{D}_L(E)+\hat{D}_R(E)=\hat{D}(E). \tag{26}$$

Here, we include spin in $\hat{D}_L(E)$ and $\hat{D}_R(E)$. From Equation 12, Equation 13 and Equation 25, the nonequilibrium part of the one-electron density matrix, in the linear bias regime, is given by

$$\Delta\hat{\rho}=\frac{eV}{2}\Big[\hat{D}_L(\mu)-\hat{D}_R(\mu)\Big]. \tag{27}$$

The system of two oscillators, we describe by an unperturbed density matrix that commutes with $\hat{N}_\pm$. Electrons and oscillators are then coupled by an interaction of the generic form

$$\begin{aligned}\hat{v}=&-\sum_{\alpha=l,r}\sum_{\beta=l,r}\hat{c}_\alpha^\dagger\hat{c}_\beta\langle\psi_\alpha|\hat{F}_X|\psi_\beta\rangle\hat{X}\\ &-\sum_{\alpha=l,r}\sum_{\beta=l,r}\hat{c}_\alpha^\dagger\hat{c}_\beta\langle\psi_\alpha|\hat{F}_Y|\psi_\beta\rangle\hat{Y},\end{aligned} \tag{28}$$

where $\hat{c}_\alpha$ and $\hat{c}_\alpha^\dagger$ are fermionic annihilation and creation operators. Then, for the resultant rates of change of the occupancies, $N_\pm$, of the anticlockwise and clockwise modes, to lowest order in $\hat{v}$, we obtain

$$\begin{aligned}\dot{N}_\pm=&\frac{\pi}{2M\omega}(N_\pm+1)\\ &\times\sum_{\alpha=l,r}\sum_{\beta=l,r}f_\alpha(1-f_\beta)|\langle\psi_\beta|(\hat{F}_X\mp i\hat{F}_Y)|\psi_\alpha\rangle|^2\\ &\times\delta(E_\beta-E_\alpha+\hbar\omega)\\ &-\frac{\pi}{2M\omega}N_\pm\\ &\times\sum_{\alpha=l,r}\sum_{\beta=l,r}f_\alpha(1-f_\beta)|\langle\psi_\beta|(\hat{F}_X\pm i\hat{F}_Y)|\psi_\alpha\rangle|^2\\ &\times\delta(E_\beta-E_\alpha-\hbar\omega),\end{aligned} \tag{29}$$

where $f_l=f_L(E_l)$ and $f_r=f_R(E_r)$ are the Fermi–Dirac distributions for electrons originating from the two respective reservoirs.

We now deliberately suppress the spontaneous phonon emission. Formally, we work in the classical limit and set $(N_\pm+1)\approx N_\pm$. Then, counting all possibilities for α and β above and observing the selection rules, setting the electronic temperature to zero, and ignoring variations in the electronic properties over energies in the region of $\hbar\omega$ or eV, we get

$$\begin{aligned}\dot{N}_\pm=&-\frac{N_\pm}{2}\frac{\pi\hbar}{M}\big(T_X+T_Y\big)\\ &\pm N_\pm\frac{2\pi}{M\omega}eV\,\mathrm{Im}\mathrm{Tr}\{\hat{D}_R(\mu)\hat{F}_Y\hat{D}_L(\mu)\hat{F}_X\},\end{aligned} \tag{30}$$

where

$$\begin{aligned}T_X=&\,\mathrm{Tr}\{\hat{D}_L(\mu)\hat{F}_X\hat{D}_L(\mu)\hat{F}_X\}\\ &+2\mathrm{Tr}\{\hat{D}_L(\mu)\hat{F}_X\hat{D}_R(\mu)\hat{F}_X\}\\ &+\mathrm{Tr}\{\hat{D}_R(\mu)\hat{F}_X\hat{D}_R(\mu)\hat{F}_X\}\end{aligned} \tag{31}$$

$$\begin{aligned}T_Y=&\,\mathrm{Tr}\{\hat{D}_L(\mu)\hat{F}_Y\hat{D}_L(\mu)\hat{F}_Y\}\\ &+2\mathrm{Tr}\{\hat{D}_L(\mu)\hat{F}_Y\hat{D}_R(\mu)\hat{F}_Y\}\\ &+\mathrm{Tr}\{\hat{D}_R(\mu)\hat{F}_Y\hat{D}_R(\mu)\hat{F}_Y\}.\end{aligned} \tag{32}$$

This is our final result. Equation 30 displays precisely the picture from [12]. Mode (+) experiences a damped driven motion. The damping (first term) is due to the ordinary electronic friction experienced by the two independent modes X and Y (each of which carries half of the energy of mode (+)). This friction is due to phonon absorption by electrons, and is present even at zero current. The driving term (the second term) comes solely from the current. It anti-drives mode (−).

To extract explicitly the curl of the effective driving force acting on the 2D oscillator, for the rate at which this force does work on mode (+) we write

$$\dot{U}_+=(\nabla\times\mathbf{F})_Z\,\pi A^2\frac{\omega}{2\pi}, \tag{33}$$

where $U_+=N_+\,\hbar\omega=M\omega^2A^2$ is the energy of the mode and A^2 is the mean square displacement in the X–Y plane. Comparison with the second term in Equation 30 gives

$$(\nabla\times\mathbf{F})_Z=4\pi eV\,\mathrm{Im}\mathrm{Tr}\{\hat{D}_R(\mu)\hat{F}_Y\hat{D}_L(\mu)\hat{F}_X\}. \tag{34}$$

In view of Equation 26 and Equation 27, this is equivalent to Equation 1 [13]. The difference is that in [12,18] this result was derived in the mixed quantum-classical framework of Ehrenfest dynamics. Herein, it has been obtained formally exactly from quantum-mechanical electron–phonon coupling: The work done by nonconservative forces around a closed path is equivalent to the stimulated emission of directional, angular-momentum-carrying phonons. The opposite sign of the effect for modes (+) and (−) originates from the directionality, introduced by the current, that breaks the symmetry between clockwise and anticlockwise atomic motion in the X–Y plane [17]. The averaging over classical trajectories, implicit in the construction of the unperturbed phonon density matrix in the present calculation, eliminates certain additional forces that become apparent, for example, in the treatments of references [13,14]. These additional forces and their effects present an interesting avenue for further work [19].

Conclusion

We have taken the analytical result for the curl of current-induced forces, derived in references [12,18], and we have related it to two physically transparent ideas. One is the electron-wind force on a test particle, determined by the local electron momentum flux. The second is the uncompensated stimulated emission of travelling phonons. The fact that the nonconservative effect is related to stimulated (as opposed to spontaneous) emission explains the remarkable, and practically very useful, earlier finding that the nonconservative dynamics of atoms under current can be captured already at the level of Ehrenfest dynamics. (Ehrenfest dynamics suppresses spontaneous transitions but retains stimulated transitions.) However, at that level, the underlying physics of the effect remains somewhat obscured by the mixed framework. Starting from the present internally consistent picture, we see explicitly that this novel and interesting effect is like a current-driven waterwheel, which works by angular-momentum transfer from the electron flow (albeit possibly in an abstract sense, depending on what X and Y denote).

Superficially, Equation 30 resembles ordinary Joule heating. Indeed, it does constitute a form of *directional* heating. But there is a key difference. *Standing*, bound phonon modes can equilibrate with the current-carrying electrons, at an effective phonon population set by the bias [20]. Equation 30 shows qualitatively different behaviour. If the second term is positive, then, once the bias V is large enough for term 2 to dominate term 1, the Equation predicts an exponential growth of the energy of the given *travelling* mode, without equilibration. This is the waterwheel effect of reference [12]. Of course, in reality this increase cannot continue indefinitely, and the possible outcomes form the subject of ongoing research. Pertinent questions are concerned with the effects of anharmonicity [12], the possible eventual failure of the device [13], and the possible current-induced corrections, under appropriate conditions, to the conservative part of the harmonic potential (which could lift the degeneracy of the modes X and Y that form the "waterwheel").

It is hoped that nonconservative forces, and the underlying mechanism of uncompensated directional phonon generation under current, will be useful in tackling not only problems in nanotechnology but also in neighbouring areas, such as the behaviour of bulk metals under large current densities.

Acknowledgements

We are grateful for discussions with Claire Buchanan during her MSci work at Queen's, and for support from the Engineering and Physical Sciences Research Council, under grants EP/C006739/1, EP/I00713X/1.

References

1. Sorbello, R. S. *Solid State Phys.* **1997,** *51,* 159. doi:10.1016/S0081-1947(08)60191-5
2. Todorov, T. N.; Hoekstra, J.; Sutton, A. P. *Phys. Rev. Lett.* **2001,** *86,* 3606. doi:10.1103/PhysRevLett.86.3606
3. Di Ventra, M.; Pantelides, S. T.; Lang, N. D. *Phys. Rev. Lett.* **2002,** *88,* 046801. doi:10.1103/PhysRevLett.88.046801
4. Brandbyge, M.; Stokbro, K.; Taylor, J.; Mozos, J.-L.; Ordejón, P. *Phys. Rev. B* **2003,** *67,* 193104. doi:10.1103/PhysRevB.67.193104
5. Todorov, T. N. *J. Phys.: Condens. Matter* **2002,** *14,* 3049. doi:10.1088/0953-8984/14/11/314
6. Ralls, K. S.; Ralph, D. C.; Buhrman, R. A. *Phys. Rev. B* **1989,** *40,* 11561. doi:10.1103/PhysRevB.40.11561
7. Holweg, P. A. M.; Caro, J.; Verbruggen, A. H.; Radelaar, S. *Phys. Rev. B* **1992,** *45,* 9311. doi:10.1103/PhysRevB.45.9311
8. Agraït, N.; Levy Yeyati, A.; van Ruitenbeek, J. M. *Phys. Rep.* **2003,** *377,* 81. doi:10.1016/S0370-1573(02)00633-6
9. Horsfield, A. P.; Bowler, D. R.; Fisher, A. J.; Todorov, T. N.; Montgomery, M. J. *J. Phys.: Condens. Matter* **2004,** *16,* 3609. doi:10.1088/0953-8984/16/21/010
10. Galperin, M.; Ratner, M. A.; Nitzan, A. *J. Phys.: Condens. Matter* **2007,** *19,* 103201. doi:10.1088/0953-8984/19/10/103201
11. Stamenova, M.; Sanvito, S.; Todorov, T. N. *Phys. Rev. B* **2005,** *72,* 134407. doi:10.1103/PhysRevB.72.134407
12. Dundas, D.; McEniry, E. J.; Todorov, T. N. *Nat. Nanotechnol.* **2009,** *4,* 99. doi:10.1038/nnano.2008.411
13. Lü, J.-T.; Brandbyge, M.; Hedegård, P. *Nano Lett.* **2010,** *10,* 1657. doi:10.1021/nl904233u
14. Bode, N.; Kusminskiy, S. V.; Egger, R.; von Oppen, F. *Phys. Rev. Lett.* **2011,** *107,* 036804. doi:10.1103/PhysRevLett.107.036804
15. Král, P.; Seideman, T. *J. Chem. Phys.* **2005,** *123,* 184702. doi:10.1063/1.2107527
16. Bailey, S. W. D.; Amanatidis, I.; Lambert, C. J. *Phys. Rev. Lett.* **2008,** *100,* 256802. doi:10.1103/PhysRevLett.100.256802
17. Pshenichnyuk, I. A.; Čížek, M. *Phys. Rev. B* **2011,** *83,* 165446. doi:10.1103/PhysRevB.83.165446
18. Todorov, T. N.; Dundas, D.; McEniry, E. J. *Phys. Rev. B* **2010,** *81,* 075416. doi:10.1103/PhysRevB.81.075416

19. Unpublished results.
20. Montgomery, M. J.; Todorov, T. N. *J. Phys.: Condens. Matter* **2003,** *15,* 8781. doi:10.1088/0953-8984/15/50/011
Erratum: *J. Phys.: Condens. Matter* **2004,** *16,* 6819.

License and Terms

Beilstein Journal of Nanotechnology

Lifetime analysis of individual-atom contacts and crossover to geometric-shell structures in unstrained silver nanowires

Christian Obermair[*1], Holger Kuhn[1] and Thomas Schimmel[*1,2]

Full Research Paper

Open Access

Address:
[1]Institute of Applied Physics and Center for Functional Nanostructures (CFN), University of Karlsruhe, Karlsruhe Institute of Technology (KIT), 76128 Karlsruhe, Germany and [2]Institute of Nanotechnology, Forschungszentrum Karlsruhe, Karlsruhe Institute of Technology (KIT), 76128 Karlsruhe, Germany

Email:
Christian Obermair[*] - christian.obermair@physik.uni-karlsruhe.de;
Thomas Schimmel[*] - thomas.schimmel@kit.edu

* Corresponding author

Keywords:
nanowires; quantum point contacts; shell effect; silver

Beilstein J. Nanotechnol. **2011,** *2,* 740–745.
doi:10.3762/bjnano.2.81

Received: 23 May 2011
Accepted: 13 October 2011
Published: 03 November 2011

This article is part of the Thematic Series "Transport through molecular junctions".

Guest Editor: J. M. van Ruitenbeek

Abstract

We study the crossover of quantum point contacts from (i) individual-atom contacts to (ii) electronic-shell effects and finally to (iii) geometric-shell effects in electrochemically deposited silver contacts. The method allows the fabrication of mechanically unstrained structures, which is a requirement for determining the individual atomic configuration by means of a detailed lifetime analysis of their conductance. Within the geometric-shell model, the sequence of conductance maxima is explained quantitatively based on the crystal structure data of silver, and the growth mechanism of the nanowires is discussed.

Introduction

Recently, the first transistor on the atomic scale was demonstrated and generated much interest [1-5]. This atomic-scale transistor was formed by electrochemical deposition of silver into a nanoscale gap between two gold electrodes. Applying a control potential relative to a third, independent gate electrode allows opening and closing of an atomic-scale gap by the controlled and reversible relocation of individual atoms. In this way, switching between a quantized conducting "on-state" and an insulating "off-state" is performed. Even multilevel quantum switches on the atomic scale were demonstrated very recently [6]. The possibility of training special atomic configurations related to certain conductance values, and the high stability of the chosen conductance levels, are unique features of the electrochemical method [4-10]. Compared with mechanical setups, and separate from purely electrochemical methods, electromigration is another promising method to produce bistable contact configurations between integer quantum conductance values [11]. In order to effectively control the behavior of an

electrochemically controlled atomic-scale transistor a detailed understanding of the mechanism of formation of the contacts bridging the nanoscale gap is necessary.

The conductance of nanocontacts strongly depends both on the type and number of atoms in the contact area and on the position of the atoms involved [12,13]. The conductance of single atoms was predicted theoretically [13-15] and investigated in detail by breaking thin wire junctions mechanically [16-19], exhibiting integer values of 1 $G_0 = 2e^2/h$ for simple metals (such as alkali metals) as well as for gold and silver; the exact behavior depending on the signature of their chemical valence. Contacts with larger contact areas show a more complex behavior including electronic-shell effects and the filling of geometric shells. In both cases there are minima in the thermodynamic potential of the contact as a function of the radius, and radii with minima in their free energy are encountered more frequently during contact formation. In electronic shells these minima in free energy are related to the configuration of the electron system of the contacting atoms by analogy with the "magic" configurations in metal cluster. In geometric shells the free energy is lowered by the change of surface energy when completing a layer of atoms on the nanowire facets, which is also known from cluster physics [20,21]. Both the electronic- and the geometric-shell effect were intensely discussed for alkali metals [17,22] and later for noble metals [23] in mechanically fabricated atomic-scale contacts. However, it remained unclear how the results obtained with mechanically fabricated metallic point contacts are influenced by defects and distortions within the contacting area, generated during the mechanical fabrication process, and how the physics of shell effects and the structural fingerprints in conductance distributions are affected.

In contrast to the mechanical fabrication of contacts, the electrochemical method allows the fabrication of atomic-scale point contacts without the need to apply mechanical deformation. In this way, plastic deformations are avoided and highly stable and defect-free nanocontacts are produced [24-28]. This is especially true for silver; due to its high electrochemical exchange-current density, electrochemically deposited silver exhibits high mobility on its surface, allowing the fabrication of defect-free metallic point contacts [13]. A sufficiently high mobility of the atoms is needed to find stable configurations, corresponding to distinct shells, which, in turn, lead to clearly observable shell effects on the conductance.

Here, we study the transport properties and conductance-distribution statistics of electrochemically fabricated silver nanowires. We give a complete description of silver nanocontacts starting from individual atomic configurations (i.e., one or two atom contacts) proceeding to electronic-shell effects and finally accomplishing the crossover to the filling of complete geometric shells corresponding to crystallographic facets of the nanowire. A detailed lifetime analysis for selected contacts helps us to obtain a detailed understanding of the correlation between the physics of quantized electronic transport and the atomic structure of the nanocontacts.

Results and Discussion

Figure 1 shows a conductance histogram for electrochemically deposited silver contacts obtained from 21385 conductance levels in the range between 0.01 G_0 and 7 G_0 with level each lasting longer than at least 200 ms. In this evaluation we counted the real number of conductance levels and not just the number of data points, as the latter (although often used in literature) would be misleading by overemphasizing the longer-living conductance levels. Consequently each data point in the histogram corresponds to a single complete conductance level. The histogram exhibits a sequence of distinct peaks at defined integer multiples of G_0 at about 1 G_0, 2 G_0, 3 G_0, 6 G_0 and a less pronounced maximum, broader as compared to the others, at about 5 G_0. The maximum at the noninteger conductance value at about 6.7 G_0 indicates a different mechanism and is discussed below.

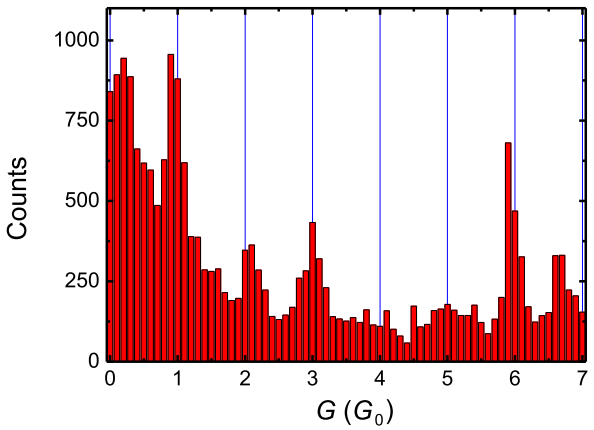

Figure 1: Conductance histogram of electrochemically deposited atomic-scale silver contacts giving evidence for different individual-atom and electronic-shell configurations. The histogram was obtained from >21000 conductance levels in the range between 0.01 G_0 and 7 G_0, each level being stable for longer than 200 ms as measured at room temperature, presented with a bin size of 0.1 G_0 (1 $G_0 = 2e^2/h$). The histogram exhibits distinct maxima at defined integer multiples of G_0 at 1 G_0, 2 G_0, 3 G_0, 6 G_0 and a less pronounced maximum at about 5 G_0. Furthermore, there is a maximum at about 6.7 G_0 which indicates the transition to the geometric-shell effect (Figure 4).

The conductance value for a single-atom silver contact is expected to be 1 G_0 [13,15]. A set of conductance peaks with the signature 1-3-(5)-6 can easily be associated with the values expected from a jellium model of electrons based on the degen-

eracy of transversal levels in a cylinder-symmetrical constriction [29-31], known as the "electronic shells" description. Even the less-pronounced maximum at approximately 5 G_0 is conclusively explained by assuming slight deviations from perfect cylindrical contact geometries, the level 5 G_0 being theoretically predicted to be less stable [30]. Only the appearance of a maximum corresponding to a conductance of 2 G_0, which indicates a two-atom contact, is not compatible with this electronic-shell description. In light of this observation we further investigated the time behavior of the conductance levels in more detail. We analyzed the number of conductance levels within a fixed conductance range of distinct maxima, as a function of their minimum level length Δt. Examples are given in Figure 2 for the maxima around 1 G_0 and 2 G_0. By fitting an exponential decay function in the period between 0.2 s and 1.2 s, an average lifetime τ was estimated as $\tau_1 \approx 0.29$ s around the maximum at 1 G_0 and $\tau_2 \approx 0.18$ s at 2 G_0. Selected average lifetimes of quantized conductance levels are listed in Table 1. These average lifetimes can be considered to be characteristic of the stability of the contacts. Table 1 shows the average lifetimes obtained for the conductance values corresponding to the electronic shells, with 0.29 s for the peak at 1 G_0, 0.26 s for the peak at 3 G_0 and 0.24 s for the peak at 6 G_0. Strikingly, these values are up to 60% higher than the lifetimes obtained at the intermediate values, namely 0.18 s for the peak at 2 G_0 and 0.19 s for the peak at 4 G_0. These last two values are comparable to the lifetime of the background, or even slightly less stable than the background in between the maxima, here given for the example of 1.5 G_0, which shows an average lifetime of $\tau = 0.21$ s.

Table 1: Average lifetimes τ of contacts from different conductance ranges as derived from the data shown in Figure 2.

Conductance range	Average lifetime τ
1 G_0 ± 0.25 G_0	≈0.29 s
2 G_0 ± 0.25 G_0	≈0.18 s
3 G_0 ± 0.25 G_0	≈0.26 s
4 G_0 ± 0.25 G_0	≈0.19 s
5 G_0 ± 0.25 G_0	—[a]
6 G_0 ± 0.25 G_0	≈0.24 s
1.5 G_0 ± 0.25 G_0	≈0.21 s

[a]Due to the broadness of the maximum around 5 G_0, τ could not be estimated.

An analysis of the entire observed conductance range up to 19.9 G_0 obtained from 36608 conductance levels, each longer than 200 ms is given in Figure 3. As suggested by Yanson et al. [22], the number of observed conductance levels is plotted as a function of the square root of the conductance G in units of $G_0 = 2e^2/h$. The square root of G/G_0 is proportional to the contact radius R according to the semiclassical Sharvin equation. The diagram can be divided into two ranges: The first range with $(G/G_0)^{1/2} \leq 2.23$ corresponds to the electronic shell sequence of maxima as discussed in relation to Figure 1. The sequence of maxima in the range with higher conductance (or contact radii) of $(G/G_0)^{1/2} > 2.23$ show the striking feature that they are equidistant on the $(G/G_0)^{1/2}$ axis. This can be seen in more detail in Figure 4 were $(G/G_0)^{1/2}$ values at the positions of the maxima in Figure 3 are plotted versus their sequentially

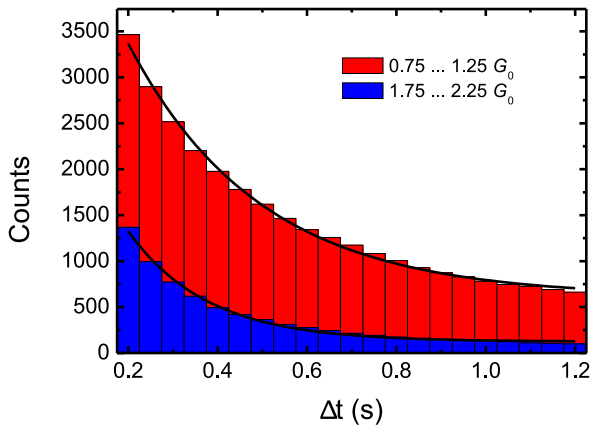

Figure 2: Number of conductance levels with level length greater than Δt as a function of Δt. The plot is given for two conductance levels: For the conductance range of 1 G_0 ± 0.25 G_0 and for the conductance range of 2 G_0 ± 0.25 G_0 taken from the histogram of Figure 1. By fitting an exponential decay function (solid lines) in the period between 0.2 s and 1.2 s, an average lifetime of the maximum at 1 G_0 was estimated as $\tau_1 \approx 0.29$ s and at 2 G_0 as $\tau_2 \approx 0.18$ s. Full results of the lifetimes analysis are found in Table 1.

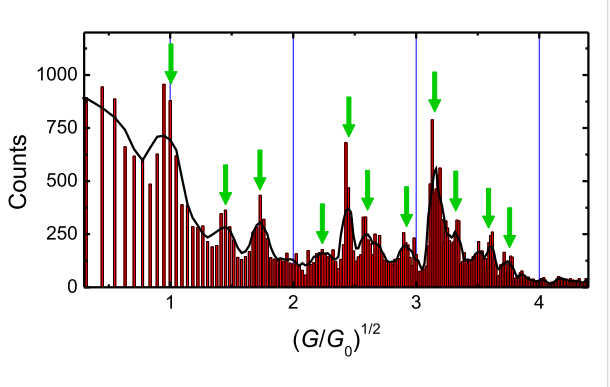

Figure 3: Conductance histogram for electrochemically deposited atomic-scale silver contacts giving evidence for the crossover from electronic-shells to geometric-shell configurations. The histogram was obtained from more than 36600 conductance levels in the range between 0.01 G_0 and 19.9 G_0, each longer than 200 ms. The x-axis is plotted as a function of the square root of conductance in units of $G_0 = 2e^2/h$, which is proportional to the contact radius R according to the Sharvin equation (see text). The solid line gives the two-neighbor average of the histogram data, which is used to identify the position of the maxima (marked by arrows).

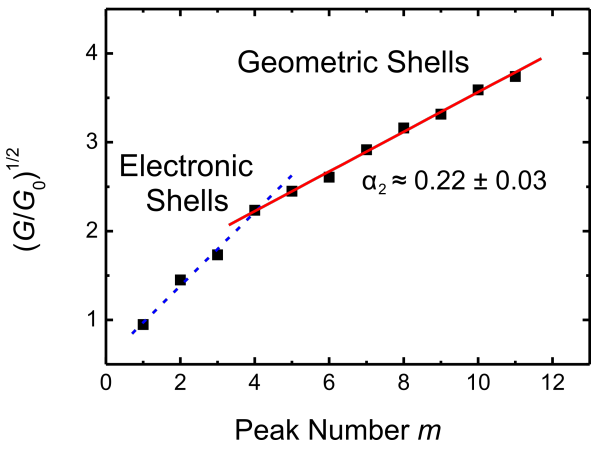

Figure 4: $(G/G_0)^{1/2}$ at the positions of the maxima observed in Figure 3 versus their sequentially numbered index. We observe two ranges: One up to the fourth maximum (dashed line) and another one from the fourth to the eleventh maximum with a slope of $\alpha_2 \approx 0.22 \pm 0.03$ (solid line). This behavior indicates two different mechanisms configuring the contact, the experimentally determined value of α_2 being in excellent agreement with the value predicted by calculations.

numbered index. Again, the range from the first to the fourth maximum can be explained by the electronic-shell structure. The second range from the fourth to the eleventh maximum exhibits an almost linear behavior with a slope of $\alpha_2 \approx 0.22 \pm 0.03$, indicating a different origin of the conductance quantization. Due to the proportionality of $(G/G_0)^{1/2}$ to the contact radius, this equidistant sequence corresponds to an increase in equidistant steps in the contact radius of the nanowires. This, in turn, can be explained by a subsequent filling of geometric shells with atoms around the contacting nanowire, also called the geometric-shell effect, as illustrated in Figure 5.

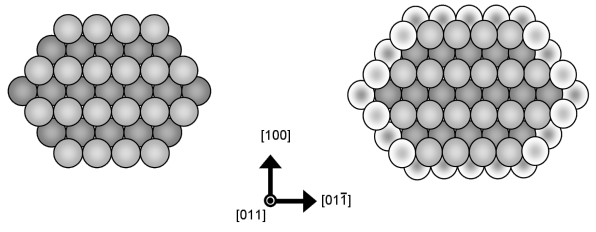

Figure 5: Illustration of a nanowire with fcc crystal structure and hexagonal cross-sectional area for two different diameters: On the right, one further shell is filled with atoms compared to the wire on the left.

It can be expected that with increasing conductance, and consequently with increasing radius, the structure of the nanowires more and more tends to their crystallographic bulk structure. For silver this is an fcc structure with a hexagonal cross-sectional area, which was also found in high-resolution transmission electron microscopy studies of atomically thin silver nanowires [32]. In Figure 5 an illustration of such nanowires is given for two different diameters. The wires are directed along the $[011]$ direction with six facets perpendicular to the $[100]$, $[1\bar{1}1]$, $[\bar{1}\bar{1}1]$, $[\bar{1}00]$, $[\bar{1}1\bar{1}]$ and $[1\bar{1}1]$ directions. Compared to the wire on the left in Figure 5, a further shell of atoms is added to the wire on the right. Within this structural model we can correlate each closed geometric-shell configuration and its corresponding cross-sectional area with a conductance according to the Sharvin equation. This gives a slope α for the trend of $(G/G_0)^{1/2}$ as a function of the peak index m:

$$\alpha = \frac{\mathrm{d}\sqrt{G/G_0}}{\mathrm{d}m} = \frac{3^{1/2}}{\pi^{1/2}2^{7/4}} k_\mathrm{F} a_0 \ , \qquad (1)$$

where a_0 is the lattice constant of the cubic lattice and k_F is the Fermi wave vector. For a free-electron metal with fcc lattice we have $k_\mathrm{F} \cdot a_0 = (12\pi^2)^{1/2}$. From Equation 1 we obtain $\alpha \approx 1.427$. This value was calculated for the complete filling of one further shell of atoms. Filling a complete shell of a crystal wire of sixfold symmetry corresponds to the subsequent filling of six crystal facets. Assuming that each completely filled facet corresponds to an energy minimum and thus to a stable configuration, each filled facet will lead to a maximum in our diagram. Thus one would expect from the above calculation a slope of $\alpha_{1/6} = \alpha/6 \approx 0.238$. This predicted value is in excellent agreement with the slope of $\alpha_2 \approx 0.22 \pm 0.03$ determined from our experimental values in Figure 4.

Thus, from the positions of the maxima in the conductance histogram of Figure 3, we can conclude a crossover from electronic-shells to geometric-shell configurations of the electrochemically deposited atomic-scale silver contacts. This transition can be explained by two competing effects: On the one hand there are oscillations of the free energy of the electron system of the contact, the amplitude of the local energy minima decreasing as $1/R$ due to shell filling [33]. On the other hand there is an oscillation in the surface energy due to the filling of geometric shells, for which the amplitude is roughly constant in radius [33]. Both effects can be of similar importance within a certain range of contact sizes, while for larger radii (corresponding to higher conductance values) the energetic effect of geometric-shell filling dominates over the effect on the electronic-shell filling.

The concrete conductance of transitions (or the number of maxima that can be observed in the electronically or in the geometrically dominated shell range) depends on the metal as well as on the experimental parameters: For mechanical break junction experiments, Mares et al. [23] found a crossover from electronic to geometric shells in silver at room temperate, at about 15 G_0 in UHV and at about 22 G_0 under ambient conditions. The authors argued that under ambient conditions adsorbates *decrease* the atom mobility, resulting in an enhanced stability of small contacts. In our case, we have exactly the opposite situation: The electrochemical environment leads to strongly *enhanced* surface-atom mobility, leading to a decrease of the transition towards the region of smaller contacts. The enhanced surface mobility results in a high degree of order of the contact area. Together with the fact that the deposition occurs without external mechanical strain, this explains the observation that electrochemically deposited silver junctions exhibit a dominance of geometric-shell effects beginning at much lower conductance levels or contact radii than in corresponding experiments with mechanical break junctions, leading to a crossover as early as 6 G_0, as compared to 15 G_0 and 22 G_0 [23] in the case of mechanical break junctions.

Calvo et al. [28] found indications of shell effects in electrochemically deposited Au contacts but reported unstable contacts in the region below 20 G_0. Compared to their experiments, electrochemically deposited silver contacts appear to exhibit a higher stability than the reported electrochemically deposited Au contacts. This may be due to the high electrochemical exchange-current density of silver, as electrochemical exchange currents provide a means for structural reconfiguration and for the healing of atomic-scale defects within the contact area [13,26]. The high degree of order of our contacts results in a transition between electronic- and geometric-shell effects at an unprecedentedly low conductance level.

Conclusion

In conclusion, the detailed experimental study of the conductance of unstrained silver point contacts obtained by electrochemical deposition allowed the direct observation of the fingerprints of atom-by-atom and subsequent layer-by-layer growth of the metallic point contacts. We gave a complete quantitative description of the different stages of nanowire growth: First, individual-atomic contacts are formed, corresponding to only one or two atoms in their cross-sectional area. With increasing contact radius the conductance is dominated by the building of electronic shells, and finally the bulk crystallization leads to the dominance of geometric shells. Our experimental data are in excellent agreement with the corresponding calculations for silver. A detailed lifetime analysis of individual conductance levels indicated an increased stability of single-atom contacts or contacts stabilized by electronic shells. The stabilization of atomic-scale point contacts, in turn, is a key prerequisite for atomic-scale quantum electronics such as used in atomic transistors.

Experimental

Two gold electrodes (with a thickness of about 100 nm) were deposited on a glass substrate with a gap of the order of 100 nm separating the electrodes. The gold electrodes were coated with an insulating layer, except for a small region with less than 25 μm in diameter around the gap, in order to keep the electrochemical leakage currents low (below 0.1%).

This arrangement was exposed to electrolytes consisting of 1 mM $AgNO_3$ (p.a., Merck) and 0.1 M HNO_3 (suprapure, Merck) as aqueous solutions within an electrochemical cell. Keeping a fixed voltage bias of 12.9 mV between the two ends of the leads allowed for simultaneous measurements of the conductance of the point contact. The (quasi-)reference electrode as well as the counter electrode consisted of 0.25 mm diameter Ag wire (99.9985%). All experiments were performed at room temperature and with the electrolyte exposed to ambient air. The data shown were obtained by deposition of silver into the gap between the working electrodes and simultaneous measurement of the conductance between them. When the conductance reached the maximum measuring range of the setup at about 20 G_0, the deposition potential (about −10 mV versus Ag/Ag^+) was changed to a dissolution potential (about 40 mV versus Ag/Ag^+) until the gap opened again. Subsequently, a new deposition cycle was started automatically with the computer-controlled setup. The conductance curves were analyzed by using an algorithm that identifies sequences of consecutive conductance values within a given tolerance (here ±0.05 G_0). Each identified level by definition had a minimum length of four consecutively measured data points (at 50 ms per data point). The conductance was recorded both during deposition and during dissolution of the contacts, and both processes were taken into account in our statistical analysis. However, in most cases, the opening process was much faster than the closing process, the complete opening process typically taking much less time than the minimum level length of 200 ms used for our evaluations. The data were derived from independent measurements of about 30 identical electrode setups. The data represent the collection of many different experiments obtained over a long time. By splitting the data into different sets each containing only part of the total data, comparable results were obtained, though with a somewhat reduced signal-to-noise ratio.

Acknowledgements

This work was funded by the Deutsche Forschungsgemeinschaft within the DFG-Center for Functional Nanostructures

and by the Baden-Württemberg Stiftung and the Ministry of Research and the Arts, Baden-Württemberg within the Network of Excellence “Functional Nanostructures”.

References

1. Xie, F.-Q.; Nittler, L.; Obermair, C.; Schimmel, T. *Phys. Rev. Lett.* **2004,** *93,* 128303. doi:10.1103/PhysRevLett.93.128303
2. Xie, F.-Q.; Obermair, C.; Schimmel, T. *Solid State Commun.* **2004,** *132,* 437. doi:10.1016/j.ssc.2004.08.024
3. Xie, F.-Q.; Obermair, C.; Schimmel, T. In *Nanoscale Devices – Fundamentals and Applications;* Gross, R.; Sidorenko, A.; Tagirov, L., Eds.; Springer: The Netherlands, 2006; pp 153 ff.
4. Xie, F.-Q.; Maul, R.; Augenstein, A.; Obermair, C.; Starikov, E. B.; Schön, G.; Schimmel, T.; Wenzel, W. *Nano Lett.* **2008,** *8,* 4493. doi:10.1021/nl802438c
5. Obermair, C. Ph.D. Thesis, Cuvillier Verlag, Göttingen, Germany, 2005.
6. Xie, F.-Q.; Maul, R.; Obermair, C.; Wenzel, W.; Schön, G.; Schimmel, T. *Adv. Mater.* **2010,** *22,* 2033. doi:10.1002/adma.200902953
7. Terabe, K.; Hasegawa, T.; Nakayama, T.; Aono, M. *Nature* **2005,** *433,* 47. doi:10.1038/nature03190
8. Beebe, J. M.; Kushmerick, J. G. *Appl. Phys. Lett.* **2007,** *90,* 083117. doi:10.1063/1.2696653
9. Morales-Masis, M.; van der Molen, S. J.; Fu, T. W.; Hesselberth, M. B.; van Ruitenbeek, J. M. *Nanotechnology* **2009,** *20,* 095710. doi:10.1088/0957-4484/20/9/095710
10. Hepel, M. *Russ. J. Electrochem.* **2008,** *44,* 663. doi:10.1134/S1023193508060062
11. Schirm, C.; Pernau, H.-F.; Scheer, E. *Rev. Sci. Instrum.* **2009,** *80,* 024704. doi:10.1063/1.3073962
12. Agraït, N.; Levy Yeyati, A.; van Ruitenbeek, J. M. *Phys. Rep.* **2003,** *377,* 81. doi:10.1016/S0370-1573(02)00633-6
13. Xie, F.-Q.; Maul, R.; Brendelberger, S.; Obermair, C.; Starikov, E. B.; Wenzel, W.; Schön, G.; Schimmel, T. *Appl. Phys. Lett.* **2008,** *93,* 043103. doi:10.1063/1.2955521
14. Cuevas, J. C.; Levy Yeyati, A.; Martín-Rodero, A. *Phys. Rev. Lett.* **1998,** *80,* 1066. doi:10.1103/PhysRevLett.80.1066
15. Pauly, F.; Dreher, M.; Viljas, J. K.; Häfner, M.; Cuevas, J. C.; Nielaba, P. *Phys. Rev. B* **2006,** *74,* 235106. doi:10.1103/PhysRevB.74.235106
16. Scheer, E.; Agraït, N.; Cuevas, J. C.; Yeyati, A. L.; Ludoph, B.; Martín-Rodero, A.; Bollinger, G. R.; van Ruitenbeek, J. M.; Urbina, C. *Nature* **1998,** *394,* 154. doi:10.1038/28112
17. Yanson, A. I.; Yanson, I. K.; van Ruitenbeek, J. M. *Nature* **1999,** *400,* 144. doi:10.1038/22074
18. Krans, J. M.; Muller, C. J.; Yanson, I. K.; Govaert, T. C. M.; Hesper, R.; van Ruitenbeek, J. M. *Phys. Rev. B* **1993,** *48,* 14721. doi:10.1103/PhysRevB.48.14721
19. Park, J.; Pasupathy, A. N.; Goldsmith, J. I.; Chang, C.; Yaish, Y.; Petta, J. R.; Rinkoski, M.; Sethna, J. P.; Abruña, H. D.; McEuen, P. L.; Ralph, D. C. *Nature* **2002,** *417,* 722. doi:10.1038/nature00791
20. de Heer, W. A. *Rev. Mod. Phys.* **1993,** *65,* 611. doi:10.1103/RevModPhys.65.611
21. Lyalin, A.; Solov'yov, I. A.; Solov'yov, A. V.; Greiner, W. *Phys. Rev. A* **2007,** *75,* 053201. doi:10.1103/PhysRevA.75.053201
22. Yanson, A. I.; Yanson, I. K.; van Ruitenbeek, J. M. *Phys. Rev. Lett.* **2001,** *87,* 216805. doi:10.1103/PhysRevLett.87.216805
23. Mares, A. I.; van Ruitenbeek, J. M. *Phys. Rev. B* **2005,** *72,* 205402. doi:10.1103/PhysRevB.72.205402
24. Li, C. Z.; Tao, N. J. *Appl. Phys. Lett.* **1998,** *72,* 894. doi:10.1063/1.120928
25. Li, C. Z.; Bogozi, A.; Huang, W.; Tao, N. J. *Nanotechnology* **1999,** *10,* 221. doi:10.1088/0957-4484/10/2/320
26. Obermair, C.; Kniese, R.; Xie, F.-Q.; Schimmel, T. In *Molecular Nanowires and Other Quantum Objects;* Alexandrov, A. S.; Demsar, J.; Yanson, I. K., Eds.; Kluwer Academic Publishers: The Netherlands, 2004; pp 233 ff.
27. Mészáros, G.; Kronholz, S.; Karthäuser, S.; Mayer, D.; Wandlowski, T. *Appl. Phys. A* **2007,** *87,* 569. doi:10.1007/s00339-007-3903-2
28. Reyes Calvo, M.; Mares, A. I.; Climent, V.; van Ruitenbeek, J. M.; Untiedt, C. *Phys. Status Solidi A* **2007,** *204,* 1677. doi:10.1002/pssa.200675319
29. Torres, J. A.; Pascual, J. I.; Sáenz, J. J. *Phys. Rev. B* **1994,** *49,* 16581. doi:10.1103/PhysRevB.49.16581
30. Stafford, C. A. *Phys. Status Solidi B* **2002,** *230,* 481. doi:10.1002/1521-3951(200204)230:2<481::AID-PSSB481>3.0.CO;2-M
31. Brandbyge, M.; Jacobsen, K. W.; Nørskov, J. K. *Phys. Rev. B* **1997,** *55,* 2637. doi:10.1103/PhysRevB.55.2637
32. Rodrigues, V.; Bettini, J.; Rocha, A. R.; Rego, L. G. C.; Ugarte, D. *Phys. Rev. B* **2002,** *65,* 153402. doi:10.1103/PhysRevB.65.153402
33. Yannouleas, C.; Bogachek, E. N.; Landman, U. *Phys. Rev. B* **1998,** *57,* 4872. doi:10.1103/PhysRevB.57.4872

License and Terms

Beilstein Journal of Nanotechnology

Towards quantitative accuracy in first-principles transport calculations: The GW method applied to alkane/gold junctions

Mikkel Strange and Kristian S. Thygesen*

Full Research Paper

Open Access

Address:
Center for Atomic-scale Materials Design, Department of Physics Technical University of Denmark, DK - 2800 Kgs. Lyngby, Denmark

Email:
Mikkel Strange - strange@fysik.dtu.dk; Kristian S. Thygesen* - thygesen@fysik.dtu.dk

* Corresponding author

Keywords:
alkanes; density functional theory; electron transport; gold junction; GW

Beilstein J. Nanotechnol. **2011,** *2,* 746–754.
doi:10.3762/bjnano.2.82

Received: 17 August 2011
Accepted: 07 October 2011
Published: 09 November 2011

This article is part of the Thematic Series "Transport through molecular junctions".

Guest Editor: J. M. van Ruitenbeek

Abstract

The calculation of the electronic conductance of nanoscale junctions from first principles is a long-standing problem in the field of charge transport. Here we demonstrate excellent agreement with experiments for the transport properties of the gold/alkanediamine benchmark system when electron–electron interactions are described by the many-body GW approximation. The conductance follows an exponential length dependence: $G_n = G_c \exp(-\beta n)$. The main difference from standard density functional theory (DFT) calculations is a significant reduction of the contact conductance, G_c, due to an improved alignment of the molecular energy levels with the metal Fermi energy. The molecular orbitals involved in the tunneling process comprise states delocalized over the carbon backbone and states localized on the amine end groups. We find that dynamic screening effects renormalize the two types of states in qualitatively different ways when the molecule is inserted in the junction. Consequently, the GW transport results cannot be mimicked by DFT calculations employing a simple scissors operator.

Introduction

The conductance of a molecule sandwiched between metallic electrodes is sensitive to the chemical and electronic structure of the molecule as well as the detailed atomic structure of the metal–molecule contact. Variations in the contact geometry beyond experimental control lead to an undesired spread in the measured conductance properties. For the most commonly used anchoring group, –thiol, these effects are rather pronounced due to the many possible contact geometries resulting from the strong Au–S interaction. Amine groups have been shown to produce more well-defined transport properties [1], which can

be understood from the relatively weak Au–NH_2 bond leading to larger structural selectivity [2].

Even for a given junction geometry, a quantitatively accurate description of electron transport from first principles remains a formidable task. Numerous studies based on density functional theory (DFT) have shown a significant overestimation of conductance relative to experimental values [3-14] (an exception to this trend occurs for small molecules, such as H_2 [15-17] and CO [18,19], which chemisorb strongly to the electrodes, resulting in resonant transport through broad, partially filled resonances). The inability of DFT to describe off-resonant tunneling in the simplest molecular junctions limits the predictive power of the DFT-based approach to qualitative trends. It is now broadly accepted that the failure of DFT is mainly due to its incorrect description of the molecular energy levels. Indeed, physically motivated correction schemes have shown that much-improved agreement with experiments can be obtained after shifting the DFT molecular energy levels [13,14]. Such corrections are supposed to remove the self-interaction errors inherent in standard DFT exchange–correlation (xc) functionals [20-22] and account for image charge effects induced by the metal contacts. The drawback of the approach is that it assumes a weak coupling between molecular orbitals and metal states and treats the image-plane position as a free parameter.

The (self-consistent) GW approximation [23], which is rooted in many-body perturbation theory, was recently found to yield a considerable improvement over DFT for the conductance of gold/benzenediamine junctions [24]. Physically, the GW approximation corresponds to Hartree–Fock theory with the bare Coulomb interaction $v = 1/|\mathbf{r} - \mathbf{r}'|$ replaced by a dynamically screened Coulomb interaction $W(\omega) = \varepsilon^{-1}(\omega)v$. In contrast to standard DFT, the GW approximation is almost self-interaction free [25] and includes screening effects through the correlation part of the self-energy [26-28]. As a consequence, it provides quantitatively accurate predictions of energy gaps in systems with highly diverse screening properties, ranging from isolated molecules [29,30], through to semiconductors [31] and metals [32]. The broad applicability of the GW approach becomes particularly important for a metal–molecule interface where the electronic structure changes from insulating to metallic over a few angstroms.

In this work we use the GW approximation to study the role of exchange–correlation effects for the energy-level alignment and electron transport in short alkane chains coupled to gold electrodes through amine linker groups. The gold/alkane junction is a benchmark system for molecular charge transport and has been exhaustively investigated experimentally [1,12,33-44]. We focus here on the amine-linked alkanes to avoid the uncertainties related to the gold–thiol contact geometry, which is presently under debate [45-50]. We note that very recently it was shown that alkanes can be bound directly to gold electrodes without the use of anchoring groups [51].

The transport mechanism in (short) saturated molecular wires is coherent tunneling through molecular orbitals with energy far from the Fermi energy. The trend of conductance versus chain length (n) thus follows an exponential law of the form

$$G_n = G_c \exp(-\beta n) \tag{1}$$

Recent experimentally reported values for the decay constant β of alkane-α,ω-diamine/gold junctions are in the range 0.9–1.0 per C atom [1,12,36], but earlier measurements also showed values around 0.8 [35]. Although previous studies based on DFT yielded β values within the experimental range, the contact conductance, G_c, is typically overestimated by around an order of magnitude [3-10]. A study based on the many-body configuration interaction method has shown similar β values, but slightly reduced G_c values, as compared to DFT [52]. By comparing DFT and GW calculations for C_n-alkanediamine molecules with n = 2,4,6 we show that the erroneous G_c values are a result of the incorrect level alignment in the DFT calculations. Indeed, GW yields a G_c in close agreement with the experimental values. We find a pronounced orbital and length dependence of the quasiparticle (QP) corrections to the DFT energies, resulting from the different shape and localization of the molecular orbitals. The QP corrections range from −0.5 to −2.5 eV and can be qualitatively explained from a classical image-charge model.

Method

The junction geometries were optimized by means of the real-space projector-augmented wave method GPAW [53,54] with a grid spacing of 0.2 Å and the PBE functional for exchange and correlation (xc) [55]. The molecules were attached to Au(111) surfaces, modeled by an eight-layer-thick 4 × 4 slab, through small four-atom tips as shown in Figure 1a. The surface Brillouin zone was sampled on a 4 × 4 Monkhorst pack k-point grid, and the structures including molecule, Au tips, and outermost Au surface layers were relaxed until the residual force was below 0.03 eV/Å. We considered n-alkanediamine junctions with n = 2, 4 and 6. The key structural parameters can be found here [56]. For calculations of the molecules in the gas-phase, we include 16 Å of vacuum between molecules in the repeated supercells. All transport calculations where performed according to the method described in detail in [24]. In brief, we employ a basis set of numerical atomic orbitals corresponding to double-zeta plus polarization (DZP) for the Au atoms and

double-zeta (DZ) for the atoms of the molecules. We use rather diffuse basis functions with a confinement-energy shift of 0.01 eV. This ensures that the calculated work function of Au(111) and the Kohn–Sham energy levels of the molecular junction are within 0.1 eV of those obtained from accurate grid calculations [24]. The transmission function is obtained from the Meir–Wingreen transmission formula [57,58]

$$T(\varepsilon) = \mathrm{Tr}[G^r(\varepsilon)\Gamma_L(\varepsilon)G^a(\varepsilon)\Gamma_R(\varepsilon)]\,. \tag{2}$$

The retarded Green's function of the extended molecule is calculated from

$$G^r(E) = [(E+i\eta)S - H_0 + V_{xc} - \Delta V_{\mathrm{H}}[G] - \Sigma_L(E) - \Sigma_R(E) - \Sigma_{xc}[G](E)]^{-1} \tag{3}$$

Here S, H_0, and V_{xc} are the overlap matrix, Kohn–Sham Hamiltonian and the local xc-potential in the atomic orbital basis, respectively; η is a positive infinitesimal.

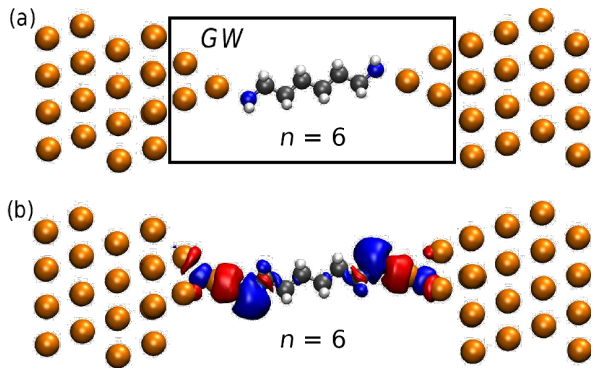

Figure 1: (a) Supercell used to model the gold/alkanediamine junctions. Similar supercells were used for n = 2 and n = 4 (not shown) and the key structural parameters can be found here [50]. The black box indicates the region of the extended molecule within which the GW self-energy is evaluated. (b) Isosurface of the electron-density difference between a DFT ground-state calculation and a constrained DFT calculation with one less electron on the molecule.

The lead self-energy, $\Sigma_{L/R}$, incorporates the coupling to the left and right electrodes and is obtained by standard techniques [59]. The term ΔV_H gives the change in the Hartree potential relative to the DFT Hartree potential already contained in H_0. Finally, the last term is the many-body xc self-energy, which in this work is either the bare exchange potential, V_x, corresponding to Hartree–Fock, or the GW self-energy. As indicated both the Hartree potential and the xc self-energy depend on the Green's function. The latter is evaluated fully self-consistently using a simple linear mixing of the Green functions. We represent all energy dependent quantities in Equation 3 on a large energy grid ranging from −200 eV to 200 eV with an energy-grid spacing of 0.01 eV.

The GW self-energy is evaluated for the extended molecule (indicated by the box in Figure 1a). However, only the part corresponding to the molecule is used while the remaining part is replaced by the DFT xc-potential. This is done to include nonlocal correlation (image-charge) effects from the electrodes in the GW self-energy of the molecule while preserving a consistent description of all metal atoms at the DFT level. We have verified that the calculations are converged with respect to the size of the extended molecules, see [24] for more details. The basis functions on the Au tip atoms extend a fair distance into the Au electrode and thus also describe screening effects to some extent in this region. The rather fast convergence of the screening effects with extended molecule size can be probed directly through a simple approach based on a constrained DFT calculation where the number of electrons on the molecule is constrained to be one less, or one more, than the number of electrons in a ground state DFT calculation. We measure the number of electrons on the molecule using a Mulliken charge analysis. The constrained DFT calculations are performed as self-consistent DFT calculations with the rigid shift of the molecular orbitals adjusted until the number of electrons is one less, thereby probing the highest occupied molecular orbital. We show in Figure 1b the isosurface of the electron-density difference obtained from a ground state DFT calculation and a constrained DFT calculation. The change in the electron density in the metal can be seen as the formation of an image charge (red color), which to a large extent is localized on the Au tip atoms closest to the molecule.

Results and Discussion

Energy-level alignment

The alignment of the molecular energy levels relative to the electrode Fermi level is of great importance for the transport properties of molecular junctions and seems to be the dominant effect at low bias voltage. At higher bias voltages, many-body calculations on small model systems suggest that electron correlations induce additional shifting and broadening of the molecular levels, which can also affect the transport properties [60]. Here we focus on the low-bias regime and postpone consideration of the finite-bias effects to a later study.

The molecular orbitals (MOs) of the alkanediamine chains comprise states that are delocalized over the carbon backbone and states that are localized on the NH_2 end group. We shall consider the highest occupied molecular orbital (HOMO) and HOMO–2 as representatives for the two classes of states (Figure 2a). We note that the HOMO–1 is similar to the

HOMO, with slightly lower energy given by the coupling of the two end groups across the wire. In Table 1 and Table 2 we list the energy of the HOMO and HOMO–2 calculated with DFT-PBE, Hartree–Fock (HF), and GW for the molecules in the gas-phase and in the junction.

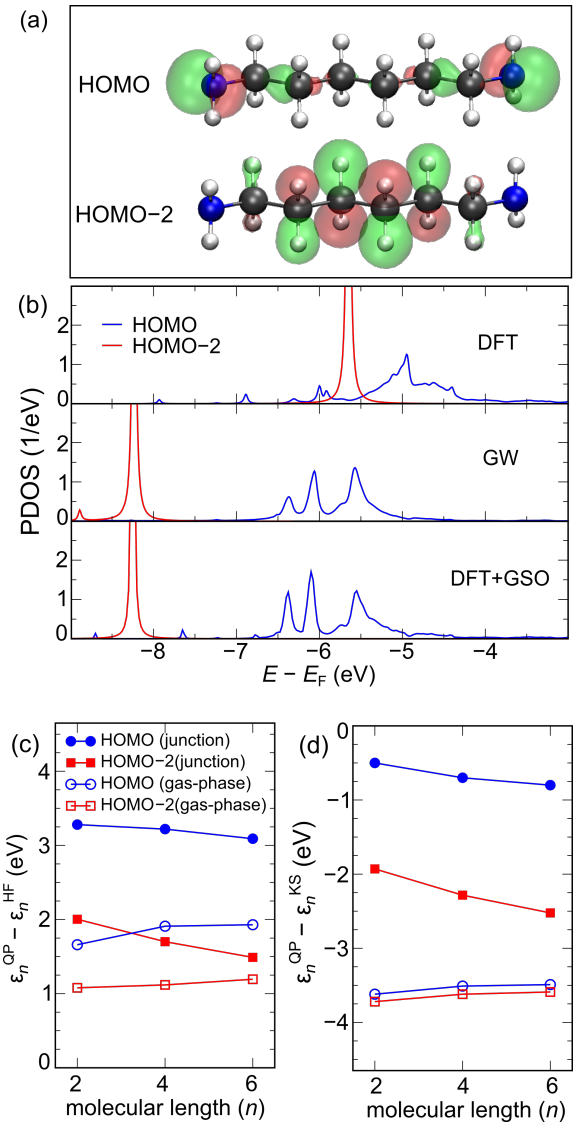

Figure 2: (a) Isosurfaces for the HOMO and HOMO−2 orbitals of the C_6-alkanediamine molecule. (b) HOMO and HOMO−2 PDOS in the junction obtained from DFT-PBE (top), GW (middle) and DFT with a generalized scissors operator (bottom). (c) Quasiparticle corrections to the Hartree–Fock levels in the gas-phase (open symbols) and in the junction (filled symbols) as a function of molecular length *n*. The HOMO and HOMO−2 are denoted by circles and squares, respectively. (d) Same as (c) but for DFT rather than Hartree–Fock.

In the gas-phase, all three methods predict the HOMO energy to be almost independent of molecular length. This is clearly due to its end-group-localized character. In contrast, the energy of the HOMO–2 level shifts upward in energy as the molecular length increases. This reflects its extended nature and can be interpreted as a band-discretization effect. To the best of our knowledge no experimental results exist for the ionization potential of alkanediamine molecules. However, for the closely related butane molecule (C_2 alkane with CH_3 end groups) we obtain a GW-calculated HOMO energy of −11.4 eV in very good agreement with the experimental ionization potential of 11.2 eV [61]. In comparison, the DFT-PBE HOMO energy is severely underestimated at −7.9 eV. This finding agrees well with previous studies on a broader range of small molecules [24,29,30].

Table 1: Calculated HOMO and HOMO–2 energies aligned to the vacuum level and in units of eV.

method	orbital	*n* = 2	*n* = 4	*n* = 6
DFT-PBE	HOMO	−4.9	−5.1	−5.1
	HOMO–2	−8.5	−8.2	−8.0
HF	HOMO	−10.2	−10.5	−10.5
	HOMO–2	−13.3	−12.9	−12.8
GW	HOMO	−8.5	−8.6	−8.6
	HOMO–2	−12.2	−11.8	−11.6

Table 2: Calculated HOMO and HOMO–2 energies in the junction relative to the electrode Fermi level.

method	orbital	*n* = 2	*n* = 4	*n* = 6
DFT-PBE	HOMO	−4.3	−4.2	−4.4
	HOMO−2	−6.5	−5.9	−5.7
HF	HOMO	−8.1	−8.1	−8.3
	HOMO−2	−10.4	−9.9	−9.7
GW	HOMO	−4.8	−4.9	−5.2
	HOMO–2	−8.4	−8.2	−8.2

In the junction, the molecular orbitals, $|\psi_n\rangle$, were obtained by diagonalizing the DFT Hamiltonian corresponding to the molecule. The projected density of states (PDOS) of such a state is then given by the spectral function, $-1/\pi \mathrm{Im}\langle\psi_n|G^r(E)|\psi_n\rangle$, where G is the appropriate Green's function (calculated with DFT, HF, or GW). The level position is defined as the first moment of the PDOS. Figure 2b shows the PDOS for the HOMO and HOMO–2 for the C_6-alkanediamine junction as calculated with DFT-PBE (upper panel) and GW (middle panel). The lower panel shows the PDOS obtained from a DFT calculation where the molecular levels have been shifted to match the GW levels, i.e., after adding to the Kohn–Sham Hamiltonian a generalized scissors operator of the form

$$\Sigma^{\mathrm{DFT}}_{\mathrm{GSO}} = \sum_n (\varepsilon_n^{\mathrm{QP}} - \varepsilon_n^{\mathrm{DFT}}) \,|\, \psi_n \rangle\langle \psi_n \,|\ .$$

Here, the $\varepsilon_n^{\mathrm{QP}}$ denote the QP energy obtained from the GW calculation. We see that the main features of the GW spectral function can be well reproduced by the shifted DFT Hamiltonian, although small differences remain. A similar conclusion was reached in [24] for a gold/benzenediamine junction.

The molecular orbital energies from a GW calculation include the dynamical response of the electron system to an added or removed electron through the correlation part of the self-energy. In general, correlations tend to shift the filled levels upwards and the empty levels downwards relative to the bare Hartree–Fock energies. This is because the inclusion of screening reduces the energy cost of removing/adding electrons to the molecule. When a molecule is brought into contact with a metallic junction its environment changes from insulating to metallic. This implies extra screening of an added or removed electron, which will cause the filled levels to shift upwards and the empty levels to shift downwards even more than for the isolated molecules, i.e., the gap will shrink relative to its gas-phase value. It has been shown previously that DFT in (semi)local approximations and Hartree–Fock completely miss this important effect [26-28].

In Figure 2c and Figure 2d, we show the QP corrections to the HF and DFT Kohn–Sham energy levels as a function of molecular length. The results for the HOMO and the HOMO–2 are denoted by circles and squares. We notice first that the QP corrections are very significant with absolute values reaching almost 4 eV and with a pronounced orbital and length dependence. The Hartree–Fock QP corrections are all positive showing that HF places the occupied levels lower than predicted by GW. This is in contrast to the corrections to the DFT levels, which are all negative, in agreement with the well-known underestimation of ionization potentials as predicted from the negative Kohn–Sham HOMO energy obtained using LDA or GGA functionals. In contrast to Hartree–Fock the Kohn–Sham QP corrections are smaller for molecules in the junction compared to the gas-phase. In fact, the position of the HOMO level by DFT is relatively close the GW level position and only lies 0.5–0.8 eV higher. The fact that the DFT-PBE description of molecular energy levels is much better in the junction than in the gas-phase agrees with previous findings [24,27,62] and can be explained from the origin of the PBE functional in the homogeneous electron gas [63].

It is instructive to consider the shift in the molecular energy levels due to correlation effects coming from the metal electrodes. In simple terms this corresponds to the shift induced by image-charge effects. In order to isolate the part of the correlation energy originating from the metallic electrodes we define the quantity

$$\Delta\varepsilon_{\mathrm{corr},n} = (\varepsilon_n^{\mathrm{QP}} - \varepsilon_n^{\mathrm{HF}})_{\mathrm{junction}} - (\varepsilon_n^{\mathrm{QP}} - \varepsilon_n^{\mathrm{HF}})_{\mathrm{gas\text{-}phase}} \quad (4)$$

which is shown in Figure 3.

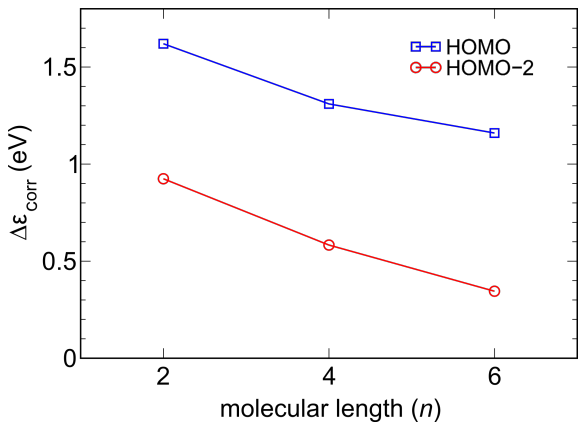

Figure 3: Change in the correlation energy of the HOMO and HOMO–2 energy levels when the molecules are taken from the gas-phase into the junction. This value represents the shift of molecular levels due to the enhanced screening provided by the metallic electrodes (an image-charge effect in simple terms).

The result can be understood qualitatively by considering a classical model to account for the screening effect of the electrodes. Classically a charge distribution close to any surface will experience an image potential. The strength of the image potential in general depends on the dielectric constant of the surface material and the local geometrical shape of the surface. Here we model the Au electrodes as perfect metals. The image potential for a point charge halfway between two metal surfaces separated by a distance L is $\approx 10.0/L$ (eV·Å) [64]. This predicts that the image-charge effect is proportional to $1/L$. The Au tip atoms in our simulations are about 8 Å apart for the C_2-alkanediamine junction giving a rough estimate of 1.3 eV for the image-charge effect in qualitative agreement with the GW calculations. The HOMO experiences a larger image-charge effect than the HOMO–2, which can be understood from the fact that its charge density is located closer to the metallic surfaces. In the limit of an infinitely long wire the HOMO–2 will be spread out over the entire molecule and the image-charge effect should vanish. On the other hand, in this limit the HOMO would stay localized near the surface and therefore approach a nonzero constant image charge potential. If we model the HOMO charge density as a point charge of half an electron on each of the amine groups we can estimate this

limiting constant to be 3.6/(2d) (eV·Å), where d is the distance to the nearest metal surface. Taking d to be about the same length as the Au–N bond (2.34 Å) gives a limiting value estimate of 0.8 eV. Again, this seems to be in qualitative agreement with our GW findings.

Finally, we discuss the coverage dependence of the energy level position for alkanediamine–Au junctions. It was shown in [65] that the DFT level position for amine-linked molecules is strongly dependent on the coverage. In contrast to the screening (image-charge) effects as discussed above, which appear in the correlation part of the self-energy, this is a purely electrostatic effect resulting from the localized surface dipoles formed at the Au–NH_2 bond. To investigate the dependence of the energy levels on the coverage for our junctions, we have performed DFT calculations for a range of transverse supercell dimensions for the geometry shown in Figure 1. In Figure 4 we show the PDOS of a methylene unit in the central part of the molecule for transverse supercells with 2 × 2 up to 8 × 8 surface atoms.

The PDOS peaks and band edge shift up in energy as the transverse supercell size is increased, in agreement with the results of [65]. The inset shows the energy shift obtained from reading off the shift in the PDOS as a function of coverage defined as $\eta = 1/N_{surface}$, where $N_{surface}$ is the number of surface atoms. For a supercell of size 3 × 3 and larger, the shift is seen to be directly proportional to the coverage, as expected for a two-dimensional array of dipoles [66]. This allow us to extract the electrostatic shift corresponding to the single-molecule limit. We find that the electrostatic energy shift when going from a 4 × 4 supercell to the single-molecule limit is indeed significant with a value around 1 eV.

Transport calculations

The transmission functions of the C_2-, C_4- and C_6-alkanediamine junction geometries were calculated by using the GW and the PBE xc potential as approximations for Σ_{xc} in Equation 3. To include the coverage dependence, we simulated the low-coverage limit $\eta = 0^+$ by performing calculations for the 4 × 4 junction (corresponding to $\eta = 1/16$) with all molecular levels shifted up by 1 eV through a simple scissors-operator self-energy.

The transmission function calculated by GW for a coverage of $\eta = 1/16$ is shown in Figure 5 on a logarithmic scale. The transmission functions for different molecular lengths have very similar shapes in the important region near the Fermi level E_F, however, the magnitude is increasingly suppressed as a function of the molecular length. The similarity of the transmission functions may at first seem surprising since we have shown that the position of the molecular energy levels shows some length dependence. In particular the HOMO level was found to decrease in energy by 0.5 eV when n increases from 2 to 6 (Table 2). This shift is indeed visible in the transmission function in the range −4.0 to −6.0 eV where the HOMO is located. On the other hand the features in the transmission function around the Fermi level are determined by the local electronic structure of the Au tips.

The zero-bias conductance is obtained from the transmission function at the Fermi level, $G = G_0T(E_F)$ where $G_0 = 2e^2/h$ is the unit of quantum conductance. The zero-bias conductance is plotted in Figure 6 as a function of the molecular length. We have also included the DFT results for comparison. The dashed lines show the best fits to the exponential form $G_n = G_c\exp(-\beta n)$.

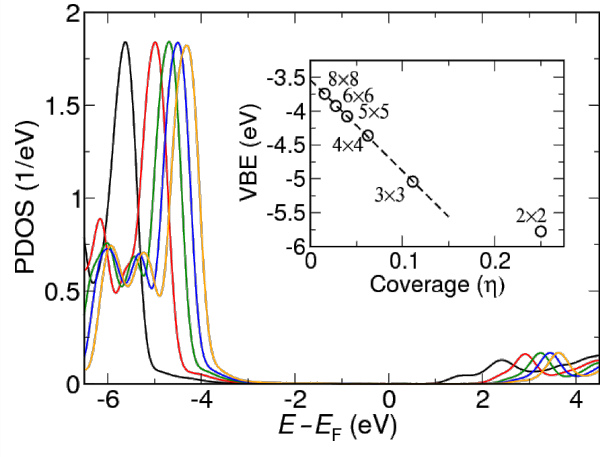

Figure 4: The molecular valence-band edge (or HOMO) as a function of coverage for an n = 6 alkane. The numbers indicate the number of surface atoms.

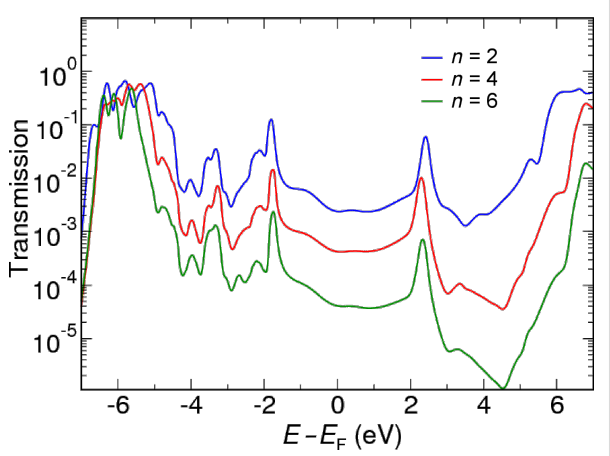

Figure 5: The transmission function calculated by GW for a molecular length of n = 2, n = 4 and n = 6 at a coverage of η = 1/16.

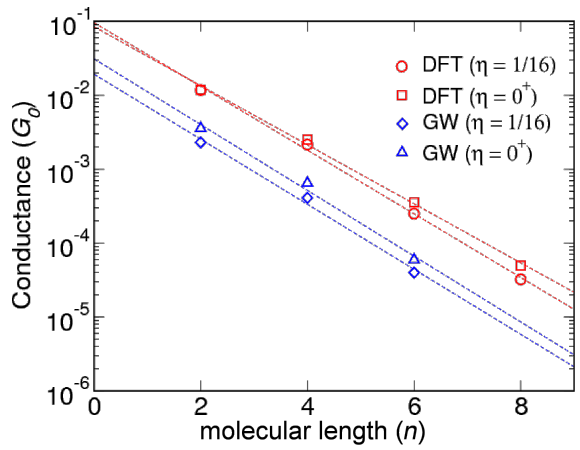

Figure 6: Calculated conductance plotted as a function of the molecular length for a coverage corresponding to 4 × 4 Au atoms per molecule (η = 1/16) and extrapolated to the single-molecule limit (η = 0).

The values for β and G_c corresponding to the single-molecule limit (η = 0) and 4 × 4 Au atoms per molecule (η = 1/16) are reported in Table 3 together with the experimental values. We note that the contact conductance was not stated in [12], but has been estimated by extrapolation to zero molecular length from the reported experimental data. When comparing to experiment it should be kept in mind that experiments are often performed in solution at room temperature and are subject to variations in the detailed atomic structure. However, it has been shown that amine-linked molecules bind preferentially to under-coordinated Au atoms, such as in the structures considered here, and show a relatively narrow conductance distribution [1].

Table 3: Calculated contact conductance G_c in units of G_0 and exponential decay constant β per carbon atom; η denotes the coverage.

	DFT		GW		exp.
η	1/16	0	1/16	0	
G_c	0.11	0.10	0.02	0.04	0.02[a], 0.030[c]
β	0.99	0.92	1.01	1.02	0.97[a], 0.93[b], 0.91[c]

[a] [12] (G_c is not stated, but is estimated from the reported data); [b] [31]; [c] [1].

The rather weak effect of coverage on the conduction properties is in agreement with the findings reported in [67] where a C_4-alkanediamine/Au junction with 3 × 3 and 4 × 4 surfaces was considered. Our DFT results are in reasonable agreement with previous DFT studies showing decay factors in the range 0.83–1.01 and conductance resistances in the range (0.09–0.28) G_0 [8-10]. While the β values obtained with GW are rather close to the DFT calculated ones, the contact conductance is reduced by a factor of 3–5, depending on the coverage. This is a direct result of the molecular levels lying further away from E_F (by 0.5–2.5 eV, Figure 2d) in GW compared to DFT.

Conclusion

We have unraveled the important role of exchange–correlation effects for the energy-level alignment and low-bias conductance of gold/alkanediamine molecular junctions. Based on many-body GW calculations we found that the origin of the overestimation of the contact conductance, G_c, by standard DFT is due to the incorrect energy-level alignment in the junction. The absence of self-interaction and the inclusion of image-charge screening effect through the GW self-energy improves the description of the energy levels and yields values for G_c and the decay constant β that are in good agreement with experimental results. The quasiparticle corrections to the DFT energy levels showed a significant orbital dependence ranging from −0.5 eV to −2.5 eV due to the different shape and localization of the molecular orbitals. Our results demonstrate that quantitatively accurate calculations of conductance from first-principles are feasible, although computationally demanding.

Acknowledgements

The authors acknowledge support from the Lundbeck Foundation's Center for Atomic-scale Materials Design (CAMD) and The Danish Center for Scientific Computing.

References

1. Venkataraman, L.; Klare, J. E.; Tam, I. W.; Nuckolls, C.; Hybertsen, M. S.; Steigerwald, M. L. *Nano Lett.* **2006,** *6,* 458–462. doi:10.1021/nl052373+
2. Kristensen, I. S.; Mowbray, D. J.; Thygesen, K. S.; Jacobsen, K. W. *J. Phys.: Condens. Matter* **2008,** *20,* 374101. doi:10.1088/0953-8984/20/37/374101
3. Tomfohr, J. K.; Sankey, O. F. *Phys. Rev. B* **2002,** *65,* 245105. doi:10.1103/PhysRevB.65.245105
4. Sen, A.; Kaun, C.-C. *ACS Nano* **2010,** *4,* 6404–6408. doi:10.1021/nn101840a
5. Kaun, C.-C.; Guo, H. *Nano Lett.* **2003,** *3,* 1521–1525. doi:10.1021/nl0346023
6. Müller, K.-H. *Phys. Rev. B* **2006,** *73,* 045403. doi:10.1103/PhysRevB.73.045403
7. Paulsson, M.; Krag, C.; Frederiksen, T.; Brandbyge, M. *Nano Lett.* **2009,** *9,* 117–121. doi:10.1021/nl802643h
8. Wohlthat, S.; Pauly, F.; Reimers, J. R. *Chem. Phys. Lett.* **2008,** *454,* 284–288. doi:10.1016/j.cplett.2008.02.011
9. McDermott, S.; George, C. B.; Fagas, G.; Greer, J. C.; Ratner, M. A. *J. Phys. Chem. C* **2009,** *113,* 744–750. doi:10.1021/jp8078698
10. Sheng, W.; Li, Z. Y.; Ning, Z. Y.; Zhang, Z. H.; Yang, Z. Q.; Guo, H. *J. Chem. Phys.* **2009,** *131,* 244712. doi:10.1063/1.3276280
11. Li, C.; Pobelov, I.; Wandlowski, T.; Bagrets, A.; Arnold, A.; Evers, F. *J. Am. Chem. Soc.* **2008,** *130,* 318–326. doi:10.1021/ja0762386

12. Hybertsen, M. S.; Venkataraman, L.; Klare, J. E.; Whalley, A. C.; Steigerwald, M. L.; Nuckolls, C. *J. Phys.: Condens. Matter* **2008,** *20,* 374115. doi:10.1088/0953-8984/20/37/374115
13. Quek, S. Y.; Venkataraman, L.; Choi, H. J.; Louie, S. G.; Hybertsen, M. S.; Neaton, J. B. *Nano Lett.* **2007,** *7,* 3477–3482. doi:10.1021/nl072058i
14. Mowbray, D. J.; Jones, G.; Thygesen, K. S. *J. Chem. Phys.* **2008,** *128,* 111103. doi:10.1063/1.2894544
15. Smit, R. H. M.; Noat, Y.; Untiedt, C.; Lang, N. D.; van Hemert, M. C.; van Ruitenbeek, J. M. *Nature (London)* **2002,** *419,* 906–909. doi:10.1038/nature01103
16. Djukic, D.; Thygesen, K. S.; Untiedt, C.; Smit, R. H. M.; Jacobsen, K. W.; van Ruitenbeek, J. M. *Phys. Rev. B* **2005,** *71,* 161402. doi:10.1103/PhysRevB.71.161402
17. Garciá, Y.; Palacios, J. J.; SanFabián, E.; Vergés, J. A.; Pérez-Jiménez, A. J.; Louis, E. *Phys. Rev. B* **2004,** *69,* 041402(R). doi:10.1103/PhysRevB.69.041402
18. Untiedt, C.; Dekker, D. M. T.; Djukic, D.; van Ruitenbeek, J. M. *Phys. Rev. B* **2004,** *69,* 081401. doi:10.1103/PhysRevB.69.081401
19. Strange, M.; Thygesen, K. S.; Jacobsen, K. W. *Phys. Rev. B* **2006,** *73,* 125424. doi:10.1103/PhysRevB.73.125424
20. Toher, C.; Filippetti, A.; Sanvito, S.; Burke, K. *Phys. Rev. Lett.* **2005,** *95,* 146402. doi:10.1103/PhysRevLett.95.146402
21. Toher, C.; Sanvito, S. *Phys. Rev. Lett.* **2007,** *99,* 056801. doi:10.1103/PhysRevLett.99.056801
22. Ke, S.-H.; Baranger, H. U.; Yang, W. *J. Chem. Phys.* **2007,** *126,* 201102. doi:10.1063/1.2743004
23. Hedin, L. *Phys. Rev.* **1965,** *139,* A796–A823. doi:10.1103/PhysRev.139.A796
24. Strange, M.; Rostgaard, C.; Häkkinen, H.; Thygesen, K. S. *Phys. Rev. B* **2011,** *83,* 115108. doi:10.1103/PhysRevB.83.115108
25. Nelson, W.; Bokes, P.; Rinke, P.; Godby, R. W. *Phys. Rev. A* **2007,** *75,* 032505. doi:10.1103/PhysRevA.75.032505
26. Neaton, J. B.; Hybertsen, M. S.; Louie, S. G. *Phys. Rev. Lett.* **2006,** *97,* 216405. doi:10.1103/PhysRevLett.97.216405
27. Garcia-Lastra, J. M.; Rostgaard, C.; Rubio, A.; Thygesen, K. S. *Phys. Rev. B* **2009,** *80,* 245427. doi:10.1103/PhysRevB.80.245427
28. Thygesen, K. S.; Rubio, A. *Phys. Rev. Lett.* **2009,** *102,* 046802. doi:10.1103/PhysRevLett.102.046802
29. Rostgaard, C.; Jacobsen, K. W.; Thygesen, K. S. *Phys. Rev. B* **2010,** *81,* 085103. doi:10.1103/PhysRevB.81.085103
30. Blase, X.; Attaccalite, C.; Olevano, V. *Phys. Rev. B* **2011,** *83,* 115103. doi:10.1103/PhysRevB.83.115103
31. Hybertsen, M. S.; Louie, S. G. *Phys. Rev. B* **1986,** *34,* 5390–5413. doi:10.1103/PhysRevB.34.5390
32. Holm, B.; von Barth, U. *Phys. Rev. B* **1998,** *57,* 2108–2117. doi:10.1103/PhysRevB.57.2108
33. Xu, B.; Tao, N. J. *Science* **2003,** *301,* 1221–1223. doi:10.1126/science.1087481
34. Engelkes, V. B.; Beebe, J. M.; Frisbie, C. D. *J. Am. Chem. Soc.* **2004,** *126,* 14287–14296. doi:10.1021/ja046274u
35. Chen, F.; Li, X.; Hihath, J.; Huang, Z.; Tao, N. *J. Am. Chem. Soc.* **2006,** *128,* 15874–15881. doi:10.1021/ja065864k
36. Park, Y. S.; Whalley, A. C.; Kamenetska, M.; Steigerwald, M. L.; Hybertsen, M. S.; Nuckolls, C.; Venkataraman, L. *J. Am. Chem. Soc.* **2007,** *129,* 15768–15769. doi:10.1021/ja0773857
37. Huang, Z.; Chen, F.; Bennett, P. A.; Tao, N. *J. Am. Chem. Soc.* **2007,** *129,* 13225–13231. doi:10.1021/ja074456t
38. Widawsky, J. R.; Kamenetska, M.; Klare, J.; Nuckolls, C.; Steigerwald, M. L.; Hybertsen, M. S.; Venkataraman, L. *Nanotechnology* **2009,** *20,* 434009. doi:10.1088/0957-4484/20/43/434009
39. Kamenetska, M.; Koentopp, M.; Whalley, A. C.; Park, Y. S.; Steigerwald, M. L.; Nuckolls, C.; Hybertsen, M. S.; Venkataraman, L. *Phys. Rev. Lett.* **2009,** *102,* 126803. doi:10.1103/PhysRevLett.102.126803
40. Song, H.; Lee, T.; Choi, N.-J.; Lee, H. *Appl. Phys. Lett.* **2007,** *91,* 253116. doi:10.1063/1.2827239
41. Kim, Y.; Hellmuth, T. J.; Buerkle, M.; Pauly, F.; Scheer, E. *ACS Nano* **2011,** *5,* 4104–4111. doi:10.1021/nn200759s
42. Martin, C. A.; Ding, D.; van der Zant, H. S. J.; van Ruitenbeek, J. M. *New J. Phys.* **2008,** *10,* 065008. doi:10.1088/1367-2630/10/6/065008
43. Nichols, R. J.; Haiss, W.; Higgins, S. J.; Leary, E.; Martin, S.; Bethell, D. *Phys. Chem. Chem. Phys.* **2010,** *12,* 2801–2815. doi:10.1039/b922000c
44. Haiss, W.; Martin, S.; Scullion, L. E.; Bouffier, L.; Higgins, S. J.; Nichols, R. J. *Phys. Chem. Chem. Phys.* **2009,** *11,* 10831–10838. doi:10.1039/b910194b
45. Cossaro, A.; Mazzarello, R.; Rousseau, R.; Casalis, L.; Verdini, A.; Kohlmeyer, A.; Floreano, L.; Scandolo, S.; Morgante, A.; Klein, M. L.; Scoles, G. *Science* **2008,** *321,* 943–946. doi:10.1126/science.1158532
46. Wang, Y.; Chi, Q.; Hush, N. S.; Reimers, J. R.; Zhang, J.; Ulstrup, J. *J. Phys. Chem. C* **2009,** *113,* 19601–19608. doi:10.1021/jp906216k
47. Voznyy, O.; Dubowski, J. J.; Yates, J. T., Jr..; Maksymovych, P. *J. Am. Chem. Soc.* **2009,** *131,* 12989–12993. doi:10.1021/ja902629y
48. Jadzinsky, P. D.; Calero, G.; Ackerson, C. J.; Bushnell, D. A.; Kornberg, R. D. *Science* **2007,** *318,* 430–433. doi:10.1126/science.1148624
49. Walter, M.; Akola, J.; Lopez-Acevedo, O.; Jadzinsky, P. D.; Calero, G.; Ackerson, C. J.; Whetten, R. L.; Grönbeck, H.; Häkkinen, H. *Proc. Natl. Acad. Sci. U. S. A.* **2008,** *105,* 9157–9162. doi:10.1073/pnas.0801001105
50. Strange, M.; Lopez-Acevedo, O.; Häkkinen, H. *J. Phys. Chem. Lett.* **2010,** *1,* 1528–1532. doi:10.1021/jz1002988
51. Cheng, Z. L.; Skouta, R.; Vazquez, H.; Widawsky, J. R.; Schneebeli, S.; Chen, W.; Hybertsen, M. S.; Breslow, R.; Venkataraman, L. *Nat. Nanotechnol.* **2011,** *6,* 353–357. doi:10.1038/nnano.2011.66
52. Fagas, G.; Greer, J. C. *Nanotechnology* **2007,** *18,* 424010. doi:10.1088/0957-4484/18/42/424010
53. Enkovaara, J.; Rostgaard, C.; Mortensen, J. J.; Chen, J.; Dulak, M.; Ferrighi, L.; Gavnholt, J.; Glinsvad, C.; Haikola, V.; Hansen, H. A.; Kristoffersen, H. H.; Kuisma, M.; Larsen, A. H.; Lehtovaara, L.; Ljungberg, M.; Lopez-Acevedo, O.; Moses, P. G.; Ojanen, J.; Olsen, T.; Petzold, V.; Romero, N. A.; Stausholm-Møller, J.; Strange, M.; Tritsaris, G. A.; Vanin, M.; Walter, M.; Hammer, B.; Häkkinen, H.; Madsen, G. K. H.; Nieminen, R. M.; Nørskov, J. K.; Puska, M.; Rantala, T. T.; Schiøtz, J.; Thygesen, K. S.; Jacobsen, K. W. *J. Phys.: Condens. Matter* **2010,** *22,* 253202. doi:10.1088/0953-8984/22/25/253202
54. Larsen, A. H.; Vanin, M.; Mortensen, J. J.; Thygesen, K. S.; Jacobsen, K. W. *Phys. Rev. B* **2009,** *80,* 195112. doi:10.1103/PhysRevB.80.195112
55. Perdew, J.; Burke, K.; Ernzerhof, M. *Phys. Rev. Lett.* **1996,** *77,* 3865–3868.

56. We use the equilibrium PBE lattice constant of 4.18 Å for Au. The distance between the second outermost Au(111) atomic surface layers in the left and right electrode was fixed at 21.59 Å, 24.10 Å and 26.63 Å for the *n* = 2, 4 and 6 junction, respectively. The resulting relaxed N–Au bond length are 2.34 Å, 2.35 Å and 2.33 Å.
57. Meir, Y.; Wingreen, N. S. *Phys. Rev. Lett.* **1992,** *68,* 2512–2515. doi:10.1103/PhysRevLett.68.2512
58. Thygesen, K. S. *Phys. Rev. B* **2006,** *73,* 035309. doi:10.1103/PhysRevB.73.035309
59. Thygesen, K. S.; Jacobsen, K. W. *Chem. Phys.* **2005,** *319,* 111–125. doi:10.1016/j.chemphys.2005.05.032
60. Thygesen, K. S. *Phys. Rev. Lett.* **2008,** *100,* 166804. doi:10.1103/PhysRevLett.100.166804
61. http://webbook.nist.gov/cgi/cbook.cgi?ID=C106978&Units=SI&Mask=20#Ion-Energetics (accessed Aug 16, 2011).
62. Dell'Angela, M.; Kladnik, G.; Cossaro, A.; Verdini, A.; Kamenetska, M.; Tamblyn, I.; Quek, S. Y.; Neaton, J. B.; Cvetko, D.; Morgante, A.; Venkataraman, L. *Nano Lett.* **2010,** *10,* 2470–2474. doi:10.1021/nl100817h
63. Rohlfing, M. *Phys. Rev. B* **2010,** *82,* 205127. doi:10.1103/PhysRevB.82.205127
64. Chen, C. J. *Introduction to Scanning Microscopy;* Oxford University Press: New York, 1993.
65. Wang, J.-g.; Prodan, E.; Car, R.; Selloni, A. *Phys. Rev. B* **2008,** *77,* 245443. doi:10.1103/PhysRevB.77.245443
66. Natan, A.; Kronik, L.; Haick, H.; Tung, R. T. *Adv. Mater.* **2007,** *19,* 4103–4117. doi:10.1002/adma.200701681
67. Feng, X. Y.; Li, Z.; Yang, J. *J. Phys. Chem. C* **2009,** *113,* 21911–21914. doi:10.1021/jp908347s

License and Terms

Beilstein Journal of Nanotechnology

Effect of the environment on the electrical conductance of the single benzene-1,4-diamine molecule junction

Shigeto Nakashima, Yuuta Takahashi and Manabu Kiguchi*

Full Research Paper

Open Access

Address:
Department of Chemistry, Graduate School of Science and Engineering, Tokyo Institute of Technology 2-12-1 W4-10 Ookayama, Meguro-ku, Tokyo 152-8551, Japan

Email:
Manabu Kiguchi* - kiguti@chem.titech.ac.jp

* Corresponding author

Keywords:
benzene-1,4-diamine; electric conductance; single-molecule junction; solvent

Beilstein J. Nanotechnol. **2011,** *2,* 755–759.
doi:10.3762/bjnano.2.83

Received: 27 June 2011
Accepted: 08 November 2011
Published: 16 November 2011

This article is part of the Thematic Series "Transport through molecular junctions".

Guest Editor: J. M. van Ruitenbeek

Abstract

We investigated the effect of the environment on the electrical conductance of a single benzene-1,4-diamine (BDA) molecule bridging Au electrodes, using the scanning tunneling microscope (STM). The conductance of the single BDA molecule junction decreased upon a change in the environment from tetraglyme, to mesitylene, to water, and finally to N_2 gas, while the spread in the conductance value increased. The order of the conductance values of the single BDA molecule junction was explained by the strength of the interaction between the solvent molecules and the Au electrodes. The order of the spread in the conductance values was explained by the diversity in the coverage of the BDA molecule at metal electrodes and atomic and molecular motion of the single-molecule junction.

Introduction

The electron transport properties through a single molecule bridging metal electrodes (single-molecule junction) have attracted much attention toward the realization of molecular scale electronics [1,2]. Electrical conductance of the single-molecule junction was investigated by means of mechanically controllable break junction (MCBJ), scanning tunneling microscope (STM), and other techniques. In the simple tunneling model, the transmission ($T(E)$) of the single-molecule junction can be represented by

$$T(E) = \sum_k \frac{(2\pi t^2 \rho C_{rk} C^*_{sk})^2}{(E-\varepsilon_k)^2 + \eta_k{}^2} \quad (1)$$

where t, ρ, C_{rk} and ε_k are the hopping integral between the metal and molecular orbitals (MO), the local density of states (LDOS) of the metals at the Fermi level (E_F), the kth MO coefficient at site r, and the kth MO energy, respectively. The infinitesimal η_k is determined by Green's function and DOS [3]. The conductance of the single molecule junction depends on the parameters of t, ρ, C_{rk}, ε_k, and η_k.

While advances have been made in the understanding of the conductance of single-molecule junctions based on intrinsic factors [4,5], uncertainties still remain, and the effects of the environment on the conductance of the single-molecule junction are still unclear. In solution, solvent molecules can interact with the molecule bridging the metal electrodes, and/or with the metal electrodes themselves. Wu et al. demonstrated that the aromatic π–π coupling between adjacent molecules affected the formation of the molecule junction and electron transport through the molecule junction [6]. Venkataraman's group and our group independently evaluated the electron-transport properties of π-stacked systems [7,8]. We showed that the conductance of the π-stacked system decreased with the number of π molecules, and the decrease in conductance per unit of electron-transport distance was comparable to that of the conventional single-molecule junction. Dahlke et al. investigated the effect of the surrounding molecules on the single phenylene diisocyanide molecule junction, by means of theoretical calculations [9]. The electronic structure and conductance of the phenylene diisocyanide molecule were affected by surrounding phenylene diisocyanide molecules when the distance between the molecules was less than 0.6 nm. Tawara et al. investigated the spread in conductance values of the single benzenedithiol molecule junction in water [10]. They showed that water molecules affected the dynamics, and more specifically, the C–S stretching mode of the single-molecule junction. The conductance of the single benzenedithiol molecule junction depended on the length of the C–S bond; thus, the spread in the conductance value was suppressed in water compared with that in vacuum. These experimental and theoretical studies suggested that the solvent molecule could affect the electron-transport properties of the single-molecule junction. In the present study, we investigated the effect of the environment on the electron-transport properties of the single benzene-1,4-diamine (BDA) molecule junction in water, tetraglyme, and mesitylene, with each medium having different viscosity and dipole moment.

Experimental

The single-molecule junctions were fabricated in an electrochemical cell mounted in a chamber, which was filled with high-purity N_2 gas (purity >99.999%) in order to avoid any effects of oxygen and water in the air. The conductance measurements were performed by using electrochemical STM (Pico-SPM, Molecular Imaging Co.) and a Nano Scope IIIa controller (Digital Instruments Co.), where the STM tip was made from a Au wire (diameter ~0.25 mm, purity >99%). Figure 1 shows the schematic view of the experimental setup. For the conductance measurement in water, the Au tip was

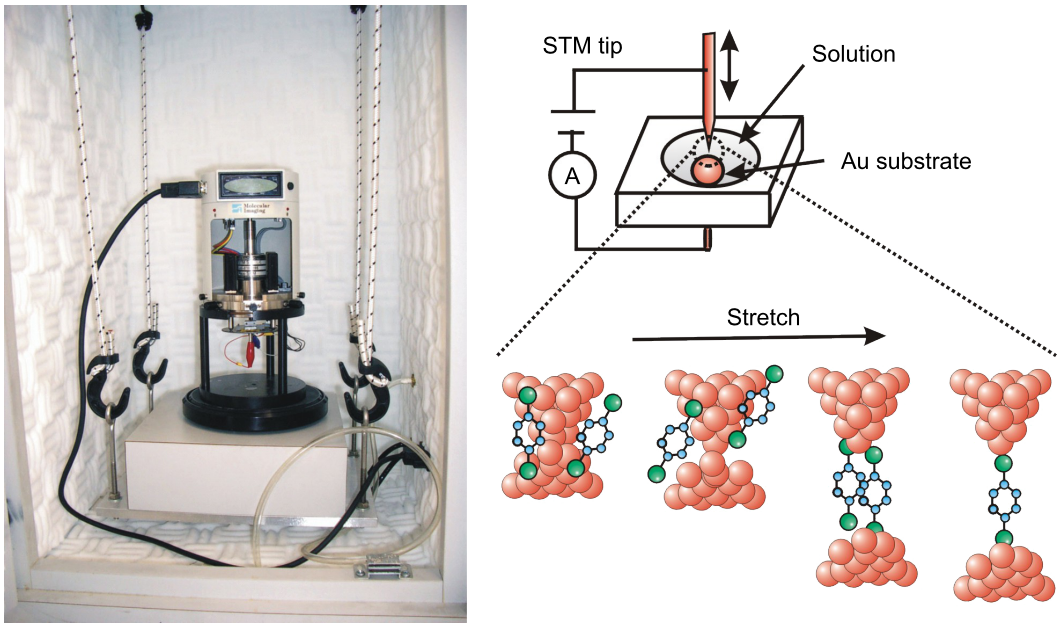

Figure 1: Experimental setup and schematic view of the formation process of the single-molecule junction during stretching of the Au contact in the solution containing the target molecules.

coated with wax to eliminate ionic conduction. The substrate was Au (111), prepared by a flame-annealing and quenching method. For the measurements in liquid, a solution of BDA (10 mM) in water, tetraethylene glycol dimethyl ether (tetraglyme), or mesitylene was fed into the electrochemical cell. The Au tip was repeatedly moved in and out of contact with the Au(111) substrate at a rate of 100 nm/s. Conductance was measured during breaking of the Au contact, and was not dependent on the breaking speed below 100 nm/s. The bias voltage between the tip and substrate was 20 mV. The experiments were performed on three independent samples for each solution. For comparison, the conductance measurement was also performed without solution. A self-assembled monolayer (SAM) of BDA on the Au substrate was prepared by exposing the substrate to methanol solution containing 10 mM BDA overnight. The conductance measurements were performed in N_2 gas.

Results

Figure 2 shows the typical conductance traces of Au contacts in tetraglyme solution containing 10 mM BDA (green curves). The conductance changed stepwise, with a step height corresponding to the quantum unit, G_0 ($G_0 = 2e^2/h$). The conductance histogram constructed from 2200 conductance traces (Figure 3) shows peaks at 1 G_0 and 2 G_0. The conductance of a metal nanocontact is represented by $G = G_0 \sum T_i$ where T_i is the transmission probability of the ith conductance channel [2]. In the case of a Au nanocontact, the single Au 6s channel with transmission of 1 is the contributor to the electron transport. The 1 G_0 plateau in the conductance trace and the 1 G_0 peak in the conductance histogram correspond to the Au atomic contact. The clean Au atomic contact was formed in tetraglyme. A clear 1 G_0 plateau in the conductance trace and 1 G_0 peaks in the conductance histograms were also observed in other environments, as shown in Figure 2 and Figure 3. The formation of the Au atomic contact and conductance of the Au atomic contact were not affected by the change of environment.

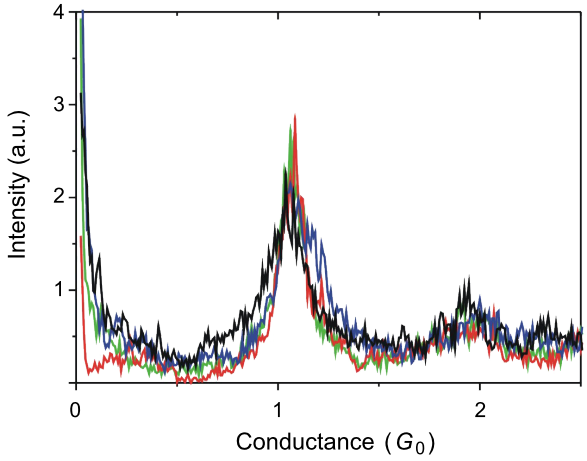

Figure 3: Conductance histograms of Au contacts in tetraglyme (green), water (red), mesitylene (blue) containing 10 mM BDA. The black curve is the result obtained from measurement in N_2 atmosphere. The conductance histograms were constructed from 2200 conductance traces without data selection. The bin size was 8×10^{-3} G_0.

Figure 4 shows the conductance traces of Au contacts in tetraglyme containing 10 mM BDA, in the low conductance regime (green curves). The trace shows a plateau around 0.01 G_0. The conductance histogram (Figure 5) constructed from 3300 conductance traces also shows a peak around 0.01 G_0. There were no steps in the conductance traces, and no

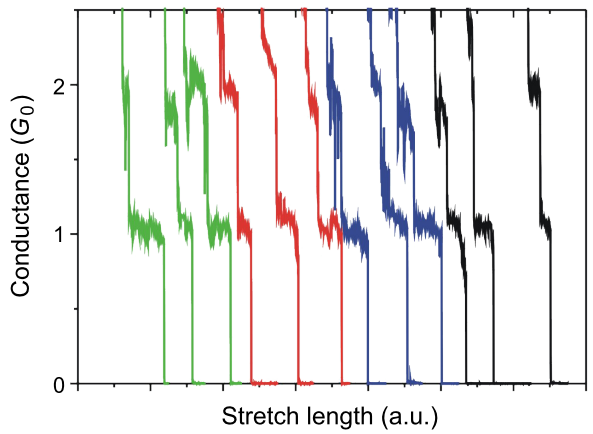

Figure 2: Typical conductance traces of Au contacts in tetraglyme (green), water (red), mesitylene (blue) containing 10 mM BDA. The black curves are results measured under a N_2 atmosphere.

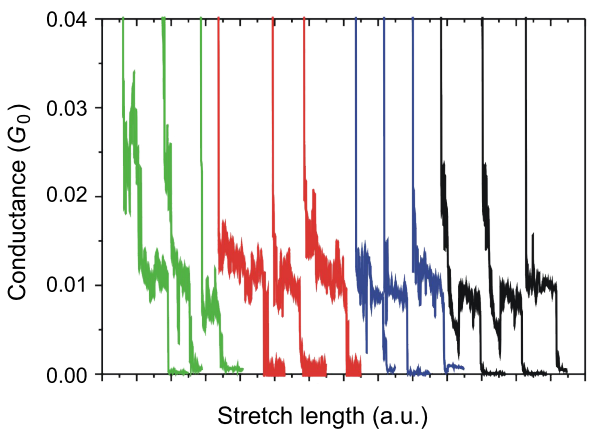

Figure 4: Typical conductance traces of Au contacts in tetraglyme (green), water (red), mesitylene (blue) containing 10 mM BDA. Black curves represent results measured in N_2 atmosphere.

features in the conductance histogram below 0.01 G_0. However, under the N_2 atmosphere few conductance traces showed steps below 0.01 G_0, leading to the appearance of a weak feature below 0.01 G_0. In the absence of BDA, neither steps nor peaks were observed in the same conductance regime. These experimental results indicate that the 0.01 G_0 plateau in the trace and 0.01 G_0 in the conductance histogram correspond to the single BDA molecule junction [4-7]. The conductance of the single BDA molecule junction was determined to be 0.010 ± 0.0014 G_0 in tetraglyme based on statistical analysis of the repeated measurements (see Supporting Information File 1 for details).

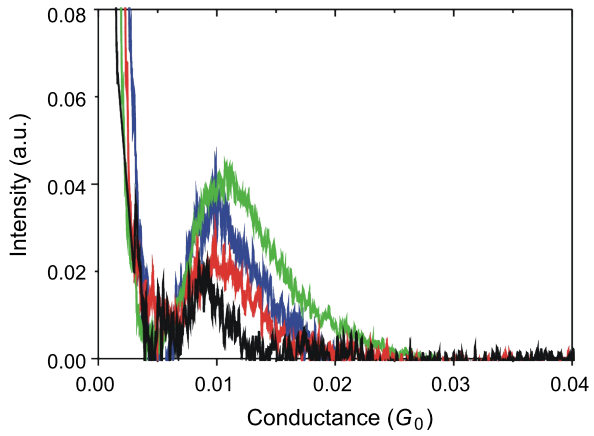

Figure 5: Conductance histograms of Au contacts in tetraglyme (green), water (red), and mesitylene (blue) containing 10 mM BDA. The black curve represents the result measured under N_2 atmosphere. The conductance histograms were constructed from 3300 conductance traces without data selection. The tunneling background has been subtracted (see Supporting Information File 1 for details). The bin size was 1.5×10^{-5} G_0.

The conductance measurements were performed in other environments (Figure 4 and Figure 5). The conductance of the single BDA molecule junctions was determined to be 0.0082 ± 0.0021 G_0, 0.0089 ± 0.0016 G_0, 0.0095 ± 0.0015 G_0 in N_2 gas, water, and mesitylene, respectively. The conductance values of the single BDA in tetraglyme, mesitylene, water, and N_2 gas decreased in that order. The conductance of the single BDA molecule junction has also been investigated by other groups. Venkataraman et al. reported the conductance of the single BDA molecule junction in 1,2,4-trichlorobenzene to be 0.006 G_0 [11], which is close to our experimental result. The difference in the conductance values between our experimental results could be attributed to different experimental conditions, such as bias voltage, solvent, etc. The conductance of the single BDA molecule junction varied with the environment. Thus, we estimate the spread in the conductance value from the standard deviation of the histogram peak position (σ) normalized by the conductance (G) of the single BDA molecule junction. Thus, σ/G was 0.26, 0.18, 0.16, and 0.14 in N_2 gas, water, mesitylene, and tetraglyme, respectively. The spread in the conductance value decreased in the order of N_2 gas, water, mesitylene, and tetraglyme.

Discussion

Here, we discuss the effect of the environment on the conductance of the single BDA molecule junction. In the single BDA molecule junction, electron transport is mediated by the highest occupied molecular orbital (HOMO) of BDA [12]. The conductance of a single BDA molecule junction increases for decreasing energy difference (ΔE) between the HOMO and the Fermi level (E_F) of Au (Equation 1). When the BDA molecule adsorbs on the Au electrode, the value of E_F increases. This is due to charge transfer from the BDA molecule to Au. In the presence of the solvent, the solvent molecule can adsorb on the Au surface by replacing the surface-bound BDA molecules. The amount of charge transfer between the solvent molecule and Au is smaller than that between the BDA molecule and Au. This is due to the relative weakness of the interaction. The value of E_F decreases through replacement of the BDA molecules with the solvent molecules. The replacement reaction decreases ΔE, and thus, the conductance of the single BDA molecule junction increases when solvent molecules adsorb on the Au surface. The replacement reaction frequently occurs in the solvent, which strongly interacts with Au (although not as strongly as the BDA molecules).

In the case of physical adsorption, the strength of the molecule–metal interaction increases with the molecule size. The molecule sizes of water and mesitylene are 0.3 nm and 0.8 nm, respectively. By considering the molecule size and other physical properties (e.g., dipole moment), the interaction between the Au electrode and solvent would decrease in the order of tetraglyme, mesitylene and water. Therefore, the conductance of the single BDA molecule junction in tetraglyme, mesitylene, water and N_2 gas decreased in that order.

The spread in the conductance value of the single BDA molecule junction in N_2 gas, water, mesitylene, and tetraglyme decreased in that order. We discuss the effect of the environment on the spread in the conductance value by considering the atomic and molecular motion of the single-molecule junction and molecular adsorption at the metal electrodes. First, the atomic and molecular motion of the single molecule junction was suppressed in the following order: N_2 gas, water, mesitylene, and tetraglyme. This was done in order to reflect the molecular weight and viscosity of the solvent; the conductance of the single-molecule junction depends on the atomic structure of the

junction. When the atomic and molecular motion of the single-molecule junction is suppressed, the conductance of the single-molecule junction does not significantly change with time, leading to a decrease in the spread of the conductance value. Therefore, the spread in conductance value decreased with the change in environment in the following order: N_2 gas, water, mesitylene, and tetraglyme. Second, the coverage of BDA molecules on a Au electrode decreased in the following order: in N_2 gas, water, mesitylene, and tetraglyme. This order reflects the strength of the interaction between the Au electrode and the solvent, as discussed in the previous section. The amount of the charge transfer from the BDA molecule to Au (decrease in conductance value) was largest for the single BDA molecule junction under N_2 atmosphere, compared to the single BDA molecule bridging clean Au electrodes. The spread in the conductance value of the single-molecule junction increased with the change in the conductance value relative to that of the single BDA molecule bridging the clean Au electrodes. Therefore, the spread in conductance value decreased with changing environment in the order of N_2 gas, water, mesitylene, and tetraglyme.

Conclusion

The electrical conductance of the single BDA molecule bridging Au electrodes was investigated in tetraglyme, mesitylene, water and N_2 atmosphere. The conductance of the single BDA molecule junction in tetraglyme, mesitylene, water, and N_2 decreased in that particular order. The energy difference between E_F and the HOMO of BDA decreased when the surface-bound BDA molecules were replaced by solvent molecules. Therefore, the conductance of the single BDA molecule junction showed higher conductance values in tetraglyme, which interacted relatively strongly with the Au electrodes. On the other hand, the spread in conductance value of the single BDA molecule junction in N_2 gas, water, mesitylene, and tetraglyme decreased in that order. The atomic and molecular motion of the single-molecule junction is suppressed by the solvent. In the organic solution, the spread in conductance value was smaller compared to the results in N_2, because the atomic and molecular motion of the single-molecule junction was suppressed. The spread in the conductance values can be also explained by the diversity of the coverage of the BDA molecules on the Au electrodes.

Supporting Information

Supporting Information File 1

Experimental details.
[http://www.beilstein-journals.org/bjnano/content/supplementary/2190-4286-2-83-S1.pdf]

Acknowledgements

This work was financially supported by Grant-in-Aid for Scientific Research from MEXT and Sumitomo foundation, and Iketani foundation.

References

1. Cuevas, J. C.; Scheer, E. *Molecular Electronics;* World Scientific Publishing: Singapore, 2010.
2. Agraït, N.; Yeyati, A. L.; van Ruitenbeek, J. M. *Phys. Rep.* **2003,** *377,* 81. doi:10.1016/S0370-1573(02)00633-6
3. Tada, T.; Yoshizawa, K. *ChemPhysChem* **2002,** *3,* 1035. doi:10.1002/cphc.200290006
4. Chen, F.; Li, X.; Hihath, J.; Huang, Z.; Tao, N. *J. Am. Chem. Soc.* **2006,** *128,* 15874. doi:10.1021/ja065864k
5. Kiguchi, M.; Miura, S.; Hara, K.; Sawamura, M.; Murakoshi, K. *Appl. Phys. Lett.* **2007,** *91,* 053110. doi:10.1063/1.2757592
6. Wu, S.; González, M. T.; Huber, R.; Grunder, S.; Mayor, M.; Schönenberger, C.; Calame, M. *Nat. Nanotechnol.* **2008,** *3,* 569. doi:10.1038/nnano.2008.237
7. Schneebeli, S. T.; Kamenetska, M.; Cheng, Z.; Skouta, R.; Friesner, R. A.; Venkataraman, L.; Breslow, R. *J. Am. Chem. Soc.* **2011,** *133,* 2136. doi:10.1021/ja111320n
8. Kiguchi, M.; Takahashi, T.; Takahashi, Y.; Yamauchi, Y.; Murase, T.; Fujita, M.; Tada, T.; Watanabe, S. *Angew. Chem., Int. Ed.* **2011,** *50,* 5708. doi:10.1002/anie.201100431
9. Dahlke, R.; Schollwöck, U. *Phys. Rev. B* **2004,** *69,* 085324. doi:10.1103/PhysRevB.69.085324
10. Tawara, A.; Tada, T.; Watanabe, S. *Phys. Rev. B* **2009,** *80,* 073409. doi:10.1103/PhysRevB.80.073409
11. Venkataraman, L.; Klare, J. E.; Tam, I. W.; Nuckolls, C.; Hybertsen, M. S.; Steigerwald, M. L. *Nano Lett.* **2006,** *6,* 458. doi:10.1021/nl052373+
12. Dell'Angela, M.; Kladnik, G.; Cossaro, A.; Verdini, A.; Kamenetska, M.; Tamblyn, I.; Quek, S. Y.; Neaton, J. B.; Cvetko, D.; Morgante, A.; Venkataraman, L. *Nano Lett.* **2010,** *10,* 2470. doi:10.1021/nl100817h

License and Terms

Beilstein Journal of Nanotechnology

Current-induced dynamics in carbon atomic contacts

Jing-Tao Lü[*1], Tue Gunst[1], Per Hedegård[*2] and Mads Brandbyge[*1]

Full Research Paper

Open Access

Address:
[1]DTU-Nanotech, Dept. of Micro- and Nanotechnology, Technical University of Denmark (DTU), Ørsteds Plads, Bldg. 345E, DK-2800 Lyngby, Denmark and [2]Niels Bohr Institute, Nano-Science Center, University of Copenhagen, Denmark

Email:
Jing-Tao Lü[*] - jtlu@nanotech.dtu.dk;
Per Hedegård[*] - hedegard@fysik.ku.dk;
Mads Brandbyge[*] - mads.brandbyge@nanotech.dtu.dk

* Corresponding author

Keywords:
carbon-nanoelectronics; current-induced forces; molecular contacts; nanoscale Joule heating; semiclassical Langevin equation

Beilstein J. Nanotechnol. **2011,** *2,* 814–823.
doi:10.3762/bjnano.2.90

Received: 14 July 2011
Accepted: 25 November 2011
Published: 16 December 2011

This article is part of the Thematic Series "Transport through molecular junctions".

Guest Editor: J. M. van Ruitenbeek

Abstract

Background: The effect of electric current on the motion of atoms still poses many questions, and several mechanisms are at play. Recently there has been focus on the importance of the current-induced nonconservative forces (NC) and Berry-phase derived forces (BP) with respect to the stability of molecular-scale contacts. Systems based on molecules bridging electrically gated graphene electrodes may offer an interesting test-bed for these effects.

Results: We employ a semi-classical Langevin approach in combination with DFT calculations to study the current-induced vibrational dynamics of an atomic carbon chain connecting electrically gated graphene electrodes. This illustrates how the device stability can be predicted solely from the modes obtained from the Langevin equation, including the current-induced forces. We point out that the gate offers control of the current, independent of the bias voltage, which can be used to explore current-induced vibrational instabilities due the NC/BP forces. Furthermore, using tight-binding and the Brenner potential we illustrate how Langevin-type molecular-dynamics calculations including the Joule heating effect for the carbon-chain systems can be performed. Molecular dynamics including current-induced forces enables an energy redistribution mechanism among the modes, mediated by anharmonic interactions, which is found to be vital in the description of the electrical heating.

Conclusion: We have developed a semiclassical Langevin equation approach that can be used to explore current-induced dynamics and instabilities. We find instabilities at experimentally relevant bias and gate voltages for the carbon-chain system.

Introduction

The effects of electric current on the motion of atoms have become particular important in the on-going quest for molecular-scale electronics [1-4]. Atomic motion due to electric current is behind the long-term breakdown of interconnects leading to failure in integrated circuits. This effect is of even greater importance for systems where the bottle-neck for the current

flow is a few chemical bonds. The inelastic scattering of electrons by atomic vibrations leads to the well-known effect of Joule heating, which can have an impact on the electrical behavior and stability. However, recently it was pointed out [5-8] that other current-induced forces can play a role. For instance, in the case of molecular contacts with conductance on the order of $G_0 = 2e^2/h = 1/12.9$ kΩ (e being the electron charge and h Planck's constant), and under "high" bias voltage (~1 V), the current-induced forces that do not conserve the energy of the atomic motion may lead to run-away behavior. However, experiments in this regime are very challenging. For example, for the typical experiments involving molecular-scale contacts between bulk electrodes it is not possible to image the atomic structure while the contacts are in place and current is flowing. Furthermore, it is far from being trivial to add additional gate potentials in order to modify the electronic structure and gain independent control of the bias voltage and current [3,9].

On the theoretical side, it is desirable to develop computer simulation techniques, such as molecular dynamics (MD), preferably without adjustable parameters, to study in detail the complex current-driven atomic processes. To this end, we recently developed an approach based on the semiclassical Langevin equation, which may form the basis of MD. In this description the nonequilibrium electronic environment is described as an effective "bath" influencing the atomic dynamics. In particular, we identified the forces acting on the atoms due to the electric current. These include "extra" fluctuating forces yielding the Joule heating, a nonconservative "electron-wind" force (denoted NC), recently discussed by Todorov and co-workers [5], and a Lorentz-like force originating from the quantum-mechanical "Berry phase" of the electronic subsystem [6] (denoted BP). The purpose of this article is twofold. We will illustrate this semiclassical Langevin approach and show how the current-induced effects could be investigated in molecular contacts connecting gated graphene or nanotube electrodes.

Graphene is now being explored very extensively due to its outstanding electrical and thermal transport properties [10-12]. Besides being highly important in their own right, carbon nanotube- or graphene-based nanostructures may offer an interesting test bed for studies of current-induced effects at the atomic scale. For such systems, experiments with atomic resolution, employing for instance state-of-the-art electron microscopes, can be performed in the presence of current, allowing the dynamics to be followed down to single adatoms [13]. Electric current has been used to induce changes in graphene-edges, which were monitored while a current was simultaneously passed through the structure [14]. This was explained as carbon edge-dimers desorbing due to Joule-heating [15]. Taking this a step further, one can imagine that nanostructured nanotubes or graphene can be used as an electrode interface to molecular devices based on organic chemistry [16]. Especially promising aspects include the inherent 2-D geometry of graphene, which enables both straightforward electrical gating, and atomic-scale imaging in the presence of current. There have been a number of microscopy studies of single-atom carbon chains bridging graphene [13,17] or nanotubes [18]. On the theoretical side, various aspects of these systems have been studied, such as the formation of chains [19,20], their stability [21], and electron-transport properties [22-24]. Here we explore the current-induced forces and nanoscale Joule heating of the carbon chain system between electrically gated graphene electrodes.

The paper is organized as follows. After a brief outline of the semiclassical Langevin method, we will use it to study the dynamics of the carbon chain as a function of bias and gate voltages. We point out that the gate, which offers independent control of bias voltage and current in the system, can be used to explore current-induced vibrational instabilities in the current-carrying chain. Finally, we illustrate how the Langevin molecular dynamics can be performed for a carbon-chain system with the Joule heating effect included, by using tight-binding and the Brenner potential.

Results and Discussion

Semiclassical Langevin dynamics

We outline the Langevin approach here. For a classical oscillator system (mass-scaled coordinate x) in a general nonlinear force-field, F, coupled linearly to a *bath* of harmonic oscillators, it is possible to eliminate the bath variables and describe the system using the generalized Langevin equation, [25-27],

$$\ddot{x} = F(x) - \int_{t_0}^{t} \Pi^r(t,t')x(t')\mathrm{d}t' + \xi(t). \qquad (1)$$

Here the bath influences the motion through two distinct force contributions, (i) a retarded time-kernel, Π^r, describing the back-action at time t after propagation in the bath due to the motion of x at an earlier time, and (ii) a force ξ of statistical nature originating from the thermal fluctuations of the bath. In the case of thermodynamic equilibrium, ξ is characterized by a temperature and is related to Π^r by the fluctuation-dissipation theorem. Note that in general x, F, and ξ are vectors and Π^r is a matrix. This method was used by Wang and co-workers [28,29] to describe thermal transport in the quantum limit, with phonons in the two connecting reservoirs with different temperature acting as baths and with their quantum fluctuations included in ξ. This reproduced the Landauer result of thermal transport in the harmonic case [28].

It is possible to reach a semiclassical Langevin equation description of the motion of the ions coupled to the electron gas if we assume a linear coupling to the electronic environment: Either in the displacement from an equilibrium or in the velocity (adiabatic expansion) of the ions. This Langevin/Brownian motion approach to atomic scattering at metal surfaces has a rather long history in the case of metal electrons in thermal equilibrium [30,31].

We have extended this to describe the dynamics of the ions in a nanoconductor between metal electrodes in the nonequilibrium case, where an electric current is present [6,32]. In order to sketch the derivation, we consider a displacement-dependent tight-binding model with electron states in the scattering region of interest *k,l*, and with H_{el} being the static electronic Hamiltonian (scattering region and its coupling to the left and right electrodes [33]),

$$H = H_{ph}(x) + H_{el} + \sum_{k,l,n} \mathbf{M}_{n,kl} c_k^\dagger c_l \, x_n . \qquad (2)$$

Here x is a column vector comprising the mass-normalized displacement operators for each degree of freedom, e.g., $x_n = \sqrt{m_n} u_n$, u_n and m_n being the displacement operator and mass, and $H_{ph} = 1/2\,\dot{x}^{\mathrm{T}}\dot{x} + 1/2 x^{\mathrm{T}} K x$ corresponds to a set of harmonic oscillators that couple with the electrons, K being the dynamical matrix. We construct a localized basis-set describing the electrons in the scattering region, where $c_k^\dagger (c_k)$ is the electron creation (annihilation) operator at site k in this region [34]. Here we only consider the coupling to the electron bath, but the linear coupling to an external phonon bath can be taken into account along the same lines and adds a contribution to Π^r. The derivation and result for a linearly coupled harmonic phonon bath is similar, and was given in [28]. Alternatively, the dynamics of some external phonons, not coupling to the electrons directly, may be treated explicitly in actual MD calculations, as we illustrate below (regions *DL, DR* in Figure 6a). The electron–phonon coupling corresponds to matrix elements of the force operator $\mathbf{M}_{n,kl} = \langle k \,|\, \nabla_{x_n} H_{el} \,|\, l \rangle$. We assumed that **M** is small by keeping only the term that is linear in x.

We may obtain an equation of motion for x using Heisenberg's equation of motion, $\ddot{x} = i[\dot{x}, H]$, based on atomic units ($\hbar$ = 1) and implicit mode index (n),

$$\ddot{x} = -Kx - \sum_{kl} \mathbf{M}_{kl} c_k^\dagger c_l \equiv -Kx + f_e . \qquad (3)$$

The term f_e describes the "forces" due to the interaction with the electron gas. Importantly, these forces are random in nature [35]. We can calculate the mean value of f_e by averaging it over the nonequilibrium electronic state,

$$\langle f_e \rangle = i\mathrm{Tr}[\mathbf{M}\mathbf{G}^<(t,t)] = \mathrm{Tr}[(-\nabla_x H_{el})\rho(t)]. \qquad (4)$$

Here we introduce the electrical lesser-Green's function, $\mathbf{G}^<_{ij}(t,t) \equiv i\langle c_i^\dagger(t) c_j(t)\rangle$, which is equivalent to the density matrix, ρ (multiplied by $-i$), and depends on $x(t)$, since the electrons are coupled to x in the Hamiltonian. This is similar to the expression for the average force in Ehrenfest dynamics [5].

We can evaluate this perturbatively by using the unperturbed-electron lesser Green's function, $\mathbf{G}_0^<$, corresponding to the case of steady-state electron transport without electron–phonon interaction [33],

$$\mathbf{G}_0^<(\omega) = i\mathbf{A}_L(\omega) n_F(\omega - \mu_L) + i\mathbf{A}_R(\omega) n_F(\omega - \mu_R), \qquad (5)$$

where $\mathbf{A}_{L/R}$ are the density of state matrices for electronic states originating in the left/right electrodes, each with chemical potential $\mu_{L/R}$ [33], which differ for finite bias voltage, V, as $\mu_L - \mu_R = eV$, and $n_F(\omega) = 1/(e^{\omega/k_B T} + 1)$ is the Fermi-Dirac distribution function. We thus treat the nonequilibrium electron system as a reservoir unperturbed by the phonons. Using the nonequilibrium Greens function (NEGF) technique [36], we may write the 2nd lowest orders in **M** of $\langle f_e \rangle$ as,

$$\langle f_e(t) \rangle \approx \int \mathrm{d}\omega \mathrm{Tr}[(-\nabla_x H_{el})\rho_0] - \int_{t_0}^{t} \Pi^r(t,t') x(t') \mathrm{d}t'. \qquad (6)$$

The first term yields a constant force due to the change in electron bonding with bias and a "direct force" due to interaction of charges with the field [37]. Here $\rho_0 = \rho_{\mathrm{eq}} + \delta\rho$ is the nonequilibrium electron-density matrix *without* electron–phonon interaction. We split it into an equilibrium contribution ρ_{eq} and a nonequilibrium correction δρ. In linear response, we obtain a term $\mathcal{E} \cdot x$ from the field in H_{el}, $\mathcal{E}$ being the external field, which yields a "direct" force involving the equilibrium ρ_{eq}. We also obtain a term involving $H_{el}(\mathcal{E} = 0)$, together with the change in density to first order in the field $\Delta\rho \propto \mathcal{E}$, in the first term of Equation 6, resulting from the change of density in the chemical bonds due to the current [38,39].

The second contribution is the retarded back-action of the electron gas due to the motion and is equivalent to the retarded phonon self-energy. In the steady state, Π^r only depends on the time difference, and it is convenient to work in the frequency (energy) domain. This can be expressed by using the coupling-weighted electron–hole-pair density of states, $\Lambda^{\alpha\beta}$, inside or between electrodes $\alpha,\beta \in L,R$,

$$\Pi^r(t-t') = \int \Pi^r(\omega) e^{-i\omega t} \frac{\mathrm{d}\omega}{2\pi}, \tag{7}$$

$$\Pi^r(\omega) = \int \frac{\Lambda(\omega')}{\omega' - \omega - i\delta} \mathrm{d}\omega', \tag{8}$$

where Λ can be expressed in terms of the electrode DOS,

$$\Lambda \equiv \sum_{\alpha\beta} \Lambda^{\alpha\beta}, \tag{9}$$

$$\begin{aligned}\Lambda^{\alpha\beta}_{mn}(\omega) = \frac{1}{\pi}\int_{-\infty}^{\infty} \frac{\mathrm{d}\omega'}{2\pi} \mathrm{Tr}[\mathbf{M}_m \mathbf{A}_\alpha(\omega')\mathbf{M}_n \mathbf{A}_\beta(\omega'-\omega)] \\ \times\Big(n_F(\omega'-\mu_\alpha) - n_F(\omega'-\omega-\mu_\beta)\Big).\end{aligned} \tag{10}$$

We have included a factor of 2 from the spin degeneracy and have explicitly included the mode index, *m,n* on the coupling matrices, **M**, and on Λ in Equation 10.

The forces described by $\Pi^r_{mn}(\omega)$ in Equation 6 contain a number of interesting current-induced effects. It is instructive to split the kernel into parts,

$$\begin{aligned}\Pi^r_{mn}(\omega) = i\pi\mathrm{Re}(\Lambda_{mn}(\omega)) - \pi\mathrm{Im}(\Lambda_{mn}(\omega)) \\ +\pi\mathcal{H}\{\mathrm{Re}(\Lambda_{mn})\}(\omega) + i\pi\mathcal{H}\{\mathrm{Im}(\Lambda_{mn})\}(\omega),\end{aligned} \tag{11}$$

where

$$\mathcal{H}\{f(x')\}(x) = \frac{1}{\pi}\mathcal{P}\int \frac{g(x')}{x'-x}\mathrm{d}x'$$

is the Hilbert transform. The Λ matrix has the following symmetry properties when exchanging modes($n \leftrightarrow m$) and electrodes($\alpha \leftrightarrow \beta$),

$$\Lambda^{\alpha\beta}_{mn}(\omega) = \Lambda^{\alpha\beta *}_{nm}(\omega), \tag{12}$$

and

$$\Lambda^{\alpha\beta}_{mn}(\omega) = -\Lambda^{\beta\alpha}_{nm}(-\omega), \tag{13}$$

which are helpful when examining the terms in Equation 11, which are summarized in the following:

- **Friction** – The first term in Equation 11 is imaginary and symmetric in mode index *m,n*. It describes the friction force due to the generation of electron–hole pairs in the electronic environment by the ionic motion. This process exists even in equilibrium [31]. For slowly varying $\mathbf{A}_{L/R}$ with energy as compared to the vibrational energies (wide-band limit) we obtain the simple time-local electron friction force, $-\eta_{el}\dot{x}$, with

$$\begin{aligned}\eta_{el} &= -\frac{\pi\mathrm{Re}(\Lambda)}{\omega}|_{\omega\to 0} \\ &\approx \frac{1}{2\pi}\sum_{\alpha,\beta}\mathrm{Tr}[\mathbf{M}\mathbf{A}_\alpha(\mu_\alpha)\mathbf{M}\mathbf{A}_\beta(\mu_\beta)]\end{aligned} \tag{14}$$

- **NC (wind) force** – The second term in Equation 11 is real and antisymmetric, which means that the general curl of this force is not zero. It describes the NC force, discussed very recently by Dundas and co-workers [5]. This force is finite, even in the limit of zero frequency, where the friction and Joule heating effect is not important anymore.
- **Renormalization** – The third term is real and symmetric and can be interpreted as a renormalization of the dynamical matrix. It contains an equilibrium part and a nonequilibrium correction. The equilibrium part is already included in the dynamical matrix when we calculate it within the Born–Oppenheimer approximation. The nonequilibrium part gives a bias-induced modification of the harmonic potential.
- **BP force** – Finally, the last term is imaginary, antisymmetric, and proportional to ω for small frequencies. It can be identified as the "Berry phase" (BP) force in [6]. Since the direction of this force is always normal to the velocity in the abstract phase space, it does no work, resembling a Lorentz force with effective magnetic field

$$\boldsymbol{\mathcal{B}} = -\pi\frac{\mathcal{H}\{\mathrm{Im}(\Lambda(\omega'))\}(\omega)}{\omega}|_{\omega\to 0}. \tag{15}$$

- **Random forces** – The randomness of the force f_e is characterized by its correlation function in the frequency domain, which can again be calculated with NEGF. However, we note that since f_e is a quantum operator, $\langle f_e(t) f_e(0)\rangle$ does not result in a real number. Instead we use the symmetrized and real $\langle f_e(t) f_e^T(0) + (f_e(0) f_e^T(t))^T\rangle$. This expression equals the semiclassical result obtained from the path-integral derivation of the Langevin equation [6,35] and reads, in Fourier space,

$$\begin{aligned}\langle \xi_e \xi_e^T\rangle(\omega) &\equiv \langle f_e f_e^T\rangle(\omega) - \langle f_e\rangle\langle f_e\rangle^T(\omega) \\ &= -\pi\sum_{\alpha\beta}\coth\left(\frac{\omega-(\mu_\alpha-\mu_\beta)}{2k_BT}\right)\Lambda^{\alpha\beta}(\omega).\end{aligned} \tag{16}$$

- This spectral power density can be used to generate an instance of the Gaussian random noise as a function of time that is needed in MD simulations. Most importantly this random force contains not only the thermal excitations but also the excess excitations leading to Joule heating [32], through the dependence of the chemical potentials $\mu_L - \mu_R = eV$. Thus with this formalism it is possible to disentangle the various contributions to the forces, being either deterministic or random in nature.

Current-induced vibrational instability

We now turn to illustrations of the use of the semiclassical Langevin equation to describe current-induced effects. In this section we employ it to study the effect of the current-induced forces and Joule heating on the stability of the system, within the harmonic approximation. We will here ignore the coupling to electrode phonons. This makes an eigen-mode analysis possible, which eases the interpretation of the results. The model system we use is shown in Figure 1, in which a four-atom carbon chain is bridged between two graphene electrodes (L and R). We assume a field effect transistor setup, in which a gate potential, V_g, is applied to the system in addition to the bias applied between the two electrodes, V_b. We will show that this offers a convenient way to explore current-induced vibrational instabilities. We can already see the effect of the gate potential in the current–voltage ($I - V_b$) characteristics shown in Figure 2.

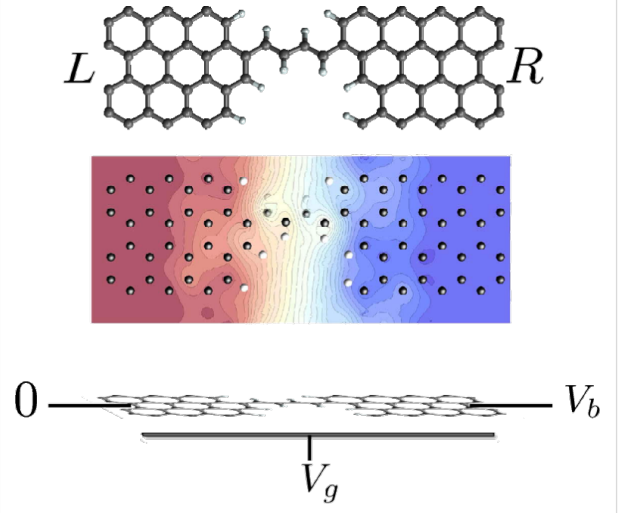

Figure 1: The system considered in the present study is a four-atom carbon chain bridging two graphene electrodes. The dangling bonds are passivated by hydrogen atoms. In addition to the bias applied between the left (L) and right (R) electrodes (V_b), a gate potential (V_g) can also be applied perpendicular to the graphene surface. The center panel shows the calculated contour plot of the electrostatic-potential drop across the junction at V_g = 0 V, and V_b = 1 V. The equal drop at the left and right electrodes reflects the electron–hole symmetry for V_g = 0 V [40].

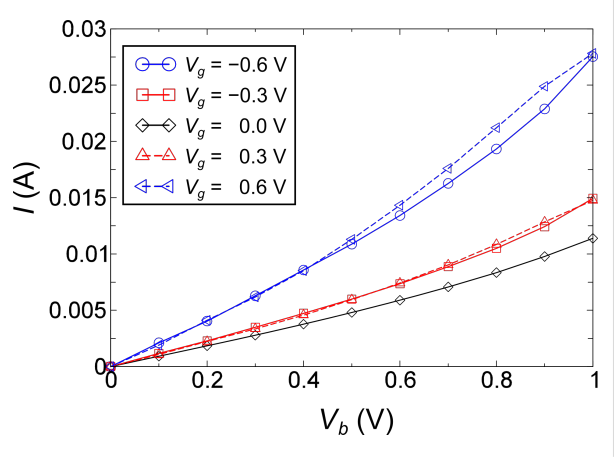

Figure 2: Current–Voltage (I–V_b) curves at different V_g.

The effect of the NC and BP forces is to couple different phonon modes with nearly similar frequencies. From now on, we will focus on the two phonon modes around 200 meV, shown in Figure 3, since the alternating-bond-length-type modes (200 meV) couple most strongly with the electric current. This type of mode also gives rise to the most intensive Raman signals in unpassivated chains between graphene-like pieces [41].

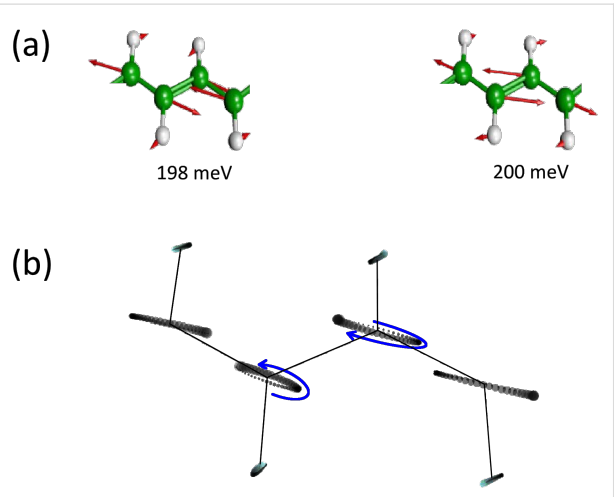

Figure 3: (a) Motion of the two phonon modes around 200 meV. (b) Motion of the runaway mode at V_g = 0.6 V, and V_b = 1 V. We depict the motion using a number of discrete time steps roughly corresponding to a full period. The position of each atom is depicted as a circle for a sequence of time steps indicated by an increasing radius with time. The motion is a phase-shifted linear combination of the two modes in (a). We can see the elliptical motion of the carbon atoms from the plot. The enclosed area indicates that work can be done by the current-induced NC force.

The calculation was performed by using the SIESTA density-functional theory (DFT) method [42], which has been extended to study elastic [33] and inelastic [34] transport in molecular

conductors. We used similar parameters as detailed in [34], and in order to keep the calculation simple and tractable, we modeled the electrodes by simply employing the Γ k-point in the transverse electrode direction. The electron–phonon coupling matrix (**M**) was calculated at zero bias, whereas we calculated the electronic structure at finite bias. We note that the voltage dependence of the coupling matrix could play a role, but this is beyond the scope of the present more illustrative purpose [43]. Based on these approximations, we can calculate the full ω-dependent Λ function, and the self-energies, Π^r. To perform the eigen-mode analysis, we further assumed linear ω-dependent friction, Berry force (BP), constant nonconservative force (NC), and ignore the renormalization of the dynamical matrix.

We model the effect of V_b as a shift of the equilibrium chemical potential, E_F. In this way we can tune the electronic structure within the bias window by changing the gate potential. In the following, we look at the bias and gate dependence of the inverse Q-factor ($1/Q$) and effective phonon number N. The inverse Q-factor for mode i (note we use index i for full modes including the current-induced forces) is defined as

$$1/Q_i \equiv -2\frac{\mathrm{Im}\{\omega_i\}}{\mathrm{Re}\{\omega_i\}}, \tag{17}$$

where ω_i are the eigenvalues of the full dynamical matrix, including the current-induced forces. These modes thus consist of linear combinations of the "unperturbed" normal modes of the system, n,m, as calculated by using the standard Born–Oppenheimer approximation. The phonon number can be calculated from the displacement correlation function,

$$N_i + \frac{1}{2} \approx \mathrm{Re}\{\omega_i\}\int \langle x_i x_i\rangle(\omega)\frac{\mathrm{d}\omega}{2\pi}. \tag{18}$$

We show the bias and gate potential dependence of the inverse Q-factor and phonon number in Figure 4 and Figure 5. The coupling of these two modes due to the bias (gate) dependent NC and BP force changes their lifetime. The two modes always have opposite dependence. The vibrational instability occurs at the critical point where $1/Q = 0$ around $V_g = \pm 0.4$ V. This corresponds to an infinite phonon number in Figure 5, and we there-

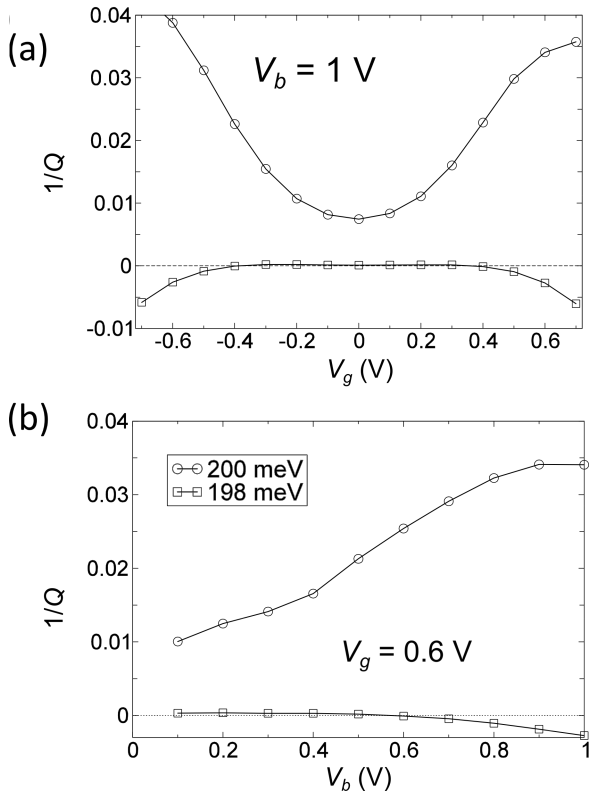

Figure 4: (a) Inverse Q-factor ($1/Q$) as a function of gate voltage, V_g, at V_b = 1 V for the two modes around 200 meV. (b) $1/Q$ as a function of bias voltage, V_b, at fixed gate voltage V_g = 0.6 V, for the same pair of phonon modes.

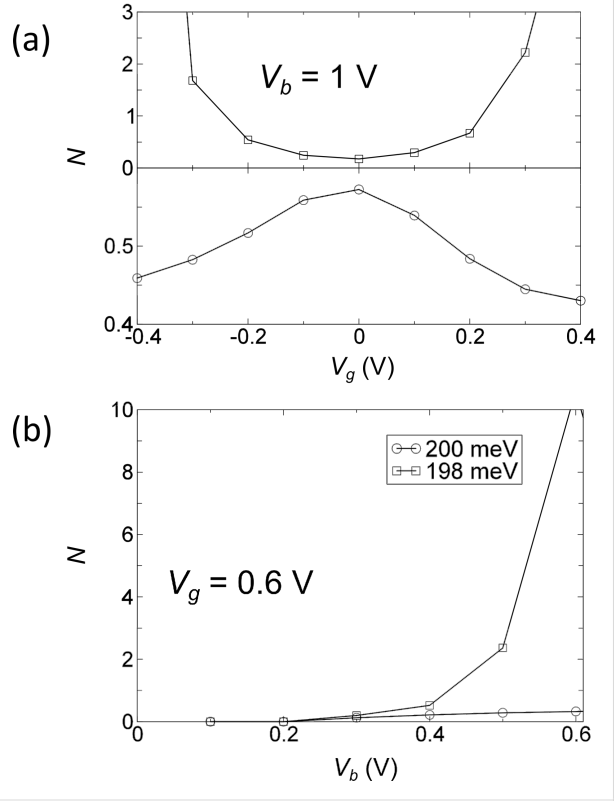

Figure 5: (a) Effective phonon number (N) for the two phonon modes around 200 meV as a function of gate voltage, V_g, at fixed bias voltage, V_b = 1 V. (b) N as a function of bias voltage, V_b, at fixed gate voltage V_g = 0.6 V. Note that it diverges at the critical point when the damping ($1/Q$) in Figure 4 goes to zero.

fore call it a "runaway" mode. The motion of this mode at $V_b = 1$ V, $V_g = 0.6$ V is plotted in Figure 3b. We can observe the elliptical motion of several atoms in real-space. This is critical because in order for the nonconservative force to do work on the atoms their motion has to enclose a finite area, either in real or in abstract phase space.

Finally, we should mention that when the current hits the instability threshold it will drive the system into a highly anharmonic regime, where the preceding eigenanalysis breaks down. One scenario is that the motion of the system will reach a limit-cycle determined by the detailed anharmonic potential and the interaction with the current [7]. In this regime the details of the damping due to the coupling with phonons in the electrodes could be important, and the electron–phonon coupling could also change from the value given around the harmonic equilibrium position. In order to address this regime we can perform molecular-dynamics simulations, taking into account both the coupling between different modes and their coupling with the electrode phonons, in order to study how the system actually reacts due to the instability.

Molecular dynamics with Joule heating

Next we illustrate the use of the Langevin equation to perform molecular-dynamics simulations of a carbon-chain system, in the presence of current flow, in the simplest possible setting, but now including coupling to the electrode phonons. Therefore we abandon the DFT approach, and instead employ the widely used π-tight-binding model with hopping parameter β = 2.7 eV, and the Brenner potential for calculations of the interatomic forces [44]. We consider the unpassivated structure in Figure 6. The electron–phonon coupling is modeled by the Harrison scaling law [45], $\beta = 2.7\text{eV}\ (a_0/d)^2$, determining how β is modified when the nearest neighbor distance, d, is changed from the equilibrium value, $a_0 = 1.4$ Å. The same model has recently been applied in the study of the effect of strain on the electronic structure of graphene [46]. In the simulation we model the coupling to the electrode phonons by a friction parameter, η_{ph}, and a corresponding white equilibrium phonon noise $\langle \xi_{ph} \xi_{ph}^T \rangle = 2\eta_{ph} k_B T$ on the L,R-electrode regions. This is similar to the stochastic boundary conditions [27] in which L,R-atoms act as a boundary. The setup for the MD is shown in (Figure 6a). We include electrode regions that have no interaction with the current (DL,DR), and a device region (D) where the current density is highest and where the nonconservative forces and Joule heating are included.

Furthermore, instead of using the full nonlocal time-kernel for the electrons in Equation 14, we use the wide-band approximation, and neglect the off-diagonal elements of the electron-noise spectral power density, $\langle \xi_e \xi_e^T \rangle(\omega)$. The diagonal of the electron spectral power can be approximated by white noise in the high-bias and wide-band limits, where variations in the electronic DOS are neglected [47]. The assumption of a white-noise spectrum implies neglect of the equilibrium zero-point motion of the atoms, but most importantly here, it includes the Joule heating effects,

$$\langle (\xi_e)_n (\xi_e)_n^T \rangle(\omega) = 2(\eta_{el})_{nn} k_B T + \mathrm{Re}\Big(\mathrm{Tr}\big[\mathbf{A}_L(\mu_L)\mathbf{M}_n \mathbf{A}_R(\mu_R)\mathbf{M}_n\big]\Big)\frac{|eV_b|}{2\pi}. \quad (19)$$

A factor of 2 should be included in the case of spin degeneracy. Based on the velocity Verlet algorithm [48] we carried out MD simulations at a varying bias voltage for zero gate bias ($V_g = 0$ V), and phonon friction, η_{ph}. The MD results are summarized in Figure 6b–f. We note that for the present system setup the nonconservative force is found not to play a dominant role compared to the effect of Joule heating. The main insight we gain from the MD example here is that the anharmonic couplings are important and effective in redistributing the energy supplied by the nonequilibrium electrons.

The approximate local phonon friction, η_{ph}, can in general be expressed from the slope of the corresponding phonon self-energy at zero frequency, as for electrons, see Equation 14. However, here we simply varied its value around this in order to quantify the dependence of the local electrical heating in the device region on this parameter (Figure 6b). The electrical heating of the chain was found not to depend much on the phonon friction when this was chosen to be sufficiently high. This is an appealing result, since it indicates that the electrical heating does not depend critically on the measurement setup, but mainly on the nature of the actual constriction. This seems to be true as long as the heat flow away from the contacts is sufficient to maintain the temperature of the heat baths, and the chain acts as a bottleneck for the heat conduction. However, we note that for heat conduction in the quantum limit it is important to go beyond the white band approximation and include realistic self-energies for the L,R-electrode phonons [49]. This will be explored in future work.

Inspired by the equipartition theorem, we define a local temperature variable for the atoms (indexed by a) with mass, m_a,

$$T_a(t) \equiv \frac{m_a}{3k_B}\langle \vec{v}_a^{\,2}(t) \rangle. \quad (20)$$

A comparison of the obtained temperature distributions with (Figure 6c, Figure 6d) and without (Figure 6e, Figure 6f) the anharmonic interactions shows that anharmonic couplings

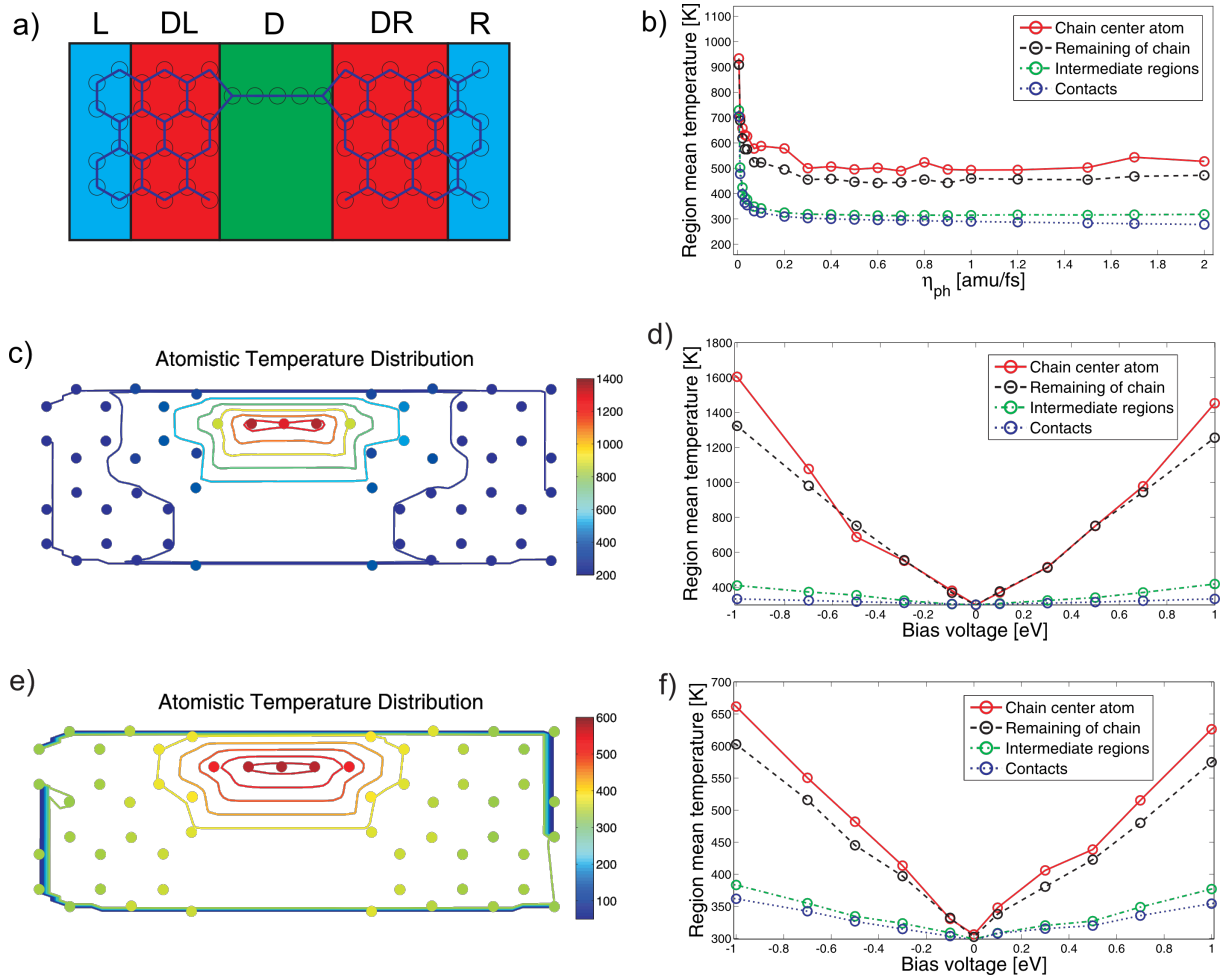

Figure 6: (a) Definition of the system regions with different types of noise contributions. Leads (*L*,*R*) have a well-defined temperature determined by the phonon noise, the device (*D*) temperature is defined from the electrical heating, and the intermediate regions (*DL*,*DR*) are free and are heated by propagation noise. In the MD setup no atoms are held fixed, but periodic boundary conditions are applied. The figure describes the setup in which the local temperatures plotted in (c) and (e) should be understood. (b) Temperature of the regions as a function of phonon friction. (c, d) Obtained temperatures at different atoms within the harmonic approximation. (c) The simulations were run at T = 300 K and at eV_b = 1 eV, and (d) varying bias voltages. (e, f) Corresponding atomistic temperature distributions including the anharmonic interactions. The lead temperature can exceed the equilibrium bath temperature due to propagation noise. In particular, the anharmonic interactions redistribute part of the energy from the modes in the chain to the bulk modes in the lead.

between the vibrational modes have a significant influence on the heat-transport properties and local Joule heating of the system. The heating is less localized in the chain due to anharmonicity. This originates from the coupling between different modes and an increased coupling to the surroundings for configurations in which the atoms are displaced from their equilibrium positions. Modes localized in the chain can be heated up to very high temperatures in the harmonic approximation. When anharmonic interactions are included the energy is redistributed and the modes are collectively heated up.

The electron–phonon interaction is typically included through a Taylor expansion of the electronic Hamiltonian around the equilibrium positions (Equation 2). Within the time-local white-noise approximation it is possible to address the effect of changes of electronic Hamiltonian and, especially, electron-phonon coupling on the motion, which was both included in the nonequilibrium force calculations here. This amounts to updating the nonconservative force, friction and noise on the fly along the path. This is possible for the simple parametrization used here. Our preliminary results based on this approximation show that the extra noise contribution from the higher-order couplings may significantly influence the results and increase the electronic heating compared to the static electronic structure approximation. A method which goes beyond white noise and includes the change in electron–phonon coupling when the system is far from the equilibrium positions, e.g., close to bond breaking, remains a challenge for the future.

Conclusion

We have developed a semiclassical Langevin equation approach, which can be used to explore current-induced atomic dynamics and instabilities in molecular conductors. The Langevin approach can be solved in the harmonic approximation to obtain eigenmodes and their excitation in the presence of current, as well as used for molecular-dynamics simulations based on the full anharmonic potential. Our simple, approximate MD simulation indicates that anharmonic couplings play an important role for the energy redistribution and effective heat dissipation to the electrode reservoirs. However, the MD is computationally very demanding beyond simplified model electronic structures and interatomic potentials, and further developments are necessary. We have used carbon-chain systems both to illustrate the Langevin approach, and in order to highlight how graphene might offer a unique test bed for research into current-induced dynamic effects. Especially, it is straightforward to employ a gate potential to the gate electrode, and thereby obtain independent control of current and bias voltage in the system. Furthermore, atomic-scale resolution can be obtained in electron microscopes in the presence of current, and Raman spectroscopy can give insights into the excitation and effective temperature originating from the electric current [50-52]. Our results for the simplified carbon-chain systems indicate that it may be possible to tune the current-induced instabilities in the atomic dynamics with gate and bias voltages in the experimentally relevant range.

Acknowledgements

We acknowledge the Lundbeck Foundation for financial support (R49-A5454), and the Danish Center for Scientific Computing (DCSC) for providing computer resources.

References

1. Tao, N. J. *Nat. Nanotechnol.* **2006,** *1,* 173–181. doi:10.1038/nnano.2006.130
2. Moth-Poulsen, K.; Bjørnholm, T. *Nat. Nanotechnol.* **2009,** *4,* 551–556. doi:10.1038/nnano.2009.176
3. Song, H.; Kim, Y.; Jang, Y. H.; Jeong, H.; Reed, M. A.; Lee, T. *Nature* **2009,** *462,* 1039–1043. doi:10.1038/nature08639
4. Seideman, T., Ed. *Curren-driven phenomena in nanoelectronics;* Pan Stanford Publishing: Singapore, 2011.
5. Dundas, D.; McEniry, E. J.; Todorov, T. N. *Nat. Nanotechnol.* **2009,** *4,* 99–102. doi:10.1038/nnano.2008.411
6. Lü, J. T.; Brandbyge, M.; Hedegård, P. *Nano Lett.* **2010,** *10,* 1657–1663. doi:10.1021/nl904233u
7. Bode, N.; Kusminskiy, S. V.; Egger, R.; von Oppen, F. *Phys. Rev. Lett.* **2011,** *107,* 036804. doi:10.1103/PhysRevLett.107.036804
8. Lü, J. T.; Hedegård, P.; Brandbyge, M. *Phys. Rev. Lett.* **2011,** *107,* 046801. doi:10.1103/PhysRevLett.107.046801
9. Kubatkin, S.; Danilov, A.; Hjort, M.; Cornil, J.; Brédas, J.; Stuhr-Hansen, N.; Hedegård, P.; Bjørnholm, T. *Nature* **2003,** *425,* 698–701. doi:10.1038/nature02010
10. Geim, A. K.; Novoselov, K. S. *Nat. Mater.* **2007,** *6,* 183–191. doi:10.1038/nmat1849
11. Castro Neto, A. H.; Guinea, F.; Peres, N. M. R.; Novoselov, K. S.; Geim, A. K. *Rev. Mod. Phys.* **2009,** *81,* 109–162. doi:10.1103/RevModPhys.81.109
12. Geim, A. K. *Science* **2009,** *324,* 1530–1534.
13. Meyer, J. C.; Girit, C. O.; Crommie, M. F.; Zettl, A. *Nature* **2008,** *454,* 319–322. doi:10.1038/nature07094
14. Jia, X.; Hofmann, M.; Meunier, V.; Sumpter, B. G.; Campos-Delgado, J.; Romo-Herrera, J. M.; Son, H.; Hsieh, Y.-P.; Reina, A.; Kong, J.; Terrones, M.; Dresselhaus, M. S. *Science* **2009,** *323,* 1701–1705. doi:10.1126/science.1166862
15. Engelund, M.; Fürst, J. A.; Jauho, A. P.; Brandbyge, M. *Phys. Rev. Lett.* **2010,** *104,* 036807. doi:10.1103/PhysRevLett.104.036807
16. Guo, X.; Gorodetsky, A. A.; Hone, J.; Barton, J. K.; Nuckolls, C. *Nat. Nanotechnol.* **2008,** *3,* 163–167. doi:10.1038/nnano.2008.4
17. Jin, C.; Lan, H.; Peng, L.; Suenaga, K.; Iijima, S. *Phys. Rev. Lett.* **2009,** *102,* 205501. doi:10.1103/PhysRevLett.102.205501
18. Börrnert, F.; Börrnert, C.; Gorantla, S.; Liu, X.; Bachmatiuk, A.; Joswig, J.-O.; Wagner, F. R.; Schäffel, F.; Warner, J. H.; Schönfelder, R.; Rellinghaus, B.; Gemming, T.; Thomas, J.; Knupfer, M.; Büchner, B.; Rümmeli, M. H. *Phys. Rev. B* **2010,** *81,* 085439. doi:10.1103/PhysRevB.81.085439
19. Hobi, E., Jr..; Pontes, R. B.; Fazzio, A.; da Silva, A. J. R. *Phys. Rev. B* **2010,** *81,* 201406. doi:10.1103/PhysRevB.81.201406
20. Erdogan, E.; Popov, I.; Rocha, C. G.; Cuniberti, G.; Roche, S.; Seifert, G. *Phys. Rev. B* **2011,** *83,* 041401. doi:10.1103/PhysRevB.83.041401
21. Lin, Z. Z.; Yu, W. F.; Wang, Y.; Ning, X. J. *EPL* **2011,** *94,* 40002. doi:10.1209/0295-5075/94/40002
22. Chen, W.; Andreev, A. V.; Bertsch, G. F. *Phys. Rev. B* **2009,** *80,* 085410. doi:10.1103/PhysRevB.80.085410
23. Fürst, J. A.; Brandbyge, M.; Jauho, A.-P. *EPL* **2010,** *91,* 37002. doi:10.1209/0295-5075/91/37002
24. Akdim, B.; Pachter, R. *ACS NANO* **2011,** *5,* 1769–1774. doi:10.1021/nn102403j
25. Adelman, S.; Doll, J. *J. Chem. Phys.* **1976,** *64,* 2375–2388. doi:10.1063/1.432526
26. Kantorovich, L. *Phys. Rev. B* **2008,** *78,* 094304. doi:10.1103/PhysRevB.78.094304
27. Kantorovich, L.; Rompotis, N. *Phys. Rev. B* **2008,** *78,* 094305. doi:10.1103/PhysRevB.78.094305
28. Wang, J.-S. *Phys. Rev. Lett.* **2007,** *99,* 160601. doi:10.1103/PhysRevLett.99.160601
29. Lü, J. T.; Wang, J.-S. *Phys. Rev. B* **2008,** *78,* 235436. doi:10.1103/PhysRevB.78.235436
30. Nourtier, A. *J. Phys. (Paris)* **1977,** *38,* 479–502. doi:10.1051/jphys:01977003805047900
31. Head-Gordon, M.; Tully, J. C. *J. Chem. Phys.* **1995,** *103,* 10137. doi:10.1063/1.469915
32. Brandbyge, M.; Hedegård, P. *Phys. Rev. Lett.* **1994,** *72,* 2919–2922. doi:10.1103/PhysRevLett.72.2919
33. Brandbyge, M.; Mozos, J. L.; Ordejón, P.; Taylor, J.; Stokbro, K. *Phys. Rev. B* **2002,** *65,* 165401. doi:10.1103/PhysRevB.65.165401
34. Frederiksen, T.; Paulsson, M.; Brandbyge, M.; Jauho, A.-P. *Phys. Rev. B* **2007,** *75,* 205413. doi:10.1103/PhysRevB.75.205413
35. Schmid, A. *J. Low Temp. Phys.* **1982,** *49,* 609–626. doi:10.1007/BF00681904

36. Haug, H.; Jauho, A.-P. *Quantum Kinetics in Transport and Optics of Semiconductors,* 2nd ed.; Springer Series in Solid State Sciences, Vol. 123; Springer: Berlin, Heidelberg, 2008.
37. Bevan, K. H.; Guo, H.; Williams, E. D.; Zhang, Z. *Phys. Rev. B* **2010,** *81,* 235416. doi:10.1103/PhysRevB.81.235416
38. Brandbyge, M.; Stokbro, K.; Taylor, J.; Mozos, J. L.; Ordejón, P. *Phys. Rev. B* **2003,** *67,* 193104. doi:10.1103/PhysRevB.67.193104
39. Brandbyge, M. *Nat. Nanotechnol.* **2009,** *4,* 81–82. doi:10.1038/nnano.2008.413
40. Brandbyge, M.; Kobayashi, N.; Tsukada, M. *Phys. Rev. B* **1999,** *60,* 17064–17070. doi:10.1103/PhysRevB.60.17064
41. Rivelino, R.; dos Santos, R. B.; de Brito Mota, F.; Gueorguiev, G. K. *J. Phys. Chem. C* **2010,** *114,* 16367–16372. doi:10.1021/jp1066154
42. Soler, J. M.; Artacho, E.; Gale, J. D.; Garcia, A.; Junquera, J.; Ordejón, P.; Sánchez-Portal, D. *J. Phys.: Condens. Matter* **2002,** *14,* 2745–2779. doi:10.1088/0953-8984/14/11/302
43. Sergueev, N.; Roubtsov, D.; Guo, H. *Phys. Rev. Lett.* **2005,** *95,* 146803. doi:10.1103/PhysRevLett.95.146803
44. Brenner, D. W. *Phys. Rev. B* **1990,** *42,* 9458–9471. doi:10.1103/PhysRevB.42.9458
45. Harrison, W. A. *Electronic Structure, the Properties of Solids: The Physics of the Chemical Bond;* Dover Publications: New York, 1989.
46. Guinea, F.; Katsnelson, M. I.; Geim, A. K. *Nat. Phys.* **2010,** *6,* 30–33. doi:10.1038/nphys1420
47. Gunst, T. Molecular Dynamics of nano-conductors in the presence of electronic current. M.Sc. Thesis, Technical University of Denmark, DTU Nanotech, Denmark, 2010.
48. Allen, M. P. Introduction to Molecular Dynamics Simulation. In *Computational Soft Matter: From Synthetic Polymers to Proteins;* Attig, N.; Binder, K.; Grubmüller, H.; Kremer, K., Eds.; NIC Series, Vol. 23; Gustav-Stresemann-Institut: Bonn, Germany, 2004; pp 1–28.
49. Wang, J.-S.; Ni, X.; Jiang, J.-W. *Phys. Rev. B* **2009,** *80,* 224302. doi:10.1103/PhysRevB.80.224302
50. Ioffe, Z.; Shamai, T.; Ophir, A.; Noy, G.; Yutsis, I.; Kfir, K.; Cheshnovsky, O.; Selzer, Y. *Nat. Nanotechnol.* **2008,** *3,* 727–732. doi:10.1038/nnano.2008.304
51. Ward, D. R.; Halas, N. J.; Ciszek, J. W.; Tour, J. M.; Wu, Y.; Nordlander, P.; Natelson, D. *Nano Lett.* **2008,** *8,* 919–924. doi:10.1021/nl073346h
52. Chae, D.-H.; Krauss, B.; von Klitzing, K.; Smev, J. H. *Nano Lett.* **2010,** *10,* 466–471. doi:10.1021/nl903167f

License and Terms

The definitive version of this article is the electronic one which can be found at:
doi:10.3762/bjnano.2.90

Beilstein Journal of Nanotechnology

When “small” terms matter: Coupled interference features in the transport properties of cross-conjugated molecules

Gemma C. Solomon*[1], Justin P. Bergfield[1], Charles A. Stafford[2] and Mark A. Ratner[3]

Full Research Paper

Open Access

Address:
[1]Nano-Science Center and Department of Chemistry, University of Copenhagen, Universitetsparken 5, 2100 Copenhagen Ø, Denmark, [2]Department of Physics, University of Arizona, 1118 East Fourth Street, Tucson, AZ 85721, USA and [3]Department of Chemistry, Northwestern University, 2145 Sheridan Rd, Evanston, IL 60208, USA

Email:
Gemma C. Solomon* - gsolomon@nano.ku.dk

* Corresponding author

Keywords:
gDFTB; Hückel model; many-body effects; molecular electronics; quantum interference; thermoelectrics; topology

Beilstein J. Nanotechnol. **2011,** *2,* 862–871.
doi:10.3762/bjnano.2.95

Received: 20 September 2011
Accepted: 25 November 2011
Published: 29 December 2011

This article is part of the Thematic Series "Transport through molecular junctions".

Guest Editor: J. M. van Ruitenbeek

Abstract

Quantum interference effects offer opportunities to tune the electronic and thermoelectric response of a quantum-scale device over orders of magnitude. Here we focus on single-molecule devices, in which interference features may be strongly affected by both chemical and electronic modifications to the system. Although not always desirable, such a susceptibility offers insight into the importance of “small” terms, such as through-space coupling and many-body charge–charge correlations. Here we investigate the effect of these small terms using different Hamiltonian models with Hückel, gDFTB and many-body theory to calculate the transport through several single-molecule junctions, finding that terms that are generally thought to only slightly perturb the transport instead produce significant qualitative changes in the transport properties. In particular, we show that coupling of multiple interference features in cross-conjugated molecules by through-space coupling will lead to splitting of the features, as can correlation effects. The degeneracy of multiple interference features in cross-conjugated molecules appears to be significantly more sensitive to perturbations than those observed in equivalent cyclic systems and this needs to be considered if such supernodes are required for molecular thermoelectric devices.

Introduction

Destructive interference effects, such as nodes in the transmission function, are a signature of coherence and offer a possible avenue for tuning the transport properties of single-molecule junctions. While not present in all systems, destructive interference features are observed in many common systems. For example, in the *meta*-substituted Au–benzenedithiol–Au junction the π-electron transmission exhibits a node in the middle of the gap between the highest occupied molecular orbital and lowest unoccupied molecular orbital [1-13], although the total conductance is nonzero, as underlying σ-system transport dominates in the vicinity of the node [8,9]. Through careful design, interference effects can be perturbed by chemical modification or an external electric field [6,14], presenting myriad strategies to control the flow of charge through a molecular circuit. Thermoelectric effects are also strongly influenced by the presence of interference features, and enhancement is predicted in the vicinity of nodes and peaks [15,16]. In certain molecules composed of node-possessing subunits, multiple degenerate interference features may combine to form higher-order nodes (supernodes) and peaks whose thermoelectric enhancement scales as the order of the feature [16]. Supernode-possessing molecules also suppress current over a wide range of energy, suggesting that they may be an important step towards realizing useful molecular devices.

Previous work on supernodes focused on cyclic systems [16], but the transport properties of both cyclic [17,18] and acyclic [19,20] cross-conjugated molecules have also been predicted to exhibit interference features in experimentally relevant energy ranges. Here we investigate the transport through several acyclic cross-conjugated molecules and show that maintaining degenerate interference features in these systems may be challenging. As a basis for comparison, we use Hückel theory transport calculations to understand what can be expected from the topology alone. Using gDFTB and many-body calculations, we find that the order of the interference feature in acyclic systems can be strongly dependent upon through-space terms and electron correlations.

Methods

Transport in a single-molecule junction is often described by using Green's function approaches, where the elastic transmission is generally calculated as [21]

$$T(E) = \mathrm{Tr}[\Gamma^{\mathrm{L}} G^{r}(E) \Gamma^{\mathrm{R}} G^{a}(E)] \ . \qquad (1)$$

$G^r(E)$ is the retarded Green's function of the junction at energy E, $G^a(E)$ is its conjugate transpose, and Γ^{L} and Γ^{R} are the broadening matrices describing the coupling to the left and right electrodes, respectively. In each of the three theoretical methods discussed below, the differences in the methods manifest themselves as differences in the Green's functions. The gDFTB and molecular Dyson equation (MDE) many-body methods used in this article are explained in detail in [22] and [23], respectively. Here we simply provide a brief overview of the aspects most relevant to transport in the cross-conjugated systems investigated here.

Hückel model calculations

A simple multisite model Hamiltonian can be constructed by representing each relevant atomic orbital of the molecule by an energy α. Between chemically bonded nearest-neighbor sites there are coupling elements, β_S and β_D, depending on whether sites have single or double bonds between them. For example, in Figure 1, a four-site system is shown.

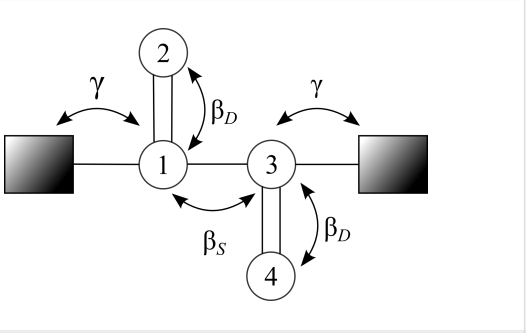

Figure 1: An example of a Hückel model for a four-site molecule, the numbering of the sites corresponds to the index in the Hamiltonian.

The Hamiltonian for this system is given by:

$$H_{\mathrm{mol}} = \begin{pmatrix} \alpha & \beta_D & \beta_S & 0 \\ \beta_D & \alpha & 0 & 0 \\ \beta_S & 0 & \alpha & \beta_D \\ 0 & 0 & \beta_D & \alpha \end{pmatrix} . \qquad (2)$$

In all calculations shown here we set $\alpha = 0$ eV, $\beta_S = -3$ eV, and $\beta_D = -4$ eV. We assume that only a single site couples to each electrode, with coupling strength $\gamma = \beta_S/3 = -1$ eV. For this system we have:

$$V_{\mathrm{L}} = \begin{pmatrix} \gamma & 0 & 0 & 0 \end{pmatrix} \text{ and } V_{\mathrm{R}} = \begin{pmatrix} 0 & 0 & \gamma & 0 \end{pmatrix} . \qquad (3)$$

The transmission is then calculated by using the nonequilibrium Green's function formalism assuming the wide-band limit for the density of states of the electrodes and setting

$$\Gamma^{\mathrm{L(R)}} = 2\pi\rho V_{\mathrm{L(R)}} V_{\mathrm{L(R)}}^{\dagger} \ , \tag{4}$$

where ρ is the density of states of the electrode, which we set to $1/2\pi$ $(eV)^{-1}$. This value is chosen to approximately reproduce the broadening seen in gDFTB calculations [9]. The purely imaginary tunneling self-energies are given by

$$\Sigma_{\mathrm{T}}^{\mathrm{L(R)}} = -\frac{i}{2}\Gamma^{\mathrm{L(R)}} \tag{5}$$

and the retarded Green's function by

$$G^{r}(E) = \left(E - H_{\mathrm{mol}} - \Sigma_{\mathrm{T}}^{\mathrm{L}} - \Sigma_{\mathrm{T}}^{\mathrm{R}}\right)^{-1} \ . \tag{6}$$

gDFTB

The Hückel model calculations allow us to model the transmission through the carbon skeleton of a conjugated molecule, i.e., the component that we anticipate will dominate the transport properties in systems exhibiting destructive interference effects. Moving to atomistic simulations, it is necessary to add binding groups (here we use thiols) to bind the organic component to gold electrodes. The systems that we compare have the same underlying carbon skeleton but differ in the fact that the sulfur binding groups appear explicitly, rather than being effectively absorbed as part of the electrodes in the Hückel calculations.

The gDFTB method [22,24,25] allows us to calculate the transport with an atomistic model of the system, going beyond simple topology to include the through-space interactions that arise from the three-dimensional nature of chemical structures. Molecular geometries were obtained by optimizing the isolated molecule using Q-Chem 3.0 [26] with density functional theory employing the B3LYP functional and 6-311G** basis. The molecules were then chemisorbed (terminal hydrogens removed) to the FCC hollow binding site of a Au(111) surface with the Au–S bond length of 2.48 Å, taken from the literature [27].

Transport calculations by means of gDFTB construct the Green's functions in the same way as the Hückel model calculations, that is simply by using the gDFTB Hamiltonian in place of the Hückel Hamiltonian. A wide-band approximation is also employed in which the density of states used to construct the self-energies is set to a value for bulk gold (1.9 eV^{-1}). No gold atoms were included in the extended molecule so that the symmetry of the molecule could be used to separate the transmission into σ- and π-components [28]. The electrode comprised a 6 × 8 atom unit cell with three layers in the transport direction, and periodic boundary conditions were used.

Many-body calculations

The many-body problem of transport through a molecular junction is generally intractable and must be solved approximately. Often this is done perturbatively by using, for example, diagrammatic methods. Phrasing the perturbative series in terms of Green's functions is advantageous since Dyson's equation allows a finite number of physical processes to be calculated to infinite order. In contrast, perturbative methods based on the density matrix often sum all processes to finite order [29-33]. In this article, we consider off-resonant transport through small molecules in which the electrode–molecule coupling is on the order of the molecule's charging energy. In this regime, the transport exhibits many nonperturbative effects (e.g., simultaneous charge quantization and quantum interference [34]) that cannot be properly described unless the processes are considered to infinite order.

For the many-body transport calculations presented in this article, we utilize a theory [23] based on the molecular Dyson equation (MDE) and nonequilibrium Green's functions (NEGFs). In the MDE method, the Green's function $G_{\mathrm{mol}}^{r}(E)$ of the junction is calculated by exactly diagonalizing the selected model Hamiltonian in the sequential-tunneling limit, including all excitations and charge states of the molecule. The effects of finite tunneling width are then included by using the equation-of-motion technique combined with diagrammatic perturbation theory for the Coulomb interactions. By using the molecular Dyson equation, the full Green's function of the system may be written as [23]

$$G^{r}(E) = G_{\mathrm{mol}}^{r}(E) + G_{\mathrm{mol}}^{r}(E)\left(\Sigma_{\mathrm{T}}^{\mathrm{L}} + \Sigma_{\mathrm{T}}^{\mathrm{R}} + \Delta\Sigma_{\mathrm{C}}\right)G^{r}(E). \tag{7}$$

In general, the correction to the Coulomb self-energy $\Delta\Sigma_{\mathrm{C}}$ must be found through NEGF methods [23]; however, in the elastic cotunneling regime $\Delta\Sigma_{\mathrm{C}} = 0$. The elastic transmission probability through a junction may be found by using Equation 1.

The molecular Green's function G_{mol}^{r} is found by exactly diagonalizing the molecular Hamiltonian. Represented in a basis of atomic orbitals, the Green's function matrix elements are given by [23]

$$\left[G_{\mathrm{mol}}^{r}\right]_{n\sigma,m\sigma'}(E) = \sum_{\nu,\nu'} \frac{[P(\nu)+P(\nu')][C(\nu,\nu')]_{n\sigma,m\sigma'}}{E - E_{\nu'} + E_{\nu} + i0^{+}} \ , \tag{8}$$

where $P(v)$ is the probability that the state v of the nearly isolated molecule is occupied and $H_{\mathrm{mol}}\left|\nu\right\rangle = E_{v}\left|\nu\right\rangle$ with the molecular Hamiltonian H_{mol}. $[C(v,v')]_{n\sigma,m\sigma'}$ are the many-body matrix elements given by

$$[C(\nu,\nu')]_{n\sigma,m\sigma'} = \langle \nu \mid d_{n\sigma} \mid \nu' \rangle \langle \nu' \mid d^{\dagger}_{m\sigma'} \mid \nu \rangle \ , \qquad (9)$$

where v and v' label molecular eigenstates with different charge. Here $d_{n\sigma}$ annihilates an electron of spin σ on the nth atomic basis function of the molecule. In linear response, $P(v)$ is given by the grand canonical ensemble.

The transport theory outlined above is generally applicable. Here we focus on single-molecule junctions and utilize a semi-empirical Pariser–Parr–Pople (PPP) [35-37] π-electron Hamiltonian, which describes Coulomb interactions, π-conjugation and screening due to the σ-electrons and solvent in order to model the electronic degrees of freedom that are most relevant for transport [6,23,38]. The molecular Hamiltonian may then be written as follows

$$H_{\mathrm{mol}} = \sum_{n,\sigma} \varepsilon_n d^{\dagger}_{n\sigma} d_{n\sigma} - \sum_{n,m,\sigma} \left(t_{nm} d^{\dagger}_{n\sigma} d_{m\sigma} + \mathrm{H.c.} \right) + \sum_{n,m} \frac{U_{nm}}{2} Q_n Q_m , \qquad (10)$$

where ε_n is the π-orbital energy, t_{nm} is the hopping-matrix element between orbitals n and m, and U_{nm} is the effective Coulomb interaction energy between orbitals n and m (where n and m may be equal) [39]. In correspondence with the Hückel and gDFTB calculations, we take the nearest-neighbor hopping-matrix elements t_{nm} for single and double bonds to be 3 eV and 4 eV, respectively. The effective charge operator for orbital n is [6,15,40]

$$Q_n = \sum_{\sigma} d^{\dagger}_{n\sigma} d_{n\sigma} - \sum_{\gamma} C_{n\gamma} \mathbf{V}_{\gamma} / e - 1 \ , \qquad (11)$$

where $C_{n\gamma}$ is the capacitive coupling between orbital n and lead γ, e is the electron charge, and $\mathbf{V}_{\gamma}$ is the voltage on electrode γ. The "−1" in the charge operator sets the midgap energy to zero. For simplicity, the atomic basis orbitals are taken to be orthonormal in our calculations, so that the anticommutator $\{d^{\dagger}_{n\sigma}, d_{m\sigma'}\} = \delta_{nm}\delta_{\sigma\sigma'}$. The effective Coulomb interaction energies for π-conjugated systems can be written as an Ohno [41] potential with dielectric ε [38]

$$U_{nm} = \delta_{nm} U_0 + \left(1 - \delta_{nm}\right) \frac{U_0}{\varepsilon \sqrt{1 + \alpha (R_{nm})^2}} \ , \qquad (12)$$

where U_0 is the on-site Coulomb repulsion, $\alpha = (U_0/14.397\ \mathrm{eV})^2$, and R_{nm} is the distance between orbital centers n and m in angstroms. Here we use $U_0 = 8.9$ eV and $\varepsilon = 1.28$ [38]. The phenomenological dielectric constant ε accounts for screening due to both the σ-electrons and any environmental considerations, such as nonevaporated solvent [38]. Calculations presented here were performed by using a chosen basis with frozen atomic nuclei whose positions were taken from DFT calculations of the same junctions.

Results

In conjugated molecules, including cross-conjugated molecules, the π-electron system dominates many of the observed physical properties. Consequently, simple descriptions of this itinerant electronic system, such as those provided by Hückel theory, can often capture a large part of the transport properties [9]. In cases where either the σ-system dominates, or where electron–electron interactions that are not included in the Hückel model calculation become important, these models will obviously break down.

For cyclic molecules, Luttinger's theorem ensures [6,16] the efficacy of (effective) single-particle theories, such as DFT and Hückel theory, to predict interference features at the Fermi energy. However, there is no analogous theorem for cross-conjugated molecules, making them an interesting subject for investigation. Here we use Hückel, gDFTB and a many-body MDE theory to calculate the transport through each molecular junction and to determine the effects of topology, through-space coupling and interactions beyond the mean-field.

The molecules considered

In this paper we study a series of molecular systems based on acyclic cross-conjugated molecules. According to Phelan and Orchin, "A cross-conjugated compound may be defined as a compound possessing three unsaturated groups, two of which although conjugated to a third unsaturated center are not conjugated to each other" [42]. An example of a cross-conjugated subunit is shown on the left of Figure 2 as both a chemical structure and the model system that we can use in a Hückel model calculation. Cross-conjugated molecules have been shown to exhibit destructive interference features in the electronic transmission near the Fermi energy [19]; however, only the single unsaturated site in the center is necessary to produce these features. Consequently, the minimal systems required in order to study interference effects in these types of acyclic compounds are those shown on the right in Figure 2. While these systems are not strictly cross-conjugated according to the Phelan-Orchin definition, we will refer to them as cross-conjugated as they contain the essential elements needed to produce the transport signatures of cross-conjugation.

The number of interference features that can be expected in the transmission will scale with the number of the minimal units,

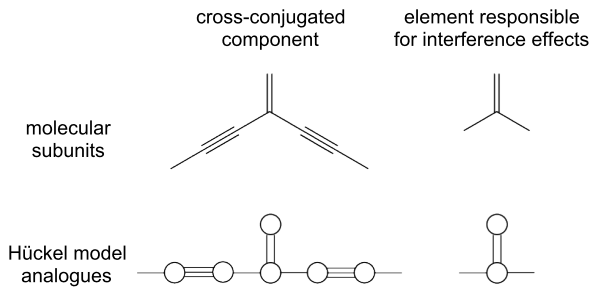

Figure 2: Examples of molecular structures (top) and the corresponding model systems (bottom) for true cross-conjugated structures (left) and the minimal systems (right) necessary to reproduce the characteristic interference features of the cross-conjugated structures in the electronic transmission.

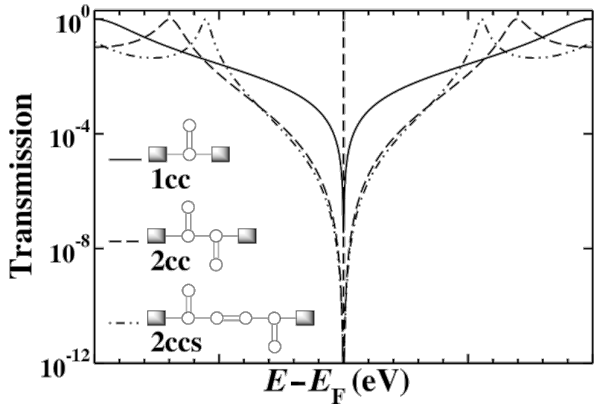

Figure 3: The transmission through three model cross-conjugated molecules calculated using Hückel theory. In each case, a single destructive interference feature (node) is evident at the Fermi energy. The order of the node increases with the number of cross-conjugated units from quadratic to quartic.

exhibiting interference effects, that appear in the structure. We will also consider molecules with multiple interference features arising from multiple subunits of the type shown on the right of Figure 2. Again while these systems are not strictly cross-conjugated by definition, they nevertheless again contain the interference features characteristic of cross-conjugated systems and will be referred to as such.

Hückel model systems: Topology and interactions through bonds

Consider three simple cross-conjugated molecules, shown as the inset to Figure 3. The smallest system ("1cc") models a single cross-conjugated unit bound between two electrodes, the middle system two cross-conjugated units ("2cc") and the largest system two cross-conjugated units separated by an extended conjugated bridge ("2ccs"). The Hückel Hamiltonian only contains information about the topology, so while we draw the larger systems with one cross-conjugated unit up and one down there would be no difference in the Hamiltonian if we instead wanted to model the system where both units were pointing in the same direction.

The transmission spectra of the 1cc, 2cc and 2ccs junctions are shown in Figure 3, calculated by means of Hückel theory. All three junctions exhibit a transmission node when $E = E_F$ (here set to zero), although the nature of the nodes appears to be different in each case. Using Equation 1 with the Hückel Green's function, Equation 6, we find that the transmission function of the 1cc junction approaches zero near the Fermi level, quadratically with respect to energy. Performing the same calculation for the 2cc molecule, composed of two cross-conjugated units, we find that the node is quartic. In both cases, this behavior has been detailed previously in similar systems in which the explicit form of the transmission around the node was detailed [15]. We also find a quartic node for the 2ccs junction. These higher order nodes are signatures of multiple degenerate interference features (supernodes). Such supernodes are potentially of technological importance, since the thermoelectric response may be significantly enhanced by their presence [16].

In molecules composed of cyclic components, such as polyphenylethers, single-particle notions, such as a Fermi surface, are protected by Luttinger's theorem [43]. Therefore, very high-order nodes are predicted to exist for molecules composed of many rings [16]. At the Hückel level, we find an analogous situation in which the quadratic node of the 1cc subunit can be used to generate higher-order nodes, when connected appropriately. In the sections that follow, we investigate this result further by including interactions at both the mean-field and many-body level.

gDFTB model systems: Interactions beyond π-bonds

Moving to an atomistic gDFTB model for these systems increases the number and changes the nature of the coupling terms that are included. In gDFTB calculations, both second and third nearest-neighbor Hamiltonian matrix elements are nonzero, and obviously these through-space terms will change if the molecular structure is varied in such a way that modifies these distances. The transmission through the smallest system (1cc) was published previously [19] and agrees well with the Hückel model calculations [44]. When we consider 2cc, however, the situation is not the same.

Figure 4 shows the 2cc model we use in gDFTB. We extend the central 2cc unit with triple-bond spacer groups in order to ensure that the only interaction between the electrodes and the 2cc component occurs "through-bonds" rather than through any unintended "through-space" interactions "short-circuiting" the

system. This modification extends the conjugation length and changes the position of the resonances; however, it has no bearing on the position of the interference features.

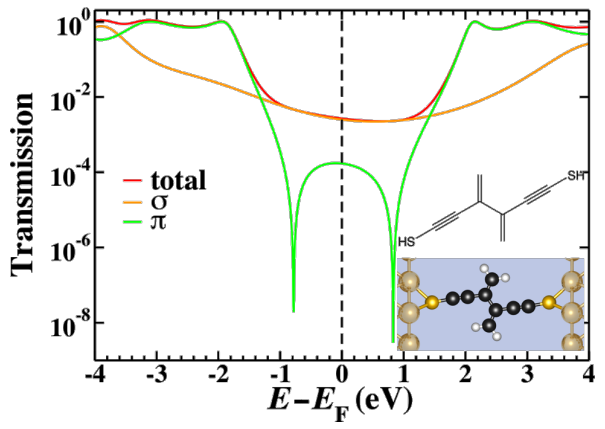

Figure 4: The chemical structure (inset top), space-filling model (inset bottom) and transmission for the 2cc system calculated by using gDFTB. The total transmission (red) is plotted along with the σ- (orange) and π- (green) components. The π- transmission exhibits two interference features separated by approximately 1.6 eV as opposed to the single interference feature observed in Figure 3.

The total transmission as well as the σ and π components (separated using the symmetry plane) of a 2cc junction are shown in Figure 4. The interference features modeled in the Hückel calculations are only present in the π-component, but in this case the degeneracy of the interference features is lifted and both features are visible, symmetrically 0.8 eV above and below the Fermi energy. As in other small molecule systems, the sharp interference features are not visible in the total transmission as the σ transport is sufficiently high as to dominate across a large energy range. If chemical modification of the molecule extended the system to such an extent that the σ-transmission dropped below the π-transmission near the Fermi energy, the two split interference features would be revealed. Consequently, a system such as this would not behave as expected based on Hückel model calculations.

A method to inspect visually the contributions to the transmission in terms of coupling elements in the molecule, is to examine the local transmission through the system [45]. With this method, it is possible to separate the contributions to the transmission in terms of the contributions between atom pairs, providing insight into the through-bond and through-space interactions that dominate. Previous work [45] on the local transmission in the vicinity of the interference feature in 1cc highlighted the significance of through-space terms in this region, and to that extent it is perhaps not particularly surprising that interference features may be coupled in this way when multiple units are placed in such close proximity as they are in 2cc. The proximity of the two cross-conjugated units means that the second nearest-neighbor terms effectively couple one side chain to the base of the other cross-conjugated unit. Indeed this is reflected in the local transmission for this system as shown in Figure 5. We have seen previously [45] that interference features are characterized by ring-current reversals in the local transmission; by this we mean cyclic patterns in the local transmission with opposite handedness on either side of the interference feature moving along the energy axis. The ring-current reversals that characterize interference features in the gDFTB calculations of 2cc have a complex pattern across both side groups, directly illustrating how non-nearest-neighbor coupling terms can influence the nature of the interference features.

In addition to the second-nearest-neighbor terms, the third-nearest-neighbor terms also show significant contribution to this system. Similar terms were observed in the local transmission through an alkane with a gauche defect [45]. All of these non-nearest-neighbor terms are quite small compared with their nearest-neighbor counterparts (approximately 1 order of magnitude smaller), so it would be generally safe to assume that their role is not highly significant. In this case, however, the precise balance of the interactions that control the energy at which the interference features are observed is very sensitive to these small terms.

The differing role of the second- and third-nearest-neighbor terms can be clarified by constructing a modified Hückel model

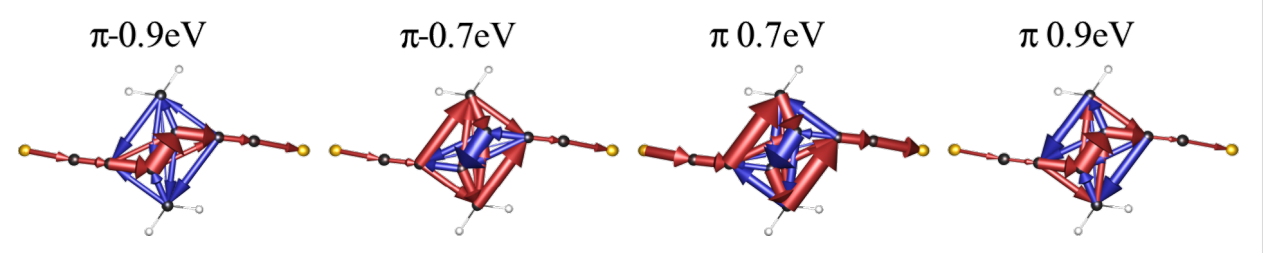

Figure 5: The local π-transmission (contributions to the transmission between pairs of atoms) for the species in Figure 4 either side of the two interference features, showing the complex ring-reversals of the coupled cross-conjugated units either side of the two interference features.

that includes these terms. The coupling elements that are included are illustrated diagrammatically in Figure 6. We set $\beta_2 = -0.25$ eV and $\beta_3 = -0.1$ eV; these values were chosen to be of approximately the same magnitude as similar elements in the gDFTB Hamiltonian. The transmission in Figure 6 shows that while the addition of second-nearest-neighbor interactions induces a partial, asymmetric splitting of the interference features, the large, symmetric splitting only arises with the inclusion of third-nearest-neighbor terms.

The role of second- and third-nearest-neighbor coupling terms in the splitting of the interference features means that extending the system to 2ccs can return the degeneracy of the interference features. Indeed that is what is observed in the transmission for 2ccs as shown in Figure 7 and was observed in similar systems previously [19] where it was noted that the site energies of the side groups controlled the position of the interference features.

As a further illustration of the effects of coupling between cross-conjugated units we can consider the molecule shown in Figure 8. This system introduces hyperconjugative coupling between the two cross-conjugated units but also removes the third-nearest-neighbor terms that induced the splitting in 2cc. The side chains of the cross-conjugated units are placed in closer proximity and the hyperconjugative interaction would seem to couple them more strongly; however, the transmission shown in Figure 8 shows no sign of split interference features. The π-transmission exhibits a single minimum, but the true zero that characterizes many interference effects is lost through the hyperconjugative coupling.

As an aside, the presence of the interference feature in this system cannot be established by ring-current reversals as the

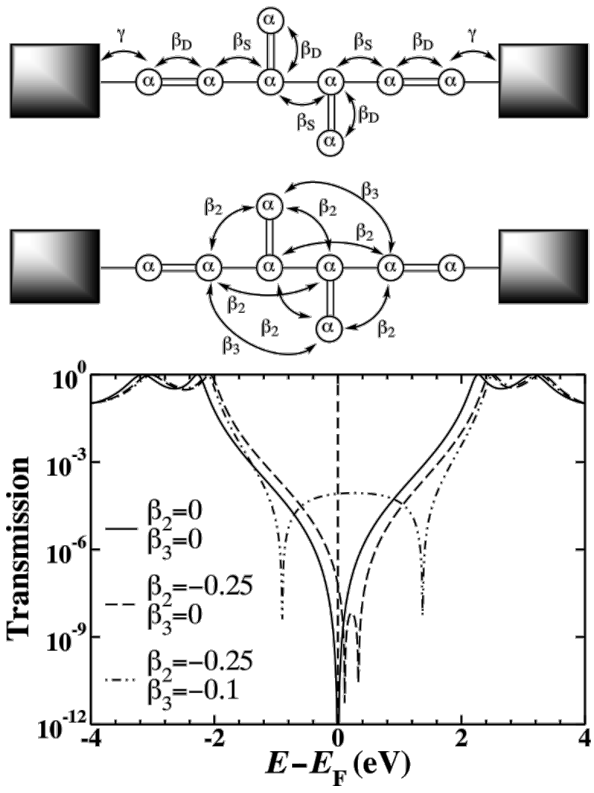

Figure 6: A modified Hückel model for 2cc with first- (solid), second- (dashed) and third- (dashed-dot) nearest-neighbor interactions included. The large, symmetric splitting of the interference features observed in the gDFTB calculations is only recovered when the very small third-nearest-neighbor coupling elements are included.

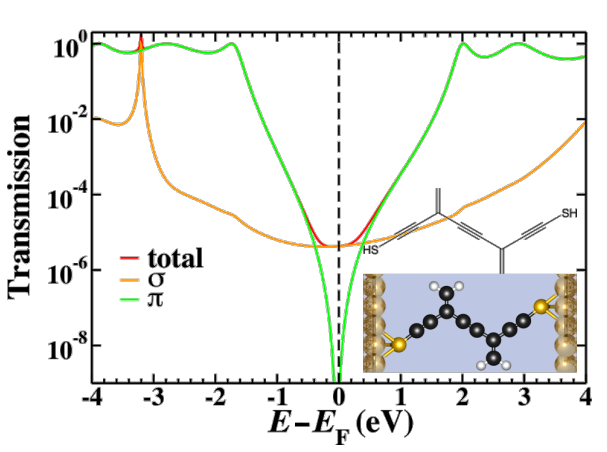

Figure 7: The chemical structure (inset top), space-filling model (inset bottom) and transmission for the 2ccs system calculated by using gDFTB. The total transmission (red) is plotted along with the σ- (orange) and π- (green) components. The π-transmission exhibits a single interference feature (which we interpret as two degenerate interference features) near the Fermi energy.

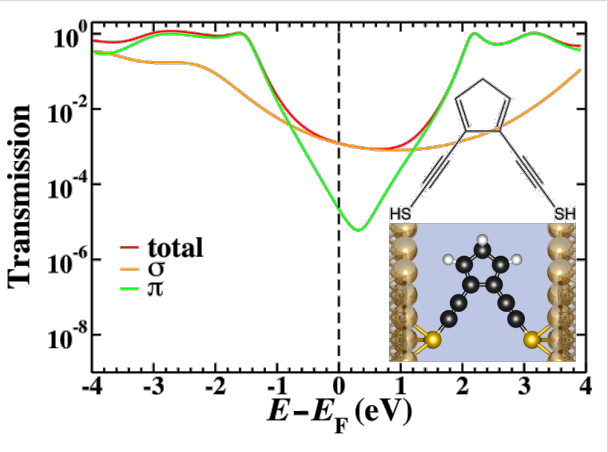

Figure 8: The chemical structure (inset top), space-filling model (inset bottom) and transmission for the 2cc-type system with hyperconjugative coupling between the cross-conjugated units as calculated by using gDFTB. The total transmission (red) is plotted along with the σ- (orange) and π- (green) components. The π-transmission exhibits degenerate interference features, while the true zero is lost through the hyperconjugative coupling.

two successive reversals return the currents to their original orientation. The characteristic ring-current reversals associated with interference features can be seen in Figure 5, as in that case the separated interference features mean that the reversed regime can be seen between −0.7 eV and 0.7 eV.

Model systems with many-body effects: Charge–charge correlations

Although electronic many-body effects are not small, their effect on transport may be minimal in certain experimentally relevant regimes. As we have seen, even weak through-space tunneling interactions in molecules composed of multiple cross-conjugated units can lift the degeneracy of the supernode predicted by Hückel theory. In this section, we use the MDE many-body theory [23] to investigate the effect of charge–charge correlations on the transport.

The transmission spectra through the π-orbitals of 1cc, 2cc and 2ccs based junctions calculated by using the MDE many-body theory (using the Hamiltonian of Equation 10) are shown in Figure 9, and no supernodes are observed. Qualitatively, the splitting of the central supernode in the 2cc and 2ccs junctions is similar to what was seen with the inclusion of through-space tunneling terms in the Hückel and gDFTb theories. However, quantitatively the splitting is much larger in the MDE spectra with values of ~5.22 eV and ~3.76 eV for the 2cc and 2ccs junctions, respectively. Only nearest-neighbor coupling elements were included in the MDE calculations ($\beta_2 = \beta_3 = 0$ eV), so the splitting of the nodes in the 2cc and 2ccs in Figure 9 is purely a consequence of the electron–electron Coulomb interactions.

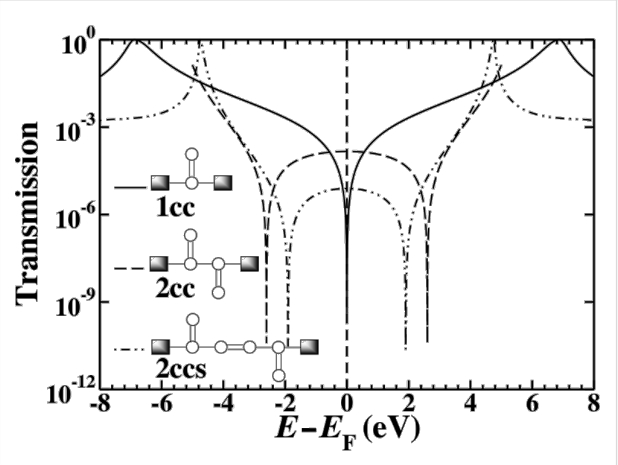

Figure 9: The same systems as calculated in Figure 3, but calculated by using the MDE many-body method. In both 2cc and 2ccs the interference features are split due to correlation effects since Coulomb interactions are always "through-space". In these calculations only the nearest-neighbor tunneling elements are included in the electronic coupling. Notice that the node splitting is symmetric about $E = E_F$.

In the acyclic 2cc system, the MDE transmission spectrum possesses two quadratic nodes rather than a single quartic supernode. Based on the Hückel and gDFTB calculations, one may predict that without through-space coupling elements, the antiresonance (node) of each 1cc subunit of the 2cc molecule would combine to produce a supernode. However, this is not the case as the Coulomb interactions are always through-space. In this system there is an avoided crossing between the two 1cc antiresonances mediated by the long-range Coulomb interactions instead of the short-range tunneling interactions. These terms, given by Equation 12, are roughly an order of magnitude larger than the through-space tunneling, and consequently the node splitting observed in the many-body spectrum is much larger than what is seen in the Hückel or gDFTB results.

The existence of supernodes in molecules composed of multiple *meta*-substituted benzene units [16] appears to be protected by Luttinger's theorem and the degeneracy of the interference features should be maintained, although exact many-body calculations for such molecules are currently prohibitively difficult. In contrast, no such theorem exists for cross-conjugated molecules and the degeneracy of transmission nodes may be lifted by interactions. There may be instances where the splitting of interference features is desirable, and in those contexts it seems that cross-conjugated molecules offer additional flexibility over multiply cyclic molecules. For thermoelectrics, however, where thermoelectric enhancement is related to the order of the supernode [16], these results suggest that devices constructed from multiple cyclic units may be preferable.

Conclusion

The sensitivity of destructive interference features to perturbations can be seen as both a strength and a weakness of these effects for the control of electron transport in molecules. On the one hand it makes these effects extremely amenable to tuning, either chemically or electrically, and thus offers a convenient option for control. On the other hand, various theoretical approaches can differ significantly, both qualitatively and quantitatively, in where they predict interference features to lie. Simple predictive schemes [46,47] based on single-particle models have been developed to provide a quick answer as to whether a particular topology will result in interference features in the HOMO–LUMO gap, but "the devil is in the details". In many molecules the HOMO–LUMO gap is on the order of a few electronvolts; however, even a small shift of ~0.5 eV away from the Fermi energy can mean that an interference feature has no bearing on the low-bias conductance. Here we show that "small" terms in the Hamiltonian can shift and change interference features considerably, and these types of effects need to be considered when designing interference-based molecular devices.

For small bias voltages, the room-temperature transport through many small, strongly-coupled, single-molecule junctions is predominantly elastic. In the vicinity of a node in the elastic transmission, other contributions to transport, e.g., from the σ-systems, inelastic processes, etc., may become physically relevant since the nodes of each contribution will not necessarily coincide. Recently, calculations of transport through biphenyl-based molecular junctions suggest that, for sufficiently large bias voltages, interference features in the elastic transport may be obscured by inelastic (phonon-assisted) contributions [48]. Although the exact magnitude of the inelastic component in acyclic cross-conjugated molecules is not known, the contribution to the transport will simply be additive, as it is in the case of the σ-system transport.

From a theoretical standpoint, these systems offer an excellent opportunity to discriminate between theoretical methods. When methods differ, the predicted conductance can change by orders of magnitude and this clearly provides a useful tool with which to probe the significance of the various approximations made in each case. Measuring the very low conductance predicted in cases where destructive interference effects dominate may not be trivial, but it is also clear that these features may result in dramatic thermoelectric properties and these may be much more amenable to comparison with theoretical predictions.

Acknowledgements

The research leading to these results received funding from the European Research Council under the European Union's Seventh Framework Programme (FP7/2007-2013)/ERC Grant agreement no. 258806. This work was partly supported by the Non-equilibrium Energy Research Center (NERC) which is an Energy Frontier Research Center funded by the U.S. Department of Energy, Office of Science, Office of Basic Energy Sciences under Award Number DE-SC0000989. CAS acknowledges support from the Department of Energy under Award Number DE-SC0006699.

References

1. Sautet, P.; Joachim, C. *Chem. Phys. Lett.* **1988,** *153,* 511–516. doi:10.1016/0009-2614(88)85252-7
2. Patoux, C.; Coudret, C.; Launay, J.-P.; Joachim, C.; Gourdon, A. *Inorg. Chem.* **1997,** *36,* 5037–5049. doi:10.1021/ic970013m
3. Yaliraki, S. N.; Ratner, M. A. *Ann. N.Y. Acad. Sci.* **2002,** *960,* 153–162. doi:10.1111/j.1749-6632.2002.tb03030.x
4. Stadler, R.; Ami, S.; Joachim, C.; Forshaw, M. *Nanotechnology* **2004,** *15,* S115–S121. doi:10.1088/0957-4484/15/4/001
5. Walter, D.; Neuhauser, D.; Baer, R. *Chem. Phys.* **2004,** *299,* 139–145. doi:10.1016/j.chemphys.2003.12.015
6. Cardamone, D. M.; Stafford, C. A.; Mazumdar, S. *Nano Lett.* **2006,** *6,* 2422–2426. doi:10.1021/nl0608442
7. Stafford, C. A.; Cardamone, D. M.; Mazumdar, S. *Nanotechnology* **2007,** *18,* 424014. doi:10.1088/0957-4484/18/42/424014
8. Ke, S.-H.; Yang, W.; Baranger, H. U. *Nano Lett.* **2008,** *8,* 3257–3261. doi:10.1021/nl8016175
9. Solomon, G. C.; Andrews, D. Q.; Van Duyne, R. P.; Ratner, M. A. *ChemPhysChem* **2009,** *10,* 257–264. doi:10.1002/cphc.200800591
10. Hansen, T.; Solomon, G. C.; Andrews, D. Q.; Ratner, M. A. *J. Chem. Phys.* **2009,** *131,* 194704. doi:10.1063/1.3259548
11. Kocherzhenko, A. A.; Grozema, F. C.; Siebbeles, L. D. A. *J. Phys. Chem. C* **2010,** *114,* 7973–7979. doi:10.1021/jp9117216
12. Mayor, M.; Weber, H. B.; Reichert, J.; Elbing, M.; von Hänisch, C.; Beckmann, D.; Fischer, M. *Angew. Chem., Int. Ed.* **2003,** *42,* 5834–5838. doi:10.1002/anie.200352179
13. Kiguchi, M.; Nakamura, H.; Takahashi, Y.; Takahashi, T.; Ohto, T. *J. Phys. Chem. C* **2010,** *114,* 22254–22261. doi:10.1021/jp1095079
14. Andrews, D. Q.; Solomon, G. C.; Van Duyne, R. P.; Ratner, M. A. *J. Am. Chem. Soc.* **2008,** *130,* 17309–17319. doi:10.1021/ja804399q
15. Bergfield, J. P.; Stafford, C. A. *Nano Lett.* **2009,** *9,* 3072–3076. doi:10.1021/nl901554s
16. Bergfield, J. P.; Solis, M. A.; Stafford, C. A. *ACS Nano* **2010,** *4,* 5314–5320. doi:10.1021/nn100490g
17. Hush, N. S.; Reimers, J. R.; Hall, L. E.; Johnston, L. A.; Crossley, M. J. *Ann. N.Y. Acad. Sci.* **1998,** *852,* 1–21. doi:10.1111/j.1749-6632.1998.tb09861.x
18. Markussen, T.; Schiötz, J.; Thygesen, K. S. *J. Chem. Phys.* **2010,** *132,* 224104. doi:10.1063/1.3451265
19. Solomon, G. C.; Andrews, D. Q.; Goldsmith, R. H.; Hansen, T.; Wasielewski, M. R.; Van Duyne, R. P.; Ratner, M. A. *J. Am. Chem. Soc.* **2008,** *130,* 17301–17308. doi:10.1021/ja8044053
20. Kalyanaraman, C.; Evans, D. G. *Nano Lett.* **2002,** *2,* 437–441. doi:10.1021/nl010074o
21. Datta, S. *Electronic Transport in Mesoscopic Systems;* Cambridge University Press: Cambridge, UK, 1995.
22. Pecchia, A.; Di Carlo, A. *Rep. Prog. Phys.* **2004,** *67,* 1497–1561. doi:10.1088/0034-4885/67/8/R04
23. Bergfield, J. P.; Stafford, C. A. *Phys. Rev. B* **2009,** *79,* 245125. doi:10.1103/PhysRevB.79.245125
24. Porezag, D.; Frauenheim, T.; Köhler, T.; Seifert, G.; Kaschner, R. *Phys. Rev. B* **1995,** *51,* 12947–12957. doi:10.1103/PhysRevB.51.12947
25. Elstner, M.; Porezag, D.; Jugnickel, G.; Elsner, J.; Haugk, M.; Frauenheim, T.; Suhai, S.; Seifert, G. *Phys. Rev. B* **1998,** *58,* 7260–7268. doi:10.1103/PhysRevB.58.7260
26. Shao, Y.; Molnar, L. F.; Jung, Y.; Kussmann, J.; Ochsenfeld, C.; Brown, S. T.; Gilbert, A. T. B.; Slipchenko, L. V.; Levchenko, S. V.; O'Neill, D. P.; DiStasio, R. A., Jr.; Lochan, R. C.; Wang, T.; Beran, G. J. O.; Besley, N. A.; Herbert, J. M.; Lin, C. Y.; Voorhis, T. V.; Chien, S. H.; Sodt, A.; Steele, R. P.; Rassolov, V. A.; Maslen, P. E.; Korambath, P. P.; Adamson, R. D.; Austin, B.; Baker, J.; Byrd, E. F. C.; Dachsel, H.; Doerksen, R. J.; Dreuw, A.; Dunietz, B. D.; Dutoi, A. D.; Furlani, T. R.; Gwaltney, S. R.; Heyden, A.; Hirata, S.; Hsu, C.-P.; Kedziora, G.; Khalliulin, R. Z.; Klunzinger, P.; Lee, A. M.; Lee, M. S.; Liang, W.; Lotan, I.; Nair, N.; Peters, B.; Proynov, E. I.; Pieniazek, P. A.; Rhee, Y. M.; Ritchie, J.; Rosta, E.; Sherrill, C. D.; Simmonett, A. C.; Subotnik, J. E.; Lee Woodcock, H., III; Zhang, W.; Bell, A. T.; Chakraborty, A. K.; Chipman, D. M.; Keil, F. J.; Warshel, A.; Hehre, W. J.; Schaefer, H. F., III; Kong, J.; Krylov, A. I.; Gill, P. M. W.; Head-Gordon, M. *Phys. Chem. Chem. Phys.* **2006,** *8,* 3172–3191. doi:10.1039/b517914a
27. Bilic, A.; Reimers, J. R.; Hush, N. S. *J. Chem. Phys.* **2005,** *122,* 094708. doi:10.1063/1.1850455

28. Solomon, G. C.; Gagliardi, A.; Pecchia, A.; Frauenheim, T.; Di Carlo, A.; Reimers, J. R.; Hush, N. S. *J. Chem. Phys.* **2006,** *125,* 184702. doi:10.1063/1.2363976
29. Harbola, U.; Mukamel, S. *Phys. Rep.* **2008,** *465,* 191–222. doi:10.1016/j.physrep.2008.05.003
30. Galperin, M.; Nitzan, A.; Ratner, M. A. *Phys. Rev. B* **2008,** *78,* 125320. doi:10.1103/PhysRevB.78.125320
31. Yeganeh, S.; Ratner, M. A.; Galperin, M.; Nitzan, A. *Nano Lett.* **2009,** *9,* 1770–1774. doi:10.1021/nl803635t
32. König, J.; Schoeller, H.; Schön, G. *Phys. Rev. Lett.* **1997,** *78,* 4482–4485. doi:10.1103/PhysRevLett.78.4482
33. Pedersen, J. N.; Wacker, A. *Phys. Rev. B* **2005,** *72,* 195330. doi:10.1103/PhysRevB.72.195330
34. Bergfield, J. P.; Solomon, G. C.; Stafford, C. A.; Ratner, M. A. *Nano Lett.* **2011,** *11,* 2759–2764. doi:10.1021/nl201042m
35. Pariser, R.; Parr, R. G. *J. Chem. Phys.* **1953,** *21,* 466–471. doi:10.1063/1.1698929
36. Pariser, R.; Parr, R. G. *J. Chem. Phys.* **1953,** *21,* 767–776. doi:10.1063/1.1699030
37. Pople, J. A. *Trans. Faraday Soc.* **1953,** *49,* 1375–1385. doi:10.1039/tf9534901375
38. Castleton, C. W. M.; Barford, W. *J. Chem. Phys.* **2002,** *117,* 3570–3582. doi:10.1063/1.1489994
39. Barr, J. D.; Bergfield, J. P.; Stafford, C. A. Effective Field Theory of Interacting π-Electrons 2011, arXiv:1108.0021v2 [cond-mat.mes-hall].
40. Stafford, C. A.; Kotlyar, R.; Das Sarma, S. *Phys. Rev. B* **1998,** *58,* 7091–7102. doi:10.1103/PhysRevB.58.7091
41. Ohno, K. *Theor. Chim. Acta* **1964,** *2,* 219–227. doi:10.1007/BF00528281
42. Phelan, N. F.; Orchin, M. *J. Chem. Educ.* **1968,** *45,* 633–637. doi:10.1021/ed045p633
43. Luttinger, J. M. *Phys. Rev.* **1960,** *119,* 1153–1163. doi:10.1103/PhysRev.119.1153
44. Solomon, G. C.; Andrews, D. Q.; Hansen, T.; Goldsmith, R. H.; Wasielewski, M. R.; Van Duyne, R. P.; Ratner, M. A. *J. Chem. Phys.* **2008,** *129,* 054701. doi:10.1063/1.2958275
45. Solomon, G. C.; Herrmann, C.; Hansen, T.; Mujica, V.; Ratner, M. A. *Nat. Chem.* **2010,** *2,* 223–228. doi:10.1038/nchem.546
46. Yoshizawa, K.; Tada, T.; Staykov, A. *J. Am. Chem. Soc.* **2008,** *130,* 9406–9413. doi:10.1021/ja800638t
47. Markussen, T.; Stadler, R.; Thygesen, K. S. *Nano Lett.* **2010,** *10,* 4260–4265. doi:10.1021/nl101688a
48. Härtle, R.; Butzin, M.; Rubio-Pons, O.; Thoss, M. *Phys. Rev. Lett.* **2011,** *107,* 046802. doi:10.1103/PhysRevLett.107.046802

License and Terms

Beilstein Journal of Nanotechnology

Transmission eigenvalue distributions in highly conductive molecular junctions

Justin P. Bergfield[*1], Joshua D. Barr[2] and Charles A. Stafford[2]

Full Research Paper

Open Access

Address:
[1]Departments of Chemistry and Physics, University of California, Irvine, California 92697, USA and [2]Department of Physics, University of Arizona, 1118 East Fourth Street, Tucson, AZ 85721, USA

Email:
Justin P. Bergfield[*] - jbergfie@uci.edu

* Corresponding author

Keywords:
benzene–platinum junction; effective-field theory; isolated-resonance approximation; lead–molecule interface; many-body theory; multichannel; quantum transport; single-molecule junction; transmission eigenchannels

Beilstein J. Nanotechnol. **2012,** *3,* 40–51.
doi:10.3762/bjnano.3.5

Received: 20 July 2011
Accepted: 01 December 2011
Published: 16 January 2012

This article is part of the Thematic Series "Transport through molecular junctions".

Guest Editor: J. M. van Ruitenbeek

Abstract

Background: The transport through a quantum-scale device may be uniquely characterized by its transmission eigenvalues τ_n. Recently, highly conductive single-molecule junctions (SMJ) with multiple transport channels (i.e., several $\tau_n > 0$) have been formed from benzene molecules between Pt electrodes. Transport through these multichannel SMJs is a probe of both the bonding properties at the lead–molecule interface and of the molecular symmetry.

Results: We use a many-body theory that properly describes the complementary wave–particle nature of the electron to investigate transport in an ensemble of Pt–benzene–Pt junctions. We utilize an effective-field theory of interacting π-electrons to accurately model the electrostatic influence of the leads, and we develop an ab initio tunneling model to describe the details of the lead–molecule bonding over an ensemble of junction geometries. We also develop a simple decomposition of transmission eigenchannels into molecular resonances based on the isolated resonance approximation, which helps to illustrate the workings of our many-body theory, and facilitates unambiguous interpretation of transmission spectra.

Conclusion: We confirm that Pt–benzene–Pt junctions have two dominant transmission channels, with only a small contribution from a third channel with $\tau_n << 1$. In addition, we demonstrate that the isolated resonance approximation is extremely accurate and determine that transport occurs predominantly via the HOMO orbital in Pt–benzene–Pt junctions. Finally, we show that the transport occurs in a lead–molecule coupling regime where the charge carriers are both particle-like and wave-like simultaneously, requiring a many-body description.

Introduction

The number of transmission channels for a single-atom contact between two metallic electrodes is simply given by the chemical valence of the atom [1]. Recently, it was argued [2] that the number of dominant transmission channels in a single-molecule junction (SMJ) is determined by the degeneracy of the molecular orbital [3] closest to the metal Fermi level. In this article, we focus on ensembles of highly conductive Pt–benzene–Pt junctions [4] in which the lead and molecule are in direct contact. Going beyond the phenomenological random-matrix model of lead–molecule coupling considered in [2], a realistic atomistic model is developed to describe lead–molecule coupling over an ensemble of energetically favored junction geometries.

For a two-terminal SMJ, the transmission eigenvalues τ_n are eigenvalues of the elastic transmission matrix [5]

$$\mathbf{T}(E) = \Gamma^{\mathrm{L}}(E)G(E)\Gamma^{\mathrm{R}}(E)G^{\dagger}(E), \qquad (1)$$

where G is the retarded Green's function [6] of the SMJ, Γ^{α} is the tunneling-width matrix describing the bonding of the molecule to lead α, and the total transmission function $T(E) = \mathrm{Tr}\{\mathbf{T}(E)\}$. The number of transmission channels is equal to the rank of the matrix (Equation 1), which is in turn limited by the ranks of the matrices G and Γ^{α} [2]. The additional two-fold spin degeneracy of each resonance is considered to be implicit throughout this work. As indicated by Equation 1, an accurate description of transport requires an accurate result for G, which can be calculated by using either single-particle or many-body methods, and which depends critically on accurate descriptions of the molecular energy levels and the lead–molecule coupling.

In effective single-particle theories, including current implementations of density functional theory (DFT), it is often necessary [7-10] to describe the transport problem by considering an "extended molecule", composed of the molecule and several electrode atoms. This procedure makes it difficult, if not impossible, to assign transmission eigenchannels to individual molecular resonances since the quantum states of the extended molecule bear little resemblance to the states of the molecule itself.

We utilize a nonequilibrium many-body theory based on the molecular Dyson equation (MDE) [6] to investigate transport distributions of SMJ ensembles. Our MDE theory correctly accounts for wave–particle duality of the charge carriers, simultaneously reproducing the key features of both the Coulomb blockade and coherent-transport regimes, alleviating the necessity of constructing an extended molecule. Consequently, we can unambiguously assign transmission eigenchannels to molecular resonances [2].

Previous applications of our MDE theory [6,11,12] to transport through SMJs utilized a semiempirical Hamiltonian [13] for the π-electrons, which accurately describes the gas-phase spectra of conjugated organic molecules. Although this approach should be adequate to describe molecules weakly coupled to metal electrodes, e.g., by thiol linkages, in junctions where the π-electrons bind directly to the metal electrodes [4], the lead–molecule coupling may be so strong that the molecule itself is significantly altered, necessitating a more fundamental molecular model.

In this work, we utilize an *effective field theory of interacting π-electrons* (π-EFT), in which the form of the molecular Hamiltonian is derived from symmetry principles and electromagnetic theory (multipole expansion) [14]. The resulting formalism constitutes a state-of-the-art many-body theory that provides a realistic description of lead–molecule hybridization and van der Waals coupling, as well as the screening of intramolecular interactions by the metal electrodes, all of which are essential for a quantitative description of strongly-coupled SMJs [4].

The bonding between the tip of electrode α and the molecule is characterized by the tunneling-width matrix Γ^{α}, where the rank of Γ^{α} is equal to the number of covalent bonds formed between the two. For example, in a SMJ where a Au electrode bonds to an organic molecule through a thiol group, only a single bond is formed, and there is only one significant transmission channel [15,16]. In Pt–benzene–Pt junctions, however, each Pt electrode forms multiple bonds to the benzene molecule and multiple transmission channels are observed [4]. In such highly conductive SMJs the lead and molecule are in direct contact and the overlap between the π-electron system of the molecule and *all* of the quasi-atomic wavefunctions of the atomically sharp electrode are relevant. Rather than the random-matrix method used in [2], we develop an atomistic approach to bonding in which the nine relevant orbitals for each Pt electrode are included (one *s*, three *p*, and five *d*), representing the evanescent tunneling modes in free space outside the apex atom of each electrode tip. This atomistic model of lead–molecule coupling allows distributions of transport coefficients to be computed directly over an ensemble of junction geometries, supplanting the phenomenological model of lead–molecule coupling employed in [2].

In the next section, we outline the relevant aspects of our MDE theory and derive transport equations in the isolated-resonance

approximation. We then develop our atomistic treatment of lead–molecule coupling, in which the electrostatic influence of the leads is treated by π-EFT and the multiorbital lead–molecule bonding is described using the quasi-atomic orbitals of the electrode tip. Finally, the transport distributions for these ensembles of Pt–benzene–Pt junctions are calculated by using both the full molecular Green's function and within the isolated-resonance approximation. The efficacy of the isolated resonance approximation is investigated in detail.

Many-body theory of transport

When macroscopic leads are bonded to a single molecule, a SMJ is formed, transforming the few-body molecular problem into a full many-body problem. The bare molecular states are dressed by interactions with the lead electrons when the SMJ is formed, shifting and broadening them in accordance with the lead–molecule coupling.

Until recently [6] no theory of transport in SMJs was available which properly accounted for the *particle and wave* character of the electron, such that the Coulomb blockade and coherent transport regimes were considered "complementary" [10]. Here, we utilize a many-body MDE theory [6,12] based on nonequilibrium Green's functions (NEGFs) to investigate transport in multichannel SMJs, which correctly accounts for both aspects of the charge carriers.

In order to calculate transport quantities of interest we must determine the retarded Green's function $G(E)$ of the junction, which may be written as

$$G(E)=\left[\mathbf{S}E-H_{\rm mol}^{(1)}-\Sigma(E)\right]^{-1}, \tag{2}$$

where $H_{\rm mol} = H_{\rm mol}^{(1)} + H_{\rm mol}^{(2)}$ is the molecular Hamiltonian, which we formally separate into one-body and two-body terms [6,12]. **S** is an overlap matrix, which in an orthonormal basis reduces to the identity matrix, and

$$\Sigma(E)=\Sigma_{\rm T}^{\rm L}(E)+\Sigma_{\rm T}^{\rm R}(E)+\Sigma_{\rm C}(E), \tag{3}$$

is the self-energy, including the effect of both a finite lead–molecule coupling, through $\Sigma_{\rm T}^{L,R}$, and many-body interactions, through the Coulomb self-energy $\Sigma_{\rm C}(E)$. The tunneling self-energy matrices are related to the tunneling-width matrices by

$$\Gamma^{\alpha}(E)\equiv i\left(\Sigma_{\rm T}^{\alpha}(E)-\left[\Sigma_{\rm T}^{\alpha}(E)\right]^{\dagger}\right). \tag{4}$$

It is useful to define a molecular Green's function $G_{\rm mol}(E)=\lim_{\Gamma^{\alpha}\to 0^{+}}G(E)$. In the sequential tunneling regime [6], where lead–molecule coherences can be neglected, the molecular Green's function within MDE theory is given by

$$G_{\rm mol}(E)=\left[\mathbf{S}E-H_{\rm mol}^{(1)}-\Sigma_{\rm C}^{(0)}(E)\right]^{-1}, \tag{5}$$

where all one-body terms are included in $H_{\rm mol}^{(1)}$ and the Coulomb self-energy $\Sigma^{(0)}$ accounts for the effect of all intramolecular many-body correlations exactly. The full Green's function of the SMJ may then be found using the molecular Dyson equation [6]

$$G(E)=G_{\rm mol}(E)+G_{\rm mol}(E)\Delta\Sigma(E)G(E), \tag{6}$$

where $\Delta\Sigma = \Sigma_{\rm T} + \Delta\Sigma_{\rm C}$ and $\Delta\Sigma_{\rm C}=\Sigma_{\rm C}-\Sigma_{\rm C}^{(0)}$. At room temperature and for small bias voltages, $\Delta\Sigma_{\rm C}\approx 0$ in the cotunneling regime [6] (i.e., for nonresonant transport). Furthermore, the inelastic transmission probability is negligible compared to the elastic transmission in that limit.

The molecular Green's function $G_{\rm mol}$ is found by exactly diagonalizing the molecular Hamiltonian, including all charge states and excited states of the molecule [6,12]

$$G_{\rm mol}(E)=\sum_{\nu,\nu'}\frac{\left[\mathcal{P}(\nu)+\mathcal{P}(\nu')\right]C(\nu,\nu')}{E-E_{\nu'}+E_{\nu}+i0^{+}}, \tag{7}$$

where $\mathcal{P}(\nu)$ is the probability that the molecular state ν is occupied, $C(\nu,\nu')$ are many-body matrix elements and $H_{\rm mol}|\nu\rangle=E_{\nu}|\nu\rangle$. In linear response, $\mathcal{P}(\nu)=e^{-\beta(E_{\nu}-\mu N_{\nu})}/\mathcal{Z}$, where $\mathcal{Z}=\sum_{\nu}e^{-\beta(E_{\nu}-N_{\nu}\mu)}$ is the grand canonical partition function.

The rank-1 matrix $C(\nu,\nu')$ has elements

$$[C(\nu,\nu')]_{n\sigma,m\sigma'}=\left\langle\nu\left|d_{n\sigma}\right|\nu'\right\rangle\left\langle\nu'\left|d_{m\sigma'}^{\dagger}\right|\nu\right\rangle, \tag{8}$$

where $d_{n\sigma}$ annihilates an electron of spin σ on the nth atomic orbital of the molecule, and ν and ν′ label molecular eigenstates with different charge. The rank of $C(\nu,\nu')$ in conjunction with Equation 6 and Equation 7 implies that each molecular resonance $\nu\to\nu'$ contributes at most one transmission channel in Equation 1, suggesting that an M-fold-degenerate molecular resonance could sustain a maximum of M transmission channels.

Isolated-resonance approximation

Owing to the position of the chemical potential of the leads relative to the molecular energy levels and the large charging energy of small molecules, transport in SMJs is typically dominated by individual molecular resonances. In this subsection, we calculate the Green's function in the isolated-resonance approximation wherein only a single (nondegenerate or degenerate) molecular resonance is considered. In addition to developing intuition and gaining insight into the transport mechanisms in a SMJ, we also find (cf. Results and Discussion section) that the isolated-resonance approximation can be used to accurately predict the transport.

Nondegenerate molecular resonance

If we consider a single non-degenerate molecular resonance then

$$G_{\mathrm{mol}}(E) \approx \frac{\left[\mathcal{P}(\nu)+\mathcal{P}(\nu')\right]C(\nu,\nu')}{E-E_{\nu'}+E_{\nu}+i0^{+}} \equiv \frac{\tilde{\lambda}|\lambda\rangle\langle\lambda|}{E-\varepsilon+i0^{+}}, \qquad (9)$$

where $\varepsilon = E_{\nu'} - E_{\nu}$, $C(\nu,\nu') \equiv \lambda|\lambda\rangle\langle\lambda|$ is the rank-1 many-body overlap matrix, and we have set $\tilde{\lambda} = \left[\mathcal{P}(\nu)+\mathcal{P}(\nu')\right]\lambda$. In order to solve G analytically, it is useful to rewrite Dyson's equation (Equation 6) as follows:

$$G(E) = \left(\mathbf{1} - G_{\mathrm{mol}}(E)\Delta\Sigma(E)\right)^{-1} G_{\mathrm{mol}}(E). \qquad (10)$$

In the elastic-cotunneling regime ($\Delta\Sigma_{\mathrm{C}} = 0$) we find

$$\begin{aligned} G(E) &= \frac{\lambda|\lambda\rangle\langle\lambda|}{E-\varepsilon+i0^{+}}\left(1+\frac{\lambda\langle\lambda|\Sigma_{\mathrm{T}}|\lambda\rangle}{E-\varepsilon+i0^{+}}+\right. \\ &\qquad \left.\left[\frac{\lambda\langle\lambda|\Sigma_{\mathrm{T}}|\lambda\rangle}{E-\varepsilon+i0^{+}}\right]^{2}+\ldots\right) \\ &= \frac{\lambda|\lambda\rangle\langle\lambda|}{E-\varepsilon-\lambda\langle\lambda|\Sigma_{\mathrm{T}}|\lambda\rangle}. \end{aligned} \qquad (11)$$

Equation 11 can be equivalently expressed as

$$G(E) \approx \frac{\left[\mathcal{P}(\nu)+\mathcal{P}(\nu')\right]C(\nu,\nu')}{E-\varepsilon-\tilde{\Sigma}}, \qquad (12)$$

where

$$\tilde{\Sigma} = \left[\mathcal{P}(\nu)+\mathcal{P}(\nu')\right]\mathrm{Tr}\left\{C(\nu,\nu')\Sigma_{\mathrm{T}}\right\} \qquad (13)$$

is the effective self-energy at the resonance, which includes the effect of many-body correlations through the $C(\nu,\nu')$ matrix.

Using Equation 1, the transmission in the isolated-resonance approximation is given by

$$T(E) = \frac{\tilde{\Gamma}^{\mathrm{L}}\tilde{\Gamma}^{\mathrm{R}}}{\left(E-\tilde{\varepsilon}\right)^{2}+\tilde{\Gamma}^{2}}, \qquad (14)$$

where $\tilde{\varepsilon} = \varepsilon + \mathrm{Re}\tilde{\Sigma}$,

$$\tilde{\Gamma}^{\alpha} = \left[\mathcal{P}(\nu)+\mathcal{P}(\nu')\right]\mathrm{Tr}\left\{C(\nu,\nu')\Gamma^{\alpha}\right\} \qquad (15)$$

is the dressed tunneling-width matrix, and $\tilde{\Gamma} = \left(\tilde{\Gamma}^{\mathrm{L}}+\tilde{\Gamma}^{\mathrm{R}}\right)/2$.

As evidenced by Equation 14, the isolated-resonance approximation gives an intuitive prediction for the transport. Specifically, the transmission function is a single Lorentzian resonance centered about $\tilde{\varepsilon}$ with a half-width at half-maximum of $\tilde{\Gamma}$. The less-intuitive many-body aspect of the transport problem is encapsulated in the effective tunneling-width matrices $\tilde{\Gamma}^{\alpha}$, where the overlap of molecular many-body eigenstates can reduce the elements of these matrices and may strongly affect the predicted transport.

Degenerate molecular resonance

The generalization of the above results to the case of a degenerate molecular resonance is formally straightforward. For an M-fold degenerate molecular resonance

$$G_{\mathrm{mol}}(E) \approx \frac{\tilde{\lambda}}{E-\varepsilon+i0^{+}}\sum_{l=1}^{M}|\lambda_l\rangle\langle\lambda_l|. \qquad (16)$$

The M degenerate eigenvectors of G_{mol} may be chosen to diagonalize Σ_{T} on the degenerate subspace

$$\tilde{\lambda}\langle\lambda_i|\Sigma_{\mathrm{T}}|\lambda_j\rangle = \delta_{ij}\tilde{\Sigma}_i \qquad (17)$$

and Dyson's equation may be solved as before

$$G(E) \approx \sum_{l=1}^{M}\frac{\left[\mathcal{P}(\nu_l)+\mathcal{P}(\nu')\right]C(\nu_l,\nu')}{E-E_{\nu'}+E_{\nu_l}-\tilde{\Sigma}_l}. \qquad (18)$$

Although Σ_{T} is diagonal in the basis of $|\lambda_l\rangle$, Γ^{L} and Γ^{R} need not be separately diagonal. Consequently, there is no general

simple expression for $T(E)$ for the case of a degenerate resonance, but **T** can still be computed using Equation 1.

In this article we focus on transport through Pt–benzene–Pt SMJs where the relevant molecular resonances (HOMO or LUMO) are doubly degenerate. Considering the HOMO resonance of benzene

$$G(E)\approx\frac{C(\nu_1,0_6)}{E-\varepsilon_{\mathrm{HOMO}}-\tilde{\Sigma}_{\nu_1\nu'}}+\frac{C(\nu_2,0_6)}{E-\varepsilon_{\mathrm{HOMO}}-\tilde{\Sigma}_{\nu_2\nu'}}, \tag{19}$$

where $\nu_{1,2}\in 0_5$ diagonalize Σ_{T} and 0_N is the N-particle ground state.

π-Electron effective field theory

In order to model the degrees of freedom most relevant for transport, we have utilized an effective field theory of interacting π-electron systems (π-EFT) as described in detail in [14]. Briefly, this was done by starting with the full electronic Hamiltonian of a conjugated organic molecule and by dropping degrees of freedom far from the π-electron energy scale. The effective π-orbitals were then assumed to possess azimuthal and inversion symmetry, and the effective Hamiltonian was required to satisfy particle–hole symmetry and be explicitly local. Such an effective field theory is preferable to semiempirical methods for applications in molecular junctions because the effective interaction is derived from Maxwell's equations, and hence can be readily generalized to include screening of intramolecular Coulomb interactions due to nearby metallic electrodes.

Effective Hamiltonian

This allows the effective Hamiltonian for the π-electrons in gas-phase benzene to be expressed as

$$H_{\mathrm{mol}}=\mu\sum_n\rho_n-t\sum_{\langle n,m\rangle,\sigma}d^\dagger_{n\sigma}d_{m\sigma}+\frac{1}{2}\sum_{nm}U_{nm}(\rho_n-1)(\rho_m-1), \tag{20}$$

where t is the tight-binding matrix element, μ is the molecular chemical potential, U_{nm} is the Coulomb interaction between the electrons on the nth and mth π-orbitals, and $\rho_n\equiv\sum_\sigma d^\dagger_{n\sigma}d_{n\sigma}$. The interaction matrix U_{nm} is calculated by way of a multipole expansion keeping terms up to the quadrupole–quadrupole interaction:

$$U_{nm}=U_{nn}\delta_{nm}+(1-\delta_{nm})\left(U^{MM}_{nm}+U^{MQ}_{nm}+U^{QM}_{nm}+U^{QQ}_{nm}\right)+\mathcal{O}\left(r^{-6}\right), \tag{21}$$

where U^{MM} is the monopole–monopole interaction, U^{QM} is the quadrupole–monopole interaction, and U^{QQ} is the quadrupole–quadrupole interaction. For two π-orbitals with arbitrary quadrupole moments Q^{ij}_n and Q^{kl}_m and centers separated by a displacement $\vec{r}$, the expressions for these are

$$\begin{aligned}U^{MM}_{nm}&=\frac{e^2}{\epsilon r},\\ U^{MQ}_{nm}&=\frac{-e}{2\epsilon r^3}\sum_{ij}Q^{ij}_m\hat{r}_i\hat{r}_j,\\ U^{QM}_{nm}&=\frac{-e}{2\epsilon r^3}\sum_{ij}Q^{ij}_n\hat{r}_i\hat{r}_j,\\ U^{QQ}_{nm}&=\frac{1}{12\epsilon r^5}\sum_{ijkl}Q^{ij}_nQ^{kl}_mW_{ijkl},\end{aligned} \tag{22}$$

where

$$W_{ijkl}=\delta_{li}\delta_{kj}+\delta_{ki}\delta_{lj}-5r^{-2}\left(r_k\delta_{li}r_j+r_kr_i\delta_{lj}+\delta_{ki}r_jr_l+r_i\delta_{kj}r_l+r_kr_l\delta_{ij}\right)+35r^{-4}r_ir_jr_kr_l \tag{23}$$

is a rank-4 tensor that characterizes the interaction of two quadrupoles and ϵ is a dielectric constant included to account for the polarizability of the core and σ electrons. Here *i, j, k*, and *l* are the Cartesian indices of the foregoing tensors and vectors. Altogether, this provides an expression for the interaction energy that is correct up to fifth order in the interatomic distance.

Benzene

The adjustable parameters in our Hamiltonian for gas-phase benzene are the nearest-neighbor tight-binding matrix element t, the on-site repulsion U, the dielectric constant ϵ, and the π-orbital quadrupole moment Q. These were renormalized by fitting to experimental values that should be accurately reproduced within a π-electron only model. In particular, we simultaneously optimized the theoretical predictions of (1) the six lowest singlet and triplet excitations of the neutral molecule, (2) the vertical ionization energy, and (3) the vertical electron affinity. The optimal parametrization for the π-EFT was found to be t = 2.70 eV, U = 9.69 eV, Q = −0.65 eÅ^2 and ϵ = 1.56 with a RMS relative error of 4.2 percent in the fit of the excita-

tion spectrum. It would be interesting to compare the values of U and Q determined by this analysis with estimates from ab initio methods such as density functional theory. Note, however, that the use of "improved" values of the parameters in our effective Hamiltonian is unlikely to improve agreement with the experimental data that we considered, precisely because we optimized the π-EFT predictions for these quantities.

The top panel of Figure 1 shows the spectral function for gas-phase benzene within π-EFT, along with experimental values for the first optical excitation of the cation (3.04 eV), the vertical ionization energy (9.23 eV), and the vertical electron affinity (−1.12 eV). As a guide for the eye, the spectrum has been broadened artificially by using a tunneling-width matrix of $\Gamma_{nm} = (0.2\ \text{eV})\delta_{nm}$. The close agreement between the experimental values and the maxima of the spectral function suggests that our model is accurate at this energy scale. In particular, the accuracy of the theoretical value for the lowest optical excitation of the cation is noteworthy, as this quantity was not fit during the renormalization procedure but rather represents a prediction of π-EFT.

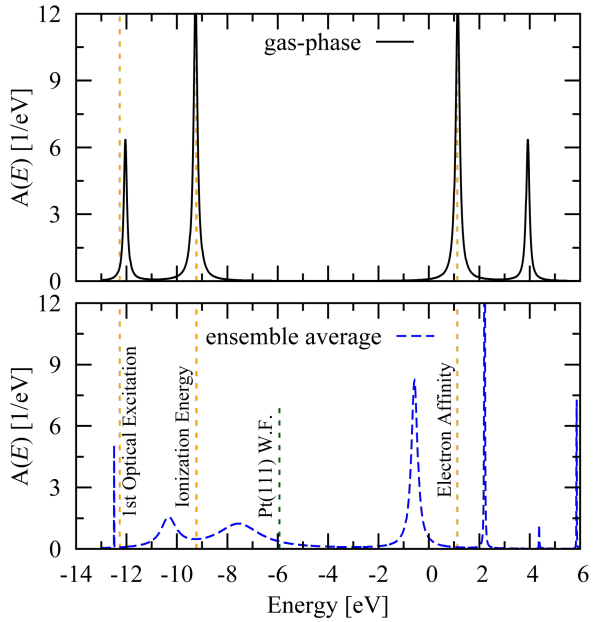

Figure 1: Spectral functions $A(E) = -(1/\pi)\mathrm{Tr}\{G(E)\}$ at room temperature for gas-phase benzene (top panel) and Pt–benzene–Pt junctions (ensemble average, bottom panel). The gas-phase resonances are broadened artificially as a guide for the eye. The dashed orange lines are fixed by (left to right) the lowest-lying optical excitation of the molecular cation [17-21], the vertical ionization energy of the neutral molecule [17-20,22], and the vertical electron affinity of the neutral molecule [23]. The asymmetry in the average spectral function arises because the HOMO resonance couples more strongly on average to the Pt tip atoms than does the LUMO resonance. The work function of the Pt(111) surface (−5.93 eV [24]) is shown for reference.

In order to incorporate screening by metallic electrodes into π-EFT, we utilized an image multipole method whereby the interaction between an orbital and image orbitals is included up to the quadrupole–quadrupole interaction in a screened interaction matrix $\tilde{U}_{nm}$. In particular, we chose a symmetric $\tilde{U}_{nm}$ that ensures the Hamiltonian gives the energy required to assemble the charge distribution from infinity with the electrodes maintained at fixed potential, namely

$$\tilde{U}_{nm} = U_{nm} + \delta_{nm}U^{(i)}_{nm} + \frac{1}{2}(1-\delta_{nm})\left(U^{(i)}_{nm} + U^{(i)}_{mn}\right),$$

where U_{nm} is the unscreened interaction matrix and $U^{(i)}_{nm}$ is the interaction between the nth orbital and the image of the mth orbital. When multiple electrodes are present, the image of an orbital in one electrode produces images in the others, resulting in an effect reminiscent of a hall of mirrors. We deal with this by including these "higher order" multipole moments iteratively until the difference between successive approximations of $\tilde{U}_{nm}$ drops below a predetermined threshold.

In the particular case of the Pt–benzene–Pt junction ensemble described in the next section, the electrodes of each junction are modeled as perfect spherical conductors. An orbital with monopole moment q and quadrupole moment Q^{ij} located a distance r from the center of an electrode with radius R then induces an image distribution at $\tilde{r} = \frac{R^2}{r}$ with monopole and quadrupole moments

$$\tilde{q} = -q\frac{R}{r} - \frac{R}{2r^3}\sum_{ij} Q^{ij}\hat{r}_i\hat{r}_j$$

and

$$\tilde{Q}^{ij} = -\left(\frac{R}{r}\right)^5 \sum_{kl} T_{ik}T_{jl}Q^{kl}$$

respectively. Here T_{ik} is a transformation matrix representing a reflection about the plane that is normal to the vector $\hat{r}$:

$$T_{ik} = \delta_{ik} - 2\hat{r}_i\hat{r}_k\ .$$

The lower panel of Figure 1 shows the Pt–benzene–Pt spectral function averaged over the ensemble of junctions described in the next section using this method. Comparing the spectrum with the gas-phase spectral function shown in the top panel of Figure 1, we see that screening due to the nearby Pt tips reduces the HOMO–LUMO gap by 33% on average, from 10.39 eV in the gas-phase to 6.86 eV over the junction ensemble.

The screening of intramolecular Coulomb interactions by nearby conductor(s) illustrated in Figure 1 leads to an attractive interaction between a molecule and a metal surface (van der Waals interaction). By diagonalizing the molecular Hamiltonian with and without the effects of screening included in U_{nm}, it is possible to determine the van der Waals interaction at arbitrary temperature between a neutral molecule and a metallic electrode by comparing the expectation values of the Hamiltonian in these two cases:

$$\Delta E_{vdW} = \left\langle \tilde{H} \right\rangle - \left\langle H \right\rangle$$

This procedure was carried out at zero temperature for benzene oriented parallel to the surface of a planar Pt electrode at a variety of distances, and the results are shown in Figure 2. Note that an additional phenomenological short-range repulsion proportional to r^{-12} has been included in the calculation to model the Pauli repulsion arising when the benzene π-orbitals overlap the Pt surface states.

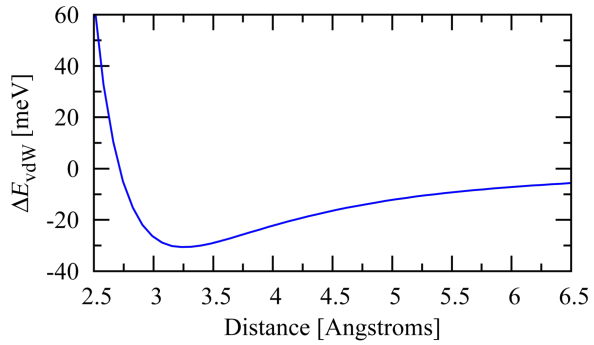

Figure 2: Calculated van der Waals contribution to the binding energy of benzene adsorbed on a Pt(111) surface as a function of distance. Here the plane of the molecule is oriented parallel to the Pt surface. A phenomenological short-range repulsion $\propto r^{-12}$ has been included to model the Pauli repulsion when the π-orbitals overlap the Pt surface states.

The lead–molecule coupling

When an isolated molecule is connected to electrodes and a molecular junction is formed, the energy levels of the molecule are broadened and shifted as a result of the formation of a lead–molecule bond and due to the electrostatic influence of the leads. The bonding between lead α and the molecule is described by the tunneling width matrix Γ^{α} and the electrostatics, including intramolecular screening and van der Waals effects, are described by the effective molecular Hamiltonian derived using the aforementioned π-EFT. Although we use the Pt–benzene–Pt junction as an example here, the techniques we discuss are applicable to any conjugated organic molecular junction.

Bonding

The bonding between the tip of electrode α and the molecule is characterized by the tunneling-width matrix Γ^{α} given by Equation 4. When a highly conductive SMJ [4] is formed, the lead and molecule are in direct contact such that the overlap between the π-electron system of the molecule and *all* of the quasi-atomic wavefunctions of the atomically sharp electrode are relevant. In this case we may express the elements of Γ^{α} as [6]

$$\Gamma^{\alpha}_{nm}(E) = 2\pi \sum_{l\in\{s,p,d,\ldots\}} C_l V_l^n \left(V_l^m\right)^* \rho_l^{\alpha}(E), \qquad (24)$$

where the sum is calculated over the evanescent tunneling modes emanating from the metal tip, labeled by their angular-momentum quantum numbers, $\rho_l^{\alpha}(E)$ is the local density of states on the apex atom of electrode α, and V_l^n is the tunneling matrix element of orbitals l [25]. The constants C_l can in principle be determined by matching the evanescent tip modes to the wavefunctions within the metal tip [25]; however, we set $C_l = C\forall l$ and determine the constant C by fitting to the peak of the experimental conductance histogram [4]. In the calculation of the matrix elements, we use the effective Bohr radius of a π-orbital $a^* = a_0/Z$, where $a_0 \approx 0.53$ Å is the Bohr radius and $Z = 3.22$ is the effective hydrogenic charge associated with the π-orbital quadrupole moment −0.65 eÅ^2, determined by π-EFT.

For each Pt tip, we include one *s*, three *p* and five *d* orbitals in our calculations, which represent the evanescent tunneling modes in free space outside the apex atom of the tip. At room temperature, the Pt density of states (DOS) $\rho^{\alpha}(E) = \Sigma_l \rho_l^{\alpha}(E)$ is sharply peaked around the Fermi energy [26] with $\rho^{\alpha}(\varepsilon_F) = 2.88$/eV [27]. In accordance with [25], we distribute the total DOS such that the *s* orbital contributes 10%, the *p* orbitals contribute 10%, and the *d* orbitals contribute 80%.

We are interested in investigating transport through stable junctions where the "atop" binding configuration of benzene on Pt has the largest binding energy [28-30]. In this configuration, the distance between the tip atom and the center of the benzene ring is ≈2.25 Å [4], giving a tip to orbital distance of ≈2.65 Å (the C–C bond distance is taken as 1.4 Å). The trace of $\Gamma^{\alpha}(\varepsilon_F)$ is shown as a function of tip position in Figure 3, where for each tip position the height was adjusted such that the distance to the closest carbon atom was 2.65 Å. From the figure, it is evident that the lead–molecule coupling strength is peaked when the tip is in the vicinity of the center of the benzene ring (whose outline is drawn schematically in black). As shown in [2], the hybridization contribution to the binding energy is

$$\Delta E_{\text{hyb}} = \sum_{\nu\in\mathcal{H}_{N-1}} \int_{\mu}^{\infty} \frac{dE}{2\pi} \frac{\text{Tr}\{\Gamma(E)C(\nu,0_N)\}}{E-E_{0_N}+E_\nu} + \sum_{\nu'\in\mathcal{H}_{N+1}} \int_{-\infty}^{\mu} \frac{dE}{2\pi} \frac{\text{Tr}\{\Gamma(E)C(0_N,\nu')\}}{-E-E_{0_N}+E_{\nu'}},$$

which is roughly $\propto \text{Tr}\{\Gamma(\varepsilon_F)\}$. Here μ is the chemical potential of the lead metal, $\mathcal{H}_N$ is the N-particle molecular Hilbert space, and 0_N is the ground state of the N-particle manifold of the neutral molecule. The sharply peaked nature of $\text{Tr}\{\Gamma^\alpha\}$ seen in Figure 3 is thus consistent with the large binding energy of the atop configuration.

This result motivates our procedure for generating the ensemble of junctions, in which we consider the tip position in the plane parallel to the benzene ring to be a 2-D Gaussian random variable with a standard deviation of 0.25 Å, chosen to correspond with the preferred bonding observed in this region. For each position, the height of each electrode (one placed above the plane and one below) is adjusted such that the closest carbon to the apex atom of each electrode is at a distance of 2.65 Å. Each lead is positioned independently of the other. This procedure ensures that the full range of possible, bonded junctions are included in the ensemble.

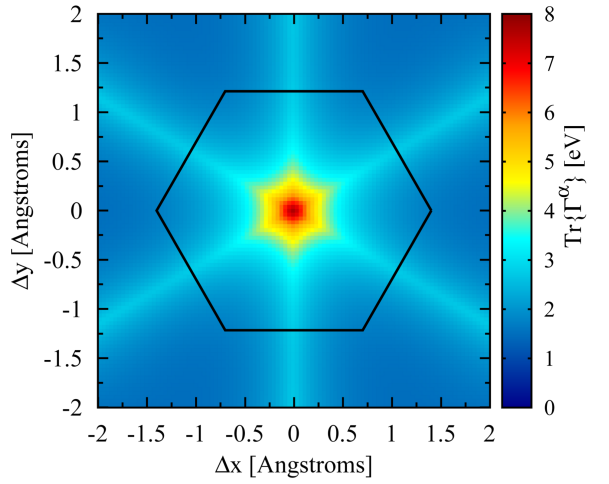

Figure 3: The trace of Γ^α for a Pt electrode in contact with a benzene molecule. Nine total basis states of the Pt tip are included in this calculation (one *s*, three *p* and five *d* states). The tip height above the plane of the molecule is adjusted at each point such that the Pt–C distance is fixed to 2.65 Å (see text). $\text{Tr}\{\Gamma^\alpha\}$ retains the (six-fold) symmetry of the molecule and is sharply peaked near the center of the benzene ring, indicating that the strongest bonds are formed when the lead is in the "atop" configuration. The benzene molecule is shown schematically with the black lines; the carbons atoms are located at each vertex.

The eigenvalue distributions of Γ^α over the ensemble are shown in Figure 4. Although we include nine (orthogonal) basis orbitals for each lead, the Γ matrix only exhibits five nonzero eigenvalues, presumably because only five linear combinations can be formed that are directed toward the molecule. Although we have shown the distribution for a single lead, the number of transmission channels for two leads, where each Γ^α matrix has the same rank, will be the same even though the overall lead–molecule coupling strength will be larger. The average coupling per orbital with two electrodes is shown in the bottom panel of Figure 5.

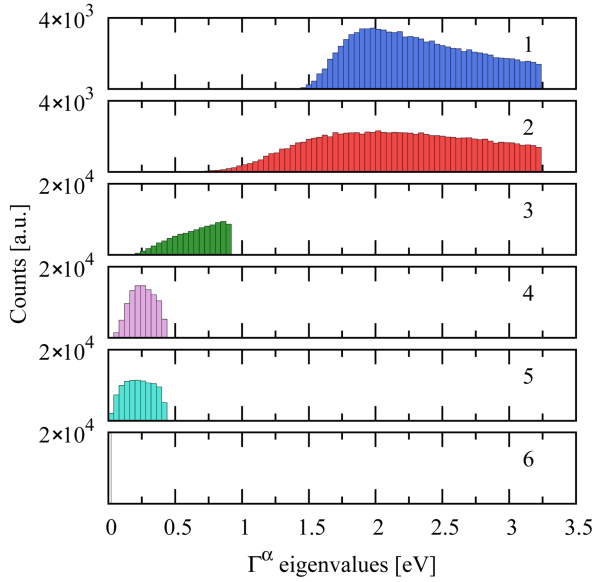

Figure 4: Eigenvalue decomposition of an ensemble of Γ^α matricies, showing that each lead–molecule contact has ~5 channels. Note that nine orthogonal basis orbitals were included in the calculation for each lead.

Screening

The ensemble of screened interaction matrices $\tilde{U}_{nm}$ is generated using the same procedure discussed above. Each Pt electrode is modelled as a conducting sphere with radius equal to the Pt polarization radius (1.87 Å). This is equivalent to the assumption that screening is due mainly to the apex atoms of each Pt tip. The screening surface is placed such that it lies one covalent radius away from the nearest carbon atom [14].

The average over the interaction matrix elements $\langle\tilde{U}_{nm}\rangle$ defines the "charging energy" of the molecule in the junction [14]. The charging energy $\langle\tilde{U}_{nm}\rangle$ and per-orbital $\text{Tr}\{\Gamma\}$ distributions are shown in the top and bottom panels of Figure 5, respectively, in which two electrodes are used in all calculations. As indicated by the figure, the $\text{Tr}\{\Gamma\}/6$ distribution is roughly four times as broad as the charging-energy distribution. This fact justifies the use of the ensemble-average $\tilde{U}_{nm}$ matrix for transport calculations [2], an approximation which makes the calculation of

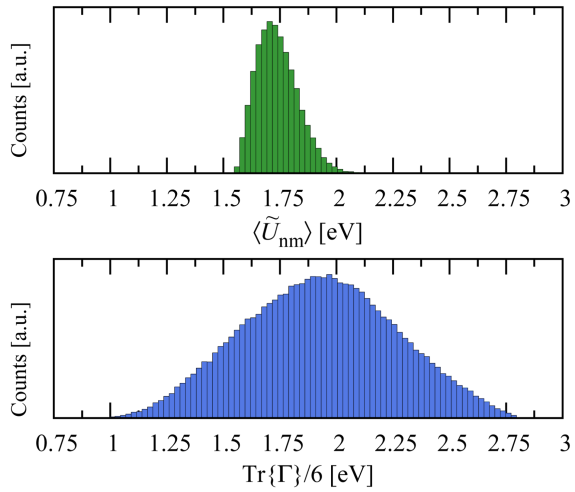

Figure 5: The distribution of charging energy $\langle \tilde{U}_{nm} \rangle$ (top panel) and Tr{Γ} (bottom panel) over the ensemble described in the text. Here $\Gamma = \Gamma^1 + \Gamma^2$ is the total tunneling-width matrix of the junction. The width of the Tr{Γ} distribution is about four times that of the $\langle \tilde{U}_{nm} \rangle$ distribution. The peaks of the $\langle \tilde{U}_{nm} \rangle$ and Tr{Γ}/6 distributions are at 1.68 eV and 1.95 eV, respectively, suggesting that transport occurs in an intermediate regime in which both the particle-like and wave-like character of the charge carriers must be considered.

thousands of junctions computationally tractable. The peak values of the $\langle \tilde{U}_{nm} \rangle$ and Tr{Γ}/6 distributions are 1.68 eV and 1.95 eV, respectively, suggesting that transport occurs in an intermediate regime in which both the particle-like and wave-like character of the charge carriers must be considered.

In addition to sampling various bonding configurations, we also consider an ensemble of junctions to sample all possible Pt surfaces. The work function of Pt ranges from 5.93 eV for the (111) surface to 5.12 eV for the (331) surface [24], and we assume that μ_{Pt} is distributed uniformly over this interval.

Using this ensemble, the conductance histogram over the ensemble of junctions can be computed, and is shown in Figure 6. The constant prefactor C appearing in the tunneling matrix elements [25] in Equation 24 was determined by fitting the peak of the calculated conductance distribution to that of the experimental conductance histogram [4]. Note that the width of the calculated conductance peak is also comparable to that of the experimental peak [4].

Results and Discussion

The transmission eigenvalue distributions for ensembles of 1.74×10^5 Pt–benzene–Pt junctions calculated by using the full many-body spectrum and in the isolated-resonance approximation are shown in Figure 7a and Figure 7b, respectively. Despite the existence of five covalent bonds between the molecule and

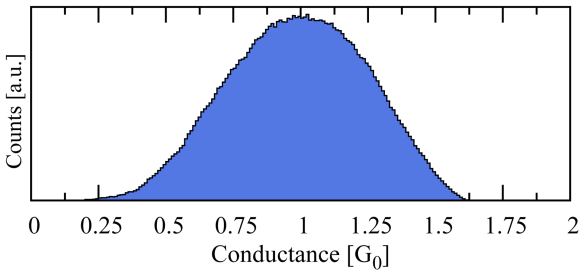

Figure 6: Calculated conductance histogram for the ensemble over bonding configurations and Pt surfaces. The value of the conductance peak has been fit to match the experimental data [4], determining the constant C in Equation 24. There is no peak for $G \sim 0$ because we designed an ensemble of junctions where both electrodes are strongly bound to the molecule.

each lead (cf. Figure 4), there are only two dominant transmission channels, which arise from the two-fold-degenerate HOMO resonance closest to the Pt Fermi level [2]. As proof of this point, we calculated the transmission eigenvalue distribution, over the same ensemble, using only the HOMO resonance in the isolated-resonance approximation (Equation 19). The resulting transmission eigenvalue distributions, shown in Figure 7b, are nearly identical to the full distribution shown in Figure 7a, with the exception of the small but experimentally resolvable [4] third transmission channel.

The lack of a third channel in the isolated-resonance approximation is a direct consequence of the two-fold degeneracy of the HOMO resonance, which can therefore contribute at most two transmission channels. The third channel thus arises from further off-resonant tunneling. In fact, we would argue that the very observation of a third channel in some Pt–benzene–Pt junctions [4] is a consequence of the very large lead–molecule coupling (~2 eV per atomic orbital) in this system. Having simulated junctions with electrodes whose DOS at the Fermi level is smaller than that of Pt, we expect junctions with Cu or Au electrodes, for example, to exhibit only two measurable transmission channels.

In order to investigate the efficacy of the isolated-resonance approximation further, we calculated the average total transmission through a Pt–benzene–Pt junction. The transmission spectra calculated using the full molecular spectrum, the isolated HOMO resonance and the isolated LUMO resonance are each shown as a function of the chemical potential of the leads μ_{Pt} in Figure 8. The spectra are averaged over 2000 bonding configurations and the blue shaded area indicates the range of possible chemical potentials for the Pt electrodes. The close correspondence between the full transmission spectrum and the isolated HOMO resonance over this range is consistent with the accuracy of the approximate method shown in

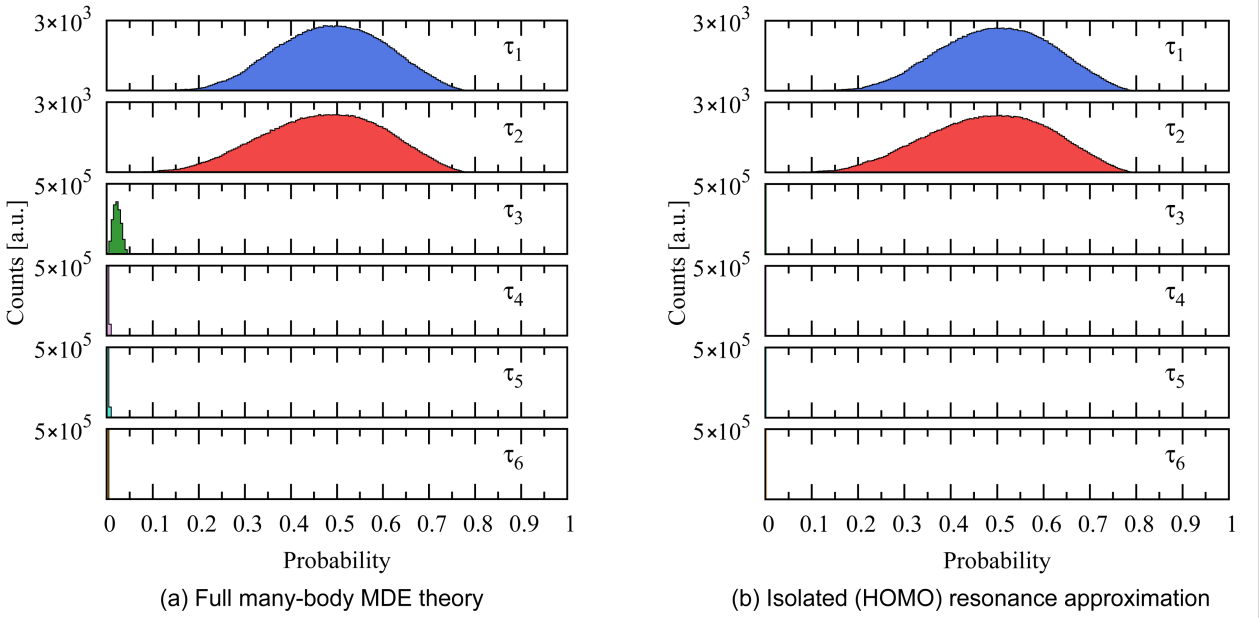

Figure 7: The calculated eigenvalue distributions for an ensemble of 1.74×10^5 (2000 bonding configurations × 87 Pt surfaces) Pt–benzene–Pt junctions using many-body theory with (a) the full spectrum and (b) the isolated-resonance approximation for the (doubly degenerate) HOMO resonance. Despite each lead forming ~5 bonds (cf. Figure 4), calculations in both cases exhibit only two dominant channels, which arise from the degeneracy of the relevant (HOMO) resonance. The weak third channel seen in (a) is a consequence of the large lead–molecule coupling and is consistent with the measurements of [4].

Figure 7. Similarly, in the vicinity of the LUMO resonance, the isolated LUMO resonance approximation accurately characterizes the average transmission. The HOMO–LUMO asymmetry in the average transmission function arises because the HOMO resonance couples more strongly on average to the Pt tip atoms than does the LUMO resonance.

It is tempting to assume, based on the accuracy of the isolated-resonance approximation in our many-body transport theory, that an analogous "single molecular orbital" approximation would also be sufficient in a transport calculation based, e.g., on density-functional theory (DFT). However, this is not the case. Although the isolated-resonance approximation can also be derived within DFT, in practice, it is necessary to use an "extended molecule" to account for charge transfer between molecule and electrodes. Analyzing transport in terms of extended molecular orbitals has proven problematic. For example, the resonances of the extended molecule in [31] apparently accounted for less than 9% of the current through the junction.

Employing an extended molecule also makes it difficult, if not impossible, to interpret transport contributions in terms of the resonances of the molecule itself [31]. Since charging effects in SMJs are well-described in our many-body theory [6,12], there is no need to utilize an extended molecule, and therefore the resonances in our isolated-resonance approximation are true molecular resonances.

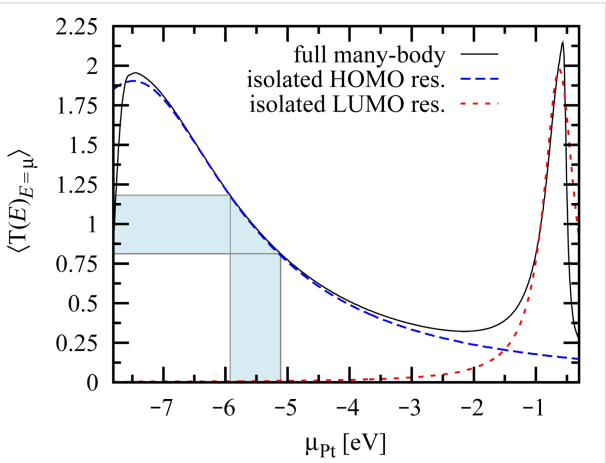

Figure 8: The calculated average total transmission averaged over 2000 bonding configurations through a Pt–benzene–Pt junction shown as a function of the chemical potential of the leads μ_{Pt}. The isolated-resonance approximation employing the HOMO or LUMO resonance accurately describes the full many-body transport in the vicinity of the HOMO or LUMO resonance, respectively. These data are in good agreement with the measurements of [4]. The work-function range for the crystal planes of Pt is shaded in blue, where $-5.93\ \text{eV} \le \mu_{Pt} \le -5.12\ \text{eV}$ [24].

The full counting statistics of a distribution are characterized by its cumulants. By using a single-particle theory to describe a single-channel junction, it can be shown [32,33] that the first cumulant is related to the junction transmission function, while the second cumulant is related to the shot-noise suppression. Often this suppression is phrased in terms of the Fano factor [34]

$$F = \sum_n \frac{\tau_n(1-\tau_n)}{\sum_n \tau_n}. \quad (25)$$

In Figure 9 we show the distribution of F for our ensemble of junctions, where the τ_n have been calculated from many-body theory. Because of the fermionic character of the charge carriers, $0 \le F \le 1$, with $F = 0$ corresponding to completely wavelike transport, and a value of $F = 1$ corresponding to completely particle-like transport. From the figure, we see that F is peaked at ~0.51 implying that both the particle *and* wave aspects of the carriers are important, a fact which is consistent with the commensurate charging energy and bonding strength (cf. Figure 5).

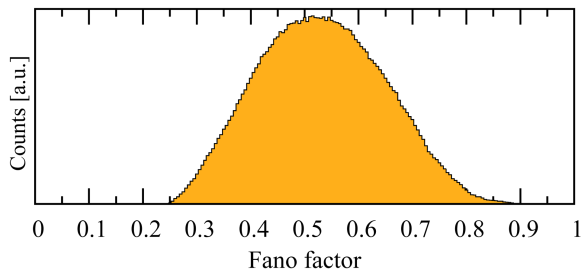

Figure 9: The calculated Fano factor F distribution for the full ensemble of 1.74×10^5 Pt–benzene–Pt junctions. F describes the nature of the transport, where $F = 0$ and $F = 1$ characterize wave-like and particle-like transport, respectively. The peak value of this distribution $F \sim 0.51$ indicates that we are in an intermediate regime.

In such an intermediate regime both "complementary" aspects of the charge carriers are equally important, requiring a many-body description and resulting in many subtle and interesting effects. For example, the transport in this regime displays a variety of features stemming from the interplay between Coulomb blockade and coherent-interference effects, which occur simultaneously [6,11]. Although the Fano factor reflects the nature of the transport, it is not directly related to the shot-noise power in a many-body theory. The richness of the transport in this regime, however, suggests that a full many-body calculation of a higher-order moment, such as the shot noise, may exhibit equally interesting phenomena.

Conclusion

We have developed a state-of-the-art technique to model the lead–molecule coupling in highly conductive molecular junctions. The bonding between the lead and molecule was described by using an "ab initio" model in which the tunneling matrix elements between all relevant lead tip wavefunctions and the molecule were included, producing multi-channel junctions naturally from a physically motivated ensemble over various contact geometries. Coulomb interactions between the molecule and the metallic leads were included by using an image multipole method within π-EFT. In concert, these techniques allowed us to accurately model SMJs within our many-body theory.

The transport for an ensemble of Pt–benzene–Pt junctions, calculated by using our many-body theory, confirmed our previous finding [2] that the number of dominant transmission channels is two, with the higher channels more strongly suppressed within the more realistic treatment of lead-molecule coupling presented here. Moreover, we find that the transport through a Pt–benzene–Pt junction can be accurately described by using only the relevant (two-fold-degenerate HOMO) molecular resonance. The exceptional accuracy of such an isolated-resonance approximation, however, may be limited to small molecules with large charging energies. In larger molecules, where the charging energy is smaller, further off-resonant transmission channels may become more important.

In metallic point contacts the number of channels is completely determined by the valence of the metal. Despite the larger number of states available for tunneling transport in SMJs, we predict that the number of transmission channels is typically more limited than in single-atom contacts because molecules are less symmetric than atoms. Channel-resolved transport measurements of SMJs therefore offer a unique probe into the symmetry of the molecular species involved.

Supporting Information

We investigate the origin of the transmission distribution widths by considering transport ensembles over Pt surfaces with fixed bonding, and over bonding configurations with a fixed Pt surface.

Supporting Information File 1

Transport distribution width decomposition
[http://www.beilstein-journals.org/bjnano/content/supplementary/2190-4286-3-5-S1.pdf]

Acknowledgements

This material is based upon work supported by the Department of Energy under Award Number DE-SC0006699.

References

1. Scheer, E.; Agraït, N.; Cuevas, J. C.; Levy Yeyati, A.; Ludoph, B.; Martín-Rodero, A.; Rubio Bollinger, G.; van Ruitenbeek, J. M.; Urbina, C. *Nature* **1998,** *394,* 154–157. doi:10.1038/28112
2. Bergfield, J. P.; Barr, J. D.; Stafford, C. A. *ACS Nano* **2011,** *5,* 2707–2714. doi:10.1021/nn1030753
3. "Molecular orbitals" are a single-particle concept and not defined in a many-body theory. Instead we define the "HOMO resonance" as the addition spectrum peak corresponding to the $N - 1 \rightarrow N$ electronic transition of the molecule, where N is the number of electrons in the neutral molecule. Similarly, we define the "LUMO resonance" as the addition spectrum peak corresponding to the $N \rightarrow N + 1$ transition.
4. Kiguchi, M.; Tal, O.; Wohlthat, S.; Pauly, F.; Krieger, M.; Djukic, D.; Cuevas, J. C.; van Ruitenbeek, J. M. *Phys. Rev. Lett.* **2008,** *101,* 046801. doi:10.1103/PhysRevLett.101.046801
5. Datta, S. *Electronic Transport in Mesoscopic Systems;* Cambridge University Press: Cambridge, UK, 1995; pp 117–174.
6. Bergfield, J. P.; Stafford, C. A. *Phys. Rev. B* **2009,** *79,* 245125. doi:10.1103/PhysRevB.79.245125
7. Toher, C.; Filippetti, A.; Sanvito, S.; Burke, K. *Phys. Rev. Lett.* **2005,** *95,* 146402. doi:10.1103/PhysRevLett.95.146402
8. Koentopp, M.; Burke, K.; Evers, F. *Phys. Rev. B* **2006,** *73,* 121403. doi:10.1103/PhysRevB.73.121403
9. Muralidharan, B.; Ghosh, A. W.; Datta, S. *Phys. Rev. B* **2006,** *73,* 155410. doi:10.1103/PhysRevB.73.155410
10. Geskin, V.; Stadler, R.; Cornil, J. *Phys. Rev. B* **2009,** *80,* 085411. doi:10.1103/PhysRevB.80.085411
11. Bergfield, J. P.; Jacquod, P.; Stafford, C. A. *Phys. Rev. B* **2010,** *82,* 205405. doi:10.1103/PhysRevB.82.205405
12. Bergfield, J. P.; Solomon, G. C.; Stafford, C. A.; Ratner, M. A. *Nano Lett.* **2011,** *11,* 2759–2764. doi:10.1021/nl201042m
13. Castleton, C. W. M.; Barford, W. *J. Chem. Phys.* **2002,** *117,* 3570–3582. doi:10.1063/1.1489994
14. Barr, J. D.; Bergfield, J. P.; Stafford, C. A. Effective Field Theory of Interacting π-Electrons 2011, arXiv:1108.0021v2 [cond-mat.mes-hall].
15. Djukic, D.; van Ruitenbeek, J. M. *Nano Lett.* **2006,** *6,* 789–793. doi:10.1021/nl060116e
16. Solomon, G. C.; Gagliardi, A.; Pecchia, A.; Frauenheim, T.; Di Carlo, A.; Reimers, J. R.; Hush, N. S. *Nano Lett.* **2006,** *6,* 2431–2437. doi:10.1021/nl0614516
17. Kovac, B.; Mohraz, M.; Heilbronner, E.; Boekelheide, V.; Hopf, H. *J. Am. Chem. Soc.* **1980,** *102,* 4314–4324. doi:10.1021/ja00533a005
18. Sell, J. A.; Kuppermann, A. *Chem. Phys.* **1978,** *33,* 367–378. doi:10.1016/0301-0104(78)87086-4
19. Kobayoshi, T. *Phys. Lett. A* **1978,** *69,* 105–108. doi:10.1016/0375-9601(78)90371-7
20. Schmidt, W. *J. Chem. Phys.* **1977,** *66,* 828–845. doi:10.1063/1.433961
21. Baltzer, P.; Karlsson, L.; Wannberg, B.; Öhrwall, G.; Holland, D. M. P.; MacDonald, M. A.; Hayes, M. A.; von Niessen, W. *Chem. Phys.* **1997,** *224,* 95–119. doi:10.1016/S0301-0104(97)00244-9
22. Howell, J. O.; Goncalves, J. M.; Amatore, C.; Klasinc, L.; Wightman, R. M.; Kochi, J. K. *J. Am. Chem. Soc.* **1984,** *106,* 3968–3976. doi:10.1021/ja00326a014
23. Burrow, P. D.; Michejda, J. A.; Jordan, K. D. *J. Chem. Phys.* **1987,** *86,* 9–24. doi:10.1063/1.452598
24. Lide, D. R., Ed. *CRC Handbook of Chemistry and Physics;* CRC Press: Boca Raton, FL, 2005.
25. Chen, C. J. *Introduction to Scanning Tunneling Microscopy,* 2nd ed.; Oxford University Press: New York, 1993.
26. Kleber, R. Z. *Phys. A: Hadrons Nucl.* **1973,** *264,* 301–308. doi:10.1007/BF01398856
27. Kittel, C. *Introduction to solid state physics,* 5th ed.; John Wiley and Sons, Inc.: New York, 1976.
28. Cruz, M. T. d. M.; Carneiro, J. W. d. M.; Aranda, D. A. G.; Bühl, M. *J. Phys. Chem. C* **2007,** *111,* 11068–11076. doi:10.1021/jp072572c
29. Morin, C.; Simon, D.; Sautet, P. *J. Phys. Chem. B* **2003,** *107,* 2995–3002. doi:10.1021/jp026950j
30. Saeys, M.; Reyniers, M.-F.; Marin, G. B.; Neurock, M. *J. Phys. Chem. B* **2002,** *106,* 7489–7498. doi:10.1021/jp0201231
31. Heurich, J.; Cuevas, J. C.; Wenzel, W.; Schön, G. *Phys. Rev. Lett.* **2002,** *88,* 256803. doi:10.1103/PhysRevLett.88.256803
32. Levitov, L. S.; Lee, H.; Lesovik, G. B. *J. Math. Phys.* **1996,** *37,* 4845–4866. doi:10.1063/1.531672
33. Levitov, L. S.; Lesovik, G. B. *JETP Lett.* **1993,** *58,* 230. http://adsabs.harvard.edu/abs/1993JETPL..58..230L
34. Büttiker, M. *Phys. Rev. Lett.* **1990,** *65,* 2901–2904. doi:10.1103/PhysRevLett.65.2901

Beilstein Journal of Nanotechnology

Current-induced forces in mesoscopic systems: A scattering-matrix approach

Niels Bode[1], Silvia Viola Kusminskiy[*1], Reinhold Egger[2] and Felix von Oppen[1]

Full Research Paper

Open Access

Address:
[1]Dahlem Center for Complex Quantum Systems and Fachbereich Physik, Freie Universität Berlin, 14195 Berlin, Germany and [2]Institut für Theoretische Physik, Heinrich-Heine-Universität, D-40225 Düsseldorf, Germany

Email:
Silvia Viola Kusminskiy[*] - silvia.kusminskiy@fu-berlin.de

* Corresponding author

Keywords:
current-induced forces; electronic transport theory; nanoelectromechanical systems; scattering matrix; S-matrix

Beilstein J. Nanotechnol. **2012,** *3,* 144–162.
doi:10.3762/bjnano.3.15

Received: 05 October 2011
Accepted: 10 January 2012
Published: 20 February 2012

This article is part of the Thematic Series "Transport through molecular junctions".

Guest Editor: J. M. van Ruitenbeek

Abstract

Nanoelectromechanical systems are characterized by an intimate connection between electronic and mechanical degrees of freedom. Due to the nanoscopic scale, current flowing through the system noticeably impacts upons the vibrational dynamics of the device, complementing the effect of the vibrational modes on the electronic dynamics. We employ the scattering-matrix approach to quantum transport in order to develop a unified theory of nanoelectromechanical systems out of equilibrium. For a slow mechanical mode the current can be obtained from the Landauer–Büttiker formula in the strictly adiabatic limit. The leading correction to the adiabatic limit reduces to Brouwer's formula for the current of a quantum pump in the absence of a bias voltage. The principal results of the present paper are the scattering-matrix expressions for the current-induced forces acting on the mechanical degrees of freedom. These forces control the Langevin dynamics of the mechanical modes. Specifically, we derive expressions for the (typically nonconservative) mean force, for the (possibly negative) damping force, an effective "Lorentz" force that exists even for time-reversal-invariant systems, and the fluctuating Langevin force originating from Nyquist and shot noise of the current flow. We apply our general formalism to several simple models that illustrate the peculiar nature of the current-induced forces. Specifically, we find that in out-of-equilibrium situations the current-induced forces can destabilize the mechanical vibrations and cause limit-cycle dynamics.

Introduction

Scattering theory has proved to be a highly successful method for treating coherent transport in mesoscopic systems [1]. Part of its appeal is rooted in its conceptual simplicity: Transport through a mesoscopic object can be described in terms of the transmission and reflection of electronic waves that are scattered by a potential. This approach was introduced by Landauer

[2,3] and generalized by Büttiker et al. [4] and leads to their well-known formula for the conductance of multiterminal mesoscopic conductors. For time-dependent phenomena, scattering-matrix expressions have been obtained for quantum pumping [5,6], a process by which a direct current is generated through temporal variations of relevant parameters of the system, such as a gate voltage or a magnetic field. The case of pumping in an out-of-equilibrium, biased system has remained largely unexplored so far [7,8].

The purpose of the present paper is to further develop the scattering-matrix approach into a simple, unifying formalism to treat nanoelectromechanical systems (NEMS). The coupling between mechanical and electronic degrees of freedom is the defining characteristic of NEMS [9,10], such as suspended quantum dots [11], carbon nanotubes or graphene sheets [12,13], one-dimensional wires [14], and molecular junctions [15,16]. For these systems, a transport current can excite mechanical modes, and vice versa, the mechanical motion affects the transport current. The reduced size and high sensitivity of the resulting devices make them attractive for applications such as sensors of mass or charge, nanoscale motors, or switches [17]. On a more fundamental level, the capability of cooling the system by means of back-action allows one to study quantum phenomena at the mesoscopic level, eventually reaching the quantum limit of measurement [18,19].

All of these applications require an understanding of the mechanical forces that act on the nanoelectromechanical system in the presence of a transport current. These are referred to as *current-induced forces*, and have been observed in seminal experiments [20,21]. Recently we have shown that it is possible to fully express the current-induced forces in terms of a scattering matrix formalism, for arbitrary (albeit adiabatic) out-of-equilibrium situations [22], thus providing the tools for a systematic approach to study the interplay between electronic and mechanical degrees of freedom in NEMS.

In the context of NEMS, two well-defined limits can be identified at which electronic and mechanical time scales decouple, and which give rise to different experimental phenomena. On one side, when the electronic time scales are slow compared with the mechanical vibrations, drastic consequences can be observed for the electronic transport, such as side bands due to phonon-assisted tunneling [23,24] or the Frank–Condon blockade effect, a phononic analogue of the Coulomb blockade in quantum dots [25-27]. In the opposite regime, electrons tunnel through the nanostructure rapidly, observing a quasi-static configuration of the vibrational modes, but affecting their dynamics profoundly at the same time [18-21]. It is on this regime that our present work focuses. We treat the vibrational degrees of freedom as classical entities embedded in an electronic environment: Pictorially, many electrons pass through the nanostructure during one vibrational period, impinging randomly on the modes. In this limit, it is natural to assume that the dynamics of the vibrational modes, represented by collective coordinates X_ν, will be governed by a set of coupled Langevin equations

$$M_\nu \ddot{X}_\nu + \frac{\partial U}{\partial X_\nu} = F_\nu - \sum_{\nu'} \gamma_{\nu\nu'} \dot{X}_{\nu'} + \xi_\nu . \qquad (1)$$

Here we have grouped the purely elastic contribution on the left-hand side (LHS) of Equation 1, M_ν being the effective mass of mode ν and $U(\mathbf{X})$ an elastic potential. On the right-hand side (RHS) we collected the current-induced forces: The mean force F_ν, a term proportional to the velocity of the modes $-\sum_{\nu'} \gamma_{\nu\nu'} \dot{X}_{\nu'}$, and the Langevin fluctuating forces ξ_ν. The main results of our work are expressions for the current-induced forces in terms of the scattering matrix and its parametric derivatives. These are given by Equation 39 for the mean force $F_\nu(\mathbf{X})$, Equation 42 for the correlator $D_{\nu\nu'}(\mathbf{X})$ of the stochastic force ξ_ν, and Equation 47, and Equation 50 for the two kinds of forces (dissipative-friction force and effective "Lorentz" force, as we discuss below) encoded by the matrix $\gamma_{\nu\nu'}(\mathbf{X})$.

These forces have been previously studied theoretically within different formalisms. The case of one electronic level coupled to one vibrational mode was studied within a Green's function approach in [28,29], in which the authors showed that the current-induced forces can lead to a bistable effective potential and consequently to switching. In [30], the authors studied the case of multiple vibrational modes within a linear approximation, finding a Lorentz-like current-induced force arising from the electronic Berry phase [31]. In simple situations, the current-induced forces have been also studied within a scattering matrix approach in the context of quantum measurement back-action [32] (see also [33]), momentum-transfer statistics [34], and of magnetic systems to describe Gilbert damping [35]. Current-induced forces have been shown to be of relevance near mechanical instabilities [36-38] and to drive NEMS into instabilities and strong nonlinear behavior [39-41]. Our formalism allows us to retain the nonlinearities of the problem, which is essential for even a qualitative description of the dynamics, while turning the problem of calculating the current-induced forces into a scattering problem for which standard techniques can be applied.

In what follows, we develop these ideas in detail, giving a thorough derivation of the expressions in terms of the scattering matrix for the current-induced forces found in [22], and include

several applications to specific systems. Moreover, we extend the theoretical results of [22] in two ways. We treat a general coupling between the collective modes X_ν and the electrons, generalizing the linear coupling expressions obtained previously. We also allow for an arbitrary energy dependence in the hybridization between the leads and the quantum dot, allowing more flexibility for modeling real systems. In the section "Microscopic derivation of the Langevin equation", we introduce the theoretical model, and derive the equations of motion of the mechanical degrees of freedom starting from a microscopic Hamiltonian. We show how the Langevin equation, Equation 1, emerges naturally from a microscopic model when employing the nonequilibrium Born–Oppenheimer (NEBO) approximation, appropriate for the limit of slow vibrational dynamics, and derive the current-induced forces in terms of the microscopic parameters. In the section "S-matrix theory of current-induced forces", we show that the current-induced forces can be written in terms of parametric derivatives of the scattering matrix (S-matrix) of the system, and state general properties that can be derived from S-matrix symmetry considerations. In the section "Current", we complete the discussion of nanoelectromechanical systems in terms of scattering matrices by providing a corresponding expression for the charge current. In the section "Applications", we apply our formalism to simple models of increasing complexity, namely a single resonant level, a two-level model, and a two-level/two-mode model. For better readability, we have relegated part of some lengthy calculations to Supporting Information File 1, together with a list of useful relations that are used throughout the main text.

Results and Discussion

Microscopic derivation of the Langevin equation

The model

We model the system as a mesoscopic quantum dot connected to multiple leads and coupled to vibrational degrees of freedom. Throughout this work we consider noninteracting electrons and we set $\hbar = 1$. The Hamiltonian for the full system reads

$$H = H_D + H_X + H_L + H_T, \tag{2}$$

where the different terms are introduced in the following.

We describe the quantum dot by M electronic levels coupled to N slow collective degrees of freedom $\mathbf{X} = (\hat{X}_1,\ldots,\hat{X}_N)$. This is contained in the Hamiltonian of the dot

$$H_D = \sum_{mm'} d_m^\dagger \left[h_0(\hat{\mathbf{X}}) \right]_{mm'} d_{m'} \tag{3}$$

which describes the electronic levels of the dot and their dependence on the coordinates of the collective modes, $\hat{X}_\nu$ ($\nu = 1,\ldots,N$), by the hermitian $M \times M$ matrix $h_0(\hat{\mathbf{X}})$. The operator $d^\dagger$ (d) creates (annihilates) an electron in the dot and the indices m, m' (= 1,…,M) label the electronic levels. Note that here we generalize our previous results obtained for a linear coupling in $\hat{\mathbf{X}}$ [22], and allow h_0 to be a general function of $\hat{\mathbf{X}}$. Our analysis is valid for any coupling strength. The free evolution of the "mechanical" degrees of freedom of the dot is described by the Hamiltonian

$$H_X = \sum_\nu \left[\frac{\hat{P}_\nu^2}{2M_\nu} + U(\hat{\mathbf{X}}) \right]. \tag{4}$$

The leads act as electronic reservoirs kept at fixed chemical potentials μ_α and are described by

$$H_L = \sum_\eta \left(\varepsilon_\eta - \mu_\alpha \right) c_\eta^\dagger c_\eta, \tag{5}$$

where we represent the electrons in the leads by the creation (annihilation) operators $c^\dagger$ (c). The electrons in the leads obey the Fermi–Dirac distribution

$$f_\alpha(\varepsilon) = \left[1 + \mathrm{e}^{(\varepsilon-\mu_\alpha)/kT} \right]^{-1}.$$

The leads are labeled by $\alpha = 1,\ldots,L$, each containing channels $n = 1,\ldots,N_\alpha$. We combine $\eta = (\alpha,n)$ into a general "lead" index, $\eta = 1,\ldots,N_0$ with $N_0 = \sum_\alpha N_\alpha$.

Finally, the Hamiltonian H_T represents the tunneling between the leads and the levels in the dot,

$$H_T = \sum_{\eta,m} (c_\eta^\dagger W_{\eta m} d_m + \text{h.c.}). \tag{6}$$

Nonequilibrium Born–Oppenheimer approximation

We use as a starting point the Heisenberg equations of motion for the mechanical modes, which can be cast as

$$M_\nu \ddot{\hat{X}}_\nu + \frac{\partial U}{\partial \hat{X}_\nu} = -\sum_{n,n'} d_n^\dagger \left[\Lambda_\nu(\hat{\mathbf{X}}) \right]_{nn'} d_{n'}, \tag{7}$$

where we have introduced the $\hat{\mathbf{X}}$-dependent matrices

$$\Lambda_\nu\left(\hat{\mathbf{X}}\right) = \frac{\partial h_0}{\partial \hat{X}_\nu}. \tag{8}$$

The RHS of Equation 7 contains the current-induced forces, expressed through the electronic operators d of the quantum dot. We now proceed to calculate these forces within a nonequilibrium Born–Oppenheimer (NEBO) approximation, in which the dynamics of the collective modes is assumed to be slow. In this limit, we can treat the mechanical degrees of freedom as being classical, acting as a slow classical field on the fast electronic dynamics.

The NEBO approximation involves averaging the RHS of Equation 7 over times long compared to the electronic time scale, but short in terms of the oscillator dynamics. In this approximation, the force operator is represented by its (average) expectation value $\langle d^\dagger \Lambda d\rangle_{\mathbf{X}(t)}$, evaluated for a given trajectory $\mathbf{X}(t)$ of the mechanical degrees of freedom, plus fluctuations containing both Johnson–Nyquist and shot noise. These fluctuations give rise to a Langevin force ξ_ν. Hence Equation 7 becomes

$$M_\nu \ddot{X}_\nu + \frac{\partial U}{\partial X_\nu} = \mathrm{tr}[i\Lambda_\nu \mathcal{G}^<(t,t)] + \xi_\nu \ , \tag{9}$$

where the trace "tr" is taken over the dot levels, and we have introduced the lesser Green's function

$$\mathcal{G}^<_{nn'}(t,t') = i\langle d^\dagger_{n'}(t') d_n(t)\rangle_{\mathbf{X}(t)} \ . \tag{10}$$

The variance of the stochastic force ξ_ν is governed by the symmetrized fluctuations of the operator $d^\dagger \Lambda d$. Given that the electronic fluctuations happen on short time scales, ξ_ν is locally correlated in time,

$$\langle \xi_\nu(t)\xi_{\nu'}(t')\rangle = D_{\nu\nu'}(\mathbf{X})\delta(t-t'). \tag{11}$$

(An alternative, but equivalent, derivation is based on a saddle-point approximation for the Keldysh action, see, e.g., [42]). Since we are dealing with noninteracting electrons, $D(\mathbf{X})$ can be expressed in terms of single particle Green's functions by using Wick's theorem. This readily yields

$$\langle \xi_\nu(t)\xi_{\nu'}(t')\rangle = \mathrm{tr}\{\Lambda_\nu \mathcal{G}^>(t,t')\Lambda_{\nu'}\mathcal{G}^<(t',t)\}_s \ , \tag{12}$$

where

$$\mathcal{G}^>_{mm'}(t,t') = -i\langle d_m(t) d^\dagger_{m'}(t')\rangle_{\mathbf{X}(t)} \tag{13}$$

is the greater Green's function. These expressions for the current-induced forces show that we need to evaluate the electronic Green's function for a given classical trajectory $\mathbf{X}(t)$. In doing so, we can exploit the assumption that the mechanical degrees of freedom are slow compared to the electrons. Thus, we can approximate the Green's function by its solution to first order in the velocities $\dot{\mathbf{X}}(t)$. We now proceed with this derivation, starting with the Dyson equation for the retarded Green's function

$$\mathcal{G}^R_{mm'}(t,t') = -i\theta(t-t')\langle\{d_m(t), d^\dagger_{m'}(t')\}\rangle_{\mathbf{X}(t)} \ . \tag{14}$$

Here $\{.,.\}$ indicates the anticommutator. We note that since we consider noninteracting electrons, we can restore the lesser and greater Green's functions (or the advanced Green's function $\mathcal{G}^A$) at the end of the calculation by standard manipulations.

The hybridization with the leads is taken into account through the self-energy [43]

$$\Sigma^R(\varepsilon) = -i\sum_\alpha \Gamma_\alpha(\varepsilon), \tag{15}$$

which is given in terms of the width functions

$$\Gamma_\alpha(\varepsilon) = \pi W^\dagger(\varepsilon)\Pi_\alpha W(\varepsilon). \tag{16}$$

Here we have defined Π_α as a projection operator onto lead α and absorbed the square root factors of the density of states in the leads into the coupling matrix W for notational simplicity. Note that we allow W to depend on energy. (Compare with the wide-band limit discussed in [22], which employs an energy-independent hybridization Γ.)

Dyson's equation for the retarded Green's function can then be written, in matrix form, as

$$\begin{aligned} -i\partial_{t'}\mathcal{G}^R(t,t') = \delta(t-t') + \int \mathrm{d}t_1 \mathcal{G}^R(t,t_1)\Sigma^R(t_1,t') \\ + \mathcal{G}^R(t,t')h_0(\mathbf{X}) \, . \end{aligned} \tag{17}$$

To perform the adiabatic expansion, it is convenient to work in the Wigner representation, in which fast and slow time scales are easily identifiable. The Wigner transform of a function $A(t_1,t_2)$ depending on two time arguments is given by

$$\tilde{A}(t,\varepsilon) = \int \mathrm{d}\tau \, \mathrm{e}^{i\varepsilon\tau} A(t+\tau/2, t-\tau/2). \tag{18}$$

Using this prescription for the Green's function $\mathcal{G}^R$, the slow mechanical motion implies that $\mathcal{G}^R$ varies slowly with the central time $t = (t_1 + t_2)/2$ and oscillates fast with the relative

time $\tau = t_1 - t_2$. The Wigner transform of a convolution $C(t_1,t_2) = \int \mathrm{d}t_3 A(t_1,t_3)B(t_3,t_2)$ is given by

$$\begin{aligned}\widetilde{C} &= \exp\left[\frac{i}{2}\left(\partial_\varepsilon^{\widetilde{A}}\partial_t^{\widetilde{B}} - \partial_t^{\widetilde{A}}\partial_\varepsilon^{\widetilde{B}}\right)\right]\widetilde{A}\widetilde{B} \\ &\approx \widetilde{A}\widetilde{B} + \frac{i}{2}\partial_\varepsilon\widetilde{A}\partial_t\widetilde{B} - \frac{i}{2}\partial_t\widetilde{A}\partial_\varepsilon\widetilde{B},\end{aligned} \tag{19}$$

where we have dropped the higher-order derivatives in the last line, exploiting the slow variation with t. Therefore, using Equation 19 we can rewrite the Dyson equation (Equation 17) as

$$1 \approx \mathcal{G}^R\left(\varepsilon - \Sigma^R - h_0\right) - \frac{i}{2}\partial_\varepsilon\mathcal{G}^R\partial_t h_0 - \frac{i}{2}\partial_t\mathcal{G}^R\left(1 - \partial_\varepsilon\Sigma^R\right), \tag{20}$$

where the Green's functions are now in the Wigner representation. Unless otherwise denoted by explicitly stating the variables, here and in the following all functions are in the Wigner representation. Finally, with the help of Equation 91 and Equation 92 from Supporting Information File 1, Section A, we obtain

$$\mathcal{G}^R \approx G^R + \frac{i}{2}\sum_\nu \dot{X}_\nu\left(\partial_\varepsilon G^R\Lambda_\nu G^R - G^R\Lambda_\nu\partial_\varepsilon G^R\right), \tag{21}$$

in terms of the strictly adiabatic Green's function

$$G^R(\varepsilon,\mathbf{X}) = \left[\varepsilon - h_0(\mathbf{X}) - \Sigma^R(\varepsilon)\right]^{-1}. \tag{22}$$

Our notation is such that $\mathcal{G}$ denotes *full* Green's functions, while G denotes the strictly adiabatic (or *frozen*) Green's functions that are evaluated for a fixed value of $\mathbf{X}$ (such that all derivatives with respect to central time in Equation 20 can be dropped). From now on, $\mathcal{G}^{(R,A,<,>)}$ denote the Green functions in the Wigner representation, with arguments (ε,t) and $\mathcal{G}^A = (\mathcal{G}^R)^\dagger$.

Using Langreth's rule (see, e.g., [43])

$$\mathcal{G}^<(t,t') = \int \mathrm{d}t_1 \int \mathrm{d}t_2\, \mathcal{G}^R(t,t_1)\Sigma^<(t_1,t_2)\mathcal{G}^A(t_2,t'), \tag{23}$$

we can relate $\mathcal{G}^<$ to $\mathcal{G}^R$. In Equation 23 we have introduced the lesser self energy $\Sigma^<$, which in the Wigner representation takes the form

$$\Sigma^<(\varepsilon) = 2i\sum_\alpha f_\alpha(\varepsilon)\Gamma^\alpha(\varepsilon). \tag{24}$$

Note that $\Sigma^<$ depends only on ε and is independent of the central time. Expanding Equation 23 up to the leading adiabatic correction according to Equation 19, we obtain $\mathcal{G}^<$ to first order in $\dot{\mathbf{X}}$,

$$\begin{aligned}\mathcal{G}^< = G^< + \frac{i}{2}\sum_\nu \dot{X}_\nu\Big[&(\partial_\varepsilon G^<)\Lambda_\nu G^A - G^R\Lambda_\nu\partial_\varepsilon G^< \\ &+ (\partial_\varepsilon G^R)\Lambda_\nu G^< - G^<\Lambda_\nu\partial_\varepsilon G^A\Big],\end{aligned} \tag{25}$$

with $G^< = G^R\Sigma^<G^A$.

Current-induced forces in terms of Green's functions

We can now collect the results from the previous section and identify the current-induced forces appearing in the Langevin Equation 1. Except for the stochastic noise force, the current-induced forces are encoded in $\mathrm{tr}(\mathcal{G}^<\Lambda_\nu)$. In the strictly adiabatic limit, i.e., retaining only the first term on the RHS of Equation 25, $\mathcal{G}^< \approx G^<$, we obtain the mean force

$$F_\nu(\mathbf{X}) = -\int\frac{\mathrm{d}\varepsilon}{2\pi i}\,\mathrm{tr}\left[\Lambda_\nu G^<\right]. \tag{26}$$

The leading-order correction in Equation 25 gives a velocity-dependent contribution to the current-induced forces, which determines the tensor $\gamma_{\nu\nu'}$. After integration by parts, we find

$$\gamma_{\nu\nu'} = \int\frac{\mathrm{d}\varepsilon}{2\pi}\mathrm{tr}\left(G^<\Lambda_\nu\partial_\varepsilon G^R\Lambda_{\nu'} - G^<\Lambda_{\nu'}\partial_\varepsilon G^A\Lambda_\nu\right).$$

This tensor can be split into symmetric and antisymmetric contributions, $\gamma = \gamma^s + \gamma^a$, which define a dissipative term γ^s and an orbital effective magnetic field γ^a in the space of the collective modes. This interpretation is based on the fact that the corresponding force takes a Lorentz-like form. Using Equation 87 in Supporting Information File 1, Section A, and noting that $2\int \mathrm{d}\varepsilon G^<\partial_\varepsilon G^< = \int \mathrm{d}\varepsilon\partial_\varepsilon(G^<)^2 = 0$, we obtain the explicit expressions

$$\gamma^s_{\nu\nu'}(\mathbf{X}) = \int\frac{\mathrm{d}\varepsilon}{2\pi}\mathrm{tr}\left\{\Lambda_\nu G^<\Lambda_{\nu'}\partial_\varepsilon G^>\right\}_s, \tag{27}$$

$$\gamma^a_{\nu\nu'}(\mathbf{X}) = -\int\frac{\mathrm{d}\varepsilon}{2\pi}\mathrm{tr}\left\{\Lambda_\nu G^<\Lambda_{\nu'}\partial_\varepsilon\left(G^A + G^R\right)\right\}_a. \tag{28}$$

Here we have introduced the notation

$$\{A_{\nu\nu'}\}_{s,a} = \frac{1}{2}\left(A_{\nu\nu'} \pm A_{\nu'\nu}\right)$$

for symmetric and antisymmetric parts of an arbitrary matrix A.

Finally, the stochastic force ξ_ν is given by the thermal and nonequilibrium fluctuations of the force operator $-d^\dagger\Lambda_\nu d$ in Equation 7. As indicated by the fluctuation–dissipation theorem, the fluctuating force is of the same order in the adiabatic expansion as the velocity-dependent force. Thus, we can evaluate the expression for the correlator $D_{\nu\nu'}(\mathbf{X})$ of the fluctuating force given in Equation 12 to lowest order in the adiabatic expansion, such that

$$D_{\nu\nu'}(\mathbf{X}) = \int \frac{d\varepsilon}{2\pi} \mathrm{tr}\left\{\Lambda_\nu G^< \Lambda_{\nu'} G^>\right\}_s . \tag{29}$$

This formalism gives the tools needed to describe the dynamics of the vibrational modes in the presence of a bias for an arbitrary number of modes and dot levels. When Equation 26–Equation 28 are inserted back into Equation 1, they define a nonlinear Langevin equation due to their nontrivial dependencies on $\mathbf{X}(t)$ [28,29].

S-matrix theory of current-induced forces

Adiabatic expansion of the S-matrix

Scattering matrix approaches to mesoscopic transport generally involve expressions in terms of the elastic S-matrix. For our problem, the S-matrix is elastic only in the strictly adiabatic limit, in which it is evaluated for a fixed value of $\mathbf{X}$,

$$S(\varepsilon,\mathbf{X}) = 1 - 2\pi i W(\varepsilon) G^R(\varepsilon,\mathbf{X}) W^\dagger(\varepsilon) . \tag{30}$$

As pointed out by Moskalets and Büttiker [8,44], this is not sufficient for general out-of-equilibrium situations, even when $\mathbf{X}(t)$ varies in time adiabatically. In their work, they calculated, within a Floquet formalism, the leading correction to the strictly adiabatic S-matrix. We follow the same approach here, rephrased in terms of the Wigner representation. The full S-matrix can be written as [45] (note that, in line with the notation established before for the Green's functions, the strictly adiabatic S-matrix is denoted by S, whereas the full S-matrix is denoted by $\mathcal{S}$)

$$\mathcal{S}(\varepsilon,t) = 1 - 2\pi i \left[W \mathcal{G}^R W^\dagger \right](\varepsilon,t) . \tag{31}$$

To go beyond the frozen approximation, we expand $\mathcal{S}$ to leading order in $\dot{\mathbf{X}}$,

$$\mathcal{S}(\varepsilon,t) \cong S(\varepsilon,\mathbf{X}(t)) + \sum_\nu \dot{X}_\nu(t) A_\nu(\varepsilon,\mathbf{X}(t)) . \tag{32}$$

Thus, the leading correction defines the matrix A, which, similar to S, has definite symmetry properties. In particular, if the system is time-reversal invariant, the adiabatic S-matrix is even under time reversal, whereas A is odd. For a given problem, the A-matrix has to be obtained along with S.

We can now derive a Green's function expression for the matrix A [46,47]. Comparing Equation 32 with the expansion to the same order of $\mathcal{S}$ in terms of adiabatic Green's functions (obtained in a straightforward manner by performing the convolution in Equation 31 explicitly and keeping terms up to $\dot{\mathbf{X}}$) we obtain

$$\begin{aligned} A_\nu(\varepsilon,\mathbf{X}) = {} & \pi\partial_\varepsilon\left[W(\varepsilon) G^R(\varepsilon,\mathbf{X}) \right] \Lambda_\nu(\mathbf{X}) G^R(\varepsilon,\mathbf{X}) W^\dagger(\varepsilon) \\ & - \pi W(\varepsilon) G^R(\varepsilon,\mathbf{X}) \Lambda_\nu(\mathbf{X}) \partial_\varepsilon\left[G^R(\varepsilon,\mathbf{X}) W^\dagger(\varepsilon) \right] . \end{aligned} \tag{33}$$

Current conservation constrains both the frozen and full scattering matrices to be unitary. From the unitarity of the frozen S-matrix, $S^\dagger S = \mathbf{1}$, we obtain the useful relation

$$\frac{\partial S^\dagger}{\partial X_\nu} S + S^\dagger \frac{\partial S}{\partial X_\nu} = 0 . \tag{34}$$

We will make use of Equation 34 repeatedly in the following sections. On the other hand, unitarity of the full S-matrix, $\mathcal{S}^\dagger\mathcal{S} = \mathbf{1}$, imposes a relation between the A-matrix and the frozen S-matrix. To first order in the velocity $\dot{\mathbf{X}}$ we have

$$\mathbf{1} = SS^\dagger + SA^\dagger + AS^\dagger + \frac{i}{2}\left(\frac{\partial S}{\partial\varepsilon}\frac{\partial S^\dagger}{\partial t} - \frac{\partial S}{\partial t}\frac{\partial S^\dagger}{\partial\varepsilon} \right) \tag{35}$$

where $A(\varepsilon,\mathbf{X}) = \sum_\nu A_\nu(\varepsilon,\mathbf{X})\,\dot{X}_\nu$. Therefore, S and A are related through

$$A_\nu S^\dagger + S A_\nu^\dagger = \frac{i}{2}\left(\frac{\partial S}{\partial X_\nu}\frac{\partial S^\dagger}{\partial\varepsilon} - \frac{\partial S}{\partial\varepsilon}\frac{\partial S^\dagger}{\partial X_\nu} \right) . \tag{36}$$

In the next section we will see that the A-matrix is essential to express the current-induced dissipation and "Lorentz" forces in Equation 27 and Equation 28.

Current-induced forces

Mean force: The mean force exerted by the electrons on the oscillator is given by Equation 26. Writing Equation 26 explicitly and using Equation 88 in Supporting Information File 1, Section A, we can express $G^<$ in terms of G^R and G^A and obtain

$$F_\nu(\mathbf{X}) = -\int \mathrm{d}\varepsilon \sum_\alpha f_\alpha \mathrm{tr}\left(\Lambda_\nu G^R W^\dagger \Pi_\alpha W G^A\right) = -\int \mathrm{d}\varepsilon \sum_\alpha f_\alpha \mathrm{tr}\left(\Pi_\alpha W G^A \Lambda_\nu G^R W^\dagger\right), \quad (37)$$

where the second equality exploits the cyclic invariance of the trace. Noting that, by Equation 93 in Supporting Information File 1, Section A,

$$W G^A \Lambda_\nu G^R W^\dagger = -\frac{1}{2\pi i} S^\dagger \frac{\partial S}{\partial X_\nu}, \quad (38)$$

Equation 37 can be expressed directly in terms of scattering matrices $S(\varepsilon,\mathbf{X})$ as

$$F_\nu(\mathbf{X}) = \sum_\alpha \int \frac{\mathrm{d}\varepsilon}{2\pi i} f_\alpha \mathrm{Tr}\left(\Pi_\alpha S^\dagger \frac{\partial S}{\partial X_\nu}\right). \quad (39)$$

Note that now the trace (denoted by "Tr") is over lead-space.

An important issue is whether this force is *conservative*, i.e., derivable from a potential. A necessary condition for this is a vanishing "curl" of the force,

$$\Omega_{\nu\nu'} \equiv \frac{\partial F_{\nu'}}{\partial X_\nu} - \frac{\partial F_\nu}{\partial X_{\nu'}} = \sum_\alpha \int \frac{\mathrm{d}\varepsilon}{\pi i} f_\alpha \ \mathrm{Tr}\left(\Pi_\alpha \frac{\partial S^\dagger}{\partial X_\nu}\frac{\partial S}{\partial X_{\nu'}}\right)_a . \quad (40)$$

From Equation 40 it is seen that the mean force is conservative in thermal equilibrium, where Equation 40 can be turned into a trace over a commutator of finite-dimensional matrices: Indeed, in equilibrium the sum over the lead indices can be directly performed since $f_\alpha = f$ for all α, and $\sum_\alpha \Pi_\alpha = 1$. Using the unitarity of the S-matrix and the cyclic property of the trace, we obtain:

$$\Omega_{\nu\nu'} = \int \frac{\mathrm{d}\varepsilon}{2\pi i} f \ \mathrm{Tr}\left(\frac{\partial S^\dagger}{\partial X_\nu}\frac{\partial S}{\partial X_{\nu'}} - \frac{\partial S^\dagger}{\partial X_{\nu'}} S S^\dagger \frac{\partial S}{\partial X_\nu}\right) = \int \frac{\mathrm{d}\varepsilon}{2\pi i} f \ \mathrm{Tr}\left(\frac{\partial S^\dagger}{\partial X_\nu}\frac{\partial S}{\partial X_{\nu'}} - \frac{\partial S}{\partial X_{\nu'}}\frac{\partial S^\dagger}{\partial X_\nu}\right) = 0, \quad (41)$$

where in the last line we have used Equation 34. In general, however, the mean force will be *nonconservative* in out-of-equilibrium situations, providing a way to exert work on the mechanical degrees of freedom by controlling the external bias potential [30,48,49].

Stochastic force: Next, we discuss the fluctuating force ξ_ν with variance $D_{\nu\nu'}$ given by Equation 29. Following a similar path as described in the previous subsection for the mean force F_ν, we can also express the variance, Equation 29, of the fluctuating force in terms of the adiabatic S-matrix. Thus,

$$D_{\nu\nu'}(\mathbf{X}) = \sum_{\alpha\alpha'} \int \frac{\mathrm{d}\varepsilon}{2\pi} F_{\alpha\alpha'} \times \mathrm{Tr}\left\{\Pi_\alpha \left[S^\dagger \frac{\partial S}{\partial X_\nu}\right]^\dagger \Pi_{\alpha'} S^\dagger \frac{\partial S}{\partial X_{\nu'}}\right\}_s , \quad (42)$$

where we have introduced the function $F_{\alpha\alpha'}(\varepsilon) = f_\alpha(\varepsilon)[1 - f_{\alpha'}(\varepsilon)]$. From Equation 42 it is straightforward to show that $D_{\nu\nu'}$ is positive-definite. By performing a unitary transformation to a basis in which $D_{\nu\nu'}$ is diagonal, using $\Pi_\alpha = \Pi_\alpha^2$ and the cyclic invariance of the trace, we obtain the expression

$$D_{\nu\nu}(\mathbf{X}) = \sum_{\alpha\alpha'} \int \frac{\mathrm{d}\varepsilon}{2\pi} F_{\alpha\alpha'} \times \mathrm{Tr}\left\{\left(\Pi_{\alpha'} S^\dagger \frac{\partial S}{\partial X_\nu}\Pi_\alpha\right)^\dagger \Pi_{\alpha'} S^\dagger \frac{\partial S}{\partial X_\nu}\Pi_\alpha\right\}_s . \quad (43)$$

which is evidently positive.

Damping matrix: So far, we were able to express quantities in terms of the frozen S-matrix only. This is no longer the case for the first correction to the strictly adiabatic approximation, given by Equation 27 and Equation 28. We start here with the first of these terms, the symmetric matrix γ^s, which is responsible for dissipation of the mechanical system into the electronic bath.

The manipulations to write the dissipation term as a function of S-matrix quantities are lengthy and the details are given in Supporting Information File 1, Section B. The damping matrix can be split into an "equilibrium" contribution, $\gamma^{s,eq}$, and a purely nonequilibrium contribution $\gamma^{s,ne}$, as $\gamma^s = \gamma^{s,eq} + \gamma^{s,ne}$. We first treat $\gamma^{s,eq}$. By the calculations given in Supporting Information File 1, Section B, we obtain

$$\gamma^{s,eq}_{\nu\nu'} = \frac{1}{4}\sum_{\alpha\alpha'} \int \frac{\mathrm{d}\varepsilon}{2\pi} \partial_\varepsilon (f_\alpha + f_{\alpha'}) \times \mathrm{Tr}\left\{\Pi_\alpha S^\dagger \frac{\partial S}{\partial X_\nu}\Pi_{\alpha'} S^\dagger \frac{\partial S}{\partial X_{\nu'}}\right\}_s = \frac{1}{2}\sum_\alpha \int \frac{\mathrm{d}\varepsilon}{2\pi}(-\partial_\varepsilon f_\alpha) \times \mathrm{Tr}\left(\Pi_\alpha \frac{\partial S^\dagger}{\partial X_\nu}\frac{\partial S}{\partial X_{\nu'}}\right), \quad (44)$$

where we have used $\sum_{\alpha'}\Pi_{\alpha'} = 1$, $S^\dagger S = \mathbf{1}$, and Equation 34 in the last line. Note that in general, $\gamma^{s,eq}$ also contains nonequilibrium contributions, but gives the only contribution to the damping matrix when in equilibrium. Equation 44 is analogous to the S-matrix expression obtained for dissipation in ferromagnets in thermal equilibrium, dubbed Gilbert damping [35].

To express $\gamma^{s,ne}$ in terms of S-matrix quantities, we have to make use of the A-matrix defined in Equation 33. Again the details are given in Supporting Information File 1, Section B, where we find, after lengthy manipulations, that

$$\gamma^{s,ne}_{\nu\nu'} = \int \frac{\mathrm{d}\varepsilon}{2\pi i}\sum_\alpha f_\alpha \mathrm{Tr}\left\{\Pi_\alpha\left(\frac{\partial S^\dagger}{\partial X_\nu}A_{\nu'} - A^\dagger_{\nu'}\frac{\partial S}{\partial X_\nu}\right)\right\}_s . \quad (45)$$

This quantity vanishes in equilibrium, as can be shown by using the properties of the S and A matrices. Since the sum over the leads can be directly performed in equilibrium, Expression 45 involves

$$\begin{aligned}\mathrm{Tr}\left\{\frac{\partial S^\dagger}{\partial X_\nu}A_{\nu'} - A^\dagger_{\nu'}\frac{\partial S}{\partial X_\nu}\right\}_s &= -\mathrm{Tr}\left\{\frac{\partial S}{\partial X_\nu}S^\dagger\left(A_{\nu'}S^\dagger + SA^\dagger_{\nu'}\right)\right\}_s \\ &= -\frac{i}{2}\mathrm{Tr}\left\{\frac{\partial S}{\partial X_\nu}S^\dagger\left(\frac{\partial S}{\partial X_{\nu'}}\frac{\partial S^\dagger}{\partial\varepsilon}\right.\right. \\ &\quad \left.\left. -S\frac{\partial S^\dagger}{\partial\varepsilon}\frac{\partial S}{\partial X_{\nu'}}S^\dagger\right)\right\}_s = 0\end{aligned} \quad (46)$$

in which we have used the unitarity of $\mathcal{S}$ and the cyclic invariance of the trace multiple times. In the first equality, we inserted $S^\dagger S = 1$ and used Equation 34; the second equality follows by inserting the identity (Equation 36) and using again Equation 34.

Finally, combining all terms, we obtain an S-matrix expression for the full damping matrix γ^s,

$$\begin{aligned}\gamma^s_{\nu\nu'}(\mathbf{X}) = &-\sum_\alpha\int\frac{\mathrm{d}\varepsilon}{4\pi}\partial_\varepsilon f_\alpha \mathrm{Tr}\left\{\Pi_\alpha\frac{\partial S^\dagger}{\partial X_\nu}\frac{\partial S}{\partial X_{\nu'}}\right\}_s \\ &+\sum_\alpha\int\frac{\mathrm{d}\varepsilon}{2\pi i}f_\alpha\mathrm{Tr}\left\{\Pi_\alpha\left(\frac{\partial S^\dagger}{\partial X_\nu}A_{\nu'} - A^\dagger_{\nu'}\frac{\partial S}{\partial X_\nu}\right)\right\}_s .\end{aligned} \quad (47)$$

Note that in equilibrium, by the relation $-\partial_\varepsilon f = f(1-f)/T$ and using Equation 34, the fluctuating force D and damping γ^s are related via

$$D_{\nu\nu'} = 2T\gamma^{s,eq}_{\nu\nu'} = 2T\gamma^s_{\nu\nu'} \quad (48)$$

as required by the fluctuation–dissipation theorem.

Following a similar set of steps as shown above for the variance $D_{\nu\nu'}$ in Equation 43, $\gamma^{s,eq}_{\nu\nu'}$ has positive eigenvalues. On the other hand, the sign of $\gamma^{s,ne}_{\nu\nu'}$ is not fixed, allowing the possibility of negative eigenvalues of γ^s. The possibility of negative damping is, therefore, a pure nonequilibrium effect. Several recent papers have demonstrated negative damping in specific out-of-equilibrium models [22,40,50,51].

Lorentz force: We turn now to the remaining term, the antisymmetric contribution γ^a given in Equation 28, which acts as an effective magnetic field. Using Equation 88 in Supporting Information File 1, Section A, it can be written as

$$\begin{aligned}\gamma^a_{\nu\nu'} = i\int\mathrm{d}\varepsilon\sum_\alpha f_\alpha\mathrm{Tr}\Big\{&\Pi_\alpha W G^A\Lambda_\nu\left(\partial_\varepsilon G^R\right. \\ &\left.+\partial_\varepsilon G^A\right)\Lambda_{\nu'}G^R W^\dagger\Big\}_a .\end{aligned} \quad (49)$$

In order to relate this to the scattering matrix, we use Equation 96 (Supporting Information File 1, Section A), which allows us to write γ^a in terms of the S-matrix as

$$\gamma^a_{\nu\nu'}(\mathbf{X}) = \sum_\alpha\int\frac{\mathrm{d}\varepsilon}{2\pi i}f_\alpha\mathrm{Tr}\left\{\Pi_\alpha\left(S^\dagger\frac{\partial A_\nu}{\partial X_{\nu'}} - \frac{\partial A^\dagger_\nu}{\partial X_{\nu'}}S\right)\right\}_a . \quad (50)$$

If the system is time-reversal invariant, γ^a vanishes in thermal equilibrium. This implies $\sum_\alpha\Pi_\alpha f_\alpha = f$, such that Equation 50 involves only

$$\begin{aligned}\mathrm{Tr}\left\{S^\dagger\frac{\partial A_\nu}{\partial X_{\nu'}} - \frac{\partial A^\dagger_\nu}{\partial X_{\nu'}}S\right\} &= \mathrm{Tr}\left\{\frac{\partial A^T_\nu}{\partial X_{\nu'}}S^* - S^T\frac{\partial A^*_\nu}{\partial X_{\nu'}}\right\} \\ &= \mathrm{Tr}\left\{-\frac{\partial A_\nu}{\partial X_{\nu'}}S^\dagger + S\frac{\partial A^\dagger_\nu}{\partial X_{\nu'}}\right\},\end{aligned}$$

yielding $\gamma^a = 0$ due to the cyclic invariance of the trace. In the last equality, we have used $S = S^T$ and $A = -A^T$ as implied by time-reversal invariance.

Out of equilibrium, γ^a generally does not vanish even for time-reversal-symmetric conductors, since the current effectively breaks time-reversal symmetry.

Current

So far we have focused on the effect of the electrons on the mechanical degrees of freedom. For a complete picture, we also need to consider the reverse effect of the mechanical vibrations on the electronic current. In the strictly adiabatic limit, this obviously has to reduce to the Landauer–Büttiker formula for the transport current. The leading adiabatic correction to the current in equilibrium is closely related to the phenomenon of quantum pumping, and we will see that our results in this limit essentially reduce to Brouwer's S-matrix formula for the pumping current [5]. Our full result is, however, more general since it gives the leading adiabatic correction to the current in arbitrary *nonequilibrium* situations [8].

The current through lead α is given by [43]:

$$I_\alpha = -e\langle \dot{N}_\alpha \rangle = ie \sum_{n,\eta\in\alpha} W_{\eta n} \langle c_\eta^\dagger(t) d_n(t)\rangle + \text{h.c.} \tag{51}$$

with $N_\alpha = \sum_{\eta\in\alpha} c_\eta^\dagger c_\eta$. Using the expressions for the self-energies this can be expressed in terms of the dot's Green's functions and self-energies,

$$I_\alpha(t) = e\int \mathrm{d}t'\, \mathrm{tr}\Big\{\mathcal{G}^R(t,t')\Sigma_\alpha^<(t',t) + \mathcal{G}^<(t,t')\Sigma_\alpha^A(t',t)\Big\} + \text{h.c.} \tag{52}$$

Again we use the separation of time scales and go to the Wigner representation, yielding

$$I_\alpha = e\int \frac{\mathrm{d}\varepsilon}{2\pi}\, \mathrm{tr}\Big\{\mathcal{G}^R\Sigma_\alpha^< + \mathcal{G}^<\Sigma_\alpha^A - \tfrac{i}{2}\Big(\partial_t\mathcal{G}^R\partial_\varepsilon\Sigma_\alpha^< + \partial_t\mathcal{G}^<\partial_\varepsilon\Sigma_\alpha^A\Big)\Big\} + \text{h.c.} \tag{53}$$

We split the current into an adiabatic contribution I_α^0 and a term proportional to the velocity X_μ:

$$X_\mu I_\alpha = I_\alpha^0 + I_\alpha^1. \tag{54}$$

We will express these quantities in terms of the scattering matrix.

Landauer–Büttiker current

The strictly adiabatic contribution to the current is given by

$$I_\alpha^0(\mathbf{X}) = e\int \frac{\mathrm{d}\varepsilon}{2\pi}\mathrm{tr}\Big\{\Big(G^R - G^A\Big)\Sigma_\alpha^< + G^<\Big(\Sigma_\alpha^A - \Sigma_\alpha^R\Big)\Big\}, \tag{55}$$

in which we have collected the purely adiabatic terms from Equation 21 and Equation 25. Inserting the expressions for the self-energies, Equation 15 and Equation 24, we can express this as

$$I_\alpha^0(\mathbf{X}) = e\int \frac{\mathrm{d}\varepsilon}{2\pi}\sum_\beta f_\beta 2\pi i\, \mathrm{Tr}\Big\{W\Big[\delta_{\alpha\beta}(G^R - G^A) + 2\pi i G^R W^\dagger \Pi_\beta W G^A\Big]W^\dagger\Pi_\alpha\Big\}, \tag{56}$$

in which we have used Equation 88 (Supporting Information File, Section A). Inserting the adiabatic S-matrix, Equation 30 yields

$$\begin{aligned} I_\alpha^0(\mathbf{X}) &= e\int \frac{\mathrm{d}\varepsilon}{2\pi}\sum_\beta f_\beta \mathrm{Tr}\Big\{\Big[\delta_{\alpha\beta} - S\Pi_\beta S^\dagger\Big]\Pi_\alpha\Big\} \\ &= e\int \frac{\mathrm{d}\varepsilon}{2\pi}\sum_\beta \Big(f_\alpha - f_\beta\Big)\,\mathrm{Tr}\Big\{S\Pi_\beta S^\dagger\Pi_\alpha\Big\}, \end{aligned} \tag{57}$$

where we used $\sum_\beta S\Pi_\beta S^\dagger = 1$ in the last line. We hence recover the usual expression for the Landauer–Büttiker current [4]. Note that the total adiabatic current depends implicitly on time through $\mathbf{X}(t)$, and is conserved at every instant of time, $\sum_\alpha I_\alpha^0(\mathbf{X}) = 0$. To obtain the *direct* current, we need to average this expression over the Langevin dynamics of the mechanical degrees of freedom. Alternatively, we can average the current expression with the probability distribution of $\mathbf{X}$, which can be obtained from the corresponding Fokker–Planck equation. Similar considerations would apply to calculations of the current noise.

First-order correction

We now turn to the first-order correction to the adiabatic approximation [8], restricting our considerations to the wide-band limit. The contribution to the current (Equation 53), which is linear in the velocity, reads

$$I_\alpha^1(\mathbf{X}) = e\int \frac{\mathrm{d}\varepsilon}{2\pi} i\sum_\mu \dot{X}_\mu\, \mathrm{tr}\Big\{(\partial_\varepsilon G^R)\Lambda_\mu G^R\Sigma_\alpha^< + \Big[(\partial_\varepsilon G^<)\Lambda_\mu G^A - G^R\Lambda_\mu(\partial_\varepsilon G^<)\Big]\Sigma_\alpha^A\Big\} + \text{h.c.}, \tag{58}$$

after integration by parts. Again, we insert Equation 88 from Supporting Information File 1, Section A, for the lesser Green's function, and Equation 15, and Equation 24 for the self-energies. In the wide-band limit, the identity $(i/2)\partial_\varepsilon\partial_{X\nu}S + A_\nu = W(\partial_\varepsilon G^R)\Lambda_\nu G^R W^\dagger$ holds, such that we can write

$$I^1_\alpha(\mathbf{X}) = -e\int\frac{\mathrm{d}\varepsilon}{2\pi}\dot{\mathbf{X}}\cdot\sum_\beta f_\beta \mathrm{Tr}\left[\left(\frac{i}{2}\frac{\partial^2 S}{\partial\varepsilon\partial\mathbf{X}}+\mathbf{A}\right)\Pi_\beta S^\dagger\Pi_\alpha\right]+\text{h.c.} \quad (59)$$

after straightforward calculation. After integration by parts, we can split this expression as

$$\begin{aligned} I^1_\alpha(\mathbf{X}) = &-\frac{e}{2\pi}\int \mathrm{d}\varepsilon\dot{\mathbf{X}} \\ &\cdot\sum_\beta \partial_\varepsilon f_\beta \mathrm{Im}\mathrm{Tr}\left\{\Pi_\alpha\frac{\partial S}{\partial\mathbf{X}}\Pi_\beta S^\dagger\right\} \\ &+\frac{e}{2\pi}\int \mathrm{d}\varepsilon\dot{\mathbf{X}} \\ &\cdot\sum_\beta f_\beta\ \mathrm{Re}\mathrm{Tr}\left\{i\Pi_\alpha\frac{\partial S}{\partial\mathbf{X}}\Pi_\beta\frac{\partial S^\dagger}{\partial\varepsilon}-2\Pi_\alpha\mathbf{A}\Pi_\beta S^\dagger\right\}. \end{aligned} \quad (60)$$

In equilibrium, the second term vanishes due to the identity in Equation 36, and the first term agrees with Brouwer's formula for the pumping current [5]. As for the strictly adiabatic contribution, the *direct* current is obtained by averaging over the probability distribution of **X**.

Applications

Resonant Level

To connect with the existing literature, as a first example we treat the simplest case within our formalism: A resonant level coupled to a single vibrational mode and attached to two leads on the left (L) and right (R). This model has been discussed in detail for zero temperature in [28,29], and it provides a simple description on how current-induced forces can be used to manipulate a molecular switch. Here we derive finite-temperature expressions for the current-induced forces for a generic coupling between electronic and mechanical degrees of freedom, starting from the scattering matrix of the system, and show how they reduce to the known results for zero temperature and linear coupling.

We consider $N = M = 1$, denoting the mode coordinate by X, the energy of the dot level by $\tilde{\varepsilon}(X)$, and the number of channels in the left and right leads by N_L and N_R, respectively. The Hamiltonian of the dot can then be written as

$$H_D = \tilde{\varepsilon}(X)d^\dagger d \quad (61)$$

and the hybridization matrix as $W^\dagger = (\mathbf{w}^L,\mathbf{w}^R)^\dagger$, with $\mathbf{w}^\alpha = (w^\alpha_1,\ldots w^\alpha_{N_\alpha})$ and $\alpha = L,R$. Hence the frozen S-matrix, Equation 30, is given by

$$S = \mathbf{1}-\frac{2\pi i}{\mathcal{L}}\begin{pmatrix}\mathbf{w}^L\left(\mathbf{w}^L\right)^\dagger & \mathbf{w}^L\left(\mathbf{w}^R\right)^\dagger \\ \mathbf{w}^R\left(\mathbf{w}^L\right)^\dagger & \mathbf{w}^R\left(\mathbf{w}^R\right)^\dagger\end{pmatrix}, \quad (62)$$

where $\mathcal{L}(\varepsilon,X) = \varepsilon-\varepsilon(X)+i\Gamma$, $\Gamma = \Gamma_L + \Gamma_R$, and $\Gamma_\alpha = \pi(\mathbf{w}^\alpha)^\dagger\cdot\mathbf{w}^\alpha$. Rotating to an eigenbasis of the lead channels, this S-matrix does not mix channels within the same lead, and hence we can project the S-matrix into a single nontrivial channel in each lead, to obtain

$$S = \mathbf{1}-\frac{2i}{\mathcal{L}}\begin{pmatrix}\Gamma_L & \sqrt{\Gamma_L\Gamma_R} \\ \sqrt{\Gamma_L\Gamma_R} & \Gamma_R\end{pmatrix}. \quad (63)$$

To calculate the mean force from Equation 39, we need an explicit expression for Equation 93 in Supporting Information File 1, Section A. This can be easily calculated to be

$$S^\dagger\frac{\partial S}{\partial X} = -\frac{\partial\tilde{\varepsilon}}{\partial X}\frac{2i}{|\mathcal{L}|^2}\begin{pmatrix}\Gamma_L & \sqrt{\Gamma_L\Gamma_R} \\ \sqrt{\Gamma_L\Gamma_R} & \Gamma_R\end{pmatrix} \quad (64)$$

and hence

$$F(X) = -\int\frac{\mathrm{d}\varepsilon}{\pi}\left[\frac{f_L\Gamma_L+f_R\Gamma_R}{|\mathcal{L}|^2}\right]\frac{\partial\tilde{\varepsilon}}{\partial X}. \quad (65)$$

Analogously, the variance of the stochastic force, Equation 42, becomes

$$D(X) = 2\int\frac{\mathrm{d}\varepsilon}{\pi}\sum_{\alpha\alpha'}\frac{\Gamma_\alpha\Gamma_{\alpha'}F_{\alpha\alpha'}}{|\mathcal{L}|^4}\left[\frac{\partial\tilde{\varepsilon}}{\partial X}\right]^2. \quad (66)$$

All that remains is to calculate the dissipation coefficient γ. Since there is only one collective mode, $\nu = 1$, γ is a scalar and hence $\gamma^a = 0$. Moreover, for energy-independent hybridization we have $\partial_\varepsilon G_R = -G_R^2$, and the A-matrix (Equation 33) can be written as [22]

$$A_\nu = -\pi W G_R[G_R,\Lambda_\nu]G_R W^\dagger. \quad (67)$$

Being the commutator of scalars, in this case $A_1 = 0$ and from Equation 47, γ^s must be positive and is given by Equation 44. (For an alternative derivation confirming the positive sign of the friction coefficient in a resonant-level system, see [52]). After

some manipulation, we obtain

$$\left(\frac{\partial S}{\partial X}\right)^{\dagger}\frac{\partial S}{\partial X}=4\left[\frac{\partial\tilde{\varepsilon}}{\partial X}\right]^{2}\frac{\Gamma}{|\mathcal{L}|^{2}}\begin{pmatrix}\Gamma_L & \sqrt{\Gamma_L\Gamma_R}\\ \sqrt{\Gamma_L\Gamma_R} & \Gamma_R\end{pmatrix}. \quad (68)$$

and hence the damping coefficient becomes

$$\gamma(X)=-\int\frac{\mathrm{d}\varepsilon}{\pi}\Gamma\frac{\Gamma_L\partial_\varepsilon f_L+\Gamma_R\partial_\varepsilon f_R}{|\mathcal{L}|^{4}}\left[\frac{\partial\tilde{\varepsilon}}{\partial X}\right]^{2}. \quad (69)$$

We can evaluate the remaining integrals analytically in the zero-temperature limit [28,29]. In the following we assume that $\mu_L \geq \mu_R$. The average force is given by

$$F(X)=-\frac{1}{\pi}\frac{\partial\tilde{\varepsilon}}{\partial X}\sum_{\alpha}\frac{\Gamma_\alpha}{\Gamma}\left[\arctan\left(\frac{\mu_\alpha-\tilde{\varepsilon}}{\Gamma}\right)+\frac{\pi}{2}\right]. \quad (70)$$

Similarly we obtain the dissipation coefficient

$$\gamma^{s}(X)=\frac{\Gamma}{\pi}\left[\frac{\partial\tilde{\varepsilon}}{\partial X}\right]^{2}\sum_{\alpha}\frac{\Gamma_\alpha}{\left[\left(\mu_\alpha-\tilde{\varepsilon}\right)^{2}+\Gamma^{2}\right]^{2}}, \quad (71)$$

together with the fluctuation kernel

$$D(X)=\frac{\Gamma_L\Gamma_R}{\pi\Gamma^{3}}\left[\frac{\partial\tilde{\varepsilon}}{\partial X}\right]^{2}\left[\arctan\left(\frac{\mu-\tilde{\varepsilon}}{\Gamma}\right)+\frac{\Gamma(\mu-\tilde{\varepsilon})}{\left(\mu-\tilde{\varepsilon}\right)^{2}+\Gamma^{2}}\right]\Bigg|_{\mu=\mu_R}^{\mu=\mu_L} \quad (72)$$

The position of the dot electronic level can be adjusted by an external gate voltage

$$eV_{\mathrm{gate}}=\frac{\mu_L+\mu_R}{2}-\varepsilon_0\,, \quad (73)$$

where the factor $(\mu_L + \mu_R)/2$ is included for convenience, in order to measure energies from the center of the conduction window. The difference in chemical potential between the leads is adjusted by a bias voltage

$$eV_{\mathrm{bias}}=\mu_L-\mu_R\,. \quad (74)$$

For a single vibrational mode, the average current-induced force is necessarily conservative and we can define a corresponding potential. Restricting our results now to linear coupling, we write the local level as $\tilde{\varepsilon}(X) = \varepsilon_0 + \lambda X$. In Figure 1, we show the effective potential $\tilde{U}(X) = \frac{M}{2}\omega_0^2X^2 - \int \mathrm{d}X F(X)$, which describes both the elastic and the current-induced forces at zero temperature and various bias voltages. Already this simple example shows that the current-induced forces can affect the mechanical motion qualitatively [29]. Indeed, the effective potential $\tilde{U}(X)$ can become multistable even for a purely harmonic elastic force, and depends sensitively on the applied bias voltage.

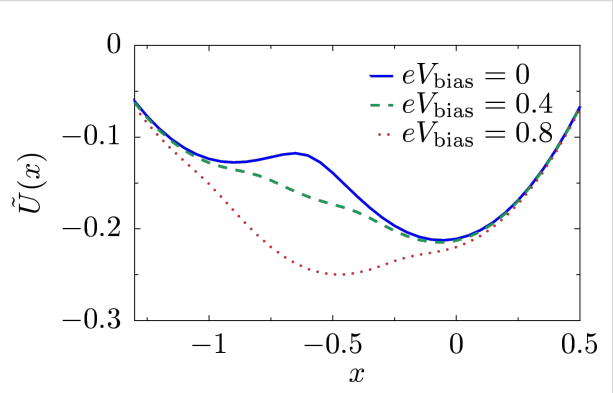

Figure 1: Resonant level. The shape of the effective potential $\tilde{U}(X)$ can be tuned by the bias voltage. We consider the parameters $eV_{\mathrm{gate}} = 0$, $\hbar\omega_0 = 0.01$ and $\Gamma = 0.1$. The dimensionless coordinate is $x = (M\omega_0^2/\lambda)X$ and energies are measured in units of $\lambda^2/(M\omega_0^2)$.

Alternative expressions for the current-induced forces for the resonant-level model, in terms of phase shifts and transmission coefficients, are given in Supporting Information File 1, Section C.

Two-level model

For the resonant-level model discussed so far, the A-matrix vanishes and the damping is necessarily positive. We now consider a model that allows for negative damping [53]. Our toy model can be seen to be inspired by a double dot on a suspended carbon nanotube, or an H_2 molecule in a break junction. The model is depicted schematically in Figure 2. The bare dot Hamiltonian corresponds to degenerate electronic states ε_0, localized on the left and right atoms or quantum dots, with tunnel coupling t in between,

$$H_0=\begin{pmatrix}\varepsilon_0 & t\\ t & \varepsilon_0\end{pmatrix}. \quad (75)$$

We consider a single oscillator mode, with coordinate X, that couples linearly to the difference in the occupation of the levels. In our previous notation, this means that $\Lambda_1 = \lambda_1\sigma_3$, where σ_μ, with $\mu = 0,\ldots, 3$, denotes the Pauli matrices acting in the two-site basis. The shift of the electronic levels is given by $\tilde{\varepsilon}_\pm(X) = \varepsilon_0 \pm \lambda_1 X$.

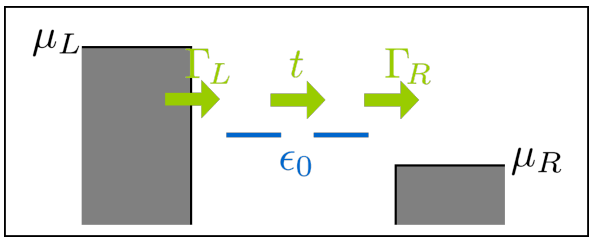

Figure 2: Sketch of the two-level model. Electrons tunnel through two degenerate energy levels between the left and right leads. The system is modulated by the coupling to the vibrational modes.

The hybridization matrices are given by $\Gamma^{\alpha} = (1/2)\Gamma_{\alpha}(\sigma^0 \pm \sigma^3)$, where the +(−) refers to $\alpha = L(R)$. We can deduce the tunneling matrix W in terms of the hybridization matrices,

$$W = 1/2\sqrt{\Gamma_L/\pi}(\sigma^0+\sigma^3)+1/2\sqrt{\Gamma_R/\pi}(\sigma^0-\sigma^3). \quad (76)$$

In the wide-band limit, we approximate W and Γ_{α} to be independent of energy. The retarded adiabatic GF takes the form

$$G^R(\varepsilon,X) = \frac{1}{\Delta}\begin{pmatrix} \varepsilon-\tilde{\varepsilon}_+ +i\Gamma_R & t \\ t & \varepsilon-\tilde{\varepsilon}_- +i\Gamma_L \end{pmatrix}, \quad (77)$$

with $\Delta(X) = \left(\varepsilon-\tilde{\varepsilon}_- +i\Gamma_L\right)\left(\varepsilon-\tilde{\varepsilon}_+ +i\Gamma_R\right)-t^2$.

For simplicity, we restrict our attention to symmetric couplings to the leads, $\Gamma_L = \Gamma_R = \Gamma/2$. Hence the frozen S-matrix $S(\varepsilon,X)$ becomes

$$S(\varepsilon,X) = 1-\frac{i\Gamma}{\Delta}\begin{pmatrix} \varepsilon-\tilde{\varepsilon}_+ +i\Gamma/2 & t \\ t & \varepsilon-\tilde{\varepsilon}_- +i\Gamma/2 \end{pmatrix}, \quad (78)$$

while the A-matrix takes the form

$$A(\varepsilon,X) = i\lambda_1\frac{\Gamma t}{\Delta^2}\sigma_2. \quad (79)$$

We can now give explicit expressions for the current-induced forces. The explicit expressions are lengthy and are given in Equation 115 and Equation 116 (Supporting Information File 1, Section D) for the mean force and damping matrix, respectively. The variance of the fluctuating force can be calculated accordingly.

The average force given in Equation 115 (Supporting Information File 1, Section D) combines with the elastic force to give rise to the effective potential $\tilde{U}(X)$ depicted, for zero temperature, in Figure 3. As in the case studied in the previous section, the system can exhibit various levels of multistability with changes in the bias.

The results for the friction coefficient, given in Equation 116 (Supporting Information File 1, Section D), are shown in Figure 4 as a function of the dimensionless oscillator coordinate x, for zero temperature. The contribution $\gamma^{s,eq}$ to the friction coefficient is peaked at $eV_{\text{gate}} \pm eV_{\text{bias}}/2 = \pm\sqrt{(\lambda_1 X)^2+t^2}$, as depicted in Figure 4a and Figure 4c. Neglecting the coupling to the leads, our toy model can be considered as a two-level system with level-spacing $2\sqrt{(\lambda_1 X)^2+t^2}$. Thus, the peaks occur when one of the electronic levels of the dot enters the conduction window. When this happens, small changes in the oscillator coordinate X can have a large impact on the occupation of the levels. This effect is more pronounced when the levels of the dots pass the Fermi levels that they are directly attached to [corresponding to $X > 0$ for current flowing from left to right, see Figure 4a, Figure 5a, and Figure 5b]. The broadening of the peaks is due to the hybridization with the leads, $\Gamma/2$. When $eV_{\text{gate}} = 0$, two peaks are expected symmetrically about $X = 0$, as shown in Figure 4a [see also Figure 5a and Figure 5b]. The effect of a finite gate voltage eV_{gate} is two-fold: It shifts the noninteracting electronic levels of the dot away from the middle of the conduction window, and hence the shifted levels $\tilde{\varepsilon}_{\pm}$ pass the Fermi levels of the right and left leads at different values of X, Figure 5c and Figure 5d. Therefore in this case four peaks are expected, with two larger peaks located at $X > 0$, and two smaller peaks located at $X < 0$. This is shown in Figure 4c. The height of the peaks in this case is reduced with respect to the case $eV_{\text{gate}} = 0$, since for a given peak, only one of the levels of the dot is in resonance with one of the leads. Note that four real values of X can be obtained only if $(eV_{\text{gate}} \pm eV_{\text{bias}}/2)^2 > t^2$. A situation with $(eV_{\text{gate}} - eV_{\text{bias}}/2)^2 < t^2$ while $(eV_{\text{gate}} + eV_{\text{bias}}/2)^2 > t^2$ is shown in Figure 4c (red-dotted line), in which a large peak is observed for $X = 1/\lambda_1\sqrt{\left(eV_{\text{gate}}+eV_{\text{bias}}/2\right)^2 - t^2}$, as well as a corresponding small peak for $X = -1/\lambda_1\sqrt{\left(eV_{\text{gate}}+eV_{\text{bias}}/2\right)^2 - t^2}$ [not displayed in Figure 4c], and a peak at $X = 0$.

For this model, the A-matrix is generally nonvanishing, which can result in negative damping for out-of-equilibrium situations. This is due to a negative contribution of $\gamma^{s,ne}$ to the total damping. This is visualized in Figure 4b and Figure 4d. Negative damping is possible when both dot levels are inside the conduction window, restricting the region in X over which negative damping can occur. Indeed, when only one level is within the conduction window, the system effectively reduces to the resonant level model for which, as we showed in the

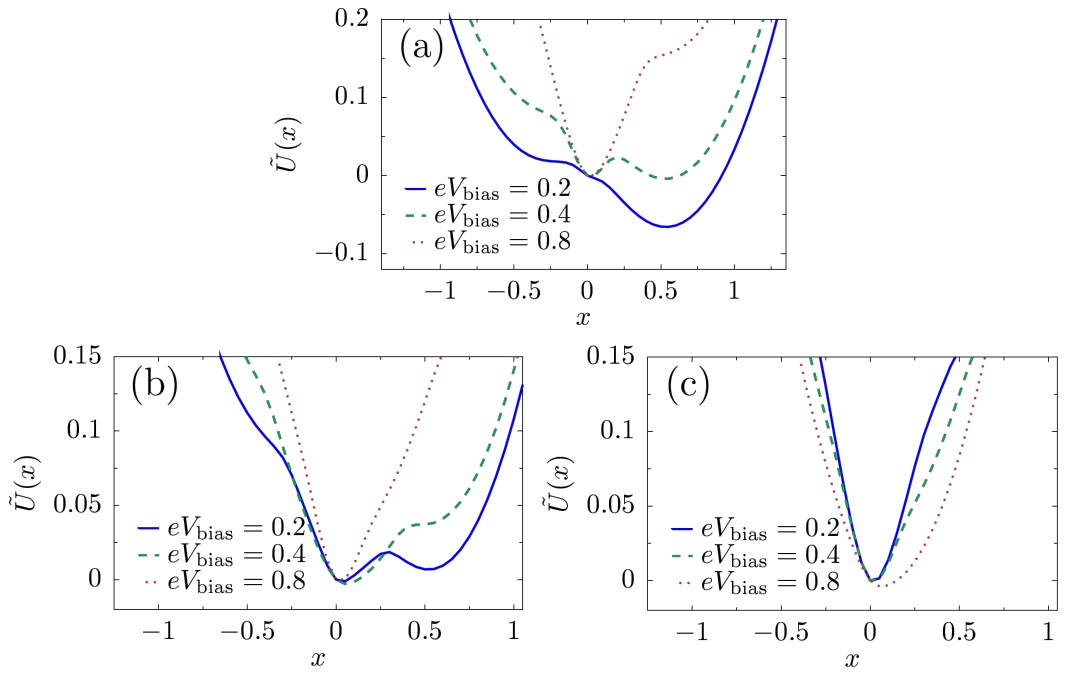

Figure 3: Effective potential for the mechanical motion in the two-level model. The shape of the potential can be tuned by changing the bias and gate voltages: (a) $eV_{\rm gate} = 0$, (b) $eV_{\rm gate} = 0.2$ and (c) $eV_{\rm gate} = 0.4$. We consider the parameters $\hbar\omega_0 = 0.01$, $t = 0.1$ and $\Gamma = 0.1$. The dimensionless coordinate is $x = (M\omega_0^2/\lambda_1)X$ and energies are measured in units of $\lambda_1^2/(M\omega_0^2)$.

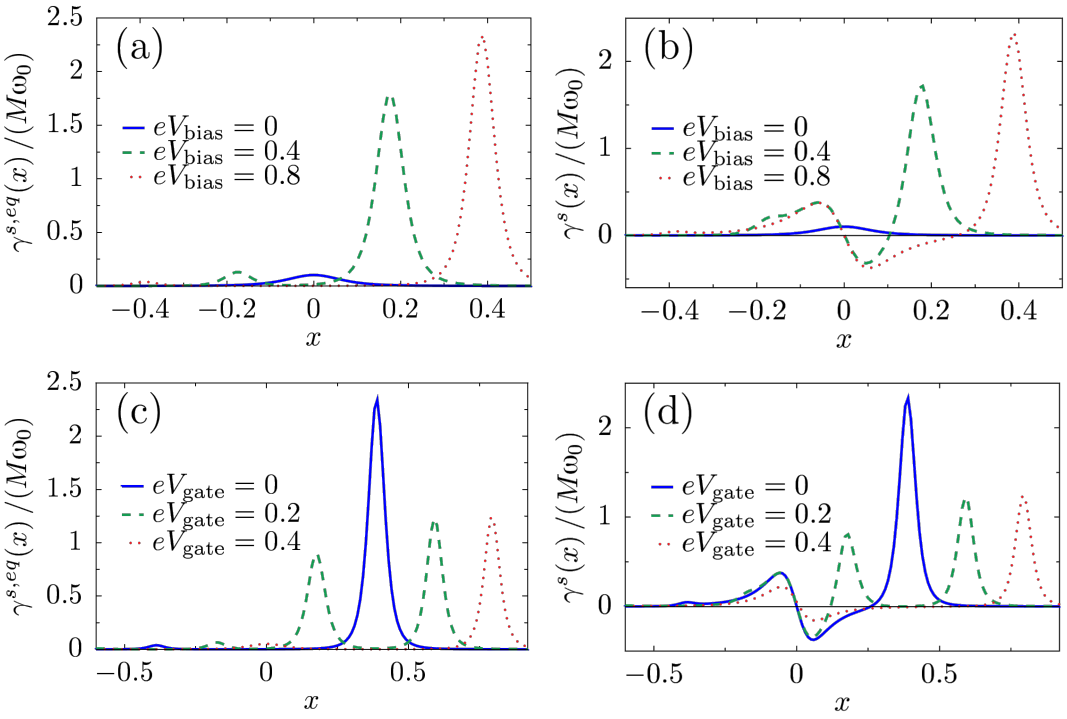

Figure 4: Damping versus mechanical displacement in the two-level model. (a) Contribution $\gamma^{s,eq}$ to the friction coefficient for various bias voltages at fixed gate voltage $eV_{\rm gate} = 0$. (b) At the same gate voltage, the total damping exhibits a region of negative damping due to the contribution of $\gamma^{s,ne}$. (c) $\gamma^{s,eq}$ for various gate voltages with the bias voltage $eV_{\rm bias} = 0.8$. Note that for both $eV_{\rm gate} = 0.2$ and $eV_{\rm gate} = 0.4$, one small peak for negative x falls outside of the range of x shown. (d) Again, the full damping γ^{s} exhibits regions of negative damping. We choose $\hbar\omega_0 = 0.01$, $\Gamma = 0.1$ and $t = 0.1$. The dimensionless coordinate is $x = (M\omega_0^2/\lambda_1)X$ and energies are measured in units of $\lambda_1^2/(M\omega_0^2)$.

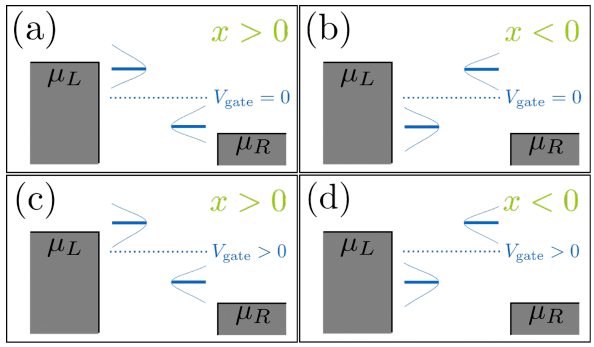

Figure 5: Cartoon of the positions of the electronic levels in the dot with respect to the Fermi levels of the leads, depending on the sign of x and the existence of a gate voltage. The levels are broadened due to the hybridization with the leads, Γ. When $x > 0$, "left" and "right" levels approach the Fermi levels of the left and right leads respectively; (a) for $eV_{\rm gate} = 0$ the levels align simultaneously for left and right; (c) a finite $eV_{\rm gate}$ produces an asymmetry between left and right. For $x < 0$ the alignment of the levels is inverted; (b) $eV_{\rm gate} = 0$; (d) finite $eV_{\rm gate}$.

previous subsection, the friction coefficient γ^s is always positive. When current flows from left to right, negative damping occurs only for positive values of the oscillator coordinate X, as shown in Figure 4b and Figure 4d. This is consistent with a level-inversion picture, as discussed recently in [51]. Pictorially, the electron–vibron coupling causes a splitting in energy of the left and right levels. When $X > 0$, electrons can go "down the ladder" formed by the energy levels by passing energy to the oscillator and hence amplifying the vibrations. For $X < 0$, electrons can pass between the two dots only by absorbing energy from the vibrations, causing additional nonequilibrium damping. For small broadening of the dot levels due to the coupling to the leads, this effect is expected to be strongest when the vibration-induced splitting $\lambda_1 X$ becomes of the same order as the strength of the hopping t. When X grows further, the increasing detuning of the dot levels reduces the current and hence the nonequilibrium damping [Figure 4b and Figure 4, and below in Figure 6]. The coexistence of a multistable potential together with regions of negative damping can lead to interesting nonlinear behavior for the dynamics of the oscillator. In particular, and as we show in the next example, limit-cycle solutions are possible, in the spirit of a Van der Pol oscillator [54].

We can also calculate the current. The pumping contribution is proportional to the velocity $\dot{X}$ and thus small. Therefore we show here results only for the dominant adiabatic part of the current. This is given by

$$I^0 = \frac{e}{h}\int \mathrm{d}\varepsilon \frac{2t^2\Gamma^2(f_L - f_R)}{|\Delta|^2}. \qquad (80)$$

For zero temperature, the behavior of the current is shown in Figure 6 as a function of various parameters. Figure 6a and Figure 6b show the current as a function of the (dimensionless) oscillator coordinate x for two different values of gate potential for which the system exhibits multistability by developing several metastable equilibrium positions. For $V_{\rm gate} = 0$, and independently of bias, the current shows a maximum at the local minimum of the effective potential $x = 0$, while $I^0 \approx 0$ for another possible local minimum, $x \approx 0.5$ (compare with Figure 3a). The true equilibrium value of x can be tuned through the bias potential, offering the possibility of perfect switching. For finite gate potential, however, the current is depleted from $x = 0$ with diminishing bias. Figure 6c and Figure 6d show the current as a function of gate or bias voltage for fixed representative values of the oscillator coordinate x. The current changes stepwise as the number of levels inside the conduction window changes, coinciding with the peaks in the friction coefficient illustrated in Figure 4. In an experimental setting, the measured *direct* current would involve an average over the probability distribution of the coordinate x, given by the solution of the Fokker–Planck equation associated with the Langevin Equation 1.

Two vibrational modes

As a final example, we present a simple model that allows for both a nonconservative force and an effective "Lorentz" force, in addition to negative damping. For this it is necessary to couple the two electronic orbitals of the previous example, see Equation 75, to at least two oscillatory modes that we assume to be degenerate. The relevant vibrations in this case can be thought of as a center-of-mass vibration X_1 between the leads, and a stretching mode X_2. (It should be noted that this is for visualization purposes only. In reality, for an H_2 molecule, the stretching mode is a high energy mode when compared to a transverse and a rotational mode [55]. Nevertheless, the H_2 molecule does indeed have two near-degenerate low-energy vibrational modes, corresponding to rigid vibrations between the leads and a rigid rotation relative to the axis defined by the two leads.) The stretch mode modulates the hopping parameter,

$$t \to \tilde{t}(X_2) = t + \lambda_2 X_2\,, \qquad (81)$$

while the center of mass mode X_1 is modeled as being coupled linearly to the density,

$$\varepsilon_0 \to \tilde{\varepsilon}(X_1) = \varepsilon_0 + \lambda_1 X_1\,, \qquad (82)$$

hence $\Lambda_1 = \lambda_1\sigma_0$ and $\Lambda_2 = \lambda_2\sigma_1$. We work in the wide-band limit, but allow for asymmetric coupling to the leads. The

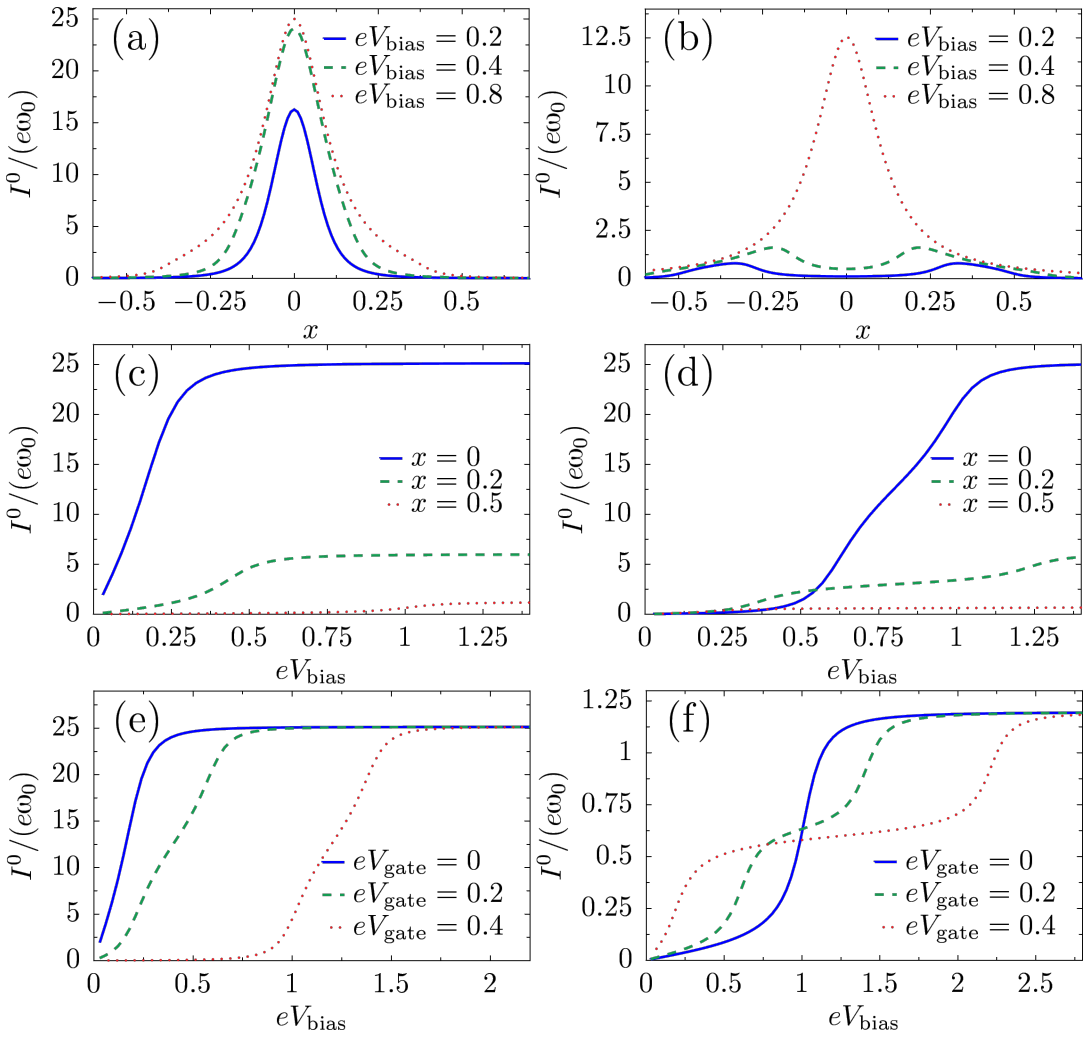

Figure 6: Dependence of the current in the two-level model on various parameters. Current as a function of mechanical displacement for (a) $V_{\rm gate}$ = 0 and (b) $V_{\rm gate}$ = 0.4; as function of bias for (c) $V_{\rm gate}$ = 0, (d) $V_{\rm gate}$ = 0.4, (e) x = 0 and (f) x = 0.5. We choose $\hbar\omega_0$ = 0.01, Γ = 0.1 and t = 0.1. The dimensionless coordinate is $x = (M\omega_0^2/\lambda_1)X$ and energies are measured in units of $\lambda_1^2/(M\omega_0^2)$.

retarded Green's function becomes

$$G^R(\varepsilon, X_1, X_2) = \frac{1}{\Delta}\begin{pmatrix} \varepsilon - \tilde{\varepsilon} + i\Gamma_R & t \\ t & \varepsilon - \tilde{\varepsilon} + i\Gamma_L \end{pmatrix}, \quad (83)$$

where now $\Delta(X_1, X_2) = (\varepsilon - \tilde{\varepsilon} + i\Gamma_L)(\varepsilon - \tilde{\varepsilon} + i\Gamma_R) - t^2$. The frozen S-matrix can be easily calculated to be

$$S(\varepsilon, X_1, X_2) = 1 - \frac{2i}{\Delta}\begin{pmatrix} (\varepsilon - \tilde{\varepsilon} + i\Gamma_R)\Gamma_L & t\sqrt{\Gamma_L\Gamma_R} \\ t\sqrt{\Gamma_L\Gamma_R} & (\varepsilon - \tilde{\varepsilon} + i\Gamma_L)\Gamma_R \end{pmatrix}. \quad (84)$$

The A-matrices also take a simple form for this model. Since Λ_1 is proportional to the identity operator,

$$A_1(\varepsilon, X_1, X_2) = -\pi\lambda_1 W G_R[G_R, \sigma_0]G_R W^\dagger = 0. \quad (85)$$

On the other hand, the A-matrix associated with X_2 is nonzero and given by

$$A_2(\varepsilon, X_1, X_2) = -\lambda_2 \frac{\sqrt{\Gamma_L\Gamma_R}\,(\Gamma_R - \Gamma_L)}{\Delta^2}\sigma_2. \quad (86)$$

From this we can compute the average force, damping, pseudo-Lorentz force, and noise terms. These are listed in Supporting

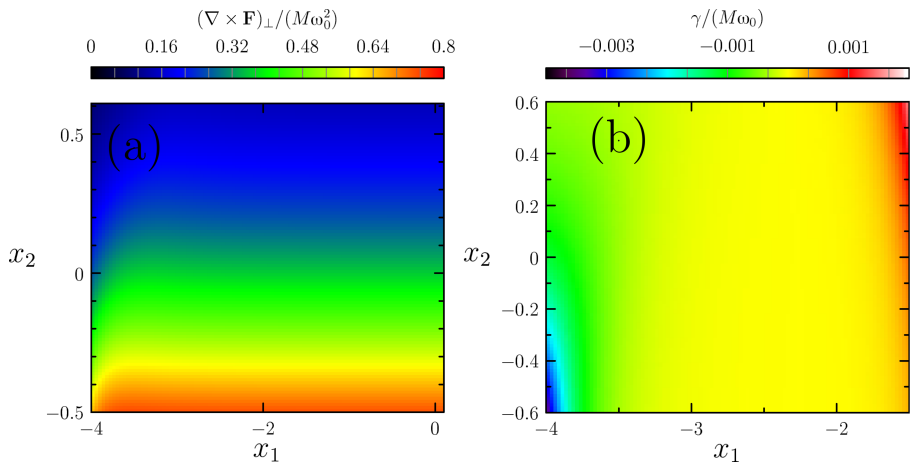

Figure 7: Curl of the average force and damping coefficient for the model with two vibrational modes: (a) The curl of the current-induced mean force **F** is, in a nonequilibrium situation, generally nonzero, indicating that the force is nonconservative. (b) One of the two eigenvalues of γ^s. Remarkably, it undergoes changes of sign. A dissipation matrix γ^s that is non-positive-definite implies destabilization of the static-equilibrium solution found at lower bias potentials, in this case driving the system into a limit cycle, see main text and Figure 8. The parameters used are such that $\lambda_1/\lambda_2 = 3/2$. The elastic modes are degenerate with $\hbar\omega_0 = 0.014$, $\Gamma_{L,R} = [(1 \pm 0.8)/2](\sigma_0 \pm \sigma_3)$, and the hopping between the orbitals is $t = 0.9$. The dimensionless coordinates are $x_i = (M\omega_0^2/\lambda)X_i$ and energies are in units of $\lambda^2/(M\omega_0^2)$, where $\lambda = (\lambda_1 + \lambda_2)/2$.

Information File 1, Section E. At zero temperature, it is possible to obtain analytical expressions for these current-induced forces. Studying the dynamics of the modes $X_{1,2}(t)$ implies solving the two coupled Langevin equations given by Equation 1, after inserting the expressions for the forces given in Supporting Information File 1, Section E. Within our formalism we are able to study the full nonlinear dynamics of the problem, which brings out a plethora of new qualitative behavior. In particular, analyses that linearize the current-induced force about a static-equilibrium point would predict run-away modes due to negative damping and nonconservative forces [30]. Taking into account nonlinearities allows one to find the new stable attractor of the motion. Indeed, we find that these linear instabilities typically result in dynamic equilibrium, namely limit-cycle dynamics [22]. We note in passing that limit-cycle dynamics in a nanoelectromechanical system was also discussed recently in [53].

We have studied the zero-temperature dynamics of our two-level, two-mode system for different ranges of parameters. In Figure 7 we map out the values of the curl of the mean force, $(\nabla \times \mathbf{F})_\perp$, indicating that the force is nonconservative throughout parameter space. We also plot one of the two eigenvalues of the dissipation matrix γ^s, showing that it can take negative values in some regions of the parameter space. We find that it is possible to drive the system into a limit cycle by varying the bias potential. The existence of this limit cycle is shown in Figure 8a, where we have plotted various Poincaré sections of the nonlinear system without fluctuations. The figure shows the trajectory in phase space of the (dimensionless) oscillator coordinate x_1 after the dynamic equilibrium is reached, for several cuts of the (dimensionless) coordinate x_2. Each cut shows two points in x_1 phase space, indicating the entry and exit of the trajectory. Each point in the plot actually consists of several points that fall on top of each other, corresponding to every instance in which the coordinate x_2 has the value indicated in the legend of Figure 8a. This shows the periodicity of the solution of the nonlinear equations of motion for x_1,x_2 for the particular bias chosen. Surveying the various values of x_2 reveals a closed trajectory in the parametric coordinate space x_1,x_2. Remarkably, signatures of the limit cycle survive the inclusion of the Langevin force. Figure 8b depicts typical trajectories in the coordinate space of the oscillator, x_1,x_2, in the presence of the stochastic force, showing fluctuating trajectories around the stable limit cycle.

Experimentally, the signature of the limit cycle would be most directly reflected in the current–current correlation function, as depicted in Figure 9. We find that in the absence of a limit cycle the system is dominated by two characteristic frequencies, shown by the peaks in Figure 9. These frequencies correspond to the shift in energy of the two degenerate vibrational modes due to the average current-induced forces F_1 and F_2. When the bias voltage is such that the system enters a limit cycle, the current–current correlation shows instead only one peak as a function of frequency. This result, as shown in Figure 9, is fairly robust to noise, making the onset of limit-cycle dynamics observable in experiment.

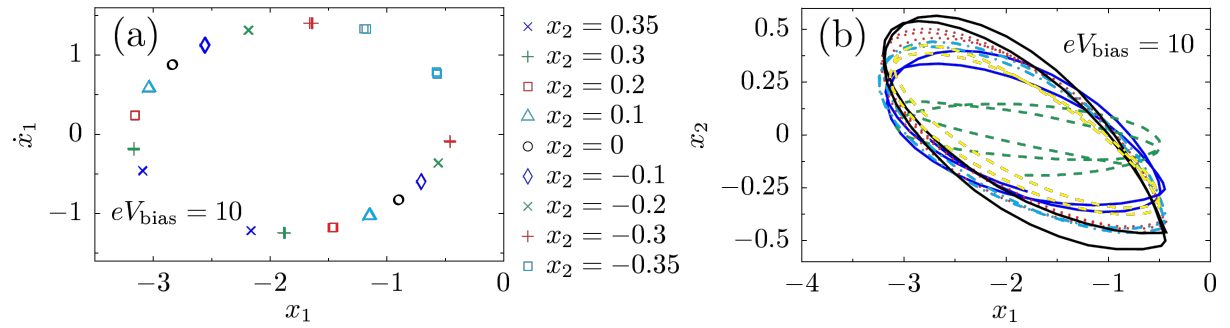

Figure 8: Limit-cycle dynamics for the model with two vibrational modes. (a) At large bias voltages, Poincaré sections of the four-dimensional phase space show the presence of a limit cycle in the Langevin dynamics without a fluctuating force. (b) Several periods of typical trajectories (for different initial conditions after a transient) in the presence of the fluctuating forces ξ are shown. The same general parameters as in Figure 7 are used here.

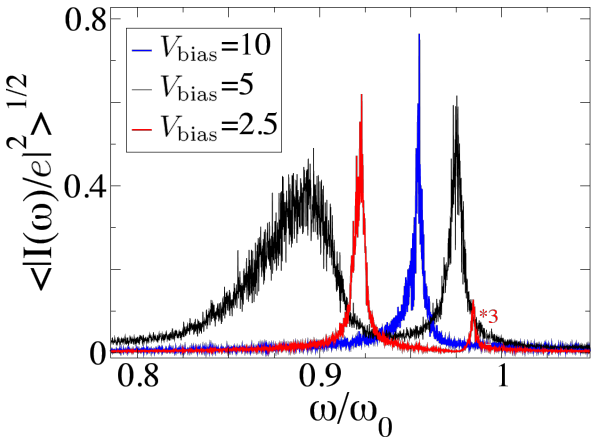

Figure 9: Current–current correlation function in the presence of noise for the system with two vibrational modes. The limit cycle is signaled by a single peak (V_{bias} = 10, see Figure 8), as opposed to two peaks in the absence of a limit cycle (V_{bias} = 2.5,5.0). Increasing the bias potential increases the noise levels, but the peaks are still easily recognizable. The results are obtained by averaging over times long enough compared with the characteristic oscillation times. The same general parameters as in Figure 7 are used here.

Conclusion

Within a nonequilibrium Born–Oppenheimer approximation, the dynamics of a nanoelectromechanical system can be described in terms of a Langevin equation, in which the mechanical modes of the mesoscopic device are subject to current-induced forces. These forces include a mean force, which is independent of velocity and due to the average net force that the electrons exert on the oscillator; a stochastic Langevin force, which takes into account the thermal and nonequilibrium fluctuations with respect to the mean force value; and a force linear in the velocity of the modes. This last, velocity-dependent force, consists of a dissipative term and a term that can be interpreted as an effective "Lorentz" force, due to an effective magnetic field acting in the parameter space of the modes.

In this work we have expressed these current-induced forces through the scattering matrix of the coherent mesoscopic conductor and its parametric derivatives, extending the results found previously in [22]. Our results are now valid for a generic coupling between the electrons and the vibrational degrees of freedom, given by a matrix $h_0(\mathbf{X})$, and for energy-dependent hybridization with the leads, given by the matrix $W(\varepsilon)$. We have shown that expressing *all* the current-induced forces in terms of the S-matrix is only possible by going beyond the strictly adiabatic approximation, and it is necessary to include the first-order correction in the adiabatic expansion. This introduces a new fundamental quantity into the problem, the A-matrix, which needs to be calculated together with the frozen S-matrix for a given system.

There are several circumstances in which the first nonadiabatic correction, encapsulated in the A-matrix, is necessary. While the average as well as the fluctuating force can be expressed solely in terms of the adiabatic S-matrix, the A-matrix enters both the frictional and the Lorentz-like force. In equilibrium, the frictional force reduces to an expression in terms of the adiabatic S-matrix. Out of equilibrium, however, an important new contribution involving the A-matrix appears. In contrast, the A-matrix is always required in order to express the Lorentz-like force, even when the system is in thermal equilibrium.

The expressions for the current-induced forces in terms of the scattering matrix allow us to extract important properties from general symmetry arguments. Driving the nanoelectromechanical system out of equilibrium by imposing a bias results in qualitatively new features for the forces. We have shown that the mean force is nonconservative in this case, and that the dissipation coefficient acquires a nonequilibrium contribution that can be negative. We have also shown that when considering more than one mechanical degree of freedom, a pseudo-Lorentz force is present even for a time-reversal invariant

system, unless one also imposes thermal equilibrium on top of the time-reversal condition.

Our model allows one to study, within a controlled approximation, the nonlinear dynamics generated by the interplay between current and vibrational degrees of freedom, opening up the path for a systematic study of these devices. By means of simple model examples, we have shown that it is possible to drive a nanoelectromechanical system into interesting dynamically stable regimes, such as a limit cycle, by varying the applied bias potential. In a limit cycle, the vibrational modes vary periodically in time, which could be the operating principle for a molecular motor. On the other hand, the possibility of nonconservative forces could also allow one to extract energy from the system, providing a controllable tool for cooling. The study of these types of phenomena in realistic systems would be an interesting application of the formalism presented in this paper.

Supporting Information

Supporting Information File 1

Useful mathematical relations and detailed calculations
[http://www.beilstein-journals.org/bjnano/content/supplementary/2190-4286-3-15-S1.pdf]

Acknowledgements

We acknowledge discussions with P. W. Brouwer, G. Zarand, and L. Arrachea as well as support by the DFG through SPP 1459, SFB TR/12, and SFB 658.

References

1. Nazarov, Y.; Blanter, Y. *Quantum Transport;* Cambridge University Press: Cambridge, UK, 2010.
2. Landauer, R. *IBM J. Res. Dev.* **1957,** *1,* 223. doi:10.1147/rd.13.0223
3. Landauer, R. *Philos. Mag.* **1970,** *21,* 863. doi:10.1080/14786437008238472
4. Büttiker, M.; Imry, Y.; Landauer, R.; Pinhas, S. *Phys. Rev. B* **1985,** *31,* 6207. doi:10.1103/PhysRevB.31.6207
5. Brouwer, P. W. *Phys. Rev. B* **1998,** *58,* R10135. doi:10.1103/PhysRevB.58.R10135
6. Avron, J. E.; Elgart, A.; Graf, G. M.; Sadun, L. *Phys. Rev. Lett.* **2001,** *87,* 236601. doi:10.1103/PhysRevLett.87.236601
7. Entin-Wohlman, O.; Aharony, A.; Levinson, Y. *Phys. Rev. B* **2002,** *65,* 195411. doi:10.1103/PhysRevB.65.195411
8. Moskalets, M.; Büttiker, M. *Phys. Rev. B* **2005,** *72,* 035324. doi:10.1103/PhysRevB.72.035324
9. Craighead, H. G. *Science* **2000,** *290,* 1532. doi:10.1126/science.290.5496.1532
10. Roukes, M. L. *Phys. World* **2001,** 14–25.
11. Weig, E. M.; Blick, R. H.; Brandes, T.; Kirschbaum, J.; Wegscheider, W.; Bichler, M.; Kotthaus, J. P. *Phys. Rev. Lett.* **2004,** *92,* 046804. doi:10.1103/PhysRevLett.92.046804
12. LeRoy, B. J.; Lemay, S. G.; Kong, J.; Dekker, C. *Nature* **2004,** *432,* 371. doi:10.1038/nature03046
13. Bunch, J. S.; van der Zande, A. M.; Verbridge, S. S.; Frank, I. W.; Tanenbaum, D. M.; Parpia, J. M.; Craighead, H. G.; McEuen, P. L. *Science* **2007,** *315,* 490. doi:10.1126/science.1136836
14. Krive, I. V.; Palevski, A.; Shekhter, R. I.; Jonson, M. *Low Temp. Phys.* **2010,** *36,* 119. doi:10.1063/1.3319350
15. Galperin, M.; Ratner, M. A.; Nitzan, A. *J. Phys.: Condens. Matter* **2007,** *19,* 103201. doi:10.1088/0953-8984/19/10/103201
16. Park, H.; Park, J.; Lim, A. K. L.; Anderson, E. H.; Alivisatos, A. P.; McEuen, P. L. *Nature* **2000,** *407,* 57. doi:10.1038/35024031
17. Eom, K.; Park, H. S.; Yoon, D. S.; Kwon, T. *Phys. Rep.* **2011,** *503,* 115. doi:10.1016/j.physrep.2011.03.002
(And references therein.)
18. Naik, A.; Buu, O.; LaHaye, M. D.; Armour, A. D.; Clerk, A. A.; Schwab, K. C.; Blencowe, M. P. *Nature* **2006,** *443,* 193. doi:10.1038/nature05027
19. Stettenheim, J.; Thalakulam, M.; Pan, F.; Bal, M.; Ji, Z.; Xue, W.; Pfeiffer, L.; West, K.; Blencowe, M. P.; Rimberg, A. J. *Nature* **2010,** *466,* 86. doi:10.1038/nature09123
20. Steele, G. A.; Hüttel, A. K.; Witkamp, B.; Poot, M.; Meerwaldt, H. B.; Kouwenhoven, L. P.; van der Zant, H. S. J. *Science* **2009,** *325,* 1103. doi:10.1126/science.1176076
21. Lassagne, B.; Tarakanov, Y.; Kinaret, J.; Garcia-Sanchez, D.; Bachtold, A. *Science* **2009,** *325,* 1107. doi:10.1126/science.1174290
22. Bode, N.; Viola Kusminskiy, S.; Egger, R.; von Oppen, F. *Phys. Rev. Lett.* **2011,** *107,* 036804. doi:10.1103/PhysRevLett.107.036804
23. Yu, L. H.; Keane, Z. K.; Ciszek, J. W.; Cheng, L.; Stewart, M. P.; Tour, J. M.; Natelson, D. *Phys. Rev. Lett.* **2004,** *93,* 266802. doi:10.1103/PhysRevLett.93.266802
24. Sapmaz, S.; Jarillo-Herrero, P.; Blanter, Y. M.; Dekker, C.; van der Zant, H. S. J. *Phys. Rev. Lett.* **2006,** *96,* 026801. doi:10.1103/PhysRevLett.96.026801
25. Leturcq, R.; Stampfer, C.; Inderbitzin, K.; Durrer, L.; Hierold, C.; Mariani, E.; Schultz, M. G.; von Oppen, F.; Ensslin, K. *Nat. Phys.* **2009,** *5,* 327. doi:10.1038/nphys1234
26. Koch, J.; von Oppen, F. *Phys. Rev. Lett.* **2005,** *94,* 206804. doi:10.1103/PhysRevLett.94.206804
27. Koch, J.; von Oppen, F.; Andreev, A. V. *Phys. Rev. B* **2006,** *74,* 205438. doi:10.1103/PhysRevB.74.205438
28. Mozyrsky, D.; Hastings, M. B.; Martin, I. *Phys. Rev. B* **2006,** *73,* 035104. doi:10.1103/PhysRevB.73.035104
29. Pistolesi, F.; Blanter, Y. M.; Martin, I. *Phys. Rev. B* **2008,** *78,* 085127. doi:10.1103/PhysRevB.78.085127
30. Lü, J.-T.; Brandbyge, M.; Hedegård, P. *Nano Lett.* **2010,** *10,* 1657. doi:10.1021/nl904233u
31. Berry, M. V.; Robbins, J. M. *Proc. R. Soc. London, Ser. A* **1993,** *442,* 659. doi:10.1098/rspa.1993.0127
32. Bennett, S. D.; Maassen, J.; Clerk, A. A. *Phys. Rev. Lett.* **2010,** *105,* 217206. doi:10.1103/PhysRevLett.105.217206
(See also *Phys. Rev. Lett.* **2011,** *106,* 199902.)
33. Bennett, S. D.; Maassen, J.; Clerk, A. A. *Phys. Rev. Lett.* **2011,** *106,* 199902. doi:10.1103/PhysRevLett.106.199902
34. Kindermann, M.; Beenakker, C. W. J. *Phys. Rev. B* **2002,** *66,* 224106. doi:10.1103/PhysRevB.66.224106
35. Brataas, A.; Tserkovnyak, Y.; Bauer, G. E. W. *Phys. Rev. Lett.* **2008,** *101,* 037207. doi:10.1103/PhysRevLett.101.037207
36. Weick, G.; Pistolesi, F.; Mariani, E.; von Oppen, F. *Phys. Rev. B* **2010,** *81,* 121409. doi:10.1103/PhysRevB.81.121409

37. Weick, G.; von Oppen, F.; Pistolesi, F. *Phys. Rev. B* **2011,** *83,* 035420. doi:10.1103/PhysRevB.83.035420
38. Weick, G.; Meyer, D. M.-A. *Phys. Rev. B* **2011,** *84,* 125454. doi:10.1103/PhysRevB.84.125454
39. Fedorets, D.; Gorelik, L. Y.; Shekhter, R. I.; Jonson, M. *Europhys. Lett.* **2002,** *58,* 99. doi:10.1209/epl/i2002-00611-3
40. Hussein, R.; Metelmann, A.; Zedler, P.; Brandes, T. *Phys. Rev. B* **2010,** *82,* 165406. doi:10.1103/PhysRevB.82.165406
41. Nocera, A.; Perroni, C. A.; Marigliano Ramaglia, V.; Cataudella, V. *Phys. Rev. B* **2011,** *83,* 115420. doi:10.1103/PhysRevB.83.115420
42. Kamenev, A.; Levchenko, A. *Advances in Physics* **2009,** *58,* 197. doi:10.1080/00018730902850504
43. Jauho, A.-P.; Wingreen, N. S.; Meir, Y. *Phys. Rev. B* **1994,** *50,* 5528. doi:10.1103/PhysRevB.50.5528
44. Moskalets, M.; Büttiker, M. *Phys. Rev. B* **2004,** *69,* 205316. doi:10.1103/PhysRevB.69.205316
45. Aleiner, I.; Brouwer, P.; Glazman, L. *Phys. Rep.* **2002,** *358,* 309. doi:10.1016/S0370-1573(01)00063-1
46. Vavilov, M. G.; Ambegaokar, V.; Aleiner, I. L. *Phys. Rev. B* **2001,** *63,* 195313. doi:10.1103/PhysRevB.63.195313
47. Arrachea, L.; Moskalets, M. *Phys. Rev. B* **2006,** *74,* 245322. doi:10.1103/PhysRevB.74.245322
48. Dundas, D.; McEniry, E. J.; Todorov, T. N. *Nat. Nanotechnol.* **2009,** *4,* 99. doi:10.1038/nnano.2008.411
49. Todorov, T. N.; Dundas, D.; McEniry, E. J. *Phys. Rev. B* **2010,** *81,* 075416. doi:10.1103/PhysRevB.81.075416
50. Clerk, A. A.; Bennett, S. *New J. Phys.* **2005,** *7,* 238. doi:10.1088/1367-2630/7/1/238
51. Lü, J.-T.; Hedegård, P.; Brandbyge, M. *Phys. Rev. Lett.* **2011,** *107,* 046801. doi:10.1103/PhysRevLett.107.046801
52. Hyldgaard, P. *Mater. Sci. Eng., C* **2003,** *23,* 243. doi:10.1016/S0928-4931(02)00275-8
53. Metelmann, A.; Brandes, T. Adiabaticity in semiclassical nanoelectromechanical systems. 2011, arXiv:1107.3762v2 [cond-mat.mes-hall].
54. Hanggi, P.; Riseborough, P. *Am. J. Phys.* **1983,** *51,* 347. doi:10.1119/1.13246
55. Djukic, D.; Thygesen, K. S.; Untiedt, C.; Smit, R. H. M.; Jacobsen, K. W.; van Ruitenbeek, J. M. *Phys. Rev. B* **2005,** *71,* 161402. doi:10.1103/PhysRevB.71.161402

License and Terms

Beilstein Journal of Nanotechnology

Strong spin-filtering and spin-valve effects in a molecular V–C_{60}–V contact

Mohammad Koleini*[1] and Mads Brandbyge*[2]

Full Research Paper

Open Access

Address:
[1]Hybrid Materials Interfaces Group, Faculty of Production Engineering and Bremen Center for Computational Materials Science, University of Bremen, 28359 Bremen, Germany and [2]DTU Nanotech, Department of Micro and Nanotechnology, Technical University of Denmark, Ørsteds Plads, Building 345E, DK-2800 Kongens Lyngby, Denmark

Email:
Mohammad Koleini* - koleini.m@gmail.com; Mads Brandbyge* - mads.brandbyge@nanotech.dtu.dk

* Corresponding author

Keywords:
fullerene; molecular spintronics; scanning tunneling microscopy; spin transport

Beilstein J. Nanotechnol. **2012,** *3,* 589–596.
doi:10.3762/bjnano.3.69

Received: 16 May 2012
Accepted: 20 July 2012
Published: 22 August 2012

This article is part of the Thematic Series "Transport through molecular junctions".

Guest Editor: J. M. van Ruitenbeek

Abstract

Motivated by the recent achievements in the manipulation of C_{60} molecules in STM experiments, we study theoretically the structure and electronic properties of a C_{60} molecule in an STM tunneljunction with a magnetic tip and magnetic adatom on a Cu(111) surface using first-principles calculations. For the case of a vanadium tip/adatom, we demonstrate how spin coupling between the magnetic V atoms, mediated by the C_{60}, can be observed in the electronic transport, which display a strong spin-filtering effect, allowing mainly majority-spin electrons to pass (>95%). Moreover, we find a significant change in the conductance between parallel and anti-parallel spin polarizations in the junction (86%) which suggests that STM experiments should be able to characterize the magnetism and spin coupling for these systems.

Introduction

Organic materials typically offer small spin–orbit and hyperfine interactions, which are prerequisites for spintronic applications, because they allow long spin lifetimes. Thus there is a great interest in organic building blocks for molecular spintronics [1-4], and a thorough understanding of spin transport and magnetism in these systems is called for. It is therefore important to establish model molecular spintronic systems where spin transport and magnetic interactions can be examined experimentally. Recently, it has been demonstrated in low temperature scanning tunneling microscopy (STM) experiments how C_{60} molecules can be picked up by the STM-tip, and how they could controllably be used to contact structures such as adatoms, clusters, and molecules placed on a substrate surface [5-7]. The C_{60} molecule is considered as an attractive anchoring group for molecular electronics due to its mechanical robustness [8]. Moreover, the lowest unoccupied molecular

orbital (LUMO) of C_{60} is close to the Fermi level of ferromagnetic elements which makes spin injection relatively easy [9], and characterizes C_{60} as a promising building block in molecular spintronics. The high symmetry of the C_{60} allows detailed characterization of the bonding geometries in STM. In particular, one can determine which part of C_{60} is pointing towards the tip/surface prior to contact formation, and also after contact formation, while the C_{60} is placed on the tip [7]. Subsequently, it is possible to investigate the interactions between tip and sample via electronic transport measurements as tip and sample are brought into contact. STM also provides a powerful tool for investigating spin-transport in magnetic nanostructures [10-17]. Direct magnetic interactions between STM tip and magnetic materials on a substrate have been studied in a number of works [18-20], and STM has been used to probe spin in organic molecules [21]. In the case of a magnetic tip and magnetic surfaces, this method may be used to study spin transport and interactions through organic molecular systems bound to the surface and gain insight into single-molecular magnetic properties. Among organic compounds, carbonic rings which are combined with transition metals are interesting for molecular spintronics purposes [22]. The interaction of the π-electron system of such rings with the d-orbitals of the transition metals, is a key to electron and subsequently to spin transport. One example of such systems is presented in a theoretical study, where calculations have been used to examine spin transport in a benzene–Co system on a Cu(001) surface contacted by a Cr tip [23]. The magnetic properties and spin transport have also been calculated for organometallic "multidecker" wires, where magnetic atoms are sandwiched between organic parts [24]. Multidecker systems involving vanadium are very promising due to their half-metallic behavior resulting in high spin polarization of the transport [24-26]. Interestingly, due to the different symmetries of the C_{60}, it might be possible to vary the electronic and magnetic properties depending on whether pentagon, hexagon or edge sites of C_{60} are in contact with the magnetic ligand atoms.

Here, we employ first-principles calculations to predict the spin transport through a spintronic model system consisting of a C_{60} molecule contacted by magnetic atoms in an STM setup. In particular, we predict that vanadium is a magnetic material which will show pronounced spin-filtering and spin-valve effects in STM experiments.

System setup and methods

In order to mimic a concrete STM experiment, we investigated the specific setup shown in Figure 1. The bulk regions of the contacts (i.e., STM tip and substrate) have been chosen to be nonmagnetic copper, which has previously been employed in manipulation experiments [5-7]. We imagine that magnetic atoms are deposited on the Cu surface prior to deposition [27] of the C_{60} molecules, and that the tip-electrode is prepared prior to the contact by either indenting a Cu tip into a cluster of these atoms in order to cover its outermost part with these, or by creating the tip from from the bulk magnetic material. We model the outermost part of the tip by a pyramid-like structure consisting of four atoms on one electrode, simulating the magnetic STM tip which is used to pick up C_{60} for subsequent contact formation to an isolated adatom on the copper(111) substrate. In the following we will show that the case of vanadium is remarkable. We used spin-polarized pseudopotential DFT calculations with the SIESTA code [28]. Electronic structures have been calculated within a GGA-PBE approximation to the exchange and correlation functional [29]. Double-ζ polarized basis sets with grid cutoff of 250 Ry have been used. Spin-polarized transport was subsequently calculated using the non-equilibrium Green's function (NEGF) formalism [30] in the limit of zero voltage. In order to eliminate basis set superposition error (BSSE) present in methods with atomic orbitals basis sets, we have used plane-wave (PW) formalism as implemented in [31] for total energy calculations. In these calculations, we have been using ultrasoft pseudopotentials, with 30/300 Ry cutoff for wavefunction/charge density.

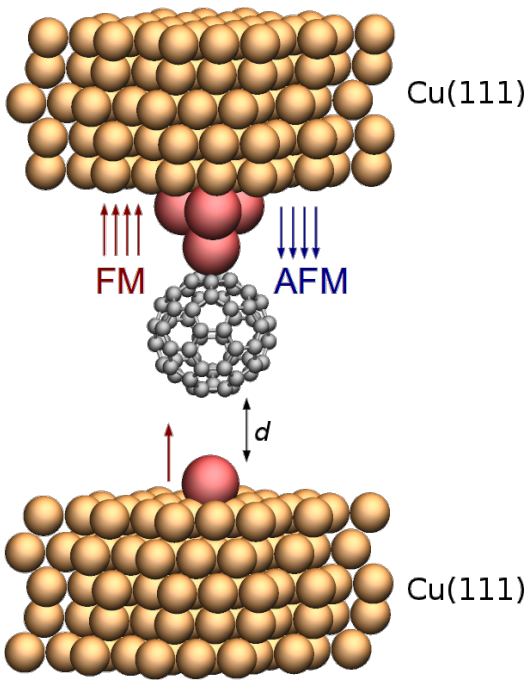

Figure 1: STM system picking up C_{60} with a magnetic tip, approaching a magnetic adatom on the nonmagnetic copper surface. The orange, red and gray spheres depict copper, vanadium and carbon atoms, respectively. A C_{60}-pentagon is facing the tip/adatom.

Results and Discussion

As an initial rough guide in our search for interesting magnetic metals to contact the C_{60}, and to select relevant bonding sites, we first performed calculations of the binding energy of a single adatom from the first row transition metals (from vanadium to copper) with C_{60}. This will clearly overestimate the binding of the C_{60} to a higher coordinated tip-atom but we are here focussing on the trends in binding energy depending on tip-atom species. Based on the simple adatom calculations we seek high magnetization and a high binding energy to get a stable contact. The results are summarized in Table 1 for different sites on the C_{60} molecule. It can be seen that nickel has the strongest binding energy but with zero total magnetization (M_T), and thus, is probably not interesting for investigations of spin transport. On the other hand, chromium enjoys the largest M_T, due to its largest unpaired electronic configuration [Ar]$3d^5 4s^1$ but with the least binding energy strength. It has already been shown that copper STM tips can pick up C_{60} [5]. Noting that the maximum of binding energy for copper to C_{60} is ≈0.8 eV, we conclude that the same action should be possible with vanadium while enjoying a decent M_T.

Based on the data of the simple guiding calculations we chose vanadium in the full C_{60}-contact simulations on the system depicted in Figure 1. In the following we demonstrate that this choice for contact material in an STM setup is successful in achieving a good spin-filter- and spin-valve performance. Here, ferromagnetic (FM) and anti-ferromagnetic (AFM) spin alignment between atoms of tip and adatom, have been considered. The site on the C_{60} with the highest binding energy for a V adatom is η^5, which is roughly over the center of a pentagon of a C_{60}, and due to the symmetric structure of the C_{60}, this site is contacted by both the tip and the adatom. We find that the binding energy of the C_{60} to the V-tip (upper part in Figure 1) is 1.3 eV, while binding of C_{60} to the adatom on the Cu substrate (lower part in Figure 1) is 1.1 eV. The spin-resolved transmissions for the FM and AFM cases are shown in Figure 2. We first focus on the highly conducting contact configuration where the atomic structure of the C_{60} along with vanadium atoms and first copper layers of both sides have been relaxed to the force threshold of 0.05 eV/Å. We also show the transmission spin polarization (TSP), defined as

$$TSP = \frac{T_{maj} - T_{min}}{T_{maj} + T_{min}}, \quad (1)$$

and channel decomposed transmission values in Figure 2. Here, we first point out a remarkable spin-filtering effect in the FM arrangement, whereby two almost open channels conduct in the vicinity of the Fermi level for the majority spin component, while the minority channels are almost closed. For the minority spin component the resonance peaks at ≈0.2 and 0.4 eV produce dips in the corresponding TSP curve, however, these will only be of importance for a voltage bias comparable to these energies. Transmission eigenvalues of the first three dominant channels are shown in the third and forth panels, that clearly show two distinct channels for the FM-majority spin channels. Furthermore, it is striking that the channels in the AFM configuration are almost closed, except for small resonance peaks at ≈0.35 eV, which again only will come into play for higher voltages.

To better understand the nature of spin transport in the system, we have calculated the spatially-resolved scattering states in the contact region [32]. The results are shown in Figure 3. Here, we consider the conducting FM arrangement and focus on the two eigenchannel scattering states with highest transmission at E_F (moving in the direction up-to-down), which both are almost fully transmitting. For the majority spins, we notice the d_{zx} and d_{yz} orbital nature of wavefunctions on the V adatoms contacting C_{60} (z chosen perpendicular to the surface). This is in accor-

Table 1: Binding energy $E_b = E_{C_{60}+adatom} - E_{C_{60}} - E_{adatom}$ and total magnetization $M_T = \int_V (n_{up} - n_{down}) dr^3$ per unit cell. The distance between the adatom and C_{60} has been optimized.

adatom	56[a] (eV)	66[b] (eV)	hexagon (eV)	pentagon (eV)	top (eV)	M_T
V	−1.13	−1.25	−0.93	−1.40	−1.06	5.00
Cr	−0.58	−0.46	1.77	2.74	−0.49	6.00
Mn	−0.39	−0.58	−0.25	−0.33	−0.40	5.00
Fe	−0.83	0.08	−0.87	−0.55	−0.75	4.00
Co	−0.90	−1.22	−0.87	−0.88	−0.80	1.00
Ni	−1.48	−1.64	−1.24	−1.44	−1.26	0.00
Cu	−0.79	−0.60	−0.08	−0.34	−0.74	0.00

[a]56 refers to sites above edges shared between a hexagon and a pentagon and top means top of a carbon atom.
[b]66 refers to sites above edges shared between two hexagons.

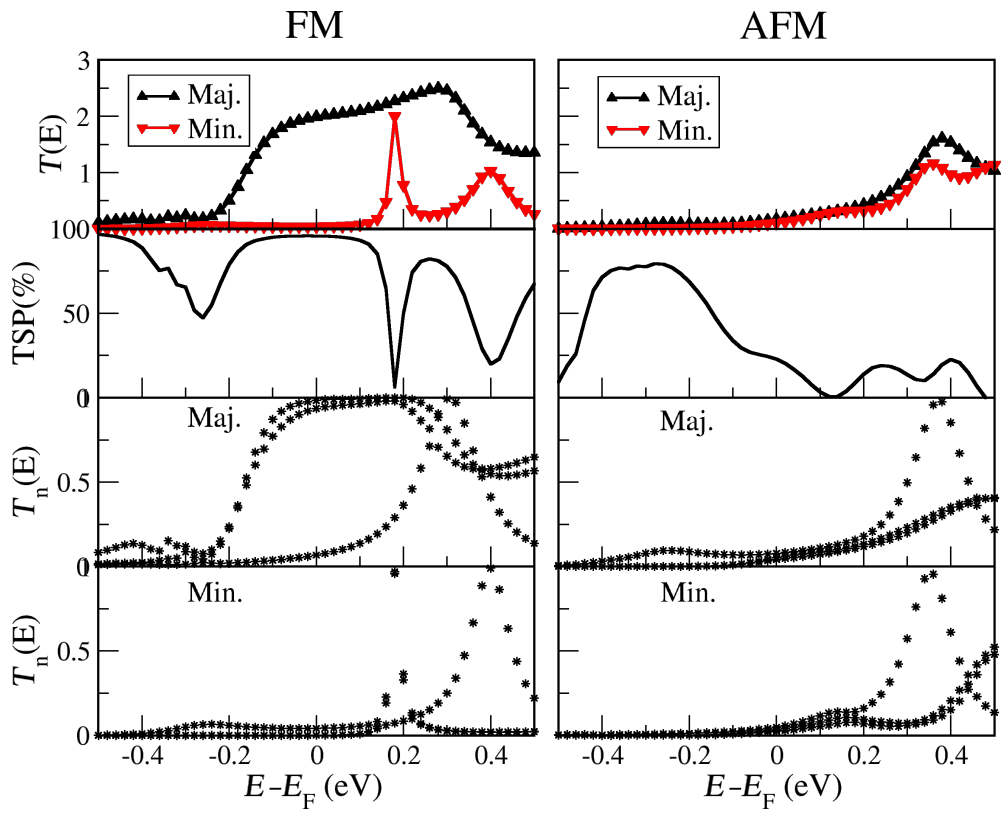

Figure 2: Transmission spectra for FM and AFM arrangements. The first row shows spin-resolved transmission spectra for each arrangement. The second row demonstrates the corresponding transmission spin polarization as defined in the text. The third and forth rows show transmission eigenvalues for three channels in each spin component.

dance with the Mulliken population analysis of the majority spin states of the V tip and adatoms, where the d_{zx} and d_{yz} each appears half-filled. On the other hand, the d_{xy}, $d_{x^2-y^2}$ and d_z^2 are closer to being filled, while the s is closer to being empty. This points to a charge transfer from the V atoms to the C_{60} leaving the d_{zx}/d_{yz} orbital energies closest to E_F. Since the d_{zx}/d_{yz} orbitals match the symmetry with angular momentum $m = 1$ for rotation around the V–C_{60}–V axis of the pentagon-prone 3-fold degenerate LUMO states (t_{1u} symmetry [33,34]), we can expect the observed orbitals in the transport channels. For minority spins d_{zx} and d_{yz} orbitals are almost empty and shifted away from E_F, resulting in a vanishing transmission. The rotational symmetric $m = 0$ channels appear as resonances in the channel transmissions above E_F and thus play a minor role.

In typical STM experiments the conductance is probed from the tunnel-regime to contact. We have performed transport calculations as the tip is approaching the surface adatom until the tip–molecule distance (d shown in Figure 1) approximately reaches the equilibrium distance discussed above. In Figure 4 we display the conductance along with the corresponding TSP as a function of the tip distance. As can be seen, there is a trend of an increasing conductance of the majority spins and thus TSP, in the FM case, while in the AFM case, the conductance values are considerably smaller all the way to the equilibrium contact distance.

The difference between the FM and AFM conductance properties indicates how it is possible to probe the spin coupling mediated by the C_{60} between the magnetic tip and substrate. The calculated magnetic interaction between the tip and adatom, the magnetic exchange energy defined as $E_{FM} - E_{AFM}$, is shown in Figure 5a when the tip molecule is approaching the adatom. This shows that the FM arrangement becomes favorable as the molecule reaches the equilibrium distance to the surface adatom. To be sure about the fidelity of the values obtained here, we have performed the same study using the PW method. We found that the trend is the same and that the values are even more pronounced in favor of FM arrangement, though of the same order of magnitude.

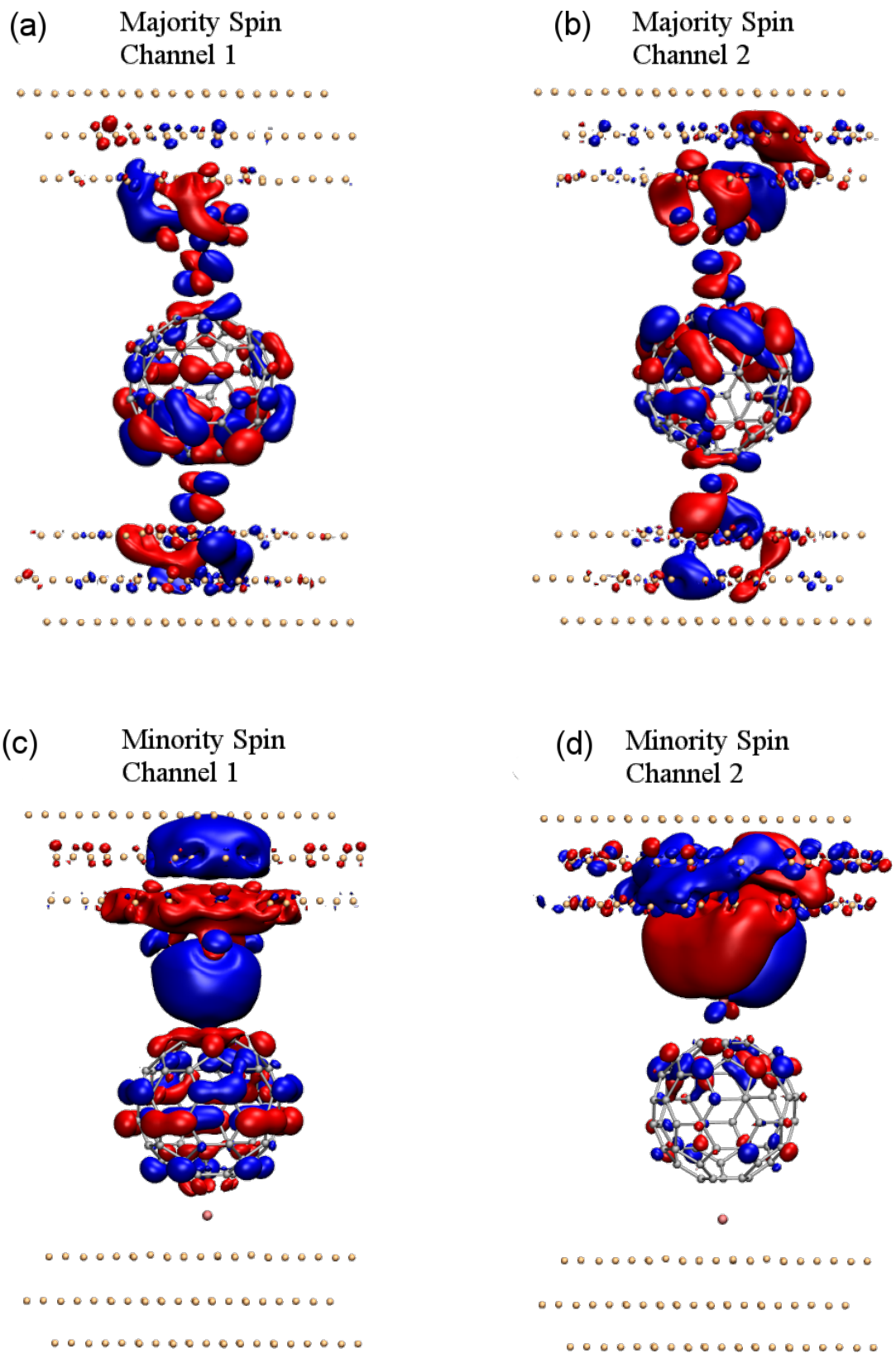

Figure 3: Scattering states at $E = E_F$ of first two dominant eigenchannels for (a,b) majority and (c,d) minority spin components in FM arrangement. Blue and red indicate the positive and negative sign of the real part of the wavefunction.

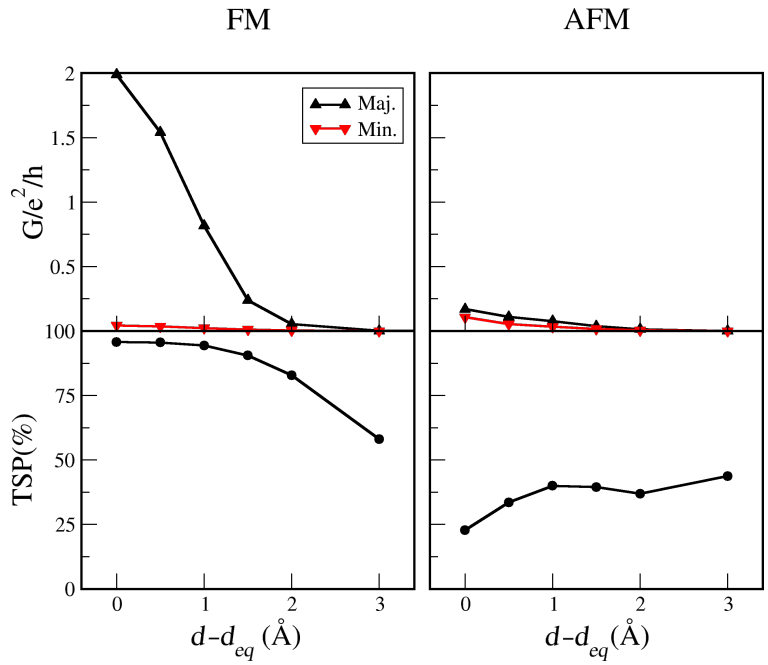

Figure 4: Spin-resolved conductance and transmission spin polarization (TSP) vs C_{60}-adatom separation.

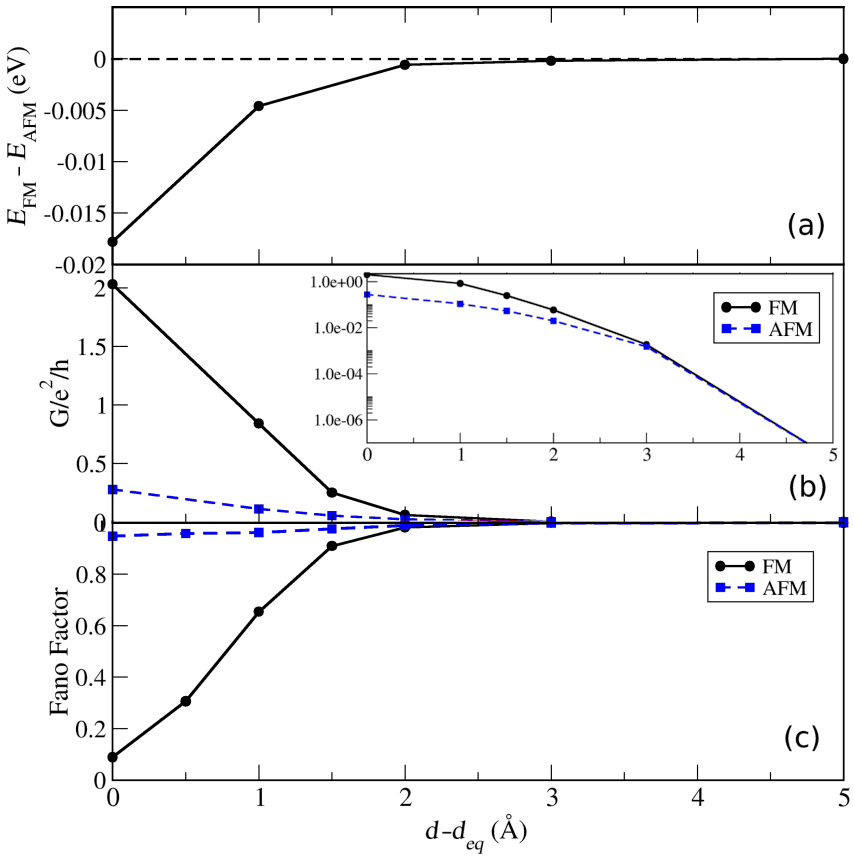

Figure 5: (a) Magnetic exchange energy, (b) conductance for FM and AFM configurations (inset in log-scale) and (c) Fano factor of transmission as a function of C_{60}-adatom separation for the FM and AFM configurations.

A graph of the total conductance versus C_{60}-adatom distance is shown in Figure 5b. The conductance behavior demonstrates a *magnetic* valve, being closed for FM and open for AFM, if we imagine an external control over the magnetization of tip/substrate. In a typical experiment with a bulk magnetic tip the magnetization of the tip will be determined by the intrinsic magnetic anisotropy of the crystalline magnetization, which fixes the magnetization axes. As the tip molecule approaches the adatom on the non-magnetic surface, its magnetization will be determined by the interaction with the tip mediated by the molecule. In this case the adatom magnetization will align according to the thermal occupations.

The absolute distance is typically not known in an actual STM experiment. In principle, a particular conductance could be realized with both FM or AFM spin configurations – a conductance of e^2/h could result from a single spin-channel with perfect transmission or two half-transmitting channels. In combination with measurements of the conductance, measurements of current shot-noise as characterized by the Fano factor,

$$F = \frac{\sum_n T_n\left(E_\mathrm{F}\right)\left(1-T_n\left(E_\mathrm{F}\right)\right)}{\sum_n T_n\left(E_\mathrm{F}\right)}, \qquad (2)$$

can provide further insights into the distribution of transmissions in the conductance channels as demonstrated for molecular contacts [35,36]. In Figure 5c, we observe how the noise is significantly smaller for the FM configuration and drops already well before contact ($d - d_{eq} \approx 1.5$ Å) is established. Since the shot noise in the FM case is low in contact, while the conductance is close to $2G_0$, it can be inferred from this that the transport is carried by two almost perfectly transmitting channels in the FM contact configuration.

Conclusion

We have performed first-principles spin-polarized density functional calculations and investigated the electron transport properties of a C_{60}-molecular junction in a setup relevant for STM experiments. Our results demonstrate how the FM and AFM configurations can be identified due to their markedly different conductance and shot noise. Thus, it may allow for the study of the magnetic coupling between tip and substrate mediated by the molecule as the contact is being formed. For the FM case only the majority channels contribute to transport and the system act as a spin-filter. This is similar to what has been predicted for vanadium multidecker systems [25,26], but the STM setup we propose here might be more accessible for experiments.

Acknowledgements

We thank Dr. Thomas Frederiksen for fruitful discussions. M. K. acknowledges the financial support from the state of Bremen.

References

1. Xiong, Z. H.; Wu, D.; Vardeny, Z. V.; Shi, J. *Nature* **2004,** *427,* 821–824. doi:10.1038/nature02325
2. Rocha, A. R.; García-Suárez, V.; Bailey, S. W.; Lambert, C. J.; Ferrer, J.; Sanvito, S. *Nat. Mater.* **2005,** *4,* 335–339. doi:10.1038/nmat1349
3. Koopmans, B.; Wagemans, W.; Bloom, F. L.; Bobbert, P. A.; Kemerink, M.; Wohlgenannt, M. *Philos. Trans. R. Soc., A* **2011,** *369,* 3602–3616. doi:10.1098/rsta.2011.0172
4. Herrmann, C.; Solomon, G. C.; Ratner, M. A. *J. Am. Chem. Soc.* **2010,** *132,* 3682–3684. doi:10.1021/ja910483b
5. Schull, G.; Frederiksen, T.; Brandbyge, M.; Berndt, R. *Phys. Rev. Lett.* **2009,** *103,* 206803. doi:10.1103/PhysRevLett.103.206803
6. Berndt, R.; Kröger, J.; Néel, N.; Schull, G. *Phys. Chem. Chem. Phys.* **2010,** *12,* 1022–1032. doi:10.1039/b908672m
7. Schull, G.; Frederiksen, T.; Arnau, A.; Sánchez-Portal, D.; Berndt, R. *Nat. Nanotechnol.* **2011,** *6,* 23–27. doi:10.1038/nnano.2010.215
8. Martin, C. A.; Ding, D.; Sørensen, J. K.; Bjørnholm, T.; van Ruitenbeek, J. M.; van der Zant, H. S. J. *J. Am. Chem. Soc.* **2008,** *130,* 13198–13199. doi:10.1021/ja804699a
9. Braun, S.; Salaneck, W. R.; Fahlman, M. *Adv. Mater.* **2009,** *21,* 1450–1472. doi:10.1002/adma.200802893
10. Bode, M. *Rep. Prog. Phys.* **2003,** *66,* 523. doi:10.1088/0034-4885/66/4/203
11. Wiesendanger, R.; Güntherodt, H.-J.; Güntherodt, G.; Gambino, R. J.; Ruf, R. *Phys. Rev. Lett.* **1990,** *65,* 247–250. doi:10.1103/PhysRevLett.65.247
12. Hirjibehedin, C. F.; Lutz, C. P.; Heinrich, A. J. *Science* **2006,** *312,* 1021–1024. doi:10.1126/science.1125398
13. Néel, N.; Kröger, J.; Berndt, R. *Phys. Rev. B* **2010,** *82,* 233401. doi:10.1103/PhysRevB.82.233401
14. Liljeroth, P.; Swart, I.; Paavilainen, S.; Repp, J.; Meyer, G. *Nano Lett.* **2010,** *10,* 2475–2479. doi:10.1021/nl100834v
15. Iacovita, C.; Rastei, M. V.; Heinrich, B. W.; Brumme, T.; Kortus, J.; Limot, L.; Bucher, J. P. *Phys. Rev. Lett.* **2008,** *101,* 116602. doi:10.1103/PhysRevLett.101.116602
16. Brede, J.; Atodiresei, N.; Kuck, S.; Lazić, P.; Caciuc, V.; Morikawa, Y.; Hoffmann, G.; Blügel, S.; Wiesendanger, R. *Phys. Rev. Lett.* **2010,** *105,* 047204. doi:10.1103/PhysRevLett.105.047204
17. Schmaus, S.; Bagrets, A.; Nahas, Y.; Yamada, T. K.; Bork, A.; Bowen, M.; Beaurepaire, E.; Evers, F.; Wulfhekel, W. *Nat. Nanotechnol.* **2011,** *6,* 185–189. doi:10.1038/nnano.2011.11
18. Tao, K.; Stepanyuk, V. S.; Hergert, W.; Rungger, I.; Sanvito, S.; Bruno, P. *Phys. Rev. Lett.* **2009,** *103,* 57202. doi:10.1103/PhysRevLett.103.057202
19. Polok, M.; Fedorov, D. V.; Bagrets, A.; Zahn, P.; Mertig, I. *Phys. Rev. B* **2011,** *83,* 245426. doi:10.1103/PhysRevB.83.245426
20. Brune, H.; Gambardella, P. *Surf. Sci.* **2009,** *603,* 1812–1830. doi:10.1016/j.susc.2008.11.055
21. Atodiresei, N.; Brede, J.; Lazić, P.; Caciuc, V.; Hoffmann, G.; Wiesendanger, R.; Blügel, S. *Phys. Rev. Lett.* **2010,** *105,* 066601. doi:10.1103/PhysRevLett.105.066601
22. Crabtree, R. *The organometallic chemistry of the transition metals;* John Wiley and Sons: Hoboken, NJ, USA, 2009.

23. Tao, K.; Stepanyuk, V. S.; Bruno, P.; Bazhanov, D. I.; Maslyuk, V. V.; Brandbyge, M.; Mertig, I. *Phys. Rev. B* **2008,** *78,* 014426. doi:10.1103/PhysRevB.78.014426
24. Wang, L.; Cai, Z.; Wang, J.; Lu, J.; Luo, G.; Lai, L.; Zhou, J.; Qin, R.; Gao, Z.; Yu, D.; Li, G.; Mei, W. N.; Sanvito, S. *Nano Lett.* **2008,** *8,* 3640–3644. doi:10.1021/nl8016016
25. Maslyuk, V. V.; Bagrets, A.; Meded, V.; Arnold, A.; Evers, F.; Brandbyge, M.; Bredow, T.; Mertig, I. *Phys. Rev. Lett.* **2006,** *97,* 097201. doi:10.1103/PhysRevLett.97.097201
26. Koleini, M.; Paulsson, M.; Brandbyge, M. *Phys. Rev. Lett.* **2007,** *98,* 197202. doi:10.1103/PhysRevLett.98.197202
27. Weber, S. E.; Rao, B. K.; Jena, P.; Stepanyuk, V. S.; Hergert, W.; Wildberger, K.; Zeller, R.; Dederichs, P. H. *J. Phys.: Condens. Matter* **1997,** *9,* 10739. doi:10.1088/0953-8984/9/48/016
28. Soler, J. M.; Artacho, E.; Gale, J. D.; García, A.; Junquera, J.; Ordejón, P.; Sánchez-Portal, D. *J. Phys.: Condens. Matter* **2002,** *14,* 2745. doi:10.1088/0953-8984/14/11/302
29. Perdew, J. P.; Burke, K.; Ernzerhof, M. *Phys. Rev. Lett.* **1996,** *77,* 3865–3868. doi:10.1103/PhysRevLett.77.3865
30. Brandbyge, M.; Mozos, J.-L.; Ordejon, P.; Taylor, J.; Stokbro, K. *Phys. Rev. B* **2002,** *65,* 165401. doi:10.1103/PhysRevB.65.165401
31. Giannozzi, P.; Baroni, S.; Bonini, N.; Calandra, M.; Car, R.; Cavazzoni, C.; Ceresoli, D.; Chiarotti, G. L.; Cococcioni, M.; Dabo, I.; Dal Corso, A.; de Gironcoli, S.; Fabris, S.; Fratesi, G.; Gebauer, R.; Gerstmann, U.; Gougoussis, C.; Kokalj, A.; Lazzeri, M.; Martin-Samos, L.; Marzari, N.; Mauri, F.; Mazzarello, R.; Paolini, S.; Pasquarello, A.; Paulatto, L.; Sbraccia, C.; Scandolo, S.; Sclauzero, G.; Seitsonen, A. P.; Smogunov, A.; Umari, P.; Wentzcovitch, R. M. *J. Phys.: Condens. Matter* **2009,** *21,* 395502. doi:10.1088/0953-8984/21/39/395502
32. Paulsson, M.; Brandbyge, M. *Phys. Rev. B* **2007,** *76,* 115117. doi:10.1103/PhysRevB.76.115117
33. Haddon, R. C.; Brus, L. E.; Raghavachari, K. *Chem. Phys. Lett.* **1986,** *125,* 459–464. doi:10.1016/0009-2614(86)87079-8
34. Hands, I. D.; Dunn, J. L.; Bates, C. A. *Phys. Rev. B* **2010,** *81,* 205440. doi:10.1103/PhysRevB.81.205440
35. Djukic, D.; van Ruitenbeek, J. M. *Nano Lett.* **2006,** *6,* 789–793. doi:10.1021/nl060116e
36. Kiguchi, M.; Tal, O.; Wohlthat, S.; Pauly, F.; Krieger, M.; Djukic, D.; Cuevas, J. C.; van Ruitenbeek, J. M. *Phys. Rev. Lett.* **2008,** *101,* 046801. doi:10.1103/PhysRevLett.101.046801

License and Terms

The definitive version of this article is the electronic one which can be found at:
doi:10.3762/bjnano.3.69